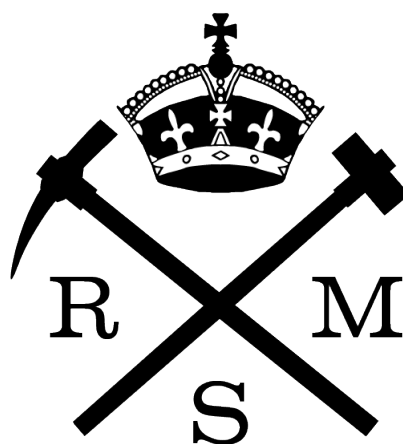# MATHEMATICAL MODELLING OF VANADIUM-BASED REDOX FLOW BATTERIES

Catalina A. Pino-Muñoz

Department of Earth Science and Engineering
Imperial College London

Supervisor: PROF. NIGEL P. BRANDON
Co-supervisor: DR. VLADIMIR YUFIT

SUBMITTED IN PARTIAL FULFILMENT OF THE REQUIREMENTS FOR THE DEGREE OF
DOCTOR OF PHILOSOPHY IN ENGINEERING AND
THE DIPLOMA OF IMPERIAL COLLEGE

LONDON
FEBRUARY 5, 2020

Abstract

Electrochemical energy storage could facilitate the integration of intermittent renewable sources, such as wind and solar, allowing for a more stable, reliable and flexible electrical grid. Vanadium redox flow batteries (VRFBs) are an attractive technology due to their capability to decouple power and energy, however they have displays limited deployment, which has been limited by cost. Hybrid-type redox flow batteries such as a Regenerative Hydrogen-Vanadium Fuel Cell (RHVFC) could allow to overcome the cost dependency of all-vanadium systems with regards to the vanadium requirements. Modelling and simulation appear as an indispensable tool to support the design and optimisation of these systems, saving time and reducing costs. On the other hand, physical-based models can capture the dependency of the cell performance on the operating conditions and physico-chemical properties. This thesis investigates the performance behaviour of RHVFC by means of mathematical representations of the system. Firstly, the conventional approach involving unit cell modelling for VRFBs is studied and implemented to understand the interplay of different phenomena and the possible similarities with the system of interest. Then, a unit cell model for a RHVFC is proposed, giving special attention to the equilibrium and kinetics equation used in describing the limiting electrode. A complete Nernst equation is derived to estimate the equilibrium potential, while a Butler-Volmer kinetics including the effect of concentration of protons and mass-transport limitations is used to describe the cathodic kinetics. This model is then modified to include the crossover phenomena, by means of a simplified treatment of transport of species in the cation-exchange membrane by means of diffusive, convective and migration mechanisms. The transport of species across the membrane controls the loss in capacity of the cell when continuous cycling operation is tested. This model allowed for the characterisation of a laboratory scale cell of a hydrogen-vanadium system and the simulation of its performance, where extensive experimental data of single-cycle charge-discharge potential, power density and cycling performance was studied. It was observed that the

crossover effect was not fully captured for a unit cell model, reproducing the trends during continuous operation but showing some discrepancies with the experimental results. These results indicated the need for a more complex model, such a continuum approach, to describe the transport of species across the electrodes and membrane. Therefore, a time-dependant model considering a Poisson-Nernst-Planck one-dimensional approach to describe the cathode and membrane of a RHVFC was implemented. Initial results allowed to assess the evolution of concentration and potential profiles across the model domains, capturing the interfacial behaviour that appears due to the selectivity of the membrane. These interfacial phenomena produced a steep change in the value of ionic potential and concentrations across a narrow thickness of nano-meters. The model was used to indicate the dependency of crossover fluxes of species across the membrane when the applied current density increases. The mass-transport limitations effects on the cell performance, which were strongly affected by the transport parameters of species, were displayed by the model. This initial crossover model is the first part of a more extensive study of crossover, which will include the testing of the model capability in predicting cell potential over continuous operation, as well as the assessment of alternative modelling approaches such a Donnan-Nernst-Planck model.

Copyright

Plagiarism declaration

I hereby declare that all of the work presented in this thesis except that which is appropriately acknowledged and referenced as such is my own, and that it has not been submitted in fulfilment of the requirements of any other degree at Imperial College London or elsewhere.

Catalina A. Pino Muñoz

February 5, 2020

Acknowledgements

I would like to first express my gratitude to my main supervisor Prof. Nigel Brandon for giving me the opportunity to transition to a different area of study and for his support and patience during this process. He is always more than willing to share his vast wisdom and experience. I would also like to thank my co-supervisor Dr. Vladimir Yufit. I extend my gratitude to current and past members of my research group, especially to Dr. Antonio Bertei for his unconditional support and always being happy to discuss my research, offering me guidance and reassurance when I needed it. Dr. Harini Hewa-Dewage, who shared her lab experience and taught me how to run a RFB cell, as well as for the many conversations and laughs. Dr.Samuel Cooper, who has always been available to have a conversation about science that usually rambled to include a million other things. An additional thanks for reading through my first paper and for encouraging me to learn LATEX and Git that ultimately has made my life easier. More recently, Dr. Aayan Banerjee with whom I have had various long lasting science discussions and research planning. Our meetings have always left me with a great feeling that there are more challenges and possibilities of collaborating in great projects in the near future. An extra thank-you for reading a chapter of this thesis and giving me detailed and very relevant feedback. A special thanks to Bowen Song, Zadariana Jamil, Yuhua Xia and Mengzheng Ouyang, for their friendship and company, especially the time we shared during lunch breaks and dinners, and how to forget the trip to Spain.

My PhD experience has been greatly enhanced by the incredible people that I have met in the Earth Science and Engineering department. Especially, everyone that is part of "Cool People" and with whom I have shared countless lunch breaks ending with the daily Guardian's crossword: Pancho, Dennis, Diego, Becky, Izzy, Robin, Jorge and Pablo. Most of them from the mineral processing group, of which I think that now I am a non-

To my mother, María Eliana Muñoz Fuenzalida

Contents

List of Figures

List of Tables

Nomenclature

Acronyms

1D	One-dimensional
2D	Two-dimensional
3D	Three-dimensional
AE	Anion exchange
CE	Cation exchange; Coulombic efficiency
CL	Catalyst layer
CNE	Complete Nernst equation
CNT	Carbon nanotube
CSTR	Continuous stirred tank reactor
DAE	Differential algebraic equation
DGM	Dusty gas model
DMAEMA	Dimethylaminoethyl methacrylate
DNP	Donnan Nernst Planck
EBM	Equation based model
EBN	Electrospun blended nano-fiber
ECES	Electrochemical energy storage
EE	Energy efficiency
EES	Electricity energy storage
EIS	Electrochemical Impedance Spectroscopy
GDL	Gas diffusion layer
HER	Hydrogen evolution reaction
HOR	Hydrogen oxidation reaction
MEA	Membrane electrode assembly
MUMPS	Multifrontal Massively Parallel Solver
NE	Nernst equation
NRMSE	Normalised root mean square error
OCP	Open circuit potential
ODE	Ordinary differential equation
ORR	Oxygen reduction reaction
PDE	Partial differential equation

PEG	Polyethylene Glycol
PEM	Polymer electrolyte membrane
PHES	Pump hydro energy storage
PNP	Poisson Nernst Planck
PSB	Polysulphide bromide flow battery
RFB	Redox flow battery
RFC	Regenerative fuel cell
RHVFC	Regenerative hydrogen vanadium fuel cell
RMSE	Root mean square error
SHE	Standard hydrogen electrode
SNE	Simplified Nernst equation
SOC	State of charge
SS	Steady state
TD	Time dependent
TV	Tafel-Volmer
VBC	Vinylbenzyl chloride
VE	Voltage efficiency
VRFB	All-vanadium redox flow battery

Latin Symbols

A	cross-sectional area, m^2	
a	specific surface area, $\mathrm{m}^3\,\mathrm{m}^{-2}$	
a_i	activity of species i, –	
b	quantity concentration, –	
c°	standard molarity, $\mathrm{mol\,L}^{-1}$	
c_i	concentration of species i, $\mathrm{mol\,m}^{-3}$	
c_V	total concentration of vanadium, $\mathrm{mol\,m}^{-3}$	
CPE	constant phase element, $\Omega^{-1}\mathrm{s}^n$ where n is the CPE exponent.	
d	diameter, m	
D_h	hydraulic diameter, m	
D_i	diffusion coefficient of species i, $\mathrm{m}^2\,\mathrm{s}^{-1}$	
$D_{i,j}$	binary diffusion coefficient of species i and j, $\mathrm{m}^2\,\mathrm{s}^{-1}$	
$D_{Kn,i}$	Knudsen diffusion coefficient of species i, $\mathrm{m}^2\,\mathrm{s}^{-1}$	
Da	Damköhler number , –	
E	potential, V	
E°	standard potential, V	
E_a	activation energy, $\mathrm{kJ\,mol}^{-1}$	
EU	electrolyte utilisation	
EW	equivalent molecular weight of polymer electrolyte membrane, $\mathrm{kg/mol_{SO_3H}}$	
f	friction resistance coefficient, –	

f_F	Fanning friction factor, –
f_{rel}	relative sensitivity factor, –
f_V	volume fraction of water in the membrane, –
F	Faraday's constant, $96\,485\,\mathrm{C\,mol^{-1}}$; flux density
G	mass flux, $\mathrm{kg\,m^{-2}\,s^{-1}}$; Gibbs free energy
G_i	sensitivity coefficient of fitting parameter i, –
h	height, m
I	current, A
j	current density, $\mathrm{A\,m^{-2}}$
j_0	exchange current density, $\mathrm{A\,m^{-2}}$
k	permeability, $\mathrm{m^2}$
k_1	Sulphuric acid dissociation coefficient, –
k_2	Bi-sulphate dissociation coefficient, –
k_B	Boltzmann constant, $\mathrm{m^2\,kg\,s^{-2}\,K^{-1}}$
K_f	minor resistance coefficient, –
K_{KC}	Kozeny-Carman constant, –
k_{-V}	backward rate constant of Volmer reaction, $\mathrm{mol\,cm^{-2}\,s^{-1}}$
k_{ad}	adsorption rate constant, $\mathrm{mol\,cm^{-2}\,s^{-1}}$
k_{ca}	cathode rate constant, $\mathrm{m\,s^{-1}}$
k_c	condensation rate constant, $\mathrm{s^{-1}}$
k_{des}	desorption rate constant, $\mathrm{mol\,cm^{-2}\,s^{-1}}$
k_d	degree of dissociation, –
k_e	evaporation rate constant, $\mathrm{atm^{-1}\,s^{-1}}$
k_m	mass-transport coefficient, $\mathrm{m^2\,s^{-1}}$
k_V	forward rate constant of Volmer reaction, $\mathrm{mol\,cm^{-2}\,s^{-1}}$
l_k	thickness of domain k, m
L	flow length, m; inductance, H
M	molecular weight, $\mathrm{kg\,mol^{-1}}$
m	mass, g
m_i	molality of species i, $\mathrm{mol\,kg^{-1}}$
M_i	molecular weight of species i, $\mathrm{kg\,mol^{-1}}$; symbol of species i
$\dot{n}_i$	molar flow rate of species i, $\mathrm{mol\,s^{-1}}$
n	number of electrons, –
N_A	Avogadro constant, $6.02 \times 10^{23}\,\mathrm{mol^{-1}}$
N_i	molar flux of species i, $\mathrm{mol\,m^{-2}\,s^{-1}}$
n_i	number of moles of species i, –
O	oxidised species, –
P	power, $\mathrm{W\,m^{-2}}$
p	pressure, Pa
p_i	partial pressure of species i, Pa

Q	flow rate, $\text{m}^3\,\text{s}^{-1}$; electric charge or capacity, $\text{A}\,\text{s}$;
Q_M	molar equilibrium dissociation quotient, –
q_e	single electron charge, $1.60 \times 10^{-19}\,\text{C}$
r	radius, m; rate of reaction, s^{-1}
R	reduced species, –
R	universal gas constant, $8.314\,\text{J}\,\text{mol}^{-1}\,\text{K}^{-1}$
R_an	roughness factor of CL, $\text{m}^2\,\text{m}^{-2}$
R_C	extra ohmic resistance, $\Omega\,\text{cm}^2$
R_k	resistance of component k, $\Omega\,\text{cm}^2$
R_s	series resistance, $\Omega\,\text{cm}^2$
R_w	phase change rate, $\text{mol}\,\text{s}^{-1}$
Re	Reynolds number, –
S	specific area of reaction, $\text{m}^2\,\text{m}^{-3}$; source term
s	liquid saturation, –
S_d	dissociation reaction term, $\text{mol}\,\text{s}^{-1}$
s_i	stoichiometric coefficient, –
SOC	state of charge, –
T	temperature, K
t	time, s
v	velocity, $\text{m}\,\text{s}^{-1}$
V	volume, m^3
V_m	molar volume of dry membrane, $\text{m}^3\,\text{mol}^{-1}$
w	width, m
x_i	molar fraction of species i, –
y_i	molar fraction of species i, –
Z	impedance, $\Omega\,\text{m}^2$
z_i	charge number of species i, –

Greek Symbols

α	transfer coefficient of charge-transfer eaction, –
β	transfer coefficient of charge-transfer reaction, –
β_d	dissociation rate constant, s^{-1}
Γ	generalised diffusion coefficient; driving force vector
γ_i	activity coefficient of species i, –
γ_des	electrolytic desorption rate coefficient in CL, s^{-1}
Δ	difference, drop, –
δ_0	Nernst diffusion layer, m
δ_D	thickness of interfacial region, m
ϵ	permittivity, $\text{F}\,\text{m}^{-1}$
ϵ_0	permittivity of free space, $\text{F}\,\text{m}^{-1}$

ϵ_i	characteristic Lennard-Jones energy of species i, $m^2\,kg\,s^{-2}$
$\epsilon_{i,j}$	characteristic binary Lennard-Jones energy, $m^2\,kg\,s^{-2}$
ε	porosity or volume fraction, –
η	overpotential, V
θ	hydrogen coverage, –; parameters; normalised potential
κ	permeability of the cathode, –
λ	content of water, mol of water per mol of sulphonic acid sites
μ	dynamic viscosity, $kg\,m^{-1}\,s^{-1}$
μ_i°	standard chemical potential if species i, –
μ_i	chemical potential if species i, –
$\tilde{\mu}_i$	electrochemical potential of species i, –
ξ_{drag}	electro-osmotic drag coefficient, –
ρ	density, $kg\,m^{-3}$; charge density, $A\,s\,m^{-3}$
σ_i	molecular radii of species i, Å
σ_k	conductivity of domain k, $S\,m^{-1}$
$\sigma_{i,j}$	characteristic binary Lennard-Jones length, Å
τ	tortuosity, –; characteristic time, s; time scale, s
ϕ	electrostatic potential, V
Ω_D	diffusion collision integral, –

Subscripts & Superscripts

0	initial value of variable ($t = 0$)
1	initial position in a pipe; reduced state
2	final position in a pipe; oxidised state
a	anodic
ac	activation; active
ad	adsroption
an	anode
an-el	anolyte
appl	applied
ave	average
b	bulk
BV	Butler-Volmer
C	convective
c	concentration; cathodic
c-m	cathode-membrane interface
ca	cathode
ca-el	catholyte
cc	current collector
CH	channel

ch	charge
CL	catalyst layer
CL-m	polymer electrolyte in the membrane
CT	charge transfer
D	Debye; Donnan, diffusion
des	desorption
diff	diffusion
dis	discharge
dm	dry membrane
Don	Donnan potential
dw	dissolved water
e	electrons; electrode; ionic; experimental
eff	effective
eq	equilibrium
evap	evaporation
ex	excess
EO	electro-osmotic drag
f	fixed charge, fibre
fix	fixed charge
g	gas phase
GDL	gas diffusion layer
geo	geometric
H_{ad}	adsorbed hydrogen
i	species i
IN	inlet
j	species j
k	domain k
l	ionic
lim	limiting
M	migration
m	membrane; molality; mean; molar
M, M'	metal phase
max	maximum
min	minimum
mom	momentum
NE	Nernst equation
nor	normalised
OCP	open circuit potential
ohm	Ohmic loss
OUT	outlet

p	pore; pressure
R	required
r	relative
react	electron-transfer reaction
ref	reference
rx	reaction
s	surface; solid
sat	saturation
sol	solution
SATP	standard ambient temperature and pressure condition
T	tank
T_{ref}	reference temperature, K
TV	Tafel-Volmer
V	Volmer reaction
v	water vapour
w	liquid water
wv	evaporation/condensation
x	molar fraction

Chapter 1

Introduction

1.1 The need for energy storage

Electrical energy demand is predicted to increase drastically in the next three decades (Alotto et al., 2014; Gür, 2018; Yang et al., 2011). Indeed the energy demand is estimated to grow 28% by 2040 with respect to the 575 Quads of energy, *i.e.* 606.7×10^{18} J, consumed in 2015 (Gür, 2018). This increase in energy demand requires a comparable electricity generation growth, of which 58% is expected to be provided by fossil fuels and more than a 31% by renewable sources (Colmenar-Santos et al., 2016; Gür, 2018), as shown in Table 1.1. These predicted figures are in line with the global interest in turning renewables into our primary source of electricity generation, diminishing fossil fuel consumption and its associated greenhouse gas emissions. However, in 2016 intermittent renewable sources, such as solar, wind and wave, provided only slightly more than 5% of global electricity generation (Gür, 2018) due to their cost, unpredictability, unavailability and output fluctuation. Major reductions in the cost of electricity produced by renewable sources like wind and solar have been observed in recent years, leading to competitive prices (*e.g.* ~$50 per MWh for wind power) when compared to coal-fired power (Gür, 2018). However, a penetration of intermittent renewable sources of over 20% could destabilise the grid if storage technologies are not considered (Alotto et al., 2014; Kear et al., 2012; Weber et al., 2011). In the past few years, energy sector de-regulation has allowed access to small and medium producers and increased renewables exploitation, resulting in an increase in the use of distributed generation units, which can be integrated to the grid according to resource availability (Colmenar-Santos et al., 2016; Manditereza and Bansal, 2016). A smart grid that combines renewable energy generation and large-scale energy storage (Cho et al., 2015; Gür, 2018) could coordinate capacity and the needs of generators, operators, end-users and market stakeholders; meanwhile, optimise asset utilisation and operation, and minimise costs and environmental impacts.

Table 1.1: Comparison of electric energy produced for major power generation technologies in 2016 with expected production in 2040 (Gür, 2018).

Technology	Electricity generation (2016)		Expected electricity generation (2040)	
	billion kW h	% of word	billion kW h	% of word
Worl total	23735.2	100	34049.0	100
Renewables	5593.8	23.57	10702.3	31.43
Hydro	3910.0	16.47	5677.9	16.68
Solar	275.6	1.16	1390.3	4.08
Wind	826.2	3.48	2524.5	7.41
Geothermal	77.1	0.32	353.4	1.04
Other	504.9	2.12	756.3	2.22
Nuclear	2510.1	10.58	3657.3	9.79
Fossil fuels	15631.3	65.86	19689.4	57.83

The integration of distributed generation units based on intermittent renewable sources and a smart grid requires of a wide range of technologies in power electronics, communication and control, micro-generation and hybrid systems, electrical energy storage (EES) and electrical vehicles, among others (Colmenar-Santos et al., 2016). Particularly, EES could facilitate a stable and reliable operation while allowing network flexibility. Energy storage could be engaged during periods of low demand, low generation cost, or for intermittent energy sources; while delivering during periods of high demand and high generation cost. This could address the variability and unpredictability of intermittent renewables, overcome transmission and distribution issues, and maintain power supply during outages (Chen et al., 2009; Colmenar-Santos et al., 2016; International Energy Agency, 2010).

1.2 Energy storage technology

EES can provide many grid services that would allow the decoupling of energy production from its supply, permitting sufficient generation capacity to satisfy only average rather than peak demand (Chen et al., 2009; Yang et al., 2011). Moreover, EES could reduce electricity costs for distributors and end-users when hourly pricing policies are applied, increase the efficiency of thermal power sources, and reduce CO_2 emissions (Chen et al., 2009; Yang et al., 2011). Also, renewable energy generation could rely on EES to address their intermittency and unpredictability. Depending on the type of applications and services, a potential energy storage technology must satisfy different performance and cost requirements (capital and life-cycle cost), together with reliability, durability and safety standards. These requirements can widely vary between services, and therefore, there is no single energy storage technology that meets all of them. Instead, a diverse combination of technologies is required to satisfy grid storage needs. Energy services can be divided into two main categories: power quality and energy management (Alotto et al., 2014; Chen et al., 2009; Yang et al., 2011). Power quality is related to charge/discharge cycles on short time-scale (seconds to minutes) where high discharge rates or high current densities are important, and the system's state-of-charge (SOC) will probably not vary widely. On the contrary, energy management is related to charge/discharge cycles on longer time-scales (minutes to hours) requiring MWh or even GWh levels, important features being high round trip energy efficiency, long deep-cycle life, and low operation and maintenance costs. A power-duration diagram for different EES systems is shown in Figure 1.1. Economically and technically competitive technologies must guarantee time-scale and storage capacity requirements, a large number of charge/discharge cycles allowing long lifetime operation, together with stable operation and performance, reliability and cost-effectiveness.
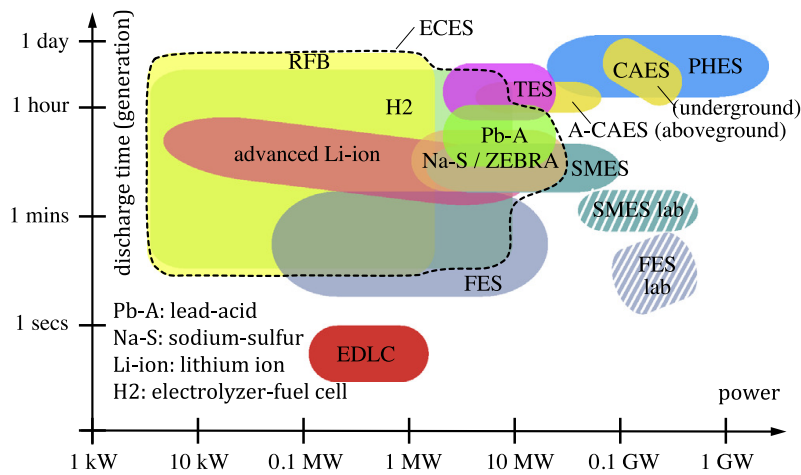
Figure 1.1: Diagram of power duration for different energy storage Technologies (Alotto et al., 2014).

Currently, installed global electricity storage represents approximately 171 GW and 1735 GWh of capacity (Sandia National Laboratories, 2016), of which pumped hydro energy storage (PHES) represents more than the 96%. Conventionally, PHES has been considered because it exhibits high energy storage levels (MW-GW and MWh-GWh) and displays low life-cycle capital cost (Alotto et al., 2014; Chen et al., 2009; Gür, 2018). PHES has been the most utilised large-scale technology and, although it offers advantages such as large volume, long storage period (hours-years) and relatively high efficiency, there are concerns that it has restrained continued development. Variables that restrained its development include specific location requirements, long lead time (~10 years), accumulating sedimentary deposition, high construction costs and environmental issues mostly related to their construction. Among prospective alternative technologies, electrochemical energy storage (ECES) systems can operate at a wide range of time-scales due to their versatility and modularity, fulfilling a wider power/duration window (Figure 1.1) and thus offering a potential solution for both power and energy management (Alotto et al., 2014; Cho et al., 2015). There are different combinations of electrode and electrolyte materials, but Li-ion batteries have been widely utilised due to their high energy density and efficiency. However, for stationary applications, they present high costs, >$600 per kWh for a battery system (Cho et al., 2015; Gallo et al., 2016; Gür, 2018). It has been estimated that for renewable energy storage without government subsidy, the cost of a storage process must be lower than $200 per kWh (Cho et al., 2015). A redox flow battery (RFB) is another attractive electrochemical energy conversion device, specially solution-based RFBs due to their capability to decouple power and energy (Alotto et al., 2014; Chen et al., 2009). RFBs can operate at a wide range of power levels and discharge times, and have the capability to scale-up in a more cost-effective form than many other systems (Perry and Weber, 2015), especially as stored energy requirements increase. Current systems display energy ranging from 10^2 to 10^7 Wh, which substantially exceeds most other ECESs (Alotto

et al., 2014). In addition, RFB can deliver a continuous release of energy at high rates of discharge, very deep discharge without impact on the cell structural integrity or electrolyte decomposition, virtually no self-discharge and long cycle life (Alotto et al., 2014; Chen et al., 2009; Leung et al., 2012; Skyllas-Kazacos et al., 2011). However, some major drawbacks include their low power density and energy density that have limited their commercialisation, the requirement for larger cell active areas, and shunt currents in manifolds and flow channels (Alotto et al., 2014) which reduce round trip efficiency. A number of different electrolyte combinations are currently available, but two appear as the basis of existing designs (Chen et al., 2009): the all-vanadium and the zinc-bromine flow battery. Alternatively, other systems have been considered, such as reversible polymer-electrolyte-membrane (PEM) fuel cells (Chen et al., 2009). In fact, reversible fuel cells are of interest to integrate with renewable power sources because of advantages such as high energy density (0.6-1.2 kWh kg-1), wide range of capacity (kW to several MW), independence in charge and discharge rates and storage capacity, and modular construction (Chen et al., 2009). Nonetheless, they present low round-trip efficiency (20-50%), especially when gas engines are used as power generation mean (Chen et al., 2009). Recently, hydrogen-based RFBs have gained attention for developing suitable ECESs, combining attractive features from RFBs and fuel cells. Some of the systems that have been studied are H_2/Fe, H_2/Br_2, H_2/Ce, and H_2/V (Hewa Dewage, 2016).

1.3 Motivation of the research

1.4 Aim of the project

The overall aim of this project is to study a hydrogen-based RFB, particularly a regenerative hydrogen vanadium fuel cell (RHVFC), by means of mathematical models that can represent the actual cell operation. This work seeks to develop mathematical models to simulate the performance of an RHVFC, as well as to study relevant transport phenomena involved in the electrodes and membrane. Unit cell models capable of simulating the potential dynamics are required, which must maintain simplicity in the model approach to make possible their use for design and control purposes. In addition, cell continuum models that can include the coupled physicochemical phenomena are required to study in detail the transport phenomena and polarisation of an RHVFC. In order to build these unit cell and continuum models, a full understanding of the processes involved is required, such as redox reactions, self-discharge, species balances, mass transport and electrochemical kinetics.

1.4.1 Objectives

The main objectives of this study are as follows:

1. To implement a unit cell model for a vanadium redox flow battery (VRFB) that can simulate the potential dynamics, and validate this model by using experimental results of an all-vanadium unit cell reported in the literature. This model will serve as a base in the development of a unit cell model for the RHVFC.

2. To propose a unit cell model for an RHVFC that can simulate the potential dynamics. This model will include on the various physicochemical phenomena involved in an RHVFC.

3. To validate the unit model for an RHVFC previously proposed by comparing simulations with experimental results from different hydrogen-vanadium cells.

4. To study, based on the validated unit cell model and the RHVFC experimental data, the cell performance in terms of polarisation curves and efficiencies.

5. To propose an improved model for an RHVFC, *i.e.*, a spatially distributed continuum model, which can simulate in detailed the species transport in the electrodes and the membrane.

6. To study and quantify the main transport phenomena involved in the self-discharge due to membrane crossover in an RHVFC, differentiating relevant processes and parameters.

1.5 Thesis structure

The present document has been organised in such a way that each chapter can be considered as a separately entity, but the whole document structure allows each chapter to build from the previous one. Thus, each chapter contains an introduction to the topic with the necessary literature to show the motivation and need for the work done. Also, a section explaining the experimental setup and methods have been included where pertinent. Finally, results and discussion and conclusion sections are included in each chapter addressing the achievement of the chapter's objectives.

Chapter 2 contains all the up-to-date background theory and tools present in the literature that is relevant to this work. A description of the all-vanadium redox flow battery and the regenerative hydrogen-vanadium fuel cell technology, along with their fundamentals, applications and limitations. This chapter presents the basics onto which the work of this thesis is built, but more importantly, signals the need for the work done in this thesis regarding the development of physical-based models of a hybrid system such as the RHVFC.

Chapter 3 outlines the mathematical framework involved in developing a unit cell (lumped) model of the most studied redox flow battery, namely an all-vanadium system. The unit cell model captures the potential dependency to operating and components parameters. Validation of this model is presented by means of comparison against experimental data and simulation results obtained from reported high-order models (two and three dimensional). This chapter lays the guidelines in the development of a dynamic reduced-order model, which are fundamental for the next chapter.

Chapter 4 presents the development and implementation of a time-dependent zero-dimensional model of a RHVFC. This model is the first reported for the vanadium-hydrogen system and builds on models previously reported for VRFBs and PEM fuel cells. This chapter contains a clear description of the fundamentals involved in the model approach, and an initial model validation using experimental data from an in-house RHVFC having $25\,\mathrm{cm}^2$. While this chapter describes one electrochemical system, in particular, it also contributes to the understanding of other systems, and therefore the model approach could be applied to similar H_2 based hybrid systems.

Chapter 5 presents a performance study of the RHVFC based on experimental data and simulations results. Extensive experimental data was collected using a $5\,\mathrm{cm}^2$ area cell, including open circuit potential, charge-discharge cycles, power curves and a cycling test. This data was used to calibrate and validate the zero-dimensional model, allowing to fit selected unknown parameters. Finally, a sensitivity analysis of the model output with respect to component parameters is carried out to identify the parameters that affect the most the cell's performance.

Chapter 6 outlines the mathematical framework involved in developing a Poisson-Nernst-Planck (PNP) model in a time-dependent one-dimensional continuum approach for an RHVFC. This model describes the one-dimensional profile of potentials, current and concentrations in the cathode and membrane, and captures their dependency to operating conditions and component properties. Quantification of the membrane crossover of vanadium and sulphuric acid species towards the anode side is studied to asses the cell degradation.

Finally, Chapter 7 contains the aggregated conclusions and achievements of all chapters in this work, including a discussion about the contributions made in each chapter and the directions of possible future work.

Chapter references

Alotto, P., Guarnieri, M., and Moro, F. Redox flow batteries for the storage of renewable energy: A review. *Renewable and Sustainable Energy Reviews*, 29:325–335, 2014.

Chen, H., Cong, T. N., Yang, W., Tan, C., Li, Y., and Ding, Y. Progress in electrical energy storage system: A critical review. *Progress in Natural Science*, 19(3):291–312, 2009.

Cho, J., Jeong, S., and Kim, Y. Commercial and research battery technologies for electrical energy storage applications. *Prog. Energy Combust. Sci.*, 48(0):84, 2015.

Colmenar-Santos, A., Reino-Rio, C., Borge-Diez, D., and Collado-Fernández, E. Distributed generation: A review of factors that can contribute most to achieve a scenario of DG units embedded in the new distribution networks. *Renewable and Sustainable Energy Reviews*, 59:1130–1148, 2016.

Gallo, A., Simões-Moreira, J., Costa, H., Santos, M., and Moutinho dos Santos, E. Energy storage in the energy transition context: A technology review. *Renewable and Sustainable Energy Reviews*, 65:800–822, 2016.

Gür, T. M. Review of electrical energy storage technologies, materials and systems: Challenges and prospects for large-scale grid storage. *Energy and Environmental Science*, 11 (10):2696–2767, 2018.

Hewa Dewage, H. *Investigation of Hydrogen based Redox Flow Batteries*. PhD thesis, Imperial College London, 2016.

International Energy Agency. *Energy Technology Perspectives: Scenarios & Strategies To 2050*. 2010. ISBN 9789264085978. doi: 10.1049/et:20060114. URL `http://www.oecd-ilibrary.org.ezproxy.library.uq.edu.au/energy/energy-technology-perspectives-2010{_}energy{_}tech-2010-en`.

Kear, G., Shah, A., and Walsh, F. Development of the allvanadium redox flow battery for energy storage: a review of technological, financial and policy aspects. *International journal of energy research*, 36:1105–1120, 2012.

Leung, P., Li, X., Ponce de León, C., Berlouis, L., Low, C. T. J., and Walsh, F. C. Progress in redox flow batteries, remaining challenges and their applications in energy storage. *RSC Advances*, 2(27):10125, 2012.

Manditereza, P. T. and Bansal, R. Renewable distributed generation: The hidden challenges A review from the protection perspective. *Renewable and Sustainable Energy Reviews*, 58:1457–1465, 2016.

Perry, M. L. and Weber, A. Z. Advanced Redox-Flow Batteries: A Perspective. *Journal of The Electrochemical Society*, 163(1):A5064–A5067, 2015.

Sandia National Laboratories. United States Department of Energy's Global Energy Storage Database (GESDB), 2016. URL `http://www.energystorageexchange.org/projects`.

Skyllas-Kazacos, M., Chakrabarti, M. H., Hajimolana, S. A., Mjalli, F. S., and Saleem, M. Progress in Flow Battery Research and Development. *Journal of The Electrochemical Society*, 158(8):R55, 2011.

Weber, A. Z., Mench, M. M., Meyers, J. P., Ross, P. N., Gostick, J., and Liu, Q. Redox flow batteries: a review. *Journal of Applied Electrochemistry*, 41(10):1137–1164, 2011.

Yang, Z., Zhang, J., Kintner-Meyer, M. C., Lu, X., Choi, D., Lemmon, J. P., and Liu, J. Electrochemical energy storage for green grid. *Chemical Reviews*, 111(5):3577–3613, 2011.

Chapter 2

General redox flow battery principles and modelling overview

2.1 Introduction

Creating an efficient and cost-competitive battery could be achieved by coupling different electrode materials and electrolytes. In a Redox Flow Battery (RFB), such electrolytes contain the active redox couples that will undergo the electrochemical reactions at each electrode. A particular case that combines the cathodic half-cell of a Vanadium Redox Flow Battery (VRFB) and the anodic half-cell of a Polymer-Electrolyte-Membrane (PEM) fuel cell is discussed here. Such a battery is referred to as a regenerative hydrogen-vanadium fuel cell and is expected to increase the efficiency and reduce the cost when compared to a conventional VRFB. Study of the different coupled phenomena inside a Regenerative Hydrogen-Vanadium Fuel Cell (RHVFC), in order to differentiate the main processes involved and to realise their relative importance, is critical to gain the understanding of how the cell performance could be improved. This is the main objective of this thesis and is discussed in the following chapters. Mathematical descriptions to obtain a representative model of the battery cell are developed and used in this thesis to study an RHVFC. Mathematical models allow the effect of component properties, design configurations, and operating conditions to be studied. They can be developed considering different levels of complexity to characterise the global cell response or specific phenomena at the component level.

This second chapter presents an introduction to Redox Flow Batteries, including its operating principles and main advantages and operating issues. A brief RFB history is also presented. Then, the RFB fundamentals are discussed, reviewing the general theory for describing equilibrium potential, electrode kinetics, and overpotentials and their relation to the operating cell potential. The figures of merit used to characterise RFB performance are also introduced. The chapter continues with the description of an RHVFC which is the main subject of this thesis and ends with a literature review on the modelling of related systems, including VRFBs and PEM fuel cells.

2.2 Introduction to redox flow batteries

2.2.1 Operation principles of redox flow batteries

A battery cell is an energy storage device that contains a positive and a negative electrode and an ion conductive separator between them. It stores or delivers energy by means of electrochemical reactions, *i.e.*, reduction-oxidation (redox) reactions, that occur at the electrodes. A redox flow battery is a particular kind of battery that uses two electrolyte solutions, namely anolyte and catholyte, which are stored in external tanks to carry the electro-active species that participate in the electrochemical reactions. Figure 2.1 presents

a schematic diagram of a conventional RFB cell, considering fully soluble redox couples, inert electrodes and separator (Skyllas-Kazacos et al., 2011), and Equations 2.2 and 2.1 present the general redox reactions for the cathode and the anode, respectively. Throughout this chapter, descriptions are provided for a conventional RFB except where otherwise stated. Two electrolyte tanks are connected to the cell by a pump system that facilitates the circulation of the electrolytes between the electrolyte tanks and half-cells. During discharge operation, in one half-cell an oxidation reaction occurring at the anode electrode generates electrons and ions. The charge-carrier ions are allowed to pass from one electrode to the other through an ion-exchange membrane that is impermeable to electrons. This ion-exchange membrane serves as a physical separator of the anolyte and catholyte solutions. The electrons are forced to circulate through an external circuit, like an electric current. Ions and electrons are then recombined in the other half-cell by means of a reduction reaction occurring at the cathode. During charge operation, the reverse process takes place, with reduction and oxidation reactions occurring at the anode and cathode, respectively. Throughout this document the following convention has been taken, the cathode, which will also be called the positive electrode, is the electrode where the reduction reaction occurs during the discharge of the battery. Therefore, the anode, which will also be called the negative electrode, is the electrode where the oxidation reaction occurs during the discharge of the battery. A more strict and consistent definition of the electrodes in the battery can be found in Section 2.3, however, it is important to clarify the concepts of cathode and anode from now onwards.
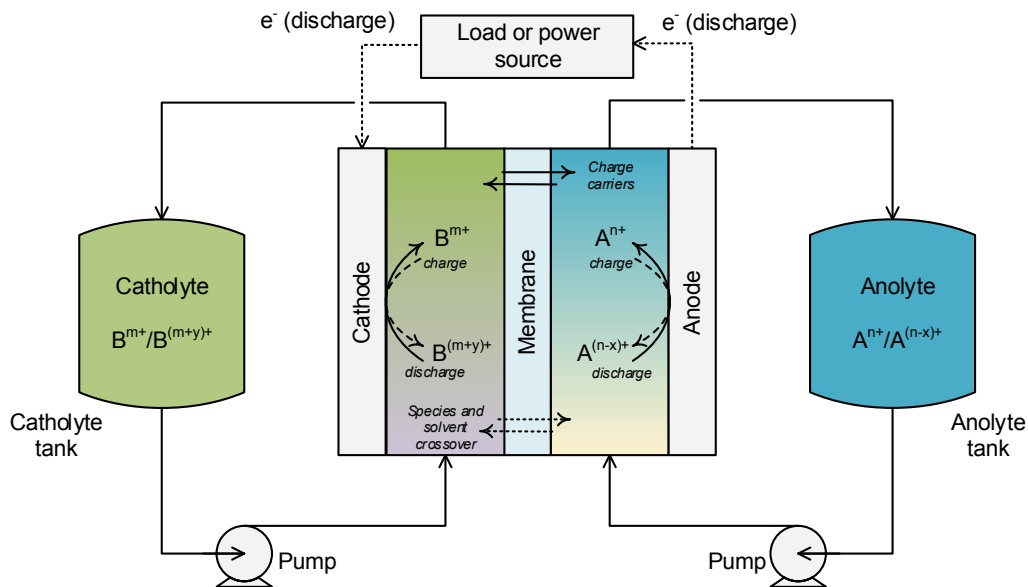
Figure 2.1: Schematic of redox flow battery with electron transport circuit and transport of ions and active species across the membranes. Adapted from Weber et al. (2011)

$$B^{m+} - ye^- \underset{\text{discharge}}{\overset{\text{charge}}{\rightleftharpoons}} B^{(m+y)+} \tag{2.1}$$

$$A^{n+} + xe^- \underset{\text{discharge}}{\overset{\text{charge}}{\rightleftharpoons}} A^{(n-x)+} \qquad (2.2)$$
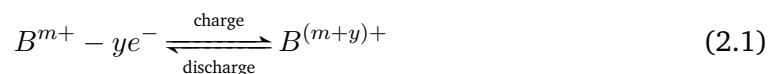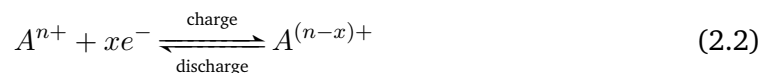
2.2.2 Cell components, advantages and operating issues of redox flow batteries

Redox flow batteries are also called regenerative fuel cells because of their similarities with fuel cells. Fuels containing chemical energy undergo charge transfer reactions at porous electrodes in both cases. However, RFBs differ from fuel cells since the electrochemical reactions involved are reversible (Skyllas-Kazacos et al., 2011; Yang et al., 2011). These reversible reactions allow for the repeated charge and the discharge of the battery. Figure 2.2 shows a typical RFB cell structure and its components. Figure 2.3a shows the Membrane Electrode Assembly (MEA) of a typical RFB along with serpentine flow field plates. This MEA is then placed in the middle of the cell when assembled as shown in Figure 2.2b. The MEA consists of an ion-exchange membrane place between two porous electrodes, while the flow field plates allow for the distribution of the electrolyte solutions on the porous electrodes. There are two flow configurations typically used in flow cells: flow-through the electrode and flow-parallel to the electrode (flow-by configuration) (Leung et al., 2012; Ye et al., 2017). The flow-by configuration, shown in Figure 2.3a, has been adopted for most of the flow batteries reported in the literature since the flow-through configuration requires very low flow rates to minimise pressure losses and presents high scale-up costs, being often impractical (Leung et al., 2012). Figure 2.2c shows three different flow channels (serpentine, parallel and interdigitated) used in a flow-by configuration. These flow channel designs have been adopted from PEM fuel cells to enhance the mass transport in RFBs. Aaron et al. (2012) proposed an RFB 'zero-gap' design which uses serpentine flow channels and demonstrated higher peak power densities than the ones reported by cells without flow channels. Nonetheless, flow channels can generate poor mechanical performance or irreversible deformation of the electrodes when an over-compression is applied. Normally, a number of cells are connected electrically to form a battery stack, both in series to increase the overall stack potential and/or in parallel to reach high current densities. Figure 2.3b presents a RFB stack with a typical first unit cell configuration. RFB stacks are normally arranged in a bipolar fashion so that current flows in series from one cell to the next (Weber et al., 2011). Manifolds are used to distribute the electrolyte solutions to the different cells of the stack, where pipes, pumps, and control valves are key components. For large-scale RFBs, pump efficiency is about 50%, which accounts for $2 - 3\%$ of the overall energy efficiency of the system (Leung et al., 2012).

The main classification of RFBs is based on their electro-active species phases (Arenas
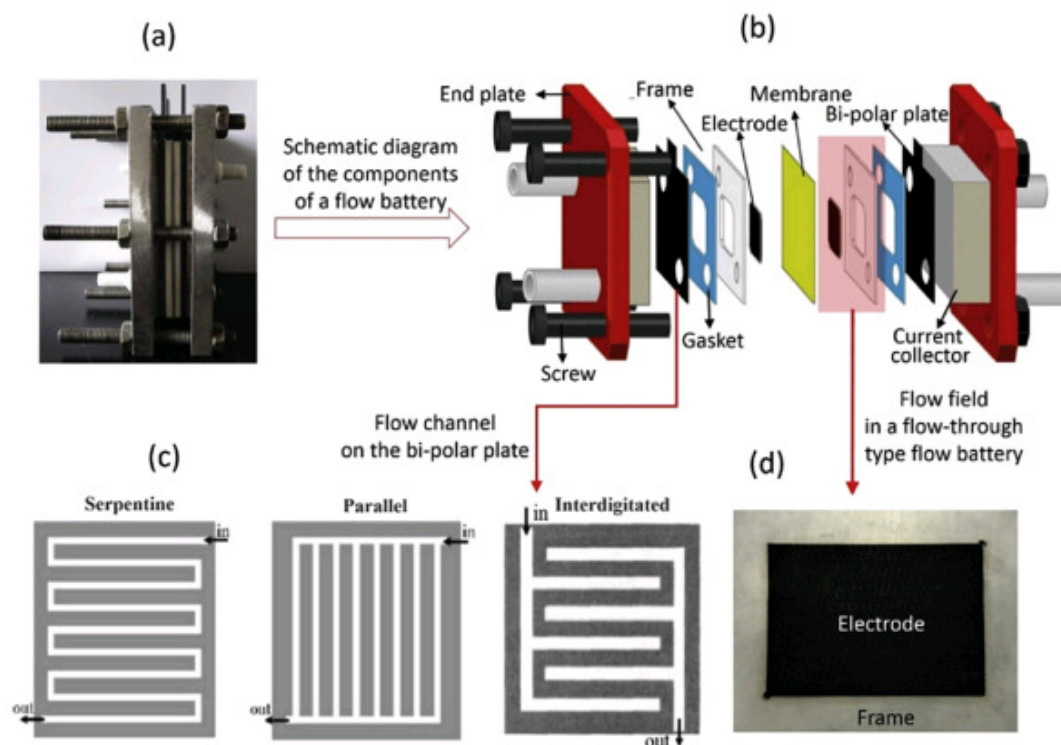
Figure 2.2: RFB cell structure (Zheng et al., 2016): (a) Picture of a single flow battery; (b) Schematic diagram of cell components for a RFB cell with separator; (c) Types of flow field plates; and (d) Picture of flow field in a flow-through configuration.
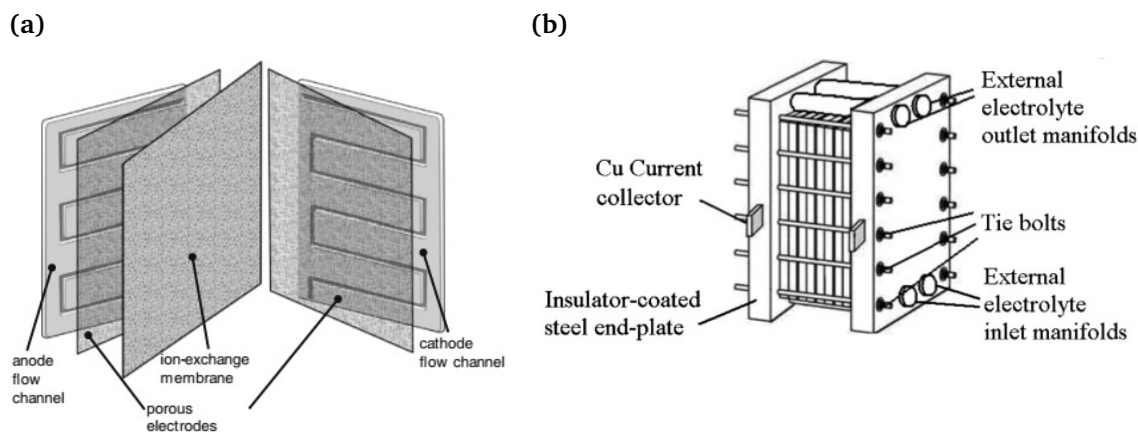
Figure 2.3: Redox flow battery components: (a) Membrane Electrode Assembly (MEA) with serpentine flow fields plates; and (b) Redox flow battery stack along with the description of a first unit cell.

et al., 2017; Leung et al., 2012; Ponce de León et al., 2006), including all liquid phases where energy is stored in dissolved reduced/oxidised species, all solid phases where energy is stored in deposits of active material in the electrodes, and a combination of liquid, solid and gas phases with at least one of the electrode reactions involving a phase change. There are additional classifications for RFBs that consider cell configurations and electrolyte types (Arenas et al., 2017; Leung et al., 2012; Ponce de León et al., 2006). For example, divided or undivided cells, which include an ion-exchange membrane be-

tween the electrodes or without the membrane respectively; electrolyte type, aqueous or non-aqueous electrolyte; and electrolyte phase, single phase or two phases (*e.g.*, slurries, suspensions, gas disperse in liquid). In general, these choices are based on the selection of redox couples. These individual redox couples are selected by considering their standard redox potentials and trying to maximise the standard cell potential. Figure 2.4 summarises various redox couples and their standard potential in aqueous systems, except for the H^+/H_2 couple that is based on the overpotential on carbon electrodes (Yang et al., 2011). In aqueous systems, the selection of a pair of redox couples is bounded by the hydrogen and oxygen evolution standard potential regions. Several RFB chemistries have been studied (Wang et al., 2013; Yang et al., 2011), including the VO_2^+/VO^{2+} *vs.* V^{2+}/V^{3+} (VRB), V^{2+}/V^{3+} *vs.* $Br^-/ClBr_2^-$, Br_2/Br^- *vs.* S/S^{2-} (PSB), Fe^{3+}/Fe^{2+} *vs.* Cr^{3+}/Cr^{2+} (Fe-Cr RFB), Br^-/Br_2 *vs.* Zn^2/Zn (Zn-Br RFB), Ce^{4+}/Ce^{3+} *vs.* V^{2+}/V^{3+}, Fe^{3+}/Fe^{2+} *vs.* Br_2/Br^-, Mn^{2+}/Mn^{3+} *vs.* Br_2/Br^-, Fe^{3+}/Fe^{2+} *vs.* Ti^{2+}/Ti^{4+}, among others. Table 2.1 summarises the main characteristic of various RFBs and the following section introduces a brief history of RFB development.
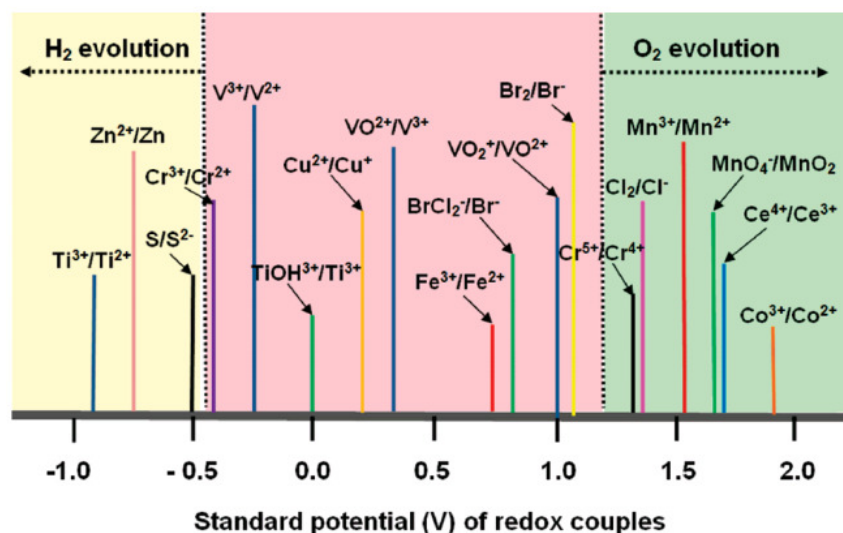
Figure 2.4: Standard potentials versus the standard potential of the hydrogen electrode of different redox couples (Yang et al., 2011).

Contrary to conventional lithium-ion or lead-acid batteries, in a conventional RFB the energy is stored in the form of reduced and oxidised electro-active species, and not within the electrode structure (Leung et al., 2012). The electrodes are commonly made of porous materials, *e.g.*, carbon felt, carbon paper and carbon nanotubes, among others, with a porosity of *ca.* 0.8, and they display enough permeability and active area to facilitate the electrochemical reactions (Alotto et al., 2014). Carbon-based materials have been used as electrodes in various RFBs such as VRFBs, polysulphide/Br, Zn/Br, and V/Ce. Electrodes are in general required to display a high surface area, suitable porosity, good wettability for electrolyte solutions, high electrical conductivity, high activity towards redox reac-

tions at the same time suppressing water electrolysis, good mechanical properties, strong chemical resistance, and to have reasonable price and long cycle life in highly oxidising environment (Leung et al., 2012; Ye et al., 2017). In particular, for VRFBs few materials can be used as a positive electrode due to the highly oxidising nature of V(V) ions, with carbon and graphite used for both positive and negative electrodes (Skyllas-Kazacos et al., 2011). Also, it has been observed that C-O-H and C=O bonds at the electrode surface allow for mechanisms of electron mediation for vanadium redox reactions and enhance hydrophilicity, and therefore, a number of chemical and electrochemical methods to increase the surface concentration of these active sites have been proposed (Skyllas-Kazacos et al., 2011; Ye et al., 2017). Among these methods are chemical treatments with nitric acid or sulphuric acid and thermal treatments. When graphite felt is treated with concentrated sulphuric acid for $5\,\mathrm{h}$, an enhancement in the VRFB performance has been observed by reaching an energy efficiency (ratio of the energy delivered by the battery during discharge to the energy stored during charge) of 88% at $25\,\mathrm{mA\,cm^{-2}}$ (Ye et al., 2017). When a combined treatment of exposure to concentrated acid followed by high temperature is used, an increase in the number of active sites and an enlarge specific area (from 0.31 to $0.45\,\mathrm{m^2\,g^{-1}}$) have also been observed (Ye et al., 2017). The ion-exchange membranes that allow for the transport of charge-carrier ions to complete the circuit, to maintain the electro-neutrality condition of the electrolyte solutions, and to prevent electrolyte mixing and the direct chemical reaction of electro-active species that could result in energy losses (Leung et al., 2012; Li et al., 2011b; Yang et al., 2011). Membranes are required to display high chemical resistance under oxidising environment to ensure the battery cycle life and stability against acid-catalysed reactions like hydrolysis, good ion conductivity to minimise the losses in voltage efficiency, high ion selectively to minimise self-discharge and allow high coulombic efficiencies and low area resistivity to decrease the ohmic losses (Leung et al., 2012; Li et al., 2011b; Skyllas-Kazacos et al., 2011; Ye et al., 2017). For aqueous electrolytes, membranes can conduct positively charged ions (cations), *e.g.*, $\mathrm{H^+}$ and $\mathrm{Na^+}$, or negatively charged ions (anions), *e.g.*, $\mathrm{Cl^-}$ and $\mathrm{NO_3^-}$, and they are called cationic or anionic exchange membranes, respectively. There are also membranes that can conduct both cations and anions. Perfluorinated membranes have been widely used in RFBs due to their high ionic conductivity and good chemical stability (Leung et al., 2012). In particular, for VRFBs the perfluorinated membranes commercialised by Nafion® (DuPont, USA) display superior chemical resistance in vanadium electrolytes, but vanadium active species can permeate through and decrease the coulombic efficiency of the battery (Leung et al., 2012). The diffusion coefficients across Nafion membranes for vanadium ionic species has been determined to be in the order: $\mathrm{V^{2+}} > \mathrm{VO^{2+}} > \mathrm{VO_2^+} > \mathrm{V^{3+}}$ (Sun et al., 2010).

Table 2.1: Typical operating conditions and technical characteristic of some redox flow batteries (Leung et al., 2012; Pino-Muñoz et al., 2017; Rubio-Garcia et al., 2018; Skyllas-Kazacos et al., 2011; Yufit et al., 2013).

RFB system	Redox reactions at electrodes	E°_{OCP} V vs.SHE	Electrolyte anode/cathode	Electrode anode/cathode	Membrane	j mA cm^{-2}	E_{OCP} V	η_{EE} %
Fe-Cr	$Cr^{3+} + e^- \rightarrow Cr^{2+}$ $Fe^{2+} - e^- \rightarrow Fe^{3+}$	1.18	1 M CrCl$_3$ in 3 M HCl/ 1M FeCl$_2$ in 3M HCl	carbon or graphite felt catalysed with Au-Pb/ carbon or graphite felt	AE-VBC, DMAEMA	30	1.05	86
All-V	$V^{3+} + e^- \rightarrow V^{2+}$ $VO^{2+} + H_2O - e^- \rightarrow VO_2^+ + 2H^+$	1.26	2M VOSO$_4$ in 2M H$_2$SO$_4$/ 1M VOSO$_4$ in 2M H$_2$SO$_4$	graphite polyethylene impregnated plate	CE perfluorinated membrane	10-130	1.35 (50% SOC)	83
V-Ce	$V^{3+} + e^- \rightarrow V^{2+}$ $Ce^{3+} - e^- \rightarrow Ce^{4+}$	1.93	0.5M V^{3+} in 1M H$_2$SO$_4$/ 0.5M Ce^{3+} in 1M H$_2$SO$_4$	carbon fiber	AE Asahi vycor glass	22	1.87 (100% SOC)	68
PS-Br$_2$	$S_4^{2-} + 2e^- \rightarrow 2S_2^{2-}$ $3Br^- - 2e^- \rightarrow Br_3^-$	1.36	1.3M Na$_2$S/ 4.0M NaBr	Co-graphite felt/ graphite felt	CE Nafion 117	40	1.7-2.0	80
Pb/PbO$_2$	$Pb^{2+} + 2e^- \rightarrow Pb$ $Pb^{2+} + 2H_2O - 2e^- \rightarrow PbO_2 + 4H^+$	1.62	1.5M Pb(CH$_3$SO$_3$)$_2$ in 0.9M CH$_3$SO$_3$H	reticulated nickel foam/ reticulated vitreous carbon	no membrane	20	1.69	65
Zn-Ni	$Zn(OH)_4^{2-} + 2e^- \rightarrow Zn + 4OH^-$ $2Ni(OH)_2 + 2OH^- - 2e^- \rightarrow 2NiOOH + 2H_2O$	1.71	1M ZnO in 10M KOH	cadmiun-plated copper/ sintered nickel hydroxide	no membrane	10	NG	86
V-Air	$V^{3+} + e^- \rightarrow V^{2+}$ $2H_2O - 4e^- \rightarrow 4H^+ + O_2$	1.49	2M V^{3+} in 3M H$_2$SO$_4$/ air	carbon/ titanium mesh catalysed with Pt-Ir	CE Nafion 117	2.4	1.0 (100% SOC)	46
Zn-Br$_2$	$Zn^{2+} + 2e^- \rightarrow Zn$ $2Br_2^- - 2e^- \rightarrow Br_2$	1.85	2M ZnBr$_2$ in 4M KCl/ 0.05M Br$_2$ + 2M ZnBr$_2$ in 4M KCL	carbon	CE Nafion 125	15	1.6	80
Zn-Cl	$Zn^{2+} + 2e^- \rightarrow Zn$ $2Cl^- - 2e^- \rightarrow Cl_2$	2.12	2M ZnCl$_2$ in 4M KCl	dense graphite/ porous graphite	no membrane	22	NG	66
H$_2$-V	$2H^+ + 2e^- \rightarrow H_2$ $VO^{2+} + H_2O - e^- \rightarrow VO_2^+ + 2H^+$	1.00	hydrogen/ 1M VOSO$_4$ in 5M H$_2$SO$_4$	platinised carbon paper/ carbon paper	CE Nafion 117	70	1.22 (100% SOC)	89
H$_2$-Mn	$2H^+ + 2e^- \rightarrow H_2$ $Mn^{2+} - e^- \rightarrow Mn^{3+}$	1.51	hydrogen/ 1M MnSO$_4$ + 1M Ti(SO$_4$)$_2$ in 3M H$_2$SO$_4$	platinised carbon paper/ carbon paper or graphite felt	CE Nafion 212	100	NG	72
LiCoO$_2$/ Li$_4$Ti$_5$O$_{12}$	$Li_{1-x}CoO_2 + xLi^+ xe^- \rightarrow LiCoO_2$ vs.Li $Li_{4+x}Ti_5O_{12} - xe^- \rightarrow Li_{4x}Ti_5O_{12} + xLi$ vs.Li	2.2	LiPF$_6$, carbonate electrolyte, Ketjen black	22.6M Li$_4$Ti$_5$O$_{12}$/ 51.2M LiCoO$_2$ suspensions	Celgard 2500 micro-porous	NG	NG	88
Li/Fe(CN)$_6$	$Li^+ + e^- \rightarrow Li$ $[FN(CN)_6]^{4-} - e^- \rightarrow [Fe(CN)_6]^{3-}$	3.40	solid electrolyte Li$_{1+x+y}$Al$_x$Ti$_{2-x}$Si$_y$P$_{3-y}$O$_{12}$/ 0.1M K$_3$Fe(CN)$_6$	Li ribbon/ aqueous K$_3$Fe(CN)$_6$	Celgard plypropylene separator	0.5	NG	NG

OCP: open circuit potential, SHE: standard hydrogen electrode, EE: energy efficiency, PS: polysulphide, AE: anion exchange, CE: cation exchange, VBC: vinylbenzyl chloride, DMAEMA: dimethylaminoethyl methacrylate, NG: not given.

A key feature of conventional RFBs is their capability to decouple power and energy storage capacity (Alotto et al., 2014; Chen et al., 2009; Skyllas-Kazacos et al., 2011; Yang et al., 2011). The power of the cell is determined by the stack size and power density, while the energy storage capacity of the cell is determined by the electrolyte volume and concentration of electroactive species. This decoupling feature enables the design of power and energy battery modules according to particular capacity and power output requirements (Skyllas-Kazacos et al., 2011). Modular designs allow the build of large systems, where electrolytes can be maintained inside low-cost tanks and just two pumps are needed. The storage capacity can be increased by simply adding more tanks, and hence the incremental cost per energy storage capacity unit is lower than for other battery technologies (Skyllas-Kazacos et al., 2011). The cost ($ per $\mathrm{kW\,h}$) can be reduced significantly when storage capacity is increased, being especially attractive for long storage times ($4-6\,\mathrm{hour}$) (Skyllas-Kazacos et al., 2011). Rapid refuelling by solution exchange, in case of need, is possible and only low maintenance is required (Alotto et al., 2014; Leung et al., 2012; Yang et al., 2011). RFBs can achieve continuous release of energy at high rates of discharge, very deep discharge without impact on the cell structural integrity or electrolyte decomposition, and virtually no self-discharge since electrolytes are stored separately. Moreover, they display long cycle life, short-time response, symmetrical charge and discharge behaviour, and quick cycle inversion (Alotto et al., 2014; Chen et al., 2009; Ferreira et al., 2013; Leung et al., 2012; Skyllas-Kazacos et al., 2011). Altogether, RFBs present advantages in terms of performance and flexibility over conventional batteries. However, major drawbacks are their low power and energy density, limiting their application in electric-vehicle and portable electronic devices. In order to achieve higher power, the electrode area needs to be enlarged, which may induce large gradients of electro-active species concentration from the bulk to the electro-active sites inside the electrodes, hence reducing the average current density (Alotto et al., 2014). Additional performance losses can appear as shunt currents in manifolds or flow channels and by the formation of precipitates (Alotto et al., 2014). Also, there are safety concerns of toxicity for some electrolytes. Despite the commercialisation of some systems such as VRFB and Zn-Br batteries, there is currently limited deployment of RFBs, though wide commercialisation could be achieved if competitive cost targets are met (Ferreira et al., 2013; Skyllas-Kazacos et al., 2011). It has been estimated that for renewable energy storage without government subsidy, the cost of a storage process must be lower than $200 per kWh (Cho et al., 2015). For a VRFB system of $1\,\mathrm{MW}$ / $4\,\mathrm{MW\,h}$, the chemical cost of V_2O_5 was estimated to be 43% of the total system cost, followed by the separator cost which was estimated to be 27% (Viswanathan et al., 2014). Direct cost reduction can be achieved by diminishing the cost of used component materials and improving the cell performance, for example with a better flow field plate and electrode design (Perry and Weber, 2015; Weber et al., 2011).

The ion-exchange membrane, electrodes and bipolar plates are the three dominant components that affect the cost of a cell/stack. When a low-cost porous separator is used in a cell, a total component cost of about $ 500 per m^2 can be observed, and a cost of $150 per kW can be reached (Perry and Weber, 2015). This cost per kW will increase to $250 per kW if fully-fluorinated ion-exchange membrane are considered and a total component cost of $1000 per m^2 can be expected (Perry and Weber, 2015).

2.2.3 A brief history of redox flow batteries

A timeline of the development of redox flow batteries reported by Leung et al. (2012) is presented in Figure 2.5. Redox flow batteries were first developed by the National Aeronautics and Space Administration (NASA) in the 1970s for bulk energy storage, load levelling, and to facilitate the use of renewable energy sources (Leung et al., 2012; Skyllas-Kazacos et al., 2011). They initially implemented cells that used iron-chromium redox couples, *e.g.,* acidified solutions of Cr(III) / Cr(II) and Fe(III) / Fe(II) due to their low cost and good availability (Skyllas-Kazacos et al., 2011; Ye et al., 2017). An iron-chromium (Fe-Cr) system of $1\,kW/13\,kW\,h$ was tested between 1973 and 1982 (Leung et al., 2012). The Fe-Cr RFB was later developed in Japan as part of the Moonlight Project, testing systems from 10 to $60\,kW$ in the 1980s (Alotto et al., 2014; Leung et al., 2012; Skyllas-Kazacos et al., 2011; Ye et al., 2017). However, Fe-Cr systems displayed operating issues that restricted their commercial development such as low energy density ($<10\,W\,h\,kg^{-1}$) due to cross-mixing of electrolytes, membrane fouling and the requirement of noble catalysts due to the slow reaction kinetics of chromium redox species. In 1984, The PolySulfide-Bromine (PSB) RFB was introduced and it was developed between 1991 and 2004 (Leung et al., 2012; Skyllas-Kazacos et al., 2011; Ye et al., 2017). This battery utilised a NaBr catholyte, a Na_2S_4 anolyte, and a cation exchange membrane that prevents the sulphur anions reacting directly with bromine (Leung et al., 2012). A $1\,MW$ system was tested at Abershaw power station in South Wales, UK, which displayed a round-trip efficiency of $60-65\%$ and an energy density of $20-30\,W\,h\,L^{-1}$ (Leung et al., 2012). This RFB has been the largest scaled-up system due to the moderate cost of un-catalysed electrodes and low-cost electrolytes (Leung et al., 2012; Weber et al., 2011). The system presents a series of technical challenges (Leung et al., 2012; Skyllas-Kazacos et al., 2011) that have affected its commercialisation such as cross-contamination during long operation period, difficulty to maintain electrolyte balance and formation of toxic fumes ($H_2S(g)$ and $Br_2(g)$). The system also requires regular removal of sulphate from the positive half-cell solution and replenishment of sodium sulphide in the negative electrolyte to avoid the build-up of sulphur species, *e.g.,* S^{2-} and HS^{-}. Currently, a larger RFB system, based in vanadium chemistry, is being developed in China (Maa et al., 2019).
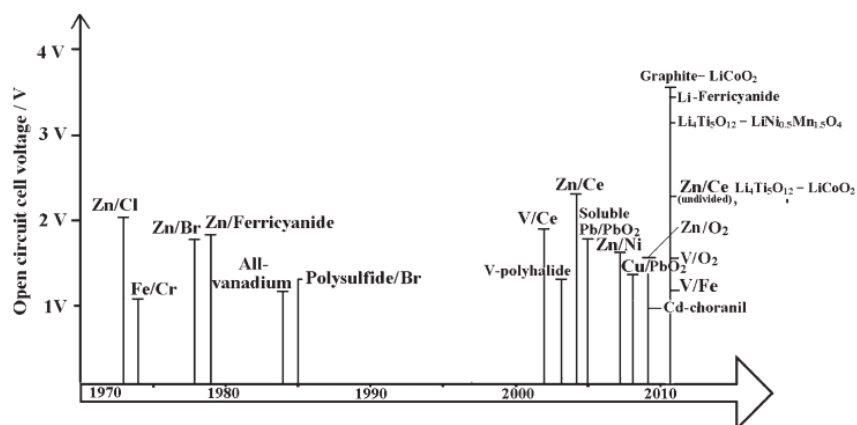
Figure 2.5: Timetable of the development of redox couples for redox flow batteries (Leung et al., 2012).

In 1977, NASA evaluated the vanadium redox couples, and then in 1985, Skyllas-Kazacos *et al.* at the University of New South Wales (UNSW) in Australia successfully demonstrated an RFB considering two redox couples V(II)/V(III) and V(IV)/V(V) (Skyllas-Kazacos et al., 2011). This all-vanadium system was proposed to eliminate the cross-contamination problem of RFBs due to the diffusion of different ions across the membrane. They were capable of preparing a highly concentrated 2 M V(V) solution, which did not precipitate over a reasonable temperature range, by electrochemical oxidation of V(IV) in sulphuric acid (Skyllas-Kazacos et al., 2011). Demonstration systems of $1-4\,kW$ were developed for stationary and vehicle applications in the late 1980s and 1990s (Skyllas-Kazacos et al., 2011). A number of prototypes up to $MW/MW\,h$ have been successfully demonstrated and commercialised for different applications in Australia, Canada, Japan, China, and Thailand, including the application of load levelling, power quality mainte-nance and energy storage associated with renewables. In 1993, Thai Gypsum products, Ltd., in collaboration with UNSW installed a VRFB system for a solar house in Thailand. This system included solar cells of $2.2\,kW$ and a VRFB system of $12\,kW\,h$, considering a 47 V 36 cells battery pack (Ye et al., 2017). In 1997, Mitsubishi Chemicals installed a $200\,kW/800\,kW\,h$ grid-connected VRFB for load-levelling (Ye et al., 2017). This system ran over 150 charge-discharge cycles and displayed a round trip energy efficiency of 80% at 80-100 $mA\,m^{-2}$ (Ye et al., 2017). Sumitomo Electric Industries (SEI) installed a VRFB system for peak shaving in 1996, capable of demonstrating total energy efficiency, includ-ing AC/DC converter and pumps, of 80% over 270 thousand cycles (Ye et al., 2017). They later installed a $4\,MW/6\,kW\,h$ VRFB plant at Subaru wind plant in Japan, with each stack power of $45\,kW$ and 108 cells in total (Ye et al., 2017). More recently, several $MW/MW\,h$ scale systems have been developed and demonstrated. However, these large-scale systems seem impractical due to high cost, and from an engineering point of view is necessary to progress in the system configuration, modularisation, and optimisation (Ye et al., 2017). The word largest VRFB is currently under construction in China to improve the Chinese

northeast grid resilience and facilitate the integration of renewables (Maa et al., 2019). This VRFB plant of $200\,\mathrm{MW}/800\,\mathrm{MW\,h}$ conducted by Dalian Rongke Power Integration Co., Ltd. (RKP), considers units with a minimum storage of $500\,\mathrm{kW}/2\,\mathrm{MW\,h}$, which could be controlled independently. These units consist of 16 cell stacks, with no obvious performance decay found after 10000 cycles (Maa et al., 2019).

Alternatively, membrane-free flow batteries have been proposed such as soluble lead-acid, zinc-nickel, and zinc-manganese dioxide (Leung et al., 2012). In these systems, energy is stored as electro-deposits in the cathode and/or anode and is released by dissolution of electro-deposits during discharge (Leung et al., 2012). In general, a single electrolyte solution is recirculated between tank and cell, and no membrane is required. These membrane-free systems present lower cost and greater simplicity since they do not require an ion-exchange membrane as conventional RFBs, with some of them displaying round-trip efficiencies over 80% with more than 1000 cycles (Leung et al., 2012). A membrane-free soluble lead-acid flow battery, which is based in an electrode reaction of Pb(II) in methane-sulphonic acid and employs Pb^{2+}/PbO_2 and Pb/Pb^{2+} redox couples at the cathode and anode, was proposed in 2004 (Leung et al., 2012). This system demonstrated a charge efficiency of over 85% and energy efficiency of about 65% with an open circuit cell potential of $1.69\,\mathrm{V}$. Later on, this technology was scaled to a several-kW pilot plant using $1000\,\mathrm{cm}^2$ bipolar electrodes. However, this system presents issues of dendrite growth of Pb and shedding of PbO_2 which generates significant energy efficiency loss and failure of the battery.

Additionally, hybrid RFBs have been investigated such as zinc-chlorine, zinc-bromine, zinc-cerium, zinc-air, vanadium-air, organic RFBs and lithium flow batteries. A hybrid RFB involves the deposition of solid species or the evolution of gaseous species in one half-cell during charge. A zinc-bromine (Zn-Br) and a zinc-chlorine (Zn-Cl) systems were developed by the Energy Development Association (EDA) from the USA during the early 1970s to mid-1980s for stationary energy storage applications (Leung et al., 2012). The Zn-Cl RFB operation is based on electrochemical and chemical reactions occurring simultaneously. The first between zinc, chlorine and a $ZnCl_2$ aqueous solution, and the second between chlorine and water. This battery was further investigated as part of the Moonlight project developed in Japan during the 1980s. Battery modules of $10\,\mathrm{kW}$ and $60\,\mathrm{kW}$ were successfully tested with energy efficiencies of 80% and 76% respectively (Leung et al., 2012). Development of this technology was discontinued because of its complexity and the evolution of toxic chlorine gas, which is a serious environmental hazard. The Zn-Br RFB is one of the earliest RFB proposed and during charge, zinc is deposited at the anode while bromide ions are oxidised to bromine at the cathode. This system displayed a practical energy density of $65 - 75\mathrm{W\,h\,kg^{-1}}$ (Leung et al., 2012). The Zn-Br system reached commercialisation being available in the range of 50-500 $\mathrm{kW\,h}$, with several demonstra-

tions (Leung et al., 2012; Yang et al., 2011). This system requires complexing agents to contain and store bromine and displays technological problems such as high-cost electrodes, material corrosion, dendrite formation during zinc deposition on charge, high self-discharge rates, low energy efficiency, relatively low cycle life, and polarisation caused by the faster rate of the reaction of Zn/Zn^{2+} in comparison with the reaction of Br_2/Br^- which ultimately produces battery failure. Recently, several lithium flow batteries have been introduced, taking advantage of concepts from both Li-ion batteries and RFBs. In 2010, Carter and co-workers proposed a battery that stores energy in "flowable" electrode materials and uses semi-solid suspensions as electrolytes (Leung et al., 2012). The equivalent concentration of these suspensions can be higher than $20\,\mathrm{mol\,dm^{-3}}$, displaying energy density per electrolyte volume about 10 times higher ($300\text{-}500\,\mathrm{W\,h\,L^{-1}}$) than conventional RFBs, which commonly use average concentrations lower than $5\,\mathrm{mol\,dm^{-3}}$ (Leung et al., 2012; Ye et al., 2017). A Lithium flow battery, using a $Li_4Ti_5O_{12}$ as flowable anode and $LiCoO_2$ as a flowable cathode, has been reported a round-trip coulombic and energy efficiency of 98% and 88%, respectively (Leung et al., 2012). Further research in relation to safety issues and the practical application of a flowable electrode is required to successfully scale-up these systems. Increasing attention has been given to Na^+ based flow batteries. Ventosa *et al.* proposed a battery using suspension electrolyte based on Na (Ye et al., 2017). This battery presented a charge capacity of $80\,\mathrm{mA\,h\,g^{-1}}$ at $0.17\,\mathrm{mA\,cm^{-2}}$ and with an average discharge potential of $0.8\,\mathrm{V}$, however, large overpotentials were observed.

Another kind of hybrid system is the hydrogen-based flow batteries such as hydrogen-bromine (H_2-Br_2), hydrogen-iron (H_2-Fe), hydrogen-chlorine (H_2-Cl_2), hydrogen-cerium (H_2-Ce), hydrogen-vanadium (H_2-V) and hydrogen-manganese (H_2-Mn). These systems combine a liquid electrolyte, *e.g.*, an acidified solution, at the cathode and gas anode. At the anode, hydrogen oxidation/evolution reaction is the main electrochemical reaction. The first H_2-Br_2 RFB was introduced in the 1960s as an alternative to the H_2-O_2 system due to the more facile reaction of Br_2 (Cho et al., 2016). However, the system displayed issues related to the highly corrosive environment, high cell ohmic resistance, cross-contamination of bromine species which decreases the overall cell efficiency and toxicity of bromine fumes. Kosek and Laconti proposed the formation of a complex between PolyEthylene Glycol (PEG) and bromine to reduce the halogen vapour pressure and mitigate materials corrosion issues, and Barna *et al.* showed that the nature of the negative electrode and the membrane were the dominant parameters for lifetime (Cho et al., 2016; Soloveichik, 2014). Livshits *et al.* used a nano-porous conducting membrane with a thickness of $100\,\mu\mathrm{m}$ and Pt-loaded catalyst electrodes for the cathode and anode to reach a maximum power density above $1.5\,\mathrm{W\,cm^{-2}}$ (Cho et al., 2016). A system of $150\,\mathrm{kW}/900\,\mathrm{kW\,h}$ was successfully demonstrated by their company EnStorage (Cho et al., 2016). Recently, Braff *et al.* developed a cost-effective, high performance,

membrane-less H_2/Br RFB displaying a peak power density of $0.795\,W\,cm^2$ with a round-trip efficiency of 92% (Cho et al., 2016; Soloveichik, 2014). EnStorage Inc. announced field tests of a $50\,kW/100\,kW\,h$ hydrogen-bromine system (Soloveichik, 2014). The H_2-Cl_2 RFB was investigated by Brookhaven National Laboratory and General Electric Company as a promising energy storage system to generate and store hydrogen and chlorine gases (Cho et al., 2016). This system requires high pressure operation to increase the solubility of Cl_2 and induce forced convection so that the catholyte flows through the positive electrode. Later, PSI technology studied the feasibility of the H_2-Cl_2 cell for space-power applications by taking advantage of its high power density, however, further improvements related to the positive and negative electrode resistance to Cl species was required for improving the cell performance (Cho et al., 2016; Soloveichik, 2014). A H_2-Cl_2 RFB with electrodes containing Pt and Ir were tried for the chlorine reduction and the hydrogen oxidation was tested, obtaining a potential of $1.0\,V$ at a current density of $100\,mA\,cm^2$ and was operated for $300\,h$ without degradation (Cho et al., 2016). Huskinson *et al.* achieved a peak power density of $1.0\,W\,cm^2$ with low precious-metal content of $(Ru_{0.09}Co_{0.91})_3O_4$ for the chlorine electrode, displaying virtually no activation losses (Cho et al., 2016; Soloveichik, 2014). Recently a H_2/Ce, a H_2/V and a H_2/Mn have been proposed by researchers at Imperial College London, UK (Hewa Dewage et al., 2015; Rubio-Garcia et al., 2018; Yufit et al., 2013). The H_2-Ce RFB uses the Ce(III)/Ce(IV) redox couple at the cathode. A $5\,cm^2$ area cell, using platinised titanium mesh cathode and a platinised carbon anode, achieved a peak power density of $148\,mW\,cm^2$ when fully charged (Hewa Dewage et al., 2015). Further research is required to improve the cell performance and solve technical issues such as asymmetry between charge and discharge processes, kinetically limited losses on the cerium half-cell and corrosion of carbon-based electrodes due to prolonged contact with the cerium electrolyte. A $5\,cm^2$ area cell of a H_2-Mn RFB was demonstrated, using a catholyte solution of Mn(III)/Mn(II) redox couple in the presence of $Ti(SO_4)_2$. This system displayed a high round trip efficiency of 82% and high power and energy density of $1410\,mW\,cm^{-2}$ and $33\,W\,h\,L^{-1}$ as well as a cost reduction of about 70% when compared to VRFBs (Rubio-Garcia et al., 2018). The H_2-V RFB that uses the same cathode redox couple V(IV)/V(V) than a VRFB is the main subject of this thesis and is described in detail in the next section.

2.2.4 The vanadium redox flow battery

A Vanadium Redox Flow Battery (VRFB) utilises two vanadium redox couples, namely VO^{2+}/VO_2^+ at the cathodic side and V^{2+}/V^{3+} at the anodic side. The redox reactions involved are shown in Equation 2.3 for the cathode, anode, and cell. The standard cell OCP is of $1.26\,V$ at $25\,°C$. During operation, protons must migrate through the membrane producing a change in the electrolyte pH, while electrons flow through the external circuit.

A schematic VRFB diagram is shown in Figure 2.6.

$$
\text{cathode:} \quad VO_2^+ + 2H^+ + e^- \underset{\text{charge}}{\overset{\text{discharge}}{\rightleftharpoons}} VO^{2+} + H_2O, \qquad E_{ca}^{\ominus} = 1.00\,\text{V } \textit{vs. } \text{SHE}
$$

$$
\text{anode:} \quad V^{2+} \underset{\text{charge}}{\overset{\text{discharge}}{\rightleftharpoons}} V^{3+} + e^-, \qquad E_{ca}^{\ominus} = -0.26\,\text{V } \textit{vs. } \text{SHE}
$$

$$
\text{cell:} \quad VO_2^+ + V^{2+} + 2H^+ \underset{\text{charge}}{\overset{\text{discharge}}{\rightleftharpoons}} VO^{2+} + V^{3+} + H_2O, \qquad E_{cell}^{\ominus} = 1.26\,\text{V } \textit{vs. } \text{SHE}
$$

$$(2.3)$$
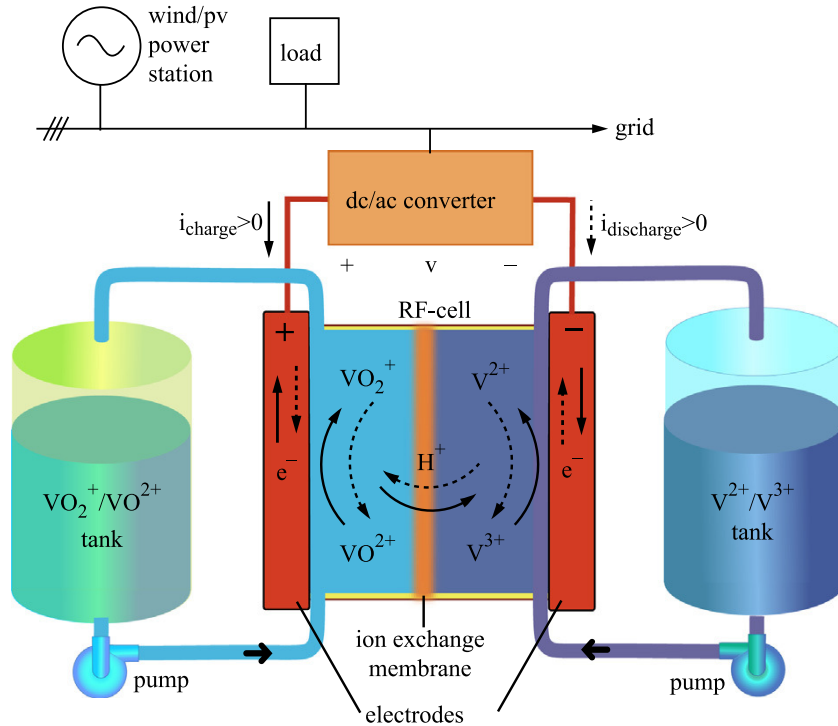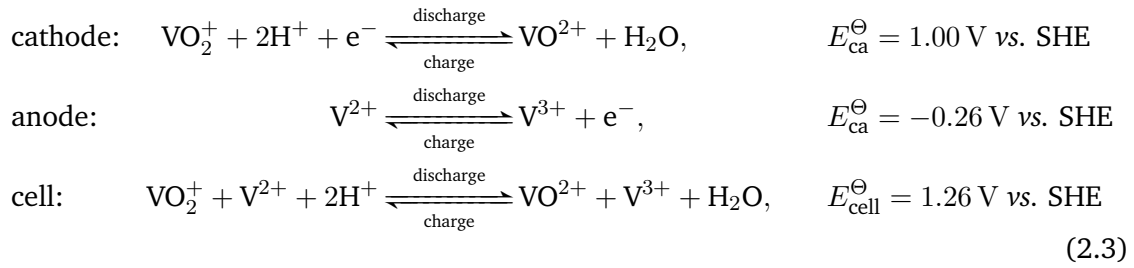
Figure 2.6: Schematic of an all-vanadium redox flow battery (Alotto et al., 2014).

Using the same element in both half-cells, namely, the four oxidation states of vanadium, solves the problem of cross-contamination (Skyllas-Kazacos et al., 2011). Even when crossover can occur, electrolytes can be regenerated electrochemically, allowing recovery of the initial cell capacity (Leung et al., 2012; Skyllas-Kazacos et al., 2011; Weber et al., 2011). The VRFB is an attractive technology for large-scale energy storage applications due to its long cycle life ($\sim$12000) and high round trip efficiencies ($>$80%) (Cho et al., 2015; Skyllas-Kazacos et al., 2011). Usually, sulphuric acid is used as supporting electrolyte in both half-cells, with a limit of concentration of vanadium and total sulphate of less than 2 and 5 M, respectively. These limits are considered to increase the stability of vanadium species and the solubility of $VOSO_4$, whose solubility depends on acid concentration and temperature (Weber et al., 2011; Yang et al., 2011). The solubility of $VOSO_4$ decreases with increasing acid concentration, and increases with temperature. The energy density of the system depends on the vanadium concentration, which is limited by

the precipitation of vanadium oxides. Vanadium concentrations over 2 M in H_2SO_4 produce V_2O_5 precipitates in the catholyte at temperatures over $40\,°C$, and VO precipitates in the anolyte at temperatures below $10\,°C$ (Yang et al., 2011). VRFBs exhibit relatively low specific energy densities (10–30 $W\,h\,kg^{-1}$) (Cho et al., 2015). To reach higher energy densities, higher vanadium concentration must be achieved. Although efforts have been made to improve the stability of electrolytes, the operating window for VRFBs continues to be 10–40 °C for vanadium concentration below of 2 M. Amongst VRB advantages are their high coulombic and voltage efficiencies due to relatively fast kinetics of vanadium redox couples that do not need precious metal catalysts, their fast charging cycles with extremely low rates of gas evolution, no permanent damage to the cell or electrolytes when the battery is over-charged or deeply discharged or cycled for any SOC, and their long cycle life as a consequence of the reusable electrolytes (Leung et al., 2012).

Despite being a promising energy storage technology and the progress achieved in recent years, material limitations and technical issues increase the cost and limit the market penetration of VRFBs. Capital costs of \$150–\$1000/kWh or higher have been reported for VRFBs (Gallo et al., 2016). Technical issues are related to scale-up and optimization, an improvement on electrolyte stability, and development of electrode materials resistant to overcharge. Enhancing the electrochemical activity of electrodes can allow higher operational currents thus reducing electrode area and cost (Skyllas-Kazacos et al., 2011). The highly oxidising environment used limits the range of materials used as electrodes, being usually graphite or carbon-based materials in forms of felt or porous structures, which are treated to increase COOH functional groups on the surface to improve their electrochemical activity (Skyllas-Kazacos et al., 2011; Yang et al., 2011). The ion-exchange membrane is directly related to the capacity and energy loss due to crossover. Species crossover depends on vanadium ion concentrations, membrane properties and temperature (Yang et al., 2011). Electrolyte balance must be maintained by limiting the water crossover due to electro-osmotic drag and the osmotic pressure difference between half-cells. Nafion membranes are usually used, but they do not prevent crossover of ionic species promoting self-discharge reactions at each half-cell, leading to capacity and efficiency loss (Weber et al., 2011; Yang et al., 2011). These membranes also display high levels of swelling when immersed in aqueous electrolytes, increasing water transport (Skyllas-Kazacos et al., 2011). The development of membranes that are inexpensive, chemically stable, and that prevent crossover, could allow the use of lower purity vanadium oxides, therefore, permitting a system cost reduction (Skyllas-Kazacos et al., 2011). Side reactions can result from high SOC operation, leading to H_2 evolution at the anode, which causes a progressive drop in the V^{2+}/V^{3+} ratio generating an imbalance between half-cell electrolytes. A similar effect is produced by air oxidation of V^{2+} in the same half-cell. SOC monitoring, and automated rebalancing and capacity restoring, to extend the cycle life of electrolytes

is required. While sealing the anolyte tank helps to reduce gassing reactions, chemical or electrochemical re-balancing methods are imperative to restore the cell initial capacity (Skyllas-Kazacos et al., 2011). Stacks experience parasitic losses typically of 3–5% of the stored energy. These losses are related to the energy needed to pump electrolytes and shunt currents through channels and manifolds. An optimal stack design of both channels and manifolds is required (Skyllas-Kazacos et al., 2011). Pump losses can be attenuated by increasing the cross-sectional area of channels and manifolds, but this produces an increase in shunt currents. The practical number of cells for a bipolar stack is of about 20–30 (Skyllas-Kazacos et al., 2011). Technical issues have been conventionally studied by means of experimental approaches, which require a high number of experiments and involve the use of expensive materials or complicated set-ups. To measure processes occurring inside the battery with non-invasive procedures is not always possible, meaning that it can be difficult to quantify the parameters that govern the battery phenomena (Xu and Zhao, 2015). Hence, interest in VRFB mathematical modelling has risen due to their fast application and low cost. The description of the operation through mathematical modelling and simulation enables understanding of the phenomena taking place inside the batteries and facilitates stack and system scale-up to fulfil the requirement of large-scale energy storage applications. The mathematical modelling of VRFBs is reviewed in more detail later in this chapter.

2.2.5 The novel regenerative hydrogen-vanadium fuel cell

A regenerative fuel cell (RFC) is an electrochemical system that can operate in both galvanic (discharge) and electrolytic (charge) mode. They are a hybrid type of RFB and as result have similar features with additional advantages than those that exist in a conventional RFB. Hydrogen is used as fuel in all RFCs because of its fast electrode kinetics even with small Pt loadings, but cell chemistry, design, components materials can be different, enabling diverse RFCs such as the ones described in the previous section. Normally, hydrogen is delivered in gaseous form from pressurised or cryogenic tanks and stored after compression or liquefaction. RFCs can include two electrochemical devices: a fuel cell for energy generation and an electrolyser for energy storage; or can consider only a singular device performing both operating modes and using a proton exchange membrane (Soloveichik, 2014). The hydrogen-oxygen RFC with an OCV of $1.23\,\mathrm{V}$ at $25\,^{\circ}\mathrm{C}$ has been widely studied. One major issue is that the cathode electro-catalyst must effectively catalyse two processes: oxygen reduction and water oxidation (Soloveichik, 2014). The bi-functional catalyst used usually contains Ir but also requires expensive Pt. Energy efficiency, which compares the total energy converted during charge and discharge, has been reported to reach values of 45% at $200\,\mathrm{mA\,cm^{-2}}$ using a bilayer Pt-Ir cathode electro-catalyst, with the Ir facing the membrane and combined with a Pt/C anode cat-

alyst (Soloveichik, 2014). Because of this issue, different cathodic oxidants have been proposed to avoid the large overpotential and the need of high concentration of electrocatalyst, such as halogen (e.g. chlorine, bromine), aqueous transition metal (e.g. vanadium, iron) and organic cathodes. In particular, a Regenerative hydrogen-Vanadium Fuel Cell (RHVFC) based on an aqueous electrolyte with a redox couple V(V)/V(IV) and hydrogen was demonstrated by Yufit et al. (2013), reaching good reversibility and a peak power density of $114\,\mathrm{mW\,cm^{-2}}$. This system potentially allows to overcome the cost dependency of VRFBs with regards to the vanadium requirements, by employing only half of it compared to traditional cells (Skyllas-Kazacos et al., 2011; Yufit et al., 2013). It has been reported that the cost of vanadium represents over 40% of the total cost of a VRFB system (Viswanathan et al., 2014). An RHVFC also eliminates the cross-mixing issue by employing a gas-liquid configuration, which allows easy separation of any electrolyte crossover to the anode side so that it can be pumped it back to the vanadium electrolyte tank (Dowd et al., 2017a,b; Hewa Dewage et al., 2015; Pino-Muñoz et al., 2017; Yufit et al., 2013).

A RHVFC, whose schematic diagram is shown in Figure 2.7, presents a standard Open Circuit Potential (OCP) of $0.99\,\mathrm{V}$. Hydrogen evolution, which is an adverse reaction in VRFBs, is the main anodic process. During discharging, V(V) is reduced to V(IV) and hydrogen is oxidised, while the reverse process occurs in charging mode and hydrogen is stored. This cell could offer a better energy storage solution because of its fast hydrogen kinetics and absence of cross-mixing, even when the crossover of catholyte is possible, this could be collected at the anode side and pumped back to the catholyte tank (Dewage et al., 2016; Yufit et al., 2013). A comparison of electrochemical devices including the RHVFC is summarised in Table 2.2. Yufit et al. (2013) studied the RHVFC performance using a $25\,\mathrm{cm^2}$ active area single-cell experimental set-up with serpentine flow field plates for the catholyte solution and the hydrogen. Their initial results were obtained using a HiSPEC M 200 Class MEA and 0.2 M V(IV)/V(V) catholyte solution. The cell was operated between 0.4 and $1.7\,\mathrm{V}$ to avoid V(IV)/V(III) redox reaction, and to minimise oxygen evolution and carbon paper corrosion which reduce coulombic efficiency. It was observed that higher current densities produce lower coulombic efficiencies, which can be explained by the increase in mass transport limitation effects (Yufit et al., 2013). This was also seen to happen when lower vanadium solution flow rates were used. An improved performance was obtained when a cell containing a commercial gas diffusion layer (GDL) with Pt loading of $0.5\,\mathrm{mg\,cm^{-2}}$ for the hydrogen half-cell, a Nafion 117 ion-exchange membrane, and an untreated carbon paper for the vanadium half-cell, was used. In the case of 1.0 M vanadium solution the voltage, coulombic and energy efficiencies were of 69%, 87% and 60%, respectively; and a peak power density of $114\,\mathrm{mW\,cm^{-2}}$ was obtained (Yufit et al., 2013). Characteristic results of the improved system are shown in Figure 2.8. They concluded

that by using a carbon paper with better wettability, no PTFE treated carbon paper, in the positive half-cell reduced the losses associated with mass transport limitations (Yufit et al., 2013).
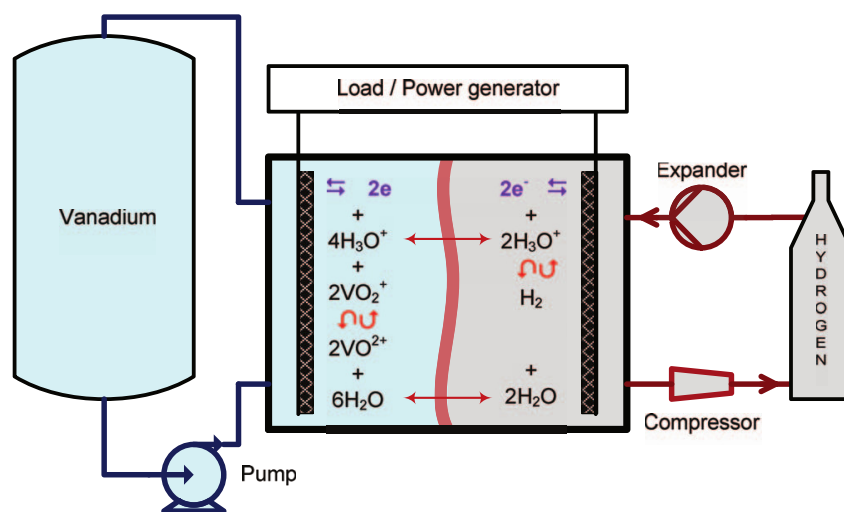
Figure 2.7: Schematic of an regenerative hydrogen-vanadium fuel cell (Yufit et al., 2013).

Table 2.2: Comparison of features of ECES systems, modified from (Alotto et al., 2014). High > good > mild > low.

System	Scalability	Flexibility	W-W h independency	Environmental impact	Safety issue
Ad. Lead-acid	Good	Good	No	Low	Low
Sodium-sulphur	Good	Good	No	Low	Mild
Sodium-nickel-chlorine	Good	Good	No	Low	Mild
Lithium-ion	High	Good	No	Low	Low
Electrolyzer/Fuel cell	High	High	Yes	Low	Mild
hydrogen-vanadium	High	High	Yes	Low	Mild
Redox flow battery	High	High	Yes	Low	Low

Hewa Dewage et al. (2015) studied the loss mechanisms of the RHVFC by means of a $25\,cm^2$ active area cell. The system, which was operated between an upper and lower cut-off voltage of $1.3\,V$ and $1\,V$, used a carbon electrode as cathode, a platinised carbon electrode as anode and Nafion 117 as membrane, and a catholyte solution of 1 M V(IV). They proposed a novel reference electrode set-up to measure half-cell Electrochemical Impedance Spectroscopy (EIS) (Hewa Dewage et al., 2015). They observed catholyte crossover during the cell operation, which could be adsorbed onto the anode Pt catalyst (Dewage et al., 2016). Negligible influence of hydrogen flow rate in comparison to the vanadium flow rate was also observed (Dewage et al., 2016). They suggested further research into minimising vanadium crossover through the ion-exchange membrane and optimisation of the electrode structure to enhance mass transport to and within the
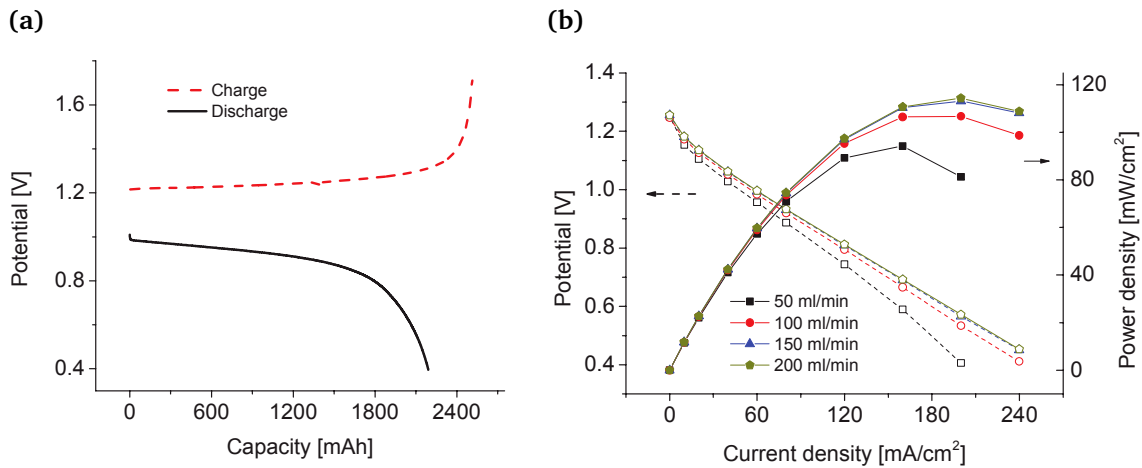
Figure 2.8: Improved RHVFC with untreated carbon paper in 1M V(IV)/V(V):(a) charge and discharge potential at $100\,\mathrm{mL/min}$ vanadium flow rate and $40\,\mathrm{mA\,cm^{-2}}$,(b) polarisation performance at 100% SOC and different flow rates of catholyte (Yufit et al., 2013).
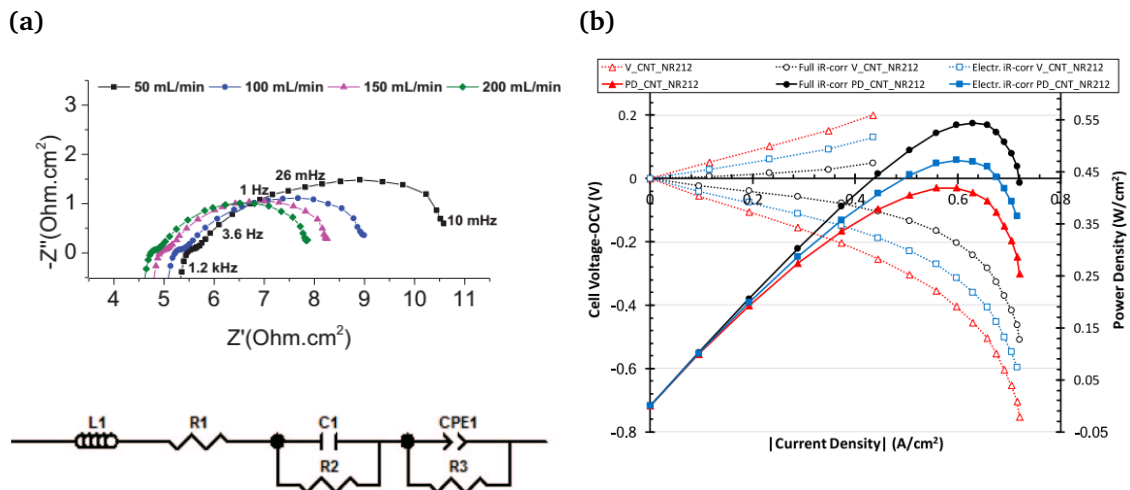
Figure 2.9: (a) Nyquist representation of the EIS response of the while cell at different vanadium flow rates and a hydrogen flow rate of $100\,\mathrm{mL\,min^{-1}}$ along with the equivalent circuit proposed to fit the EIS data (Hewa Dewage et al., 2015). (b) Polarisation and discharge power density curves of the RHVFC using a CNT vanadium electrode and a NR212 membrane before and after IR correction (Dowd et al., 2017a).

electrode (Hewa Dewage et al., 2015). Later Dowd et al. (2017b) studied the crossover of vanadium ions (VO^{2+} and VO$_2^+$) for a fully assembled cell when using Nafion membranes and Electrospun Blended Nanofiber (EBN) membranes. The performance of this last type of membranes was similar to the one displayed by the RHVFC using a Nafion 212 membrane with peak power density of $250\,\mathrm{mW\,cm^{-2}}$, however, the EBN membranes significantly reduced the crossover rates of vanadium ions (Dowd et al., 2017b). Also, Dowd et al. (2017a) investigated the performance of the RHVFC by using different vanadium carbon electrodes and membranes, a Pt/C hydrogen electrode and interdigitated flow field plates at both half-cells. The system reached a peak power density of $540\,\mathrm{mW\,cm^{-2}}$ and a limiting current density of $700\,\mathrm{mA\,cm^{-2}}$ when a Carbon NanoTube (CNT) electrode for

the positive electro and an NR212 membrane (Dowd et al., 2017a). This improved performance was attributed to the use of an interdigitated flow field, a thinner membrane, and an advanced CNT electrode. They observed that during discharge operation mass transport limitations dominate as the overpotential is increased.

Further improvements in component materials and operating conditions can be done, which could increase RHVFC performance. Modelling and simulation is an important tool, saving time and reducing cost, for achieving this task. It is of interest to model this hybrid redox flow system to understand the physicochemical processes involved in RHVFCs and to identify the dominant phenomena. Mathematical descriptions of an RHVFC was developed as part of this research (Pino-Muñoz et al., 2017) and is discussed in detail in later chapters.

2.3 Fundamentals of electrochemistry

The understanding of the thermodynamic principles and general laws that describe the relationship between species electrochemical potential, electrostatic potential, current density, and other electrochemical variables is fundamental for building a mathematical description of a battery. Such a theory is used to describe the electrode kinetic behaviour, with respect to potential and species activities, to rationalise the highly complex electrochemical reactions that occur at the interface between the electrolyte phase and the electrode surface. This section first explains the electrode equilibrium and kinetic principles for a general electron-transfer reaction case, while more detailed explanations can be found in the references cited in this section (Bard and Faulkner, 2001; Bazant, 2013; Bazant et al., 2009; Ferguson and Bazant, 2012; Gileadi, 1993; Newman and Thomas-Alyea, 2004; Pletcher, 2009; Walsh, 1993). Then, the definitions of practical characteristic parameters and figures of merit used to evaluate the performance of an RFB are defined.

2.3.1 Thermodynamics and cell potential

The potential of a cell is the difference in the thermodynamic electrochemical potential of electrons at the two leads, of identical composition, temperature and pressure, connected at the positive and negative electrode, divided by Faraday's constant, *i.e.*, $-^{\text{M'}}\Delta^{\text{M''}}\tilde{\mu}_{\text{e}}/F = {}^{\text{M'}}\Delta^{\text{M''}}\phi$ (Gileadi, 1993). Chemical potential is used for neutral species (μ_{i}), while electrochemical potential is used for charged species such as electrons ($\tilde{\mu}_{\text{e}}$) and ions ($\tilde{\mu}_{\text{i}}$ or just μ_{i}). The electrochemical potential is a measure of the energy of the species, which is described macroscopically by thermodynamics as the dependence of free energy on temperature, pressure, composition, and electrical state (Bazant, 2013; Newman and Thomas-Alyea, 2004). Neutral species, however, are unaffected by an electric field. The thermo-

dynamic definition of electrochemical potential is given in Equation 2.4 (Ferguson and Bazant, 2012; Newman and Thomas-Alyea, 2004), where G is the Gibbs free energy, n_i is the number of moles of species i, μ_i^{Θ} is the reference chemical potential, R is the gas constant, T is the system temperature, a_i is the chemical activity of species i, z_i is the charge number of species i, F is the Faraday's constant, ϕ is the electrostatic potential, $\bar{c}_i$ is the dimensionless concentration ($\bar{c}_i$), and $\tilde{\mu}_i^{ex}$ is the excess electrochemical potential.

$$\tilde{\mu}_i = \left(\frac{\delta G}{\delta n_i}\right)_{T,p,n_j,i \neq j} = \mu_i^{\Theta} + RT \ln(a_i) + z_i F \phi = RT \ln(\bar{c}_i) + \tilde{\mu}_i^{ex} \qquad (2.4)$$

In thermodynamics there is no absolute value of chemical potential, instead only relative values to a reference have meaning. The chemical potential is defined relative to a reference state (Θ) of unit activity ($a_i = 1$), which is usually defined at a concentration of $1 \, \mathrm{mol \, m^{-3}}$, room temperature of 25 °C and standard atmospheric pressure of 101325 Pa. The activity coefficient accounts for all other contributions to the chemical potential such as the interaction with other components in the solution, and is normally scaled so that for infinite dilution is equal to one ($\gamma_i = 1$). The species activity (Equation 2.5) can be expressed in terms of its dimensionless concentration ($\bar{c}_i = c_i/c_{ref}$), dimensionless molality ($\bar{m}_i = m_i/m_{ref}$), mole fraction (dimensionless, x_i) or dimensionless gas partial pressure ($\bar{p}_i = p_i/p_{ref}$). Depending of the way of measuring concentration the reference concentration is normally chosen to be $c_{ref} = 1 \, \mathrm{mol \, L^{-1}}$, $m_{ref} = 1 \, \mathrm{mol \, kg^{-1}}$ or $p_{ref} = 1$ atm. The activity coefficient, which accounts for all non-ideal contributions to the species chemical potential in a concentrated solution, is sometimes considered as an excess chemical potential (μ_i^{ex}).

$$a_i = \gamma_i^c \bar{c}_i = \gamma_i^m \bar{m}_i = \gamma_i^x x_i = \gamma_i^p \bar{p}_i \qquad (2.5)$$

The electrochemical potential of an ion is defined so that the difference of its value in two phases is the work of transferring reversibly, at constant temperature and constant volume, $1 \, \mathrm{mol}$ from one phase to the other (Newman and Thomas-Alyea, 2004). The electrochemical potential of an ion has both a chemical and an electrostatic contribution as shown in Equation 2.4 (Bazant, 2013; Bazant et al., 2009; Newman and Thomas-Alyea, 2004; Smith and Bazant, 2017). This is an arbitrary way of dividing the electrochemical potential into a chemical and an electrical term. It is important to notice that the electric potential difference between two phases of different chemical composition is undefined and cannot be measured, however, an electrical variable is usually defined as shown in Equation 2.4, which is useful for computation purposes in transport processes. The definition of ϕ must satisfy the condition given in Equation 2.6 for two phases α and β of identical chemical composition at constant temperature and pressure. This is that the

only difference between the phases α and β is of electrical nature, and their difference in the electrical state is given by their difference in electrical potential (Newman and Thomas-Alyea, 2004).

$$\mu_i^\alpha - \mu_i^\beta = z_i F(\phi^\alpha - \phi^\beta) \tag{2.6}$$

An electrochemical cell can operate in two modes: galvanic and electrolytic. Galvanic cells are spontaneous or self-driving cells that produce electrical energy to carry useful work when a load is connected between the electrodes, while electrolytic or driven cells require an input of electrical energy as a power supply to produce a chemical change. The Gibbs free energy change (ΔG) of the cell can be calculated as the difference between its value for products and reactants which can be related to the electrochemical potential of species participating in the electron-transfer half-cell reactions (Newman and Thomas-Alyea, 2004; Walsh, 1993), as defined in Equation 2.7. In this equation, s_i is the stoichiometric coefficient of species i when the electron-transfer half-cell reactions are written following the convention shown in Equation 2.8, where charge conservation requires that $\sum_i s_i z_i = -n$. The term M_i is the symbol for the chemical formula of species i and n is the number of electrons that are transferred. In an anodic reaction $s_i > 0$ for reactants and $s_i < 0$ for products, while in a cathodic reaction the signs are reversed. If ΔG is negative, electrons will flow spontaneously from the anode (an) to the cathode (ca), and therefore, the cathode will be the more positive electrode and in which electrons will have lower electrochemical potential. It is important to clarify the following convention used to name the electrodes in a battery (Gileadi, 1993; Newman and Thomas-Alyea, 2004). The positive electrode, in which the potential decreases during galvanic operation causing the energy of electrons to be increased, and therefore, causing the reduction of species while generating a reduction current (*i.e.*, electrons flow into the electrode, and from the electrode into the reactant species), is called the cathode. The negative electrode, in which the potential increases during galvanic operation causing the energy of electrons to be decreased, and therefore, causing the oxidation of species while generating an oxidation current (*i.e.*, electrons are removed from the reactant species), is called the anode. By definition oxidation (anodic) currents are positive and reduction (cathodic) currents are negative. During electrolytic operation, the reverse process happens, and the positive and negative electrodes are swapped. However, in a battery, the names given to the electrodes follow the convention during galvanic operation or discharge.

$$\Delta G = \sum_i \left(s_i \tilde{\mu}_i \right)_{ca} - \sum_j \left(s_j \tilde{\mu}_j \right)_{an} \tag{2.7}$$

$$\sum_i s_i M_i^{z_i} \rightarrow ne^- \tag{2.8}$$

The cell equilibrium or open circuit potential (E_{OCP}) is defined as the Gibbs free energy change of the system per unit charge passing through the external circuit as shown in Equation 2.9 (Bazant, 2013; Gileadi, 1993; Newman and Thomas-Alyea, 2004; Pletcher, 2009; Walsh, 1993). At this equilibrium condition, the rate of forward and backward electrode reactions are equal.

$$E_{OCP} = \frac{\Delta G}{-nF} \tag{2.9}$$

2.3.2 The electro-neutrality approximation and Faraday's law

The electro-neutrality approximation states that charge separation is impossible in electrolytic solution (Dickinson et al., 2011; Newman and Thomas-Alyea, 2004). This assumption has been widely used to allow for the solution of the set of transport equations of species, where concentrations and electrical potential are unknowns. Otherwise, if charge separation is present in an electrochemical system, the transport of the ionic species will be affected by the Coulombic forces present, and therefore this induced migration must be correlated to the electric field with the degree of charge separation in the solution (Dickinson et al., 2011). The relation between electric potential and charge density can be described by Gauss's law, which can be reorganised as shown in Equation 2.10, where r_D is the Debye length, θ is the normalised potential, ϵ_r is the relative permittivity of the medium, ϵ_0 is the permittivity of free space, and c^* is the bulk concentration of electrolyte. The Debye length indicates the extent over which the electric field can vary for a given charge separation (Dickinson et al., 2011). If the length scale of the system is big enough, the Debye length can be approximated as $r_D = 0$, leading to the electroneutrality condition, which would appear a strong approximation. In the case of electrochemical systems, the Debye length is typically of the order of nanometers, and therefore, very large potentials are required to produce a small separation of electrical charge (Dickinson et al., 2011; Newman and Thomas-Alyea, 2004). As a result, the flow of current is continuous, and at the interface of the electrode and electrolyte the charge-carrier species changes, from electrons to ions, due to a charge-transfer reaction. The electroneutrality approximation was initially considered to facilitate the analytical solution of Nernst-Planck equations and has been widely used, however, it suffers from an intrinsic paradox when trying to determine the electric field. This is that such an electric field arises in the presence of charge separation due to Coulombic forces, so if a zero charge separation is assumed, the electric field must take any value possible in order to maintain electroneutrality and to damp any

charge separation instantaneously (Dickinson et al., 2011).

$$2r_{\mathrm{D}}^2 \nabla^2 \theta + \sum_i z_i c_i = 0, \quad r_{\mathrm{D}} = \sqrt{\frac{RT\epsilon_{\mathrm{r}}\epsilon_0}{2F^2 c^*}} \tag{2.10}$$

Faraday's law of electrolysis relates the rate of charge-transfer reaction to the current density by an electrochemical reaction (K, 1991; Newman and Thomas-Alyea, 2004; Walsh, 1993). This law establishes that the amount of material (reactant or product) undergoing electrochemical change is proportional to the amount of electrical energy applied. Equation 2.11 shows the rate of reaction (r_k) with units of $[\mathrm{mol\,m^{-3}\,s^{-1}}]$ for a reaction k in a electrochemical reactor in terms of the current density (j), and Equation 2.12 shows the rate of production of species when the electron-transfer reaction is written following the convention shown in Equation 2.8. Where n_i^{rx} is the molar rate of production of species i with unit of $[\mathrm{mol\,m^{-2}\,s^{-1}}]$, j is the current density, and S is the specific surface area (active area per unit volume). Faraday's constant is equivalent to the charge associated with a unit amount of electrons ($96\,485\,\mathrm{C\,mol^{-1}}$) (*i.e.*, the product of the Avogadro constant, $N_{\mathrm{A}} = 6.02 \times 10^{23}\,\mathrm{mol^{-1}}$, and the fundamental charge of a single electron, $q_{\mathrm{e}} = 1.60 \times 10^{-19}\,\mathrm{C}$).

$$r_{\mathrm{k}} = \frac{jS}{nF} \tag{2.11}$$

$$n_i^{\mathrm{rx}} = -s_i \frac{j}{nF} \tag{2.12}$$

2.3.3 Nernst equation and open circuit potential

A general faradaic reaction is presented in Equation 2.13, considering the reduced state R and oxidised state O (Bazant, 2013). This half-cell reaction represents an electrode process with species O and R participating in a n-electron transfer reaction at an electrode/electrolyte interface. The electrostatic potential is ϕ_{e} for electrons in the electrode and ϕ for ions in the electrolyte, and the difference between them is the interfacial potential $\Delta\phi = \phi_{\mathrm{e}} - \phi$. This potential difference is always defined as the potential of the electrode minus the potential of the electrolyte.

$$R \rightleftarrows O + ne^- \tag{2.13}$$

where,

$$R = \sum_{s_i > 0} s_i M_i^{z_i}, \quad O = \sum_{s_i < 0} |s_i| M_i^{z_i} \tag{2.14}$$

At equilibrium, the electrochemical potential of each side of the half-cell reaction must be equal, as shown in Equation 2.15, where μ_e is the electrochemical potential of the electron (Equation 2.16). The potential of an electrode at equilibrium is a measure of the electrochemical potential of electrons in equilibrium with the reactant and product species (Bazant, 2013; Newman and Thomas-Alyea, 2004).

$$\sum_i s_i \tilde{\mu}_i = n\tilde{\mu}_e \tag{2.15}$$

$$\tilde{\mu}_e = \mu_e^\Theta + RT \ln(a_e) - F\phi_e \tag{2.16}$$

Using the definitions of the electrochemical potential of ions and the electron along with the charge conservation condition, Equation 2.15 can be rearranged into the Nernst equation as shown in Equation 2.17 (Bazant, 2013). This equation defines the interfacial potential at equilibrium ($\Delta\phi^{eq}$), which is a function of species activities and the standard potential ($\Delta\phi^\Theta$), namely the interfacial potential when all species are at their standard states.

$$\Delta\phi^{eq} = \Delta\phi^\Theta + \frac{RT}{nF} \ln\left(\frac{a_O a_e^n}{a_R}\right)$$
$$\Delta\phi^\Theta = \frac{\mu_O^\Theta + n\mu_e^\Theta - \mu_R^\Theta}{nF} \tag{2.17}$$

where,

$$a_R = \prod_{s_i > 0} a_i^{s_i}, \quad a_O = \prod_{s_i < 0} a_i^{|s_i|}, \quad \mu_R^\Theta = \sum_{s_i > 0} s_i \mu_i^\Theta, \quad \mu_O^\Theta = \sum_{s_i < 0} |s_i| \mu_i^\Theta \tag{2.18}$$

Standard potential of electrodes ($E_e^\Theta = \Delta\phi^\Theta - \Delta\phi_{ref}^\Theta$) are defined relative to a standard reference potential ($\Delta\phi_{ref}^\Theta$) (Bazant, 2013). For aqueous electrolytes, the Standard Hydrogen Electrode (SHE) is commonly used as the reference electrode. The SHE consists of H_2 gas at a partial pressure of 1 atm at room temperature undergoing reversible oxidation in a platinum electrode submerged in an acidic solution (pH = 0). Electrode reactions with negative standard potentials, *i.e.*, $E_e^\Theta < 0$, act as an anode producing electrons, while electrode reactions with a positive standard potential, *i.e.*, $E_e^\Theta > 0$, act as a cathode consuming electrons.

An electrochemical cell contains two electrodes, namely a cathode and an anode, where half-cell faradaic reactions take place. The equilibrium cell potential (E_{eq}), also called reversible potential or Open Circuit Potential (OCP, E_{OCP}), is the difference of the two equilibrium interfacial potentials as shown in Equation 2.19, and it is the potential at which no current flows through the cell (Newman and Thomas-Alyea, 2004; Walsh, 1993),

which is related to the nature of the species and the temperature. Similarly, the standard cell potential will consider all species at their standard states (Equation 2.20), *i.e.*, the free energy of reaction for the net cell reaction under standard conditions. Equation 2.19 could be also expressed in terms of reactants and products participating in the full cell reaction. In a battery, the OCP depends on the State of Charge (SOC) of the battery, *i.e.*, the concentration of reactants and products present at a specific moment.

$$E_{\text{OCP}} = \Delta \phi_{\text{ca}}^{\text{eq}} - \Delta \phi_{\text{an}}^{\text{eq}} = E_{\text{ca}}^{\text{eq}} - E_{\text{an}}^{\text{eq}}$$

$$E_{\text{OCP}} = E^{\Theta} - \frac{RT}{nF} \ln \left(\prod_i a_i^{s_i} \right)_{\text{ca}} + \frac{RT}{nF} \ln \left(\prod_j a_j^{s_j} \right)_{\text{an}} \tag{2.19}$$

where,

$$E^{\Theta} = \Delta \phi_{\text{ca}}^{\Theta} - \Delta \phi_{\text{an}}^{\Theta} = \frac{\Delta G^{\Theta}}{-nF} \tag{2.20}$$

2.3.4 Cell overpotentials and electrode kinetics

The cell potential observed experimentally results from several coupled phenomena. Conventionally, three main causes of overpotential are considered: the activation overpotential (η_{ac}), the ohmic overpotential (η_{ohm}), and the concentration overpotential (η_{c}). Figure 2.10 presents a diagram of the current flowing in the system against the potential applied between two electrodes. It can be observed that three control regions exist: activation, mixed and mass-transport. At low current densities, the main contribution to the cell overpotential is the activation overpotential due to the charge-transfer reaction occurring at the electrode-electrolyte interface, *i.e.*, the charge transfer process occurs at a slow rate when compared to the rate at which reactants/products are supplied/removed from the electrode surface. At higher current densities, the concentration overpotential becomes dominant due to mass-transport limitations that affect the availability of the reactants at the electro-active sites of the electrode. Here, the charge-transfer rate at the electrode surface is very fast and the reaction rate is limited by the mass-transport of species, assuming that electron transport is very fast which is normally the case. In the mixed control region, the ohmic overpotential becomes important because of material resistances that include both electronic and ionic, and the charge-transfer and mass-transport have a similar effect on the reaction rate. Conceptually, the total cell overpotential can be obtained by accounting for these three overpotential contributions, *i.e.*, $E_{\text{cell}} = E_{\text{OCP}} \pm (|\eta_{\text{ac}}| + |\eta_{\text{ohm}}| + |\eta_{\text{c}}|)$, however, it is important to keep in mind that η_{ac} and η_{c}, and to a lesser extent η_{ohm}, are related so attempting to obtain independently each value of overpotential leads to an intrinsic error (Gileadi, 1993).
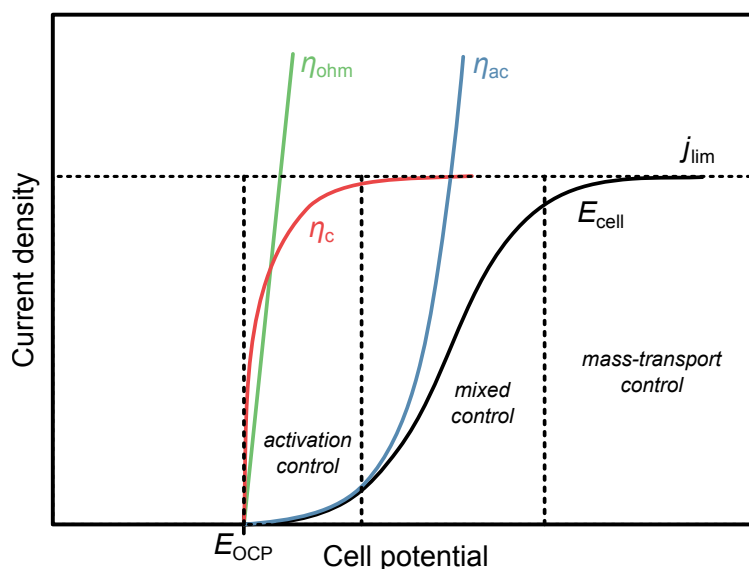
Figure 2.10: Current against cell potential, with different overpotential contributions. The term E_{cell} is the cell potential, E_{OCP} is the open circuit potential, η_{ac} is the activation overpotential, η_c is the concentration overpotential, η_{ohm} is the ohmic overpotential, and j_{lim} is the limiting current density.

The activation overpotential represents the displacement from equilibrium needed to overcome the activation energy barrier of the reaction, which produces a reaction current. This behaviour is studied by means of reaction kinetic theory, and in the case of electron-transfer reactions, the most common approach is the use of Butler-Volmer kinetics, which is reviewed in detail below. The ohmic overpotential in electrochemical cells is calculated by means of Ohm's law, *i.e.*, $\eta_{ohm} = \sum_k jAR_k$, considering the ohmic resistance (R_k) due to electron conduction in electrodes, bipolar plates, current collectors and external connecting wires, and due to the flow of ionic current in the electrolyte solutions and the membrane, if present. The concentration overpotential is usually considered in the kinetic expression for the electron-transfer reaction by means of the ratio between the current density and the limiting current density (j_{lim}). The mass-transport of species occurs by three mechanisms, including diffusion which is the movement of species due to a gradient of chemical potential (or concentration gradient if a dilute solution is considered), migration which is the movement of charged species or ions due to a gradient of electrical potential, and convection which is the movement of species as result of natural or forced convection. In general, the limiting current density is obtained by assuming the formation of a stagnant layer (Nernst diffusion layer) of thickness δ at the electrode surface, with migration transport usually being neglected. The mass-transport in this layer is represented by Fick's first law of diffusion in a steady-state condition, $N = -k_m(c^s - c^*)$, where, $k_m = D/\delta$ is the mass-transport coefficient, c^s is the concentration at the electrode surface, and c^* is the bulk concentration. The molar flux of species in the Nernst diffusion layer can be matched to the rate of reaction at the electrode surface, and for the particular case

at which the process occurs at the maximum rate possible, *i.e.*, $c^s = 0$, the limiting current density can be estimated as $j_{\lim} = nFk_m c^*$ (for a positive current and a reactant). From this analysis, the relation between the surface and bulk concentration, given as a quotient in Equation 2.21, can be accounted for in the kinetic expression for the reaction rate.

$$\frac{c^s}{c^*} = 1 - \frac{j}{j_{\lim}} \tag{2.21}$$

General electrode kinetics is now reviewed for the general faradaic reaction presented in Equation 2.13, $S_1 = R \rightleftarrows O + ne^- = S_2$, where the forward reaction is considered to produce electrons, namely an oxidation reaction, with state S_1 and reduce species R ($s_i > 0$), and state S_2 and oxidised species O ($s_i < 0$). In the thermodynamic description of reaction kinetics, the reaction complex (*i.e.*, the range of transient configurations that a collection of atoms passes through in between clearly defined products and reactants) explores a landscape of excess chemical potential ($\mu^{ex}(x)$) along a reaction coordinate (x) between two local minima states (μ_1^{ex} and μ_2^{ex}) with a transition state over an activation barrier ($\mu_{\ddagger}^{ex}$) (Bazant, 2012). Out of equilibrium the net rate of reaction (r) is given by Equation 2.22 (Bazant, 2012, 2013; Newman and Thomas-Alyea, 2004). At thermal equilibrium the net rate of reaction is zero ($r = 0$) and we must have $\mu_1 = \mu_2$, therefore, the standard rate of reaction for the forward and backward reactions are equal, *i.e.*, $r_{1\to2}^{\ominus} = r_{2\to1}^{\ominus}$.

$$r = r_{1\to2} - r_{2\to1}$$
$$r = r_{1\to2}^{\ominus} c_R \exp\left(\frac{-(\mu_{\ddagger}^{ex} - \mu_1^{ex})}{RT}\right) - r_{2\to1}^{\ominus} c_O \exp\left(\frac{-(\mu_{\ddagger}^{ex} - \mu_2^{ex})}{RT}\right) \tag{2.22}$$
$$r = r_0\left[\exp\left(\frac{-(\mu_{\ddagger}^{ex} - \mu_1)}{RT}\right) - \exp\left(\frac{-(\mu_{\ddagger}^{ex} - \mu_2)}{RT}\right)\right]$$

where,

$$c_R = \prod_{s_i>0} c_i^{s_i}, \quad c_O = \prod_{s_i<0} c_i^{|s_i|}, \tag{2.23}$$

It is possible to define μ_1 and μ_2 by accounting for the contribution of electrostatic potential and chemical potential, separately, for state 1 and 2, as presented in Equation 2.24.

$$\mu_1 = \mu_R + q_R \phi$$
$$\mu_2 = \mu_O + q_O \phi + n\mu_e - nF\phi_e \tag{2.24}$$

where,

$$\mu_R = \sum_{s_i>0} s_i \mu_i, \quad \mu_O = \sum_{s_i<0} |s_i| \mu_i, \quad q_R = \sum_{s_i>0} s_i z_i F, \quad q_O = \sum_{s_i<0} |s_i| z_i F, \quad \mu_{R/O} = \ln(a_{R/O})$$
$$\tag{2.25}$$

When the equilibrium condition is considered, it is possible to use Equations 2.22 and Equation 2.24 to obtain a kinetic derivation of the Nernst equation (Equation 2.17). Away from equilibrium, the half-cell reaction rate is controlled by a surface or activation overpotential, which is defined as the difference between the electrode potential and it value at equilibrium, $\eta_{ac} = \Delta\phi - \Delta\phi^{eq}$, defining the half-cell reaction current density, $j_{ac} = nFr$. Specific models of charge transfer kinetics correspond to different choices of $\mu_{\ddagger}^{ex}$ (Bazant, 2012). The Butler-Volmer hypothesis states that the electrostatic energy of the transition state can be estimated as the weighted average of the electrostatic energies of the initial and final states, as presented in Equation 2.26. In this equation, the first term on the right hand side is the excess chemical potential of the transition state with activity coefficient $\gamma_{\ddagger}$, the second term on the right hand side is the electrostatic energy of the transition state, where α_c and α_a are the cathodic and anodic transfer coefficients. These transfer coefficients are related to the symmetry factor ($0 < \alpha < 1$), $\alpha_a = 1 - \alpha$ and $\alpha_c = \alpha$. Substituting Equations 2.24 and 2.26 in Equation 2.22, the net rate of reaction can be expressed in terms of the activation overpotential (η_{ac}) as shown in Equation 2.27. When a dilute solution is considered, *i.e.*, $\gamma_R = \gamma_O = \gamma_e = \gamma_{\ddagger} = 1$, the exchange current density (j_0) is expressed in terms of concentrations instead of activities, Equation 2.28, which is normally the case used. The Butler-Volmer kinetic approach has been widely used to describe the electrode kinetics of a single-step charge-transfer reaction, allowing the value of the current transfer at the electrode-electrolyte interface to be calculated as a function of the activation overpotential and the concentration of species.

$$\mu_{\ddagger}^{ex} = RT \ln\left(\gamma_{\ddagger}\right) + \left[\alpha_c q_R \phi + \alpha_a (q_O \phi - nF\phi_e)\right] \tag{2.26}$$

where,

$$j_{ac} = j_0 \left[\exp\left(\frac{\alpha_a nF\eta_{ac}}{RT}\right) - \exp\left(\frac{-\alpha_c nF\eta_{ac}}{RT}\right) \right] \tag{2.27}$$

$$j_0 = nFr_0 (a_R)^{\alpha_c} (a_O a_e^n)^{\alpha_a} \gamma_{\ddagger}^{-1} \tag{2.28}$$

Figure 2.11 presents a diagram of the typical current-overpotential relation obtained from Equation 2.27. Four cases of electron-transfer control can be distinguished depending on the magnitude and sign of the activation overpotential (Bard and Faulkner, 2001). At very negative values of η_{ac}, the first exponential term in Equation 2.27 can be neglected and the current density can be approximated as the cathodic current density ($j_{ac} \approx j_c$). Therefore, the potential is much lower than the equilibrium potential $\Delta\phi << \Delta\phi^{eq}$. At very positive values of η_{ac}, the second exponential term in Equation 2.27 can be neglected and the current density can be approximated as the anodic current density ($j_{ac} \approx j_a$). Therefore, the potential is much higher than the equilibrium potential $\Delta\phi >> \Delta\phi^{eq}$. At

very small negative or positive values of η_{ac}, Equation 2.27 can be reduced to a linear relation, $j_{ac} = j_0(nF\eta_{ac}/(RT))$. Finally, the equilibrium occurs at $\eta_{ac} = 0$, where the net current density is equal to zero and the cathodic and anodic currents densities are equal to the exchange current density, $j_0 = j_a = -j_c$, and as expected the potential is equal to the equilibrium potential.
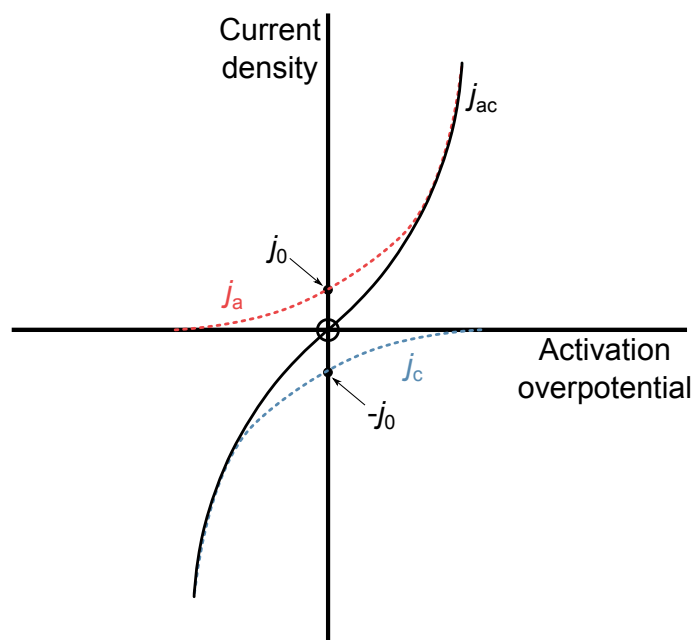
Figure 2.11: Current-overpotential curve for the faradaic reaction $R \rightleftarrows O + ne^-$, with $\alpha = 0.5$. Dashed lines show the cathodic (j_c) and anodic (j_a) components of the current density. The term j_{ac} is the activation or transfer current density and j_0 is the exchange current density.

2.3.5 Definitions and performance figures of redox flow batteries

The theoretical State of Charge (SOC) of a battery is a measurement of how much charge has been stored or released with respect to a theoretical maximum capacity (Q_{max}). This maximum or available charge depends on the total amount of active species available, as shown by Equation 2.29 (Pletcher, 2009; Walsh, 1993). Where m is the dissolved mass of the active species in the electrolyte solution, and n_e is the number of electrons involved in the charge-transfer reaction. In an ideal battery, there is no loss of electric charge during operation or stand-by, and therefore, the SOC of the battery can be obtained by accounting for the total electric current (I) applied or delivered, either in charging or discharging mode, with respect to the maximum charge available. Equation 5.15 shows the SOC of a battery for a given current, an initial SOC at time t_0, and a final time t. This is the amount of reactants and products undergoing electrochemical change within a period of time is related to the number of electrons passed through the external circuit (Pletcher, 2009; Walsh, 1993). The electrical charge (Q) is defined as the integral of the electric

current over time. For the specific case of galvanostatic operation, $Q = It$.

$$Q_{\text{max}} = \frac{mFn_{\text{e}}}{M} \tag{2.29}$$

$$SOC(t) = SOC(t_0) + \frac{Q}{Q_{\text{max}}} = SOC(t_0) + \frac{1}{Q_{\text{max}}} \int_{t_0}^{t} I(t)\,\mathrm{d}t \tag{2.30}$$

It is important to note that in an actual cell the useable capacity differs from the theoretical one due to loss mechanisms related to parasitic chemical or electrochemical reactions, crossover of active species through the membrane, and shunt currents, among others. The Electrolyte Utilisation (EU) during discharge is defined as the ratio of the actual discharge capacity to the theoretical maximum capacity of the electrolyte, as shown in Equation 2.31. This utilisation is affected by operating parameters such as the current density, potential operating window and electrolyte flow rate.

$$EU = \frac{\int_0^t I_{\text{dis}}\,\mathrm{d}t}{Q_{\text{max}}} \tag{2.31}$$

The output power or power density of the cell is a characteristic parameter that is usually measured under certain discharge conditions. Equation 2.32 is used to calculate the power density (P) as a function of the current, potential (E) and electrode area (A). This output power is mainly affected by the active area available, and in the case of a stack by the number of single cells considered. A characteristic plot, including a polarisation curve and a power density curve, has been taken from PEM fuel cells to evaluate RFB performance (Zheng et al., 2014b). Figure 2.12a displays the typical characteristic plots for a VRFB operating with different membranes. These curves are taken as a reference to improve the battery performance by decreasing the polarisation during discharge or by increasing the peak power density when different components or operating conditions are used. Also, polarisation curves are used to study the different potential losses observed for a certain cell configuration, operating conditions and a range of applied current densities. RFBs do not display a unique characteristic plot of polarisation and power density, as the cell response also depends on the SOC, and therefore, comparison of such responses must be made with care. Figure 2.12b shows the performance of a H_2-Mn RFB at different SOCs.

$$P(t) = \frac{E(t)I(t)}{A} \tag{2.32}$$

Commonly, figures of merit are used to indicate performance efficiency of charge-discharge tests on RFBs (Tang et al., 2014; Zhao et al., 2006; Zheng et al., 2014b). These

(a)   **(b)**
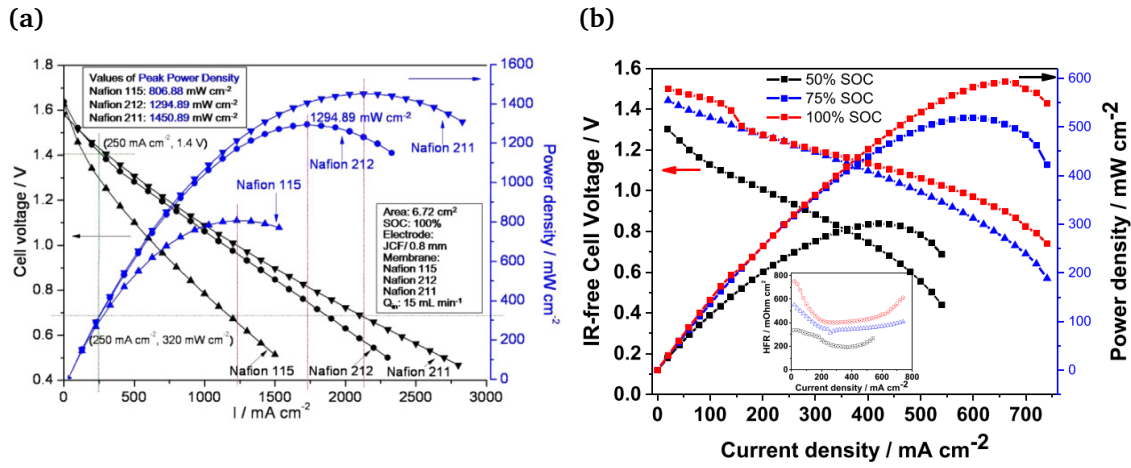
Figure 2.12: Characteristic plot of polarisation and power density. (a) $6.72\,\mathrm{cm}^2$ area VRFB using carbon felt electrodes and different membranes (Nafion 115, 212 and 211), and catholyte and anolyte solutions of 1.5 M V(IV) and V(III) in 3 M H_2SO_4, respectively, at electrolyte flow rate of $15\,\mathrm{mL\,min}^{-1}$ and 100% SOC (Zheng et al., 2014b). (b) Differentt SOC (50%, 75% and 100%) for a $5\,\mathrm{cm}^2$ area H_2-Mn RFB using a carbon paper cathode, platinised carbon paper anode, Nafion 212 membrane and a catholyte solution of 1 M $MnSO_4$, 1 M $Ti(SO_4)_2$ and 3 M H_2SO_4, at a flow rate of hydrogen and catholyte of 100 and $50\,\mathrm{mL\,min}^{-1}$ respectively (Rubio-Garcia et al., 2018).

figures of merit consider the ratio between the output and input of a characteristic quantity. Commonly used figures are the coulombic, voltage and energy efficiencies. The Energy Efficiency (EE, η_E) is defined as the ratio of the energy delivered by the battery during discharge to the energy stored during charge, as shown in Equation 2.33.

$$\eta_E = \frac{\int_0^{t_{dis}} E_{dis} I_{dis}\,\mathrm{d}t}{\int_0^{t_{ch}} E_{ch} I_{ch}\,\mathrm{d}t} = \frac{\int_0^{t_{dis}} P_{dis}\,\mathrm{d}t}{\int_0^{t_{ch}} P_{ch}\,\mathrm{d}t} \tag{2.33}$$

The Coulombic Efficiency (CE, η_C) is defined as the ratio of the capacity taken from the cell during discharge to the capacity supplied during charge, as shown in Equation 2.34. In general, a higher CE is related to a lower capacity loss during the cell operation due to a decrease in the crossover flux of electroactive species through the membrane and self-discharge reactions.

$$\eta_C = \frac{\int_0^{t_{dis}} I_{dis}\,\mathrm{d}t}{\int_0^{t_{ch}} I_{ch}\,\mathrm{d}t} = \frac{Q_{dis}}{Q_{ch}} \tag{2.34}$$

The Voltage or potential Efficiency (VE, η_N) is defined as the ratio of the integral of the cell potential during discharge to the integral of the cell potential during charge when a constant current is applied. Also, it can be obtained as the ratio of the energy efficiency to the coulombic efficiency since the current is considered to have a constant value. The VE is directly related to the thermodynamic reduction potential of the electrochemical reaction at each electrode and the overpotential losses of the cell.

$$\eta_N = \frac{\int_0^{t_\text{dis}} E_\text{dis} \, \mathrm{d}t}{\int_0^{t_\text{ch}} E_\text{ch} \, \mathrm{d}t} = \frac{\eta_E}{\eta_C} \tag{2.35}$$

In a cycling test, the battery is operated continuously at constant current density for a number of charge-discharge cycles. The electrolyte utilisation is usually tracked along the number of cycles to study how fast the capacity fades. The energy, coulombic and voltage efficiencies are also tracked with the number of cycles to evaluate any decrease in the cell performance either by an increase in the capacity loss due to crossover or increase of overpotential losses due to degradation of electrodes or membrane.

2.4 Modelling overview

In the past, several models addressing different types of RFBs have been published. These models differ in the type of geometry considered, the level of sophistication, the assumptions taken when coupling the conservation equations and electrochemical processes, among other subjects. This section presents the main previous modelling contributions in modelling, including cell level models and stating main assumptions, distinctive approaches, and conclusions drawn from these studies. Since the aim of this work is the study of an RHVFC and considering that there are several different types of RFB systems as described in Section 2.2, the modelling overview presented in this section only includes contributions published for VRFBs and PEM fuel cells. Even though PEM fuel cells are not RFB systems, they are of importance for the RHVFC since they share the same anodic redox reaction and reactants. Also, it is relevant to review PEM fuel cell models since most of the modelling approaches proposed for RFBs, and in particular, for VRFBs, have been taken from earlier modelling developments for PEM fuel cells. First, a brief description of the system is given followed by a summary and discussion of the main contributions in their mathematical description.

2.4.1 Vanadium redox flow batteries

Mathematical modelling and simulation have proven efficient and accessible in other electrochemical systems such as PEM fuel cells, and have recently represented an important tool for VRFBs (Zheng et al., 2014a). Electrochemical systems can be addressed by considering their particular set of conditions such as the number of phases participating in the process, boundary conditions and assumptions. Models capable of reproducing the system operation and fulfil computational requirements providing enough accuracy are required to optimise design, operating conditions, and performance. VRFB modelling has been approached by including conservation laws and auxiliary equations. VRFB models

cover a wide range of complexity and accuracy, and the review given here is shortened and summarised, for further explanations refer to the modelling reviews reported by Xu and Zhao (2015) and Zheng et al. (2014a). Mathematical models have been developed to simulate different effects in VRFBs such as cell geometry, or phenomenological effect such as undesired side-reactions, or to support the development of control systems, which could allow autonomous operation (Skyllas-Kazacos et al., 2011). Different length-scale approaches can be considered in VRFB modelling, including macro, micro and molecular/atomic approach (Zheng et al., 2014a). Figure 2.13 shows some of these different approaches along with the subjects commonly studied at each scale. The macro approach includes market, stack/system and cell-level models. Cell models, which are of interest for this work, can be developed considering different approaches such as Equivalent Circuit Models (ECMs), lumped or zero-dimensional models and continuum models. ECMs use electrical components to represent the complex physicochemical phenomena inside a cell, which can be readily assembled to represent a stack; zero-dimensional (0D) models describe the time-dependent behaviour of electrochemical phenomena at the electrodes using mass and energy conservation equations along with equilibrium and kinetics expressions; and continuum models describe the electrodes assuming that the materials are continuously distributed and can be characterised by averaged structural and transport properties while solving a number of conservation equations such as mass, momentum, energy, and species conservation (Zheng et al., 2014a). The micro approach aims to connect the continuum and molecular/atomic scale analysis by considering the material microstructure and phases at the micropore scale, where the objects are described as microscopic particles that incorporate molecular details implicitly such as in a Lattice Boltzmann Method (LBM) (Zheng et al., 2014a). The molecular/atomic approach aims to understand to an elementary scale the structure and nature of the materials inside a cell, such as Molecular Dynamics (MD), which predicts the time evolution of the interaction of particles (atoms, molecules, etc.) to estimate relevant physical properties, and Density Functional Theory (DFT), which investigates the electronic structure of atoms and the interactions due to the motion of electrons (Zheng et al., 2014a).

In order to accurately simulate electrochemical system operation, stack models considering multi-scale approaches must be used. These models can include cell models to accurately reproduce cell performance, which can consider continuum models to precisely describe transport phenomena or even material models to describe the redox reactions taking place at each electrode. Control tools should include a stack model considering sufficient detail of the physicochemical processes involved possibly by means of a continuum or material model, while also incorporating thermal-electrical phenomena between half-cells through a cell or equivalent circuit model (Zheng et al., 2014a). These modelling tools could facilitate the control of the performance of individual cells during cycling,
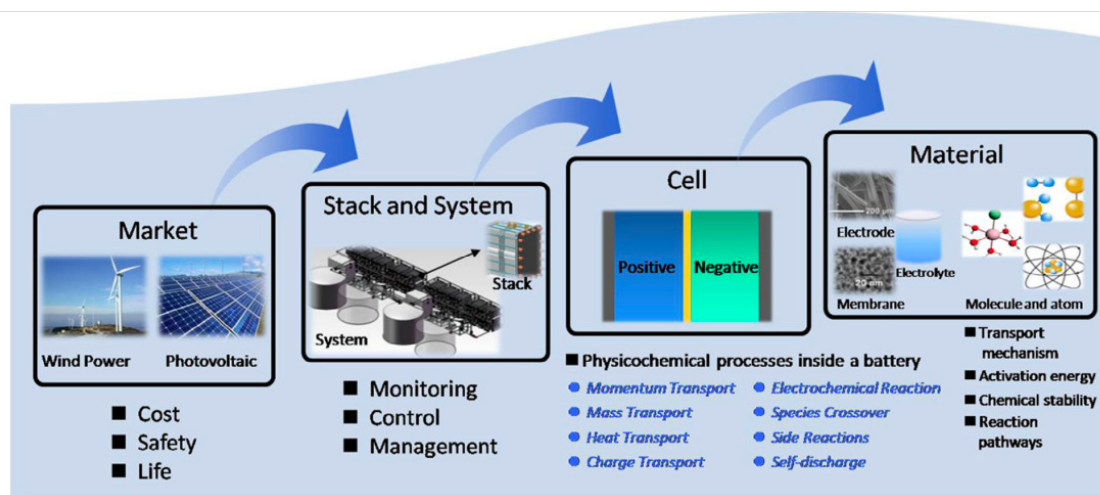
Figure 2.13: Schematic of VRFB model approaches and topics studied (Zheng et al., 2014a)

allowing the increase of system efficiency and safety by means of adequate control decisions. Multi-scale stack simulations of VRFBs have not been achieved because of the extensive computational power required, as well as uncertainty about how to combine the continuum, material and lumped models. It is imperative to develop multi-scale models to support design and optimization of VRFBs, and hence promote their commercialisation (Zheng et al., 2014a). Zero-dimencional (lumped) and continuum models for cell description are of interest in this work, and only they are reviewed.

Both zero-dimensional and continuum models have been reported for VRFBs. Zero-dimensional (0D) models describe time dependent phenomena using a set of differential algebraic equations and considering a uniform spatial distribution of species concentrations (Zheng et al., 2014a). These models consider mass and energy conservation along with the electrochemical processes, and a number of assumptions are taken into account. For example, fully filled tanks, electro-neutrality, instantaneous self-discharge reactions, uniform concentrations and temperature, Continuous Stirred Tank Reactor (CSTR) behaviour of electrodes and tanks, and constant material resistances (Zheng et al., 2014a). Li and Hikihara (2008) proposed a dynamic 0D model based on physical phenomena and electrochemical reaction kinetics (Li and Hikihara, 2008), but neglecting the recirculation effect on the species concentrations, making the model not appropriate for control applications. The recirculation effect, between the electrolyte tank and half-cells, was introduced for a lumped model by Shah et al. (2011b). This model represented the relationship between performance and system properties considering polarisation losses, electrode kinetics and the recirculation of electrolytes, but neglects crossover of vanadium species and self-discharge reactions (Shah et al., 2011b). The conservation of species was developed for vanadium species, protons and water at each half-cell, considering electrode reactions and recirculation and allowing for the transport of protons through the membrane and the

electro-osmotic drag of water. Since protons were considered to be the only ionic species to be mobile in the membrane, their molar flux through the membrane was assumed to be equal to the applied current density, while the molar flux of water through the membrane was estimated by means of an electro-osmotic drag coefficient for water transport through a Nafion membrane (Shah et al., 2008, 2011b; Springer et al., 1993). Other effects were included, such as thermal effects (Al-Fetlawi et al., 2009; Tang et al., 2012c), pump power losses (Xiong et al., 2013), and self-discharge and side reactions (Tang et al., 2011). Thermal studies concluded that current density has an effect on heat generation, while the electrolyte flow rate has an important impact on heat transfer and dissipation (Xu and Zhao, 2015; Zheng et al., 2014a). The heat from self-discharge reactions can contribute importantly to increase electrolyte temperature during long periods of stand-by, but was seen to be negligible during charge-discharge operation (Zheng et al., 2014a). The description of transport within the membrane presented above is simplified and sometimes non-realistic because of crossover of other ions that produce a loss of capacity after long-term charge-discharge cycling due to self-discharge reactions. Xu et al. (2014) used a similar approach to obtain the equations for the conservation of species, including crossover of vanadium species and protons but did not consider recirculation effects. The conservation of protons at each electrolyte was built considering electrode reactions, self-discharge reactions, transfer of proton between half-cells due to a concentration gradient, and the transfer of protons due to charge balance (Xu et al., 2014). Self-discharge reactions will take place between vanadium ions with different charge numbers (Tang et al., 2012c; You et al., 2011). At the anode, transport of V(IV) and V(V) from the cathode will produce the following self-discharge reactions when reacting with V(II) and V(III), as shown in Equation 2.36. In the cathode, diffusion of V(II) and V(III) from the anode will react with V(IV) and V(V), as shown in Equation 2.37.

$$VO^{2+} + V^{2+} + 2H^+ \rightarrow 3V^{3+} + H_2O$$
$$VO_2^+ + 2V^{2+} + 4H^+ \rightarrow 3V^{3+} + 2H_2O \quad (2.36)$$
$$VO_2^+ + V^{3+} \rightarrow 2VO^{2+}$$

$$V^{2+} + 2VO_2^+ + 2H^+ \rightarrow 3VO^{2+} + H_2O$$
$$V^{3+} + VO_2^+ \rightarrow 2VO^{2+} \quad (2.37)$$
$$V^{2+} + VO^{2+} + 2H^+ \rightarrow 2V^{3+} + H_2O$$
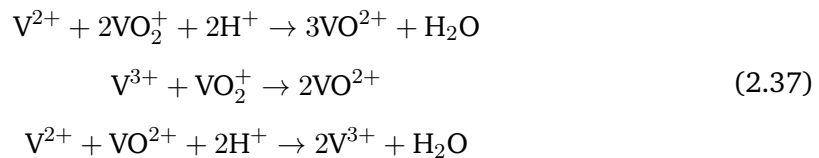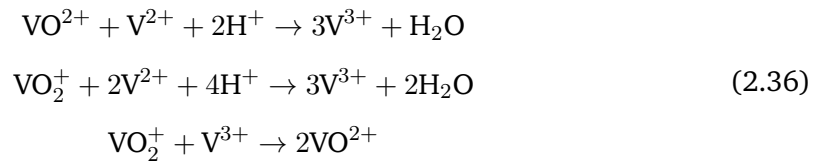
It has been shown that the magnitude and direction of ionic crossover flux are related to the SOC, showing a net transfer direction towards the negative electrolyte at an initial SOC of 0% (Zheng et al., 2014a). The crossover of vanadium species is inevitable in VRFBs that use Nafion membranes and their fluxes have been usually mathematically rep-

resented by Fick's law (Equation 2.38) and assuming a steady-state condition. Equations for the conservation of ionic species have been proposed including crossover through the membrane and side reactions in 0D models (Tang et al., 2012c; Xu et al., 2014; You et al., 2011; Yu and Chen, 2014a). Self-discharge reactions are commonly assumed to be instantaneous, allowing the molar fluxes through the membrane to be directly related to the consumption/production of species due to self-discharge reactions at the opposite electrode. More recently, more complete expressions for the crossover molar fluxes of ionic species accounting for migration, diffusion, and convection fluxes by means of the Nernst-Plack equation (Equation 2.38) have been used in 0D models (Darling et al., 2015; Pugach et al., 2018; Xu and Zhao, 2015). The molar flux equation can be simplified by considering protons as the dominant charge carrier and estimating the bulk velocity as the molar flux of water (Darling et al., 2015). This allows for the integration of the flux equation over the membrane thickness and its incorporation in the species conservation equations. Predicting capacity as a function of time could support the periodic electrolyte re-balancing or re-mixing (Zheng et al., 2014a). However, VRFB 0D models display deviation from experimental results due to the simplified representation of water and ion transport across the membrane. In reality, the crossover of water and ions through an ion-exchange membrane is a complex problem, which would require a concentrated-solution theory framework for being fully described. Side reactions, like gas evolution during charge, also produce a significant capacity loss on cycling and are normally neglected in cell models (Zheng et al., 2014a).

$$
\begin{aligned}
\text{Fick:} \qquad & N_i = -D_i \nabla c_i \\
\text{Nernst-Plank:} \qquad & N_i = c_i v - D_i \nabla c_i - z_i \mu_i F c_i \nabla \phi
\end{aligned}
\qquad (2.38)
$$

Zero-dimensional models are commonly used for stack modelling because the set of equations is relatively simple and easy to integrate to use in a control system. Ontiveros and Mercado (2014) developed a VRFB stack model that accounted for potential and coulombic losses (Xu and Zhao, 2015). A zero-dimensional model has been introduced by Blanc and Rufer (2008), which solved the hydraulics and electrochemistry of the cell allowing for the study of the optimal operating conditions at constant current or potential. Moreover, Xu and Zhao (2015) proposed a power-based efficiency model that considered cell performance and pumping power and facilitate the study of flow field designs. Their results have shown that there is an optimal flow rate condition for each flow field type at which a maximum power-based efficiency is achieved, recognising that serpentine flow fields are more suitable for VRFB since they produce the highest energy-based and round-trip efficiencies. On the other hand, shunt currents have also been studied. Xing et al. (2011) developed a stack model to investigate this effect, obtaining the shunt current distribution in a stack and its effect on the charge-discharge cell potential. This study has

shown that reducing the number of single cells in series could decrease the resistance of manifolds and channels, therefore, increasing the power of a single cell. Nevertheless, 0D model approaches are insufficient to describe complex physicochemical processes taking place in a battery. To study these processes is necessary to develop a lumped model capable of representing the different mechanisms that can affect the cell performance while maintaining its simplicity to make possible its use in design and control applications.

In general, processes involving complex phenomena are in detail addressed by continuum models, which simulate the physicochemical processes within a continuum domain at cell scale using average properties and transport phenomena combined with electrochemical reaction kinetics (Zheng et al., 2014a). These continuum models have been developed considering one-dimensional (1D), two-dimensional (2D) or three-dimensional (3D) domains. A schematic diagram of the domains for 2D and 3D models is presented in Figure 2.14a. Macroscopic models of electrodes are the most utilised for modelling VRFB, and consider that materials are continuously distributed throughout the cell volume, therefore, materials and structures are taken as homogenised domains (Xu and Zhao, 2015; Zheng et al., 2014a). The governing equations are conservation laws, which can be solved in steady-state or transient conditions. In order to solve the coupled phenomena, initial and boundary conditions must be provided, and to simplify the problem a set of different assumptions are considered. Common assumptions are incompressible and laminar flow, no gravity effect, dilute-solution approximation, and that the membrane is impermeable to all ions except for protons. Moreover, volume conservation is assumed when gas evolving reactions occur or negligible evolution reactions. Isothermal conditions in the domains are assumed, and heat loss within pipes and electrolyte tanks are usually neglected (Xu and Zhao, 2015; Zheng et al., 2014a). Conservation of species in the electrolyte considers effective parameters to account for the porosity (ε) and tortuosity (τ) of electrodes, such as effective diffusion coefficients (D_i^{eff}) in the porous electrodes. A Bruggeman expression ($\tau = \epsilon^{-0.5}$), taken from the PEM fuel cell literature, is typically used to account for tortuosity in carbon electrodes. The flux of species normally considers hydrodynamic dispersion, electro-kinetic effects and convection (Equation 2.38) (Gandomi et al., 2016; Xu and Zhao, 2015; Zheng et al., 2014a). Moreover, a condition of electro-neutrality within the electrolyte solutions is used in almost all reported models, and because of this assumption, the divergence of the total current density is zero (the charge entering the electrolyte is equal to the charge leaving from the electrode). Additionally, at the electrode pore-scale the mass transport of reactants/products to/from the pore wall (Figure 2.14b) is described by a mass-transport coefficients, which depends on the morphology of the pore wall, electrolyte properties, and local velocity of the electrolyte, and almost always steady-state conditions are assumed (Gandomi et al., 2016; Xu and Zhao, 2015).

(a)

(b)
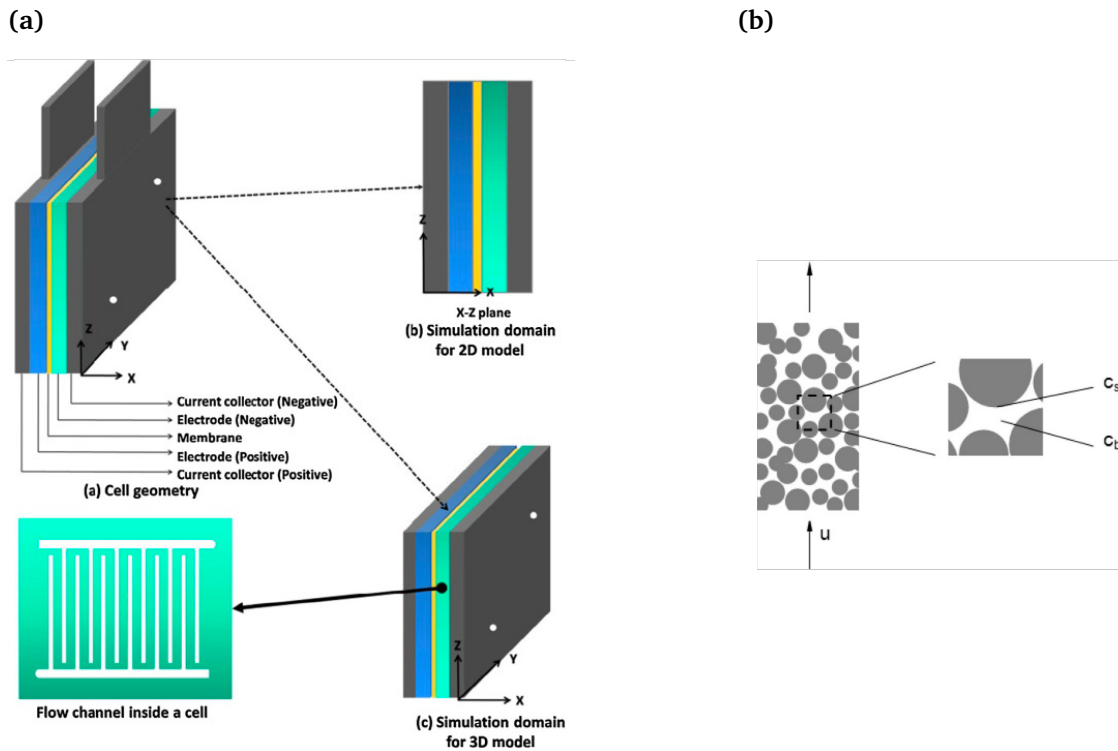
Figure 2.14: (a) Schematic diagram of considered domains for 2D and 3D models of VRFB (Zheng et al., 2014a). (b) Schematic of the species transport within a porous electrode (Xu and Zhao, 2015).

Flow models that only include momentum transport equations have been proposed to study the distribution of electrolyte solution flow within a VRFB (Zheng et al., 2014a). Fluid flow through the porous media can be described by means of the Brinkman equation, but instead, Darcy law is most commonly used to describe porous media flow, neglecting friction due to macroscopic shear in the fluid/porous media interface (Brinkman extent) and inertial energy of the fluid (Forchheimer term) (Zheng et al., 2014a). Darcy's law is used to obtain the macroscopic superficial velocity of the electrolyte (Gandomi et al., 2016), and its use has been justified because the Reynolds number is less than the unity, when based on the pore-size length scale. Generally, electrolytes are assumed incompressible having constant density, and therefore, a simplified continuity equation ($\nabla \cdot v = 0$) is employed for obtaining the mass-averaged velocity. Models that consider mass and charge conservation and electrochemical reaction kinetics have been also reported. One of the first such models, which took into account the 2D effects, was successfully demonstrated by Shah et al. (2008). Figure 2.15 displays an example of their results. Subsequently, additional phenomena were added, such as hydrogen and oxygen evolution and thermal effects (Al-Fetlawi et al., 2010; Shah et al., 2010c; Zheng et al., 2014a). Transport across the membrane has been considered in continuum models, normally assuming that only protons are mobile. In general, a condition of electro-neutrality is considered in the membrane, where the concentration of protons must balance the fixed charge concentration of the membrane. A continuity equation within the membrane, considering incompressible

flow with constant density, as well as conservation of charge are considered. Proton flux in the membrane is normally simplified by only including the flux due to the potential gradient, and therefore, the current density through the membrane can be calculated as a function of this flux (Gandomi et al., 2016; Xu and Zhao, 2015). In some models, convective flux is considered to contribute to the transport of protons through the membrane by using Schlogl's equation along with the continuity equation to obtain the solvent velocity in the membrane (Knehr et al., 2012b; Yang et al., 2015b). A transient 2D model able to predict capacity loss by means of the crossover was developed by Knehr et al. (2012b), considering the transport of all ionic species and water through the membrane. This model has indicated that vanadium transport in Nafion membranes is dominated by diffusive transport (Zheng et al., 2014a). Six ionic species (V(II), V(III), V(IV), V(V), H^+, HSO_4^-) were considered and the jump in potential at each membrane-electrolyte interfaces was included (Knehr et al., 2012b). Since a condition of electro-neutrality was assumed, a discontinuous profile was obtained for one of the species at the membrane/electrolyte interface, while continuous profiles were obtained for all other concentrations and potential. Recently, Lei et al. (2015) has proposed a model considering a 0D approach for electrodes and a 1D approach for the membrane, considering the conservation of vanadium species and protons. They considered two membrane-electrolyte interfacial regions where charge density is related to potential by eliminating the electroneutrality assumption and solving the Poisson equation. These regions were modelled as membrane domains with no electrochemical reactions, while charge conservation was considered. A more realistic variation of all concentrations and potential across the interfacial regions and membrane was reported, with the Donnan potential promoting the vanadium species crossover as the fixed charge concentration of the membrane increases (Lei et al., 2015).

(a) **(b)** **(c)**
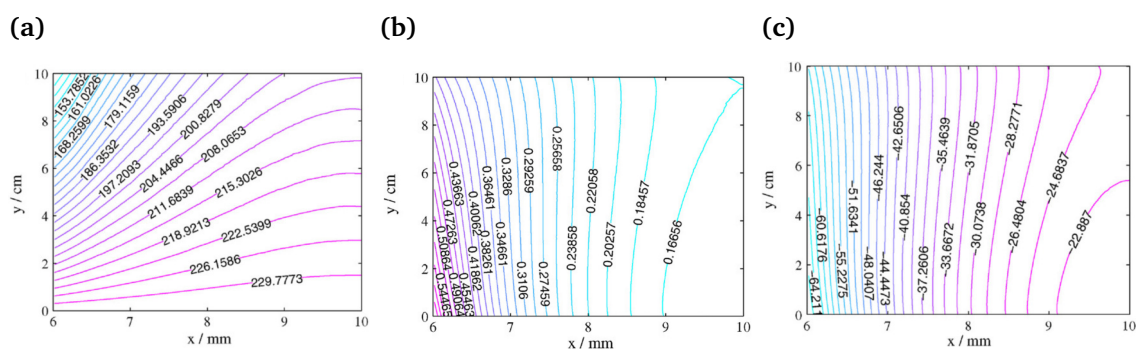
Figure 2.15: Simulated contours of: (a) V(III) concentration; (b) transfer current density; and (c) overpotential, in the negative electrode at end of charge for a flow rate of $2\,\text{mL}\,\text{s}^{-1}$ with an initial concentration of V(III) of $1080\,\text{mol}\,\text{m}^{-3}$. Line x = 6 mm: current collector/electrode interface, and x = 10 mm: membrane/electrode interface. (Shah et al., 2008).

Normally, 3D VRFB models include the effect of cell geometry, such as flow fields and manifolds, and are mainly applied for optimising battery structure and scale-up stud-

ies (Zheng et al., 2014a). Detailed spatial distribution of concentration, velocity, over-potential and current density inside the battery have been obtained by Ma et al. (2011) by means of 2D to 3D models (Zheng et al., 2014a). Temperature distribution has been included in a 3D model developed by Zheng et al. (2014c), showing that temperature increases rapidly during discharge, producing an elevated temperature pattern over cycling. This demonstrated that cell/stack temperature can rise to inappropriate levels, establishing the requirement of effective heat management and appropriate materials and structure selection (Zheng et al., 2014a). A different approach also investigated contemplates reducing a transient model, generally in a 2D or 3D level, into a quasi-steady-state model, generally in 1D or 0D level, without losing much simulation accuracy when comparing to experimental data. This method is applicable if a quasi-steady-state condition is satisfied along with boundary, initial conditions and simplifications, such as a narrow gap approximation or a plug flow behaviour (Sharma et al., 2014, 2015; Zheng et al., 2014a). In a VRFB, operation at SOC larger than 85% will most probably produce side reactions, *i.e.*, the evolution of oxygen at the positive electrode and evolution of hydrogen at the negative electrode. Some continuum models have included liquid and gas phase flow equations to model these side reactions (Al-Fetlawi et al., 2010; Shah et al., 2010b). Liquid and gas phase velocities are related through the slip velocity, which can be obtained via a balance of force on a bubble. Moreover, the pressure difference for gas and liquid phases is related to the capillary pressure (Xu and Zhao, 2015). Even when, including detailed physico-chemical phenomena in a cell model improves its fidelity, it increases the computational requirement, and hence, simplified models are preferred for specific applications such as control and design (Zheng et al., 2014a).

In the modelling of electrochemical processes, the open circuit potential and the polarisation losses are considered. The OCP (E_{OCP}) for VRFBs has been explained by a Nernst equation, usually not including the membrane effect. In general, a Simplified Nernst Equation (SNE) (Equation 2.39) has been used assuming that the activity of each species remains constant and equal to one, and neglecting the variations of standard potentials with respect to temperature (Al-Fetlawi et al., 2009, 2010; Badrinarayanan et al., 2014; Bayanov and Vanhaelst, 2011; Pugach et al., 2018; Shah et al., 2008, 2010a; Tang et al., 2013a, 2014; Vynnycky, 2011; Wandschneider et al., 2014; Yin et al., 2014a,b; You et al., 2009b; Yu and Chen, 2014a; Zheng et al., 2014c). However, this equation ignores two important mechanisms (Knehr and Kumbur, 2011): the effect of proton concentration that is involved in the cathode redox reaction and has a chemical potential that affects the E_{eq}; and the Donnan potential that exists across the membrane due to unequal proton concentration between the two electrodes. The effect of the concentration of protons has been reported to account for about $100\,\mathrm{mV}$ of the discrepancy between simulated and experimental OCP in VRFBs (Knehr and Kumbur, 2011). The difference in concentration

of protons between half-cell electrolytes has been attributed to the electrolyte preparation procedure, which can result in the imbalance of H$^+$ due to the formation or dissociation of water. These preparation methods produce a higher concentration of protons in the catholyte when compared with the anolyte concentration (Knehr and Kumbur, 2011). The concentration of protons in the catholyte is commonly assumed to have a negligible effect, while the Donnan potential is generally not included in RFB modelling - most probably because Nernst equation was originally proposed based on fuel cell literature, where the Donnan potential does not exist (Knehr and Kumbur, 2011). Recently a Nernst equation including the effect of the concentration of protons in the cathode side have been commonly used to simulate the OCP (Bromberger et al., 2014; Chen et al., 2014; Knehr et al., 2012b; Lei et al., 2015; Merei et al., 2015; Shah et al., 2011b; Sharma et al., 2014, 2015; Wei et al., 2014; Xiong et al., 2014; Xu et al., 2014; Yang et al., 2015b). Knehr and Kumbur (2011) proposed a Complete Nernst Equation (CNE) for VRFBs by including the concentration of protons effect and the Donnan effect across both membrane-electrolyte interfaces (Equation 2.39) (Knehr and Kumbur, 2011). They reported a better agreement of this equation with experimental OCP data inside the normal operating range for VRFB, namely 5% to 95% SOC. While the discrepancies at extreme conditions, *i.e.*, outside the SOC window, were explained by the assumption of unity activity coefficients for all species.

$$\text{SNE:} \qquad E_{\text{OCP}} = E_{\text{cell}}^{\circ} + \frac{RT}{F} \ln \left(\frac{c_{\text{VO}_2^+}^{\text{ca}} \, c_{\text{V}^{2+}}^{\text{an}}}{c_{\text{VO}^{2+}}^{\text{ca}} \, c_{\text{V}^{3+}}^{\text{an}}} \right)$$

$$\text{CNE:} \qquad E_{\text{OCP}} = E_{\text{cell}}^{\circ} + \frac{RT}{F} \ln \left(\frac{c_{\text{VO}_2^+}^{\text{ca}} \, c_{\text{V}^{2+}}^{\text{an}} \, (c_{\text{H}^+}^{\text{ca}})^2}{c_{\text{VO}^{2+}}^{\text{ca}} \, c_{\text{V}^{3+}}^{\text{an}}} \right)$$

$$(2.39)$$

The Donnan potential calculation is based on the same theoretical framework used to develop the Nernst equation, considering that at equilibrium a VRFB will display a potential jump at each membrane/electrolyte phase boundary. These potential jumps arise from the positive and negative charged layers that exist at each membrane/electrolyte interfaces due to the difference in concentration of protons at each electrolyte and in the membrane bulk. Figure 2.16 presents a schematic representation of the Donnan potential effect at each membrane-electrolyte interface proposed by Knehr and Kumbur (2011). From Figure 2.16 and the Donnan additional term (Equation 2.40, Knehr and Kumbur (2011)) it can be seen that the OCP of the cell will be increased by adding the potential jumps at each membrane/electrolyte interfaces. However, this equation is not consistent with the equilibrium condition observed at OCP. This can be shown by considering a typical VRFB operation, where the concentration of protons at the catholyte will be higher than the concentration of protons at the anolyte, and therefore, a concentration gradient or driving force will exist for the ionic transport of protons from the cathode to the anode side. Then, in order to maintain an equilibrium condition, there must be an opposite driving force for

the ionic transport of protons that must counteract the concentration gradient. This opposite gradient will appear on the form of a potential gradient that will decrease the total observed OCP. Recently, Pavelka et al. (2015) have stated that the Donnan correction proposed by Knehr and Kumbur (2011), and consequently, the CNE proposed by them is not consistent with thermodynamic principles. A different Donnan correction (Equation 2.40, Kontturi et al. (2008); Pavelka et al. (2015)) has been reported (Pavelka et al., 2015). This Donnan potential has been incorporated in the Nernst equation, explaining any discrepancy with OCP experimental data primarily by the assumption of unity activity coefficients (Pavelka et al., 2015). Even though the complete Nernst equation proposed by Knehr and Kumbur (2011) has been proven to be incorrect and not thermodynamically consistent, it nonetheless continues to be the most used in recent publications (Gandomi et al., 2016; Xu et al., 2014).
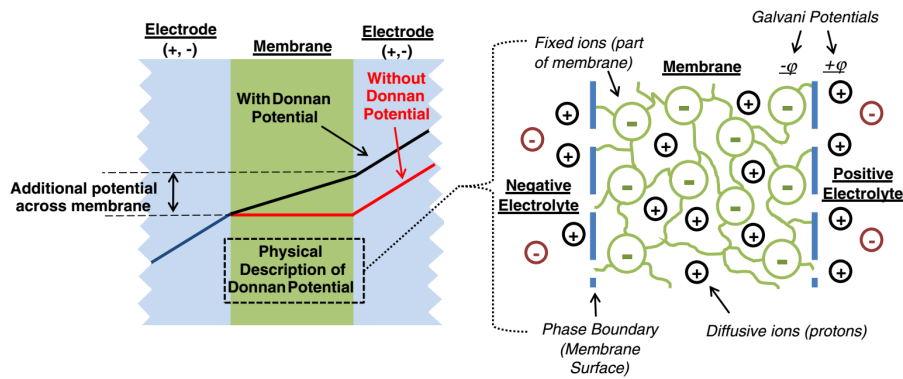
Figure 2.16: Reversible potential with and without the membrane potential and physical representation of the electrolytic double layer proposed by Knehr and Kumbur (2011).

$$\text{Knehr and Kumbur (2011):} \qquad E_{\text{Don}}^{\text{m}} = \frac{RT}{F} \ln \left(\frac{c_{\text{H}^+}^{\text{ca}}}{c_{\text{H}^+}^{\text{an}}} \right)$$

$$\text{Pavelka et al. (2015):} \qquad E_{\text{Don}}^{\text{m}} = \frac{RT}{F} \ln \left(\frac{c_{\text{H}^+}^{\text{an}}}{c_{\text{H}^+}^{\text{ca}}} \right) \tag{2.40}$$

When accounting for changes in the concentration of protons at each half-cell electrolyte, the majority of the reported models assume complete dissociation of sulphuric acid. Since VRFBs are typically modelled assuming electro-neutrality, which is also considered at the initial conditions, the full acid dissociation causes unrealistic initial concentrations to be considered in order to maintain a valid electro-neutrally assumption (Gandomi et al., 2016). Instead, a calculation of the dissociated species of H_2SO_4 can be applied through its two reaction steps of dissociation (Knopf et al., 2003). Given that the first acid dissociation step is considered to account for the dissociation of a strong acid, the first dissociation step is considered complete. While the second acid dissociation step is considered incomplete due to its much lower dissociation constant. This assumption

facilitates the calculation of the actual concentration of hydronium (H_3O^+), bi-sulphate (HSO_4^-) and sulphate (SO_4^{2-}) ions. Knopf et al. (2003) studied the dissociation of sulphuric acid solutions at a different initial concentration of acid and temperatures. Based on this data, Knehr et al. (2012b) proposed a relation to calculate a dissociation source term (S_d) that was included in the conservation equation of the sulphuric acid species. This dissociation source term has been employed in recent papers (Gandomi et al., 2016; Knehr et al., 2012b; Yang et al., 2015b).

The estimation of polarisation losses or overpotentials is approached differently, depending on the model type (cell or 1D to 3D). These overpotentials account for an activation and a mass-transfer (concentration or diffusion) overpotential (η_{ac} and η_{con}) and an ohmic overpotential (η_{ohm}). In the case of 0D models, the different overpotentials are calculated independently and then added (charge) or subtracted (discharge) to the OCP to obtain the cell operating potential. Considering the activation barrier of the electrode redox reaction, a Butler-Volmer kinetic expression can be derived by considering an anodic and a cathodic reaction (Newman and Thomas-Alyea, 2004). For a VRFB, it is normally assumed than the transfer coefficients of these reactions are equal to 0.5 and unity activity coefficients are considered, while the exchange current density (j_0) is written solely in terms of concentrations. The effect of the concentration of protons on the kinetics of the redox reaction happening at the cathode is normally neglected. Equation 2.41 presents the typical expression used for calculating the activation overpotential of the electrodes as reported in 0D models (Shah et al., 2011b; Sharma et al., 2015; Tang et al., 2014; Yu and Chen, 2014a). Where the rate constant (k_e, e= {an, ca}) of each electrode reaction depends on the temperature and the corresponding reference rate constant, and follows an Arrhenius behaviour (Shah et al., 2011b; Yu and Chen, 2014a). Since equal transfer coefficients are assumed, the activation overpotential as a function of the applied current can be calculated by inverting Equation 2.41. Mass-transport limitation effects result from concentration gradients between the bulk electrolyte solution and electrode surface (Figure 2.14b). These effects are more predominant at large current densities and at the end of charge or discharge when the concentration of active species is very low. To represent this mass-transport limitation in 0D models, the Nernst equation and Fick's law are used to account for the effect of the limiting current density (j_{lim}) into the overpotential, relating active species concentration at electrolyte bulk and electrode surface (Bard and Faulkner, 2001; Tang et al., 2014; Xiong et al., 2014; Yu and Chen, 2014a). Equation 2.43 presents a Butler-Volmer equation including the mass-transport limitation effects, where $j_{lim,c}$ and $j_{lim,a}$ are the limiting current density for the cathodic and anodic reaction, c_b is the bulk concentrations, k_m is the local mass-transfer coefficient, and A is the flux cross-sectional area. The limiting current density is obtained by considering a linear concentration profile of species within a diffusion layer, separating the bulk concentration and the surface

concentration, and assuming that at limiting conditions the surface concentration is equal to zero. The limiting current density is achieved when the electrode process occurs at the maximum rate possible for the mass-transport conditions. The local mass-transfer coefficient can be approximated, considering the fluid velocity (v) by $k_\mathrm{m} = 1.6 \times 10^{-4} v^{0.4}$ (Ma et al., 2011; Shah et al., 2008; Tang et al., 2014). Equation 2.43 is sometimes approximated when high positive or negative current densities are applied, so that the anodic or the cathodic reaction is neglected (Bard and Faulkner, 2001; Yu and Chen, 2014a).

$$j_\mathrm{e} = j_{0,\mathrm{e}} \left[\exp\left(\frac{0.5 F \eta_{\mathrm{ac,e}}}{RT}\right) - \exp\left(\frac{-0.5 F \eta_{\mathrm{ac,e}}}{RT}\right) \right], \quad \mathrm{e} = \{\mathrm{an, ca}\} \tag{2.41}$$

where,

$$j_{0,\mathrm{an}} = F k_\mathrm{an} c_{\mathrm{V}^{3+}}^{0.5} c_{\mathrm{V}^{2+}}^{0.5}, \quad j_{0,\mathrm{ca}} = F k_\mathrm{ca} c_{\mathrm{VO}^{2+}}^{0.5} c_{\mathrm{VO}_2^+}^{0.5} \tag{2.42}$$

$$\frac{j}{j_0} = \left(1 - \frac{j}{j_{\mathrm{lim,c}}}\right) \exp\left(\frac{-0.5 F \eta}{RT}\right) - \left(1 - \frac{j}{j_{\mathrm{lim,a}}}\right) \exp\left(\frac{0.5 F \eta}{RT}\right) \tag{2.43}$$

where,

$$j_{\mathrm{lim}} = n F A k_\mathrm{m} c_\mathrm{b} \tag{2.44}$$

In 0D models, ohmic losses within VRFBs due to electronic and ionic resistances are assumed to vary linearly with current density and are represented by Ohms law (Shah et al., 2011b; Yu and Chen, 2014a). The total ohmic overpotential of a cell is obtained by adding the contribution of the different cell components, such as current collectors, membrane, electrolytes and electrodes. To account for the porous media an effective conductivity is commonly used for electrodes and electrolytes (σ^eff). In the case of the membrane, its conductivity is normally estimated by means of an empirical relation accounting for its water content and temperature.

In continuum models, the overpotential contributions cannot be calculated separately, but the conservation of species and charge and the electrochemical kinetics are solved together (Chen et al., 2014; Gandomi et al., 2016; Knehr et al., 2012b; Shah et al., 2008; Vynnycky, 2011; You et al., 2009b). Conservation of species normally considers the flux of species by means of Nernst-Plank equation (Equation 2.38) and the production/consumption of species due to the electrochemical reaction, using a Butler-Volmer approach to describe the reaction kinetics and including mass-transport limitations effects, as shown for example in Equation 2.45 for the cathode of a VRFB. This kinetic approach has been widely used in VRFB models, neglecting the effect of the concentration of protons, and sometimes neglecting the mass-transport limitations effect (*i.e.*, $c_\mathrm{i}^\mathrm{s} = c_\mathrm{i}$). The electrode overpotential at every point of the continuum domain is given by the difference between the electrode and electrolyte potential minus the equilibrium potential, *i.e.*,

$\eta = \phi_s - \phi_l - E_{eq}$. Charge conservation without accumulation of charge is normally used to relate species transport, electrochemical reactions and electronic and ionic currents in the electrodes. Equation 2.47 describes the balance between electronic current density (j_s) calculated using Ohm's law and the ionic current density (j_l) estimated as the total flux of ionic charge. The current entering/leaving the electrolyte is balanced by the current leaving/entering the electrode, while they are equal to the transfer current density (j_{ca}) produced by the electrochemical reaction times the specific surface area of the electrode (a).

$$j_{ca} = j_{0,ca} \left[\frac{c^s_{VO_2^+}}{c_{VO_2^+}} \exp\left(\frac{-\alpha_c F \eta_{ca}}{RT} \right) - \frac{c^s_{VO^{2+}}}{c_{VO^{2+}}} \exp\left(\frac{\alpha_a F \eta_{ca}}{RT} \right) \right] \tag{2.45}$$

where,

$$j_{0,ca} = F k_{ca} c^{\alpha_c}_{VO^{2+}} c^{\alpha_a}_{VO_2^+} \tag{2.46}$$

$$\nabla \cdot j_l = -\nabla \cdot j_s = a j_{ca}, \quad \text{where,} \quad j_l = F \sum_i z_i N_i, \quad j_s = \sigma_s \nabla \phi_s \tag{2.47}$$

In a few cases, the transport properties of electrolytes have been studied to describe effects such as the change of electrolyte viscosity with SOC. A change in electrolyte viscosity directly affects the pressure drop through the electrode as well as the local electrolyte velocity (Xu and Zhao, 2015). The change in concentration of species in the electrolyte that take place during charge-discharge cycles causes a variation in the electrolyte viscosity. Absolute rate theory and a semi-ideal hydration model can be used to analyse the mixing behaviour of viscosities of electrolytes under isobaric equilibrium (Xu and Zhao, 2015), using the viscosities of binary solutions (i-H_2O) to predict the mixed electrolyte viscosity. The SOC dependency of the electrolyte viscosity allows for the simulation of the distribution of overpotential and current density in the electrode in a more realistic manner, and to estimate more accurately the pump work and system efficiency (Xu and Zhao, 2015). A comparison between the results of models reported in the literature with constant and variable viscosity are presented in Figure 2.17. Other effects that have been studied are the ionic interactions of species in the electrolytes. It has been experimentally observed that cross-coefficients ($L_{i,j}$) for ionic-interactions can be significant in comparison to the chemical drag-coefficients when the electrolyte becomes non-dilute (Xu and Zhao, 2015). This includes the contributions of independent motion of an ion i and its interaction with other ions through the chemical potential of ion j (μ_j) and $L_{i,j}$. This last interaction term describes the drag of species i due to the thermodynamic force of species j. This complete ionic flux approach can be used to obtain an accurate mass conservation expression. It has been reported that contributions of ionic-interactions to the ionic flux is higher close to the

ionic sources and decreases away from these sources, where it is possible to neglect the ionic-interaction contributions (Xu and Zhao, 2015). Finally, an isothermal cell condition is a valid assumption when the reservoirs and flow rates are sufficiently large, but in other cases, thermal effects should be considered (Xu and Zhao, 2015). Temperature effects on transport parameters are normally included, still considering an isothermal overall condition. To account for thermal effects, an energy conservation equation can be included, considering conduction and convective heat transport, heat generation by reactions, and Joule heating. Moreover, it is common to assume that the liquid and solid phases have the same temperature (Xu and Zhao, 2015).

(a) **(b)**
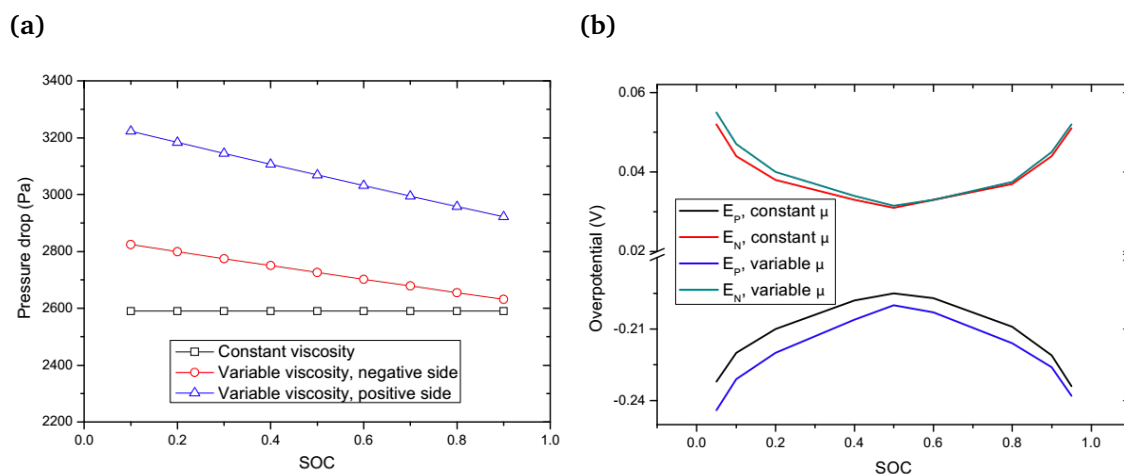
Figure 2.17: Comparison of reported model with SOC-dependent viscosity and constant viscosity for a VRFB electrolyte of 1.5 M $VOSO_4$ and 3 M H_2SO_4 (Xu and Zhao, 2015). (a) Pressure drop; and (b) Overpotential.

2.4.2 Polymer-electrolyte-membrane fuel cells

An electrochemical cell that is important to review is the Polymer-Electrolyte-Membrane (PEM) fuel cell since the anode side of an RHVFC considers hydrogen and possess similar characteristics that a PEM fuel cell. The anodic side of an RHVFC undergoes hydrogen oxidation and reduction in electrolytic or galvanic mode, while PEM fuel cells only operate in electrolytic mode, *i.e.*, only oxidation of hydrogen occurs at the node. It is important to keep in mind this difference, however, the modelling of RFBs and electrolysers has been widely based in PEM fuel cell modelling, and therefore, a brief overview of PEM fuel cell models is given. The review presented here is shortened and summarised, and for further explanations refer to Bavarian et al. (2010); Siegel (2008); Sousa and Gonzalez (2005); Weber and Newman (2004); Wu (2016).

PEM fuel cells convert chemical energy directly to electricity, by means of hydrogen and oxygen which participate in the redox reactions at each electrode as presented in Equation 2.48 for the cathode, anode and cell. These equations are written in global

terms, however, the actual reaction mechanisms include sub-steps, such as single-electron-transfer reactions or gas adsorption and desorption (Weber and Newman, 2004). Figure 2.18a presents a typical cell structure with its main components.

$$\text{cathode:} \quad \frac{1}{2}O_2 + 2H^+ + 2e^- \longrightarrow H_2O, \qquad E_{ca}^{\ominus} = 1.23\,\text{V } \textit{vs. } \text{SHE}$$

$$\text{anode:} \qquad H_2 \longrightarrow 2H^+ + 2e^-, \qquad E_{ca}^{\ominus} = 0.0\,\text{V } \textit{vs. } \text{SHE} \qquad (2.48)$$

$$\text{cell:} \qquad H_2 + \frac{1}{2}O_2 \longrightarrow H_2O, \qquad E_{cell}^{\ominus} = 1.23\,\text{V } \textit{vs. } \text{SHE}$$
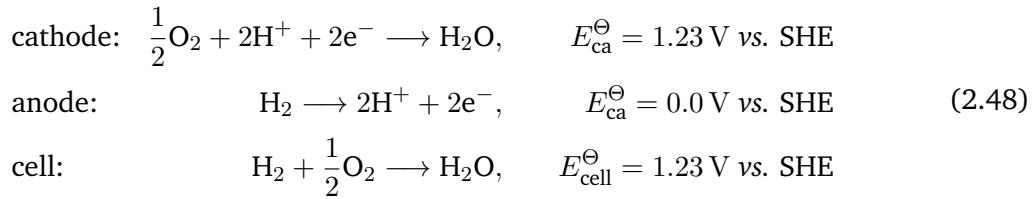
Physico-chemical processes can be analysed and described by a number of mathematical equations. These include differential and algebraic equations highly nonlinear, complex and stiff (Bavarian et al., 2010). Early PEM fuel cell models were built as 1D in the y direction (sandwich), Figure 2.18b, which were useful to analyse Catalyst Layers (CLs). While 2D models, which uses a sandwich approach in the $x - y$ direction or along the channel in the $y - z$ direction, offer a more realistic description of the phenomena (Siegel, 2008). Models with a 3D approach that consider the $x - y - z$ directions usually by the combination of a 1D and a 2D description are utilised to represent overall performance and have the capability of describing blocking effect of bipolar plates, current density distributions, or effectiveness of flow field design (Siegel, 2008). Every model approach considers a number of simplifications and assumptions to better represent the system, which has been summarised by Siegel (2008), along with the key modelling features that are shown in Table 2.3.

(a)   **(b)**
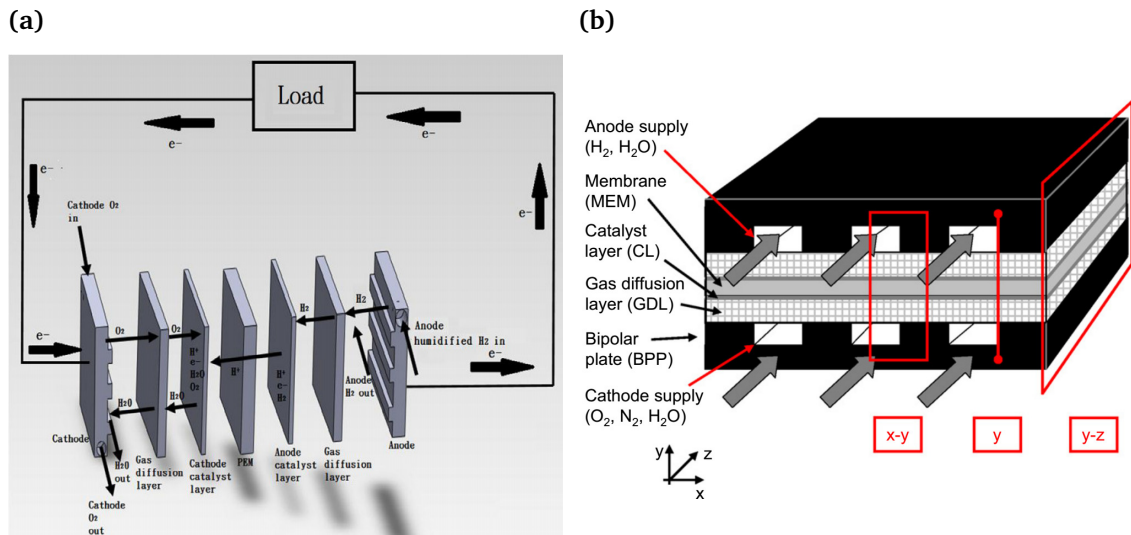
Figure 2.18: PEM fuel cell schematic diagram: (a) Typical fuel cell structure (Wu, 2016); and (b) Domains considered in 1D, 2D and 3D computational PEM fuel cell models (Siegel, 2008).

Mathematical models seek to explain performance by describing the polarisation curves (Figure 2.19a) and are able to predict it for a wide range of operating conditions. Macro-

Table 2.3: Key features of PEM fuel cell modelling (Siegel, 2008).

Key feature	Modelling topic
Approach	Analytical, semi-empirical, empirical, theoretical-mechanistic (macroscopic/microscopic)
State	Steady state, dynamic (transient), real time
System boundary	Single component, single PEM fuel cell, fuel cell stack, fuel cell stack including auxiliary component
Domains	Single domain; multi-domains
Spatial dimension	0-,1-, 2-, 3-dimensional (1+1, 2+1, 2 1/2 dimensions are possible if quantities only change in n-1 spatial dimensions or when coupled to lower-dimensional models)
Complexity/details	Thermal analyses, two-phase flow, droplet movement, pore details level modelling, CO kinetics and poisoning, gas impurities, catalyst degradation, gas channel design, cooling design, contact resistances, gravitational effects, impedance spectroscopy, structural and mechanical analysis

scopic models represent continuum and average phenomena over the domain, being widely utilized because they use less computational time and do not require exact knowledge of microstructure (Bavarian et al., 2010; Weber and Newman, 2004). Components are described as randomly arranged porous structures characterised by a small number of variables (e.g. porosity and specific surface area). Assumptions commonly used are incompressible and laminar flows due to small gas pressure gradients and Reynolds number, ideal gases, homogeneous and isentropic properties, and negligible gravity effects (Wu, 2016). These models could be used as the basis of a methodology for an RHVFC model and therefore only they will be reviewed. The set of mathematical relations must agree with the degree of freedom of the system (Newman, 1995). These relations are classified into five types: conservation, transport, reactions, equilibrium and auxiliary (Bavarian et al., 2010; Siegel, 2008; Sousa and Gonzalez, 2005; Weber and Newman, 2004). Conservation equations that are virtually used in all models and electrochemical devices (Wu, 2016; Zheng et al., 2014a) include conservation of mass, momentum, charge and energy, and an electro-neutrality condition (Bird et al., 1964; Li et al., 2014; Newman and Thomas-Alyea, 2004; Weber and Newman, 2004; Wu, 2016; Zheng et al., 2014a). The simplest macroscopic models (0D) describe the polarization curve by a single equation, usually empirical (Weber and Newman, 2004). Although, they are used to determine kinetic parameters and overall ohmic resistance and compare losses; but do not reveal process mechanisms, interacting phenomena, or predict performance. These lumped parameter models are usually used to predict transient and dynamic response. Amphlett et al. (1996) introduced a quasi-steady-state model, considering mass and heat transfer

and electrochemical kinetics (Bavarian et al., 2010). Later, Pukrushpan et al. (2002) developed a dynamic model, including flow characteristics, and compressor and manifold filling model (Figure 2.19a). This allowed the evolution of component partial pressures and membrane humidity to be studied (Bavarian et al., 2010). Faraday's law was used to calculate the hydrogen reacting, while Fick's law and an electro-osmotic coefficient were used to calculate the water crossover through the membrane. Yerramalla et al. (2003) studied the dynamic response using a linear and non-linear model, and including energy and mass transfer, electrochemical reactions and inverter load (Bavarian et al., 2010). Results showed that the linear model did not well represent cell behaviour. Benziger et al. (2004) introduced a lumped parameter model considering stirred tank reactors and a membrane (Bavarian et al., 2010). This was a pseudo 1D model since spatial gradients were only considered in the membrane and describe the kinetic overpotential as a function of the water activity and load resistance. These authors studied the cell's start-up, dynamic responses with a change in load, temperature, and reactant flow rates. The 1D or sandwich model is the most utilised and considers a normal flow of species to a number of layers (Figure 2.18), such as flow channels, diffusion media, CLs and membrane (Weber and Newman, 2004). It was recognized that the redox reaction happens in a thin layer (few μm) and that platinum efficiency decreased at higher current densities (Bavarian et al., 2010; Siegel, 2008; Sousa and Gonzalez, 2005). Fuller (1993) developed a transport model considering water and thermal management, which found a strong relation between the equilibrium adsorption of water and temperature and the critical effect of heat removal rate, while Yi and Nguyen (1998) highlighted the need for efficient heat removal to avoid membrane dehydration (Bavarian et al., 2010; Siegel, 2008; Sousa and Gonzalez, 2005). Bernardi and Verbrugge (1991, 1992) developed early models of a PEM attached to a porous electrode, finding that the Oxygen Reduction Reaction (ORR) was an important polarisation factor (Figure 2.19b) and that the operating conditions affect water transport due to pressure and potential gradients. At the same time, Springer et al. (1991) introduced a 1D isothermal model that accounted for water diffusion and electro-osmotic effects, showing the direct dependence of membrane resistance with current density.

2D and 3D models for isothermal/no-isothermal and transient/steady-state conditions have been developed to analyse polarisation under different operating conditions or specific phenomena. 2D models including electrochemical kinetics, current distribution, hydrodynamics, and multi-component transport, allowed the study of hydrogen dilution at the anode (Bavarian et al., 2010; Sousa and Gonzalez, 2005). Reported 3D models including diffusion media at anode and cathode sides, showed that mass transport through the membrane is driven by pressure and concentration gradients (Bavarian et al., 2010; Siegel, 2008). Capillary pressure was found to be the dominant effect on water transport, which was studied by means of two-phase models (Bavarian et al., 2010; Sousa and

(a)

(b)
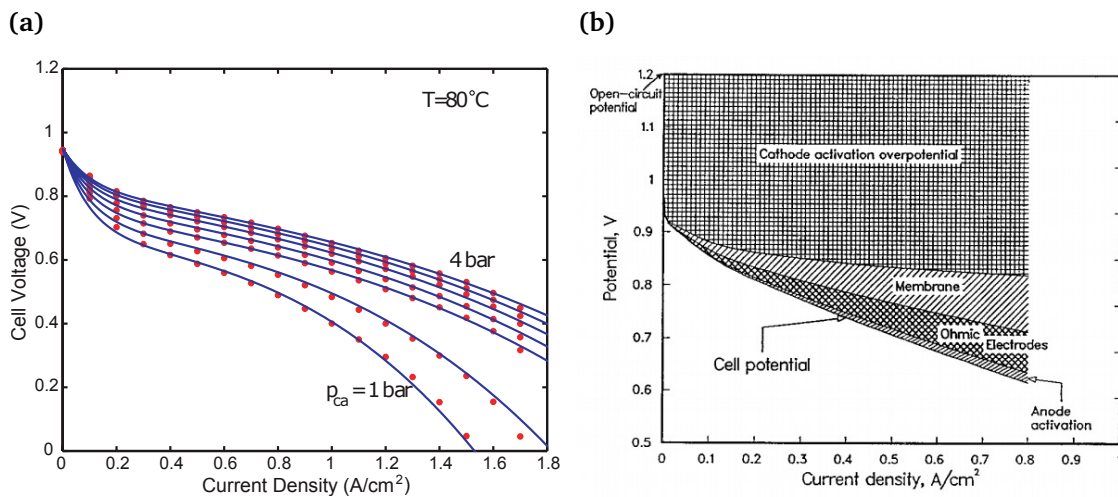
Figure 2.19: (a) Fuel cell polarization curve fitting result at constant temperature of 80 °C and at cathode pressure of 1, 1.5, 2, 2.5, 3, 3.5, 4 bar (Pukrushpan et al., 2002). (b) Potential loss contributions to fuel cell potential as a function of current density (Bernardi and Verbrugge, 1992).

Gonzalez, 2005). 3D model developed showed the importance of temperature gradients within the cell and the relevant impact of a 3D approach in the distribution of current and limiting current density (Bavarian et al., 2010; Siegel, 2008). 3D models were also used to account for the formation and transport of liquid water, finding that polarisation is overestimated if liquid water formation is not considered and that electro-osmotic transport is more relevant in cells with complex configurations (Bavarian et al., 2010; Sousa and Gonzalez, 2005). 3D single-phase isothermal models were used to study electron transport in diffusion media, concluding that the electronic resistance depended on electronic conductivity and thickness, also that gas channel width strongly influenced current distributions, which was affected importantly by electronic resistance at high voltages and oxygen concentration at low voltages (Bavarian et al., 2010; Siegel, 2008). A time of 10 s was estimated to be needed to reach a steady-state condition in PEM fuel cells due to water accumulation in the membrane (Bavarian et al., 2010).

The mathematical description of each layer within a PEM fuel cell considers a number of equations. Macroscopic membrane models are divided into single and two phases approach, but all of them consider three components: membrane, protons and water, neglecting any other ions (Weber and Newman, 2004). Hydrogen and oxygen crossover have been normally been neglected because they do not impact water or proton transport (Weber and Newman, 2004). Different membrane structures that have been considered are shown in Figure 2.20a. A single-phase approach has been widely used in diffusive models and considers a vapour-equilibrated membrane as a homogeneous phase where water and proton dissolve and diffuse (Figure 2.20ac) (Weber and Newman, 2004). The simplest model assumes water movement as constant and models proton movement based on Ohm's law and dilute solution theory (Weber and Newman, 2004; Wu, 2016). Water

movement can be described by an electro-osmotic flow caused by proton-water interaction (no dilute solution effect), which is proportional to the current density by an electro-osmotic drag coefficient. Proton-water interaction is not significant, but under conditions of large water gradients, it becomes important (e.g. low humidity or high current density) (Weber and Newman, 2004). A drawback of this approach is that pressure difference cannot be represented, and therefore fully hydrated membranes where the driving force is the liquid pressure are not well described (Weber and Newman, 2004). Springer et al. (1991) related the electro-osmotic drag coefficient (ξ_{drag}) to the membrane water content (λ), which was obtained from an experimental relation with the water vapour activity, representing the Nafion water uptake isotherm as shown in Equation 2.49 (Springer et al., 1991). Where, ξ_{drag} was found to be 2.5 for a fully hydrated membrane ($\lambda = 22$) and the water vapour activity (a_{v}) was calculated as the quotient between the vapour partial pressure and its saturation pressure ($p_{\mathrm{v}}^{\mathrm{sat}}$), Equation 2.50.

$$\lambda_{30^{\circ}\mathrm{C}} = 0.043 + 17.81a_{\mathrm{v}} - 39.85a_{\mathrm{v}}^2 + 36.0a_{\mathrm{v}}^3 \tag{2.49}$$

$$\log(p_{\mathrm{v}}^{\mathrm{sat}}) = -2.1794 + 0.02953T - 9.1837 \times 10^{-5}T^2 + 1.4454 \times 10^{-7}T^3 \tag{2.50}$$

(a)   **(b)**
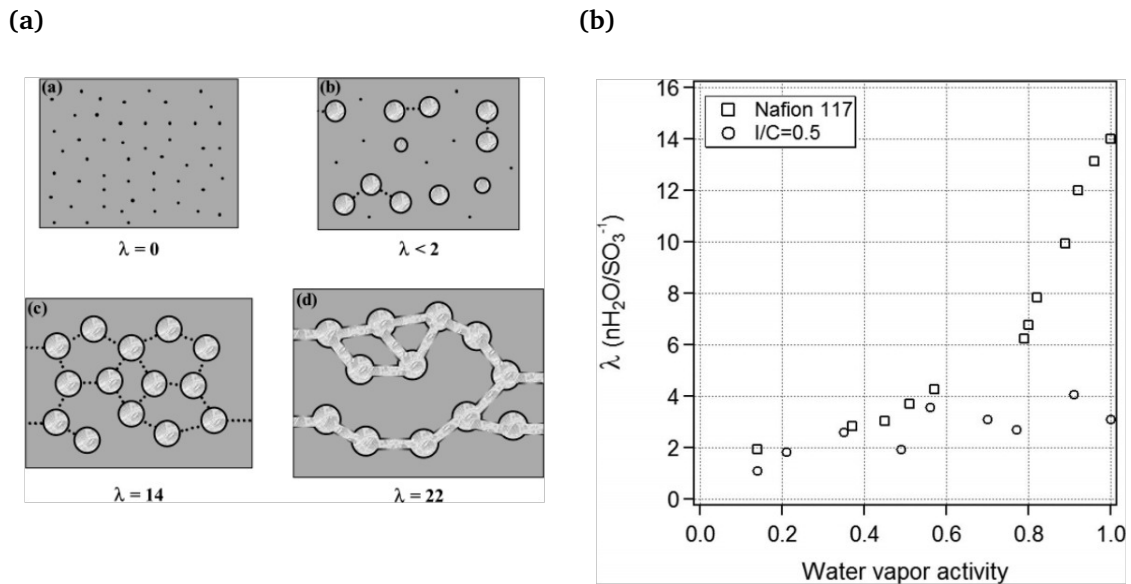
Figure 2.20: (a) Membrane structure as function of λ (Weber and Newman, 2004): grey - fluorocarbon matrix; black - polymer side chain; light grey - liquid water; dotted line - collapsed channel. (b) Water uptake for Nafion 117 (Springer et al., 1991) and CL with I/C = 0.5 at 30°C (Sun et al., 2013).

Another model approach for membranes is hydraulic models, which consider the membrane to be formed by two phases –liquid equilibrated membrane (Figure 2.20ad)–

with the capability of sustaining a pressure gradient (Weber and Newman, 2004). A pioneering model utilised a dilute solution condition and the Nernst-Plank equation and describes water velocity through Schlogl's relation, where water movement is explained by the potential and pressure gradients, and therefore, it was possible to describe well hydrated membranes (Weber and Newman, 2004). In addition, this model included a vapour fraction in the membrane that remained constant, accounting for gas crossover. Moreover, reported models have tried to represent diffusive and convective flow in one membrane, based in concentrated solution theory with gas phase pressure as driving force (Weber and Newman, 2004), but demonstrating inconsistencies because Schroeder's paradox is ignored. A correct approach must facilitate the superposition of the two models, which describe separate parts of transport. The Weber and Newman model –a macroscopic approach that includes microscopic effects– has successfully fitted experimental data, considering two transport modes, which are used in parallel and switched continuously: diffusive for vapour-equilibrated membrane and hydraulic for liquid-equilibrated membrane (Weber and Newman, 2004). Transport parameters and the concentration of water in the membrane have been expressed as a function of temperature and water content. A relation between water content and water vapour activity is usually used (Equation 2.49).

Gas diffusion media considers a single Gas Diffusion Layer (GDL) or a composite of a GDL and a microporous layer. Almost all reported models describe only the GDL and neglect the electronic conducting process because of carbon high conductivity (Weber and Newman, 2004). Alternatively, Ohm's law can be used to describe the electronic conduction since it could be a limiting factor due to structure or composition. A Bruggeman expression is typically used to account for tortuosity (τ) and porosity (ϵ), in the electrodes and membrane (Weber and Newman, 2004; Wu, 2016). Mass balances of species can be obtained, with zero flux for inert gases and Faraday's law used for reactant and product gases. Water evaporation/condensation can be included assuming that in the presence of liquid water the gas is saturated (Weber and Newman, 2004) as shown in Equation 2.51. Where r_{evap} is the rate of evaporation/condensation, k_{m} is the mass-transfer coefficient per unit of interfacial surface area, and $a_{\mathrm{G,L}}$ is the interfacial surface area between the gas phase (G) and liquid (L) phase. To describe gas transport of hydrogen and vapour in the fuel side and air and vapour in the oxidant side, a Stefan-Maxwell equation or its modifications are used, such as the Dusty Gas Model (DGM) presented for a binary mixture in Equation 2.52 (Bertei and Nicolella, 2015), which includes pressure-driven flow (Sousa and Gonzalez, 2005; Weber and Newman, 2004). Knudsen diffusion (D_{K}) dominates when the pore radius is less than 0.5 $\mu\mathrm{m}$, being more important for microporous or CLs. In addition, pressure gradient has been seen insignificant, and therefore a uniform pressure assumption is sometimes taken (Weber and Newman, 2004). However, small pressure differences together with thermal gradients can influence water transport.

The pressure gradient becomes relevant for fuel cells with inter-digitated flow channels, where gas transport is affected by convection and diffusion. In Equation 2.52, J_i is flux density of species i, p is pressure, x_i is molar fraction of species i, $D_{K,i}$ is Knudsen diffusion coefficient of species i, $D_{i,j}$ is binary diffusion coefficient of species i and j, k is effective hydraulic permeability, μ is viscosity, and M_i is molar weight of species i. Liquid water transport in GDLs is ignored or modelled by single-phase models. The simplest models assume water as static solid species that occupies a portion of the pore volume and reduces gas volume. This decreases the gas diffusion coefficients and allows electrode flooding of the electrode to be represented (Weber and Newman, 2004). Another approach assumes droplets of water carried by the gas flow while evaporation/condensation happens (Weber and Newman, 2004). This approach presents water as a component of the gas with a non-significant effect on its flow and velocity, but the change in the gas volume fraction is considered. These models take into consideration the presence of liquid water and in some degree accounts for water pressure and concentration variations. To precisely describe the liquid transport, two-phase models are required which consider only pressure driven flow and concentrations gradients are not present, accounting for gas pressure and liquid pressure. These methods describe isolated gas and liquid pores that are in accordance with the presence of hydrophilic and hydrophobic pores, but not representing the mass transfer between the phases or their change in volume fraction, which are expected in reality (Weber and Newman, 2004). A phase mixture approach has been also proposed, considering the two phases as a single one, but not accounting for pressure driving force because the liquid pressure is a result of the velocity, which the same for gas and liquid (Weber and Newman, 2004). These models are simplified versions of multiphase mixture models and predict the water balance reasonably well. Rigorous two-phase flow models have been proposed to describe gas and liquid interaction in pores, by means of capillary pressure, contact angle, surface tension and pore radius (Weber and Newman, 2004). These are based in liquid wetting properties and can describe liquid saturation (pore volume filled with liquid) along the electrode position. Liquid saturation affects gas diffusion coefficients and therefore electrode flooding can be described (Weber and Newman, 2004). These models require pressure profiles of both phases. Typically, Darcy's law is used, relating gas and liquid pressure, and using capillary pressure as a driving force for liquid. These mixture approaches utilise averaged parameters and obtain a mass-average velocity, recognising the interfacial drag between phases and facilitating the description of individual phase velocities (Weber and Newman, 2004). Issues related to a difficult average treatment, no capability of representing pore size distribution or wettability effects, and lower saturation predictions, have been reported (Weber and Newman, 2004).

$$r_{\text{evap}} = k_{\text{m}} a_{\text{G,L}} (p_{\text{v}} - p_{\text{v}}^{sat}) \qquad (2.51)$$

$$J_i = -\frac{p}{RT}\alpha_i^{-1}\nabla x_i - \frac{x_i}{RT}\left(\alpha_i^{-1}\left(1 + \frac{D_{K,i}}{D_{i,j}}\right) + \frac{kp}{\mu}\right)\nabla p \qquad (2.52)$$

where,

$$\alpha_i = \frac{1}{D_{K,i}} + \frac{x_j}{D_{i,j}}\left(1 + \frac{x_i}{x_j}\sqrt{\frac{M_i}{M_j}}\right) \qquad (2.53)$$

The Catalyst Layer (CL) is usually described in the same fashion as the membrane and GDL, but also includes electrochemical kinetic expressions for the redox reactions. A three-phase interface process, including gas, electrolyte and electro-catalyst, has been postulated, however, a two-phase interface process is believed to be more probable, considering only the electro-catalyst and the electrolyte and the gas phase dissolved in the electrolyte phase (Weber and Newman, 2004), Figure 2.21a. Alternatively, a thin layer of liquid water on top of the membrane layer is sometimes assumed. Macroscopic models are usually used to describe CLs and are subdivided by length scale (Weber and Newman, 2004). Interface models use a single equation without regarding CL structure, while 1D models account for changes across the layer (macro-homogeneous models) or the agglomerate (agglomerate models). When both length scales are used, the models are called embedded macro-homogeneous models (Weber and Newman, 2004). CLs contain different phases, and hence effective transport parameters must be used for describing transport phenomena. Water content in CLs has been measured observing a lower water uptake in comparison with Nafion membranes (Figure 2.20b). Water evaporation/condensation relating water and vapour content can be represented by a relation like the one presented in Equation 2.51. Charge balance in CLs assumes that only faradaic reactions are present and neglects double-layer effects under steady-state condition. A catalyst loading parameter (amount of catalyst in grams per cross-sectional area of the electrode) together with the reactive surface area of Pt can be used to obtain the interfacial area between the electro-catalyst and electrolyte (Weber and Newman, 2004).

Alternatively, interface models assume that the CL exists only at the diffusion media, *i.e.*, in the membrane interface as an infinitely thin layer with uniform properties. These models are normally used when the emphasis is on membrane water balance or multi-dimensional effects (Weber and Newman, 2004). The more common approach includes kinetic expressions at the interface, which allows multidimensional effects to be described with a change in current density or potential (Weber and Newman, 2004). Activation overpotential and reactant concentrations are assumed uniform and are used in the kinetic expression to calculate the current density at the CL. Macro-homogeneous models assume that all species exist at all points, and properties and phases are described by a number of parameters, such as volume fraction and specific surface area (Weber and Newman, 2004). Two length scales are usually studied: over the CL (porous electrode models) and

(a)   **(b)**
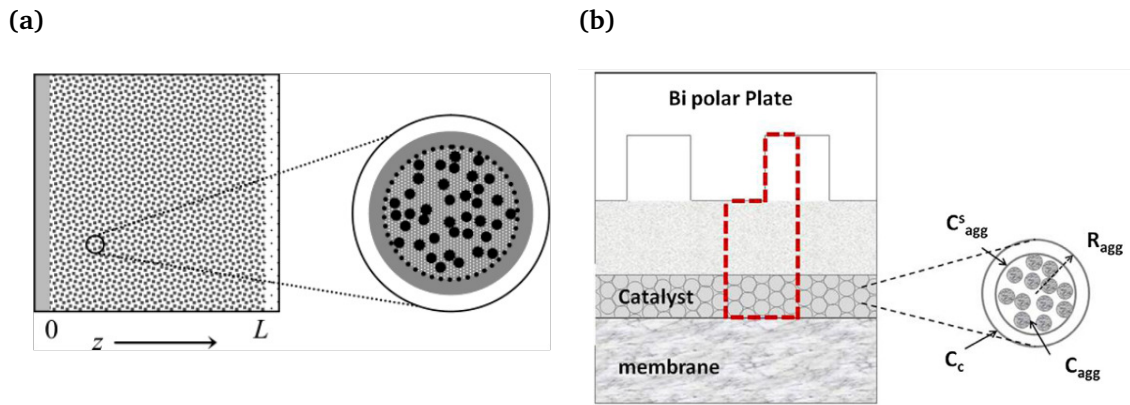
Figure 2.21: (a) Schematic of CL: grey - membrane, white - gas, black - electro-catalyst, and external grey region - external film of water on top of agglomerate (Weber and Newman, 2004); and (b) Schematic of electrode with agglomerate (Wu, 2016).

over the agglomerate. Porous electrode models describe the overall reaction distribution, assuming that agglomerates have a uniform concentration and potential, and using the thickness as characteristic length (Weber and Newman, 2004). Among agglomerate models, the simplest approach considers only effects present at the agglomerate length scale with its radius as characteristic length (Weber and Newman, 2004), Figure 2.21b. These models assume a uniform reaction distribution, considering a uniform gas concentration and surface overpotential through the thickness. Catalyst flooding can be represented by an agglomerate model with liquid water present in the CL, where a liquid film covering the membrane layer is assumed. When two-phase models are used, liquid saturation in the CL can be calculated and the interfacial area is adjusted, which usually is represented by a linear expression depending on the saturation.

An extensive number of cathode models for the oxygen redox reaction compared to anode models for the hydrogen redox reaction have been reported, because cathode mass-transport effects are more important. Anode kinetic models are simplifications of cathode ones but consider poisoning of the electro-catalyst. Equations 2.54 and 2.55 have been normally used to describe the oxygen and hydrogen kinetics (Weber and Newman, 2004; Wu, 2016). These kinetic expressions relate potential and current, as well as govern the consumption and production of reactants and products. At low current density ($<20\,\mathrm{mA\,cm^{-2}}$), activation polarisation occurs mainly due to the slow Oxygen Reduction Reaction (ORR) at normal operating temperatures (<100 °C), and is represented by a Tafel kinetics with first-order dependence on p_{O_2}. Tafel slopes have agreed with a transfer coefficient equal to 1 (Weber and Newman, 2004). For the Hydrogen Oxidation Reaction (HOR), the reaction is fast and is usually modelled by a Butler-Volmer expression, Equation 2.55, but if the feed contains poison such as carbon monoxide the reaction rate will significantly diminish because carbon monoxide can be adsorbed in the reaction sites of the CL (Weber and Newman, 2004; Wu, 2016). This Bulter-Volmer expression does not

use proton concentration because the polymer electrolyte has a defined fixed acid concentration, which sets the proton concentration to be constant when electro-neutrality is assumed (Weber and Newman, 2004). Both electrode polarisations are referred to reference conditions and operating temperature. Mass-transfer limitations arise due to diffusive resistances that impede hydrogen/oxygen transport to/from reaction sites, or electronically/ionically conducting resistances that impede protons/electrons to reach/leave these active sites (Bavarian et al., 2010; Weber and Newman, 2004). The main cause is flooding in the CL or the GDL, restricting the oxygen transport in the cathode. In addition, dehydration can decrease the membrane conductivity, and insulating solid (e.g. Teflon) in the transport media can affect the electron conduction. To represent the oxygen transport effect, Faraday's and Fick's laws are arranged to obtain a limiting current density (j_{lim}), relating partial pressure of oxygen (p_{O_2}) in the CL and the bulk, Equation 2.56.

$$j_{\text{ORR}} = -j_{0,\text{ORR}} \left(\frac{p_{\text{O}_2}}{p_{\text{O}_2}^{\text{ref}}} \right) \exp \left(\frac{-\alpha_{\text{ca}} F \eta_{ORR}}{RT} \right) \tag{2.54}$$

$$j_{\text{HOR}} = j_{0,\text{HOR}} \left[\left(\frac{p_{\text{H}_2}}{p_{\text{H}_2}^{\text{ref}}} \right) \exp \left(\frac{\alpha_{\text{an}} F \eta_{\text{HOR}}}{RT} \right) - \exp \left(\frac{-\alpha_{\text{ca}} F \eta_{\text{HOR}}}{RT} \right) \right] \tag{2.55}$$

$$p_{\text{O}_2}^{\text{CL}} = p_{\text{O}_2}^{\text{bulk}} \left(1 - \frac{j}{j_{\text{lim}}} \right) \tag{2.56}$$

A Nernst's equation has been normally used to calculate the equilibrium cell potential. This equation considers ideal gases, negligible electrolyte gradients and unity activity coefficients as shown in Equation 2.57 (Weber and Newman, 2004). Where p is the partial pressure of species i, including hydrogen (H_2), oxygen (O_2) and vapour water (v). The concentration of protons effect is normally neglected due to the electro-neutrality condition.

$$E_{\text{eq}} = E^0 + \frac{RT}{2F} \ln \left(\frac{p_{\text{H}_2} p_{\text{O}_2}^{0.5}}{p_{\text{v}}} \right) \tag{2.57}$$

The ohmic overpotential, including electronic and ionic ohmic losses, has been reported to be essentially constant with respect to current density and potential (Bavarian et al., 2010; Weber and Newman, 2004). Most models only consider the membrane contribution using Ohm's law and estimating the membrane conductivity by Equation 2.58 (Pukrushpan et al., 2002; Springer et al., 1991). This membrane conductivity is expressed as a function of the membrane conductivity (σ_{m}), the membrane thickness (w_{m}), the water content (λ) and the temperature.

$$\sigma_{\mathrm{m}} = (0.5139\lambda - 0.326)\exp\left(1268\left[\frac{1}{303} - \frac{1}{T}\right]\right) \tag{2.58}$$

A small number of models have integrated non-isothermal effects (Weber and Newman, 2004). The isothermal assumption has been validated through non-isothermal models, recognising a temperature distribution in the membrane electrode assembly (MEA) of 1 °C, showing larger distributions in inlet/outlet depending on operating conditions (Weber and Newman, 2004). Almost all non-isothermal models account for the change in properties and parameters due to temperature, assuming a uniform sandwich temperature, because this effect can be more important than temperature gradients (Weber and Newman, 2004). The set of equations that describe each layer must be modified in order to include thermal effects, where inclusion of an energy conservation equation is the more relevant change (Weber and Newman, 2004). The undefined chemical potential in non-uniform temperature is an important effect that requires to use a thermodynamically rigorous expression for the driving forces in the transport phenomena, including a term that relates temperature and the molar entropy of species (Weber and Newman, 2004). Additional thermal diffusion effects are generally small and usually neglected. Mixing thermal effects are negligible if ideal gas conditions are considered. Local thermal equilibrium between phases (gas and liquid) is assumed due to the close contact between them within the small pores, which allows the same temperature to be assumed in the phases (Weber and Newman, 2004). This allows a single energy equation to be considered including an overall effective thermal conductivity. At each sandwich layer, the energy conservation equation can consider different effects (Weber and Newman, 2004): gas channels include convection of enthalpy, conduction through graphite plates, and heat transfer with the ambient or cooling fluid; GDLs include conduction of heat but not convection, no external heat transfer, and Joule heating; CLs have the same effects that GDLs along with heat generation; and membranes have conduction, Joule heating, and enthalpy carried by diffusion and convection.

2.5   Conclusions

The rapid growth in the deployment of renewable energy sources has increased interest in electrochemical energy storage. VRFBs have drawn increasing attention from researchers, however, the low solubility and stability of vanadium ions in sulphuric acid solutions, and the high cost of vanadium-based electrolytes and membranes have limited their commercialisation. An RHVFC benefits from the advantages of the mixed liquid-gas RFBs and reduces the overall system cost by utilising only half of the vanadium electrolyte required for a VRFB. A better understanding of the RHVFC operation and its limitations, rational-

isation of experimental findings and the study possible performance improvements are crucial. Electrochemical principles can be used to describe the equilibrium and kinetics of the faradaic reactions involved in electrochemical cells. Cell and continuum models, considering conservation laws, equilibrium, and kinetics, are useful to optimise the design of electrochemical cells and stacks, to understand the coupled phenomena, and to utilise in control applications. Development of models for describing hybrid-RFBs, such as the RHVFC, are of interest. Reported cell and continuum models of VRFB and PEM fuel cells have allowed to progress in the understanding of these systems and to enhance their performance. These models could be used as a basis for the development of RHVFC models, and other hybrid-RFB models.

In electrochemical cell modelling, it is of importance to understand that what is being simulated is the departure from an equilibrium condition, and therefore, care must be taken in how such an equilibrium condition is assessed, as well as the kinetic representation of the deviation from equilibrium. This will be considered when selecting an equilibrium and kinetic expression for the hydrogen-vanadium cell while taking into account the equation conventionally used for VRFBs. This is a complete Nernst equation and a Butler-Volmer equation, respectively. The lumped modelling approach used in VRFBs and PEM fuel cells will be first considered when proposing an initial model. This model will be then modified to incorporate the crossover effect with a similar approach to the ones proposed for the transport of vanadium and sulphuric acid species in Nafion membranes of VRFBs, namely describing the ionic flux by means of a Nernst-Planck equation. Previous reported RHVFC studies have indicated that the cathodic half-cell is the limiting side affecting the cell performance. Transport of species in the anodic half-cell will be incorporated into the lumped model by a conventional gas transport model, namely a dusty gas model, simplifying the treatment of liquid water. Testing of the model against experimental data is shown in VRFB to be an important step to test the capabilities and limitation of the mathematical representations, and therefore, it will be considered an important step. The effect of capacity loss in VRFB is dominated by the transport of species across the ion-exchange membrane. This is expected to have a similar effect on a hybrid RFB. A continuum model, considering the transport by diffusion, convection and migration have been considered in VRFB. A similar approach will be considered for an RHVFC in order to characterise the transport across the membrane. Additionally, a non-electroneutral solution is considered to represent the interface between the electrode and membrane, which will allow simulating the change in ionic potential and concentration of species at this interface.

Chapter 3 describes the framework commonly used in developing unit cell models of VRFBs, along with a discussion of limitations and areas of interest. Then, Chapter 4 introduces an RHVFC model along with an initial model testing against experimental data.

Chapter references

Aaron, D. S., Liu, Q., Tang, Z., Grim, G. M., Papandrew, A. B., Turhan, A., Zawodzinski, T. A., and Mench, M. M. Dramatic performance gains in vanadium redox flow batteries through modified cell architecture. *Journal of Power Sources*, 206:450–453, 2012.

Al-Fetlawi, H., Shah, A., and Walsh, F. Non-isothermal modelling of the all-vanadium redox flow battery. *Electrochimica Acta*, 55(1):78–89, dec 2009.

Al-Fetlawi, H., Shah, A., and Walsh, F. Modelling the effects of oxygen evolution in the all-vanadium redox flow battery. *Electrochimica Acta*, 55(9):3192–3205, mar 2010.

Alotto, P., Guarnieri, M., and Moro, F. Redox flow batteries for the storage of renewable energy: A review. *Renewable and Sustainable Energy Reviews*, 29:325–335, 2014.

Amphlett, J., Mann, R., Peppley, B., Roberge, P., and Rodrigues, A. A model predicting transient responses of proton exchange membrane fuel cells. *Journal of Power Sources*, 61(1-2):183–188, jul 1996.

Arenas, L. F., León, C. P. D., and Walsh, F. C. Engineering aspects of the design , construction and performance of modular redox flow batteries for energy storage Electrochemical Engineering Laboratory , Energy Technology Research Group , Faculty of. *Journal of Energy Storage*, 11:1–72, 2017.

Badrinarayanan, R., Zhao, J., Tseng, K. J., and Skyllas-Kazacos, M. Extended dynamic model for ion diffusion in all-vanadium redox flow battery including the effects of temperature and bulk electrolyte transfer. *Journal of Power Sources*, 270:576–586, dec 2014.

Bard, A. J. and Faulkner, L. R. *ELECTROCHEMICAL METHODS: Fundamentals and applications*. 2001. ISBN 0471043729. doi: 10.1146/annurev.matsci.30.1.117. URL http://tocs.ulb.tu-darmstadt.de/95069577.pdf.

Bavarian, M., Soroush, M., Kevrekidis, I. G., and Benziger, J. B. Mathematical Modeling, Steady-State and Dynamic Behavior, and Control of Fuel Cells: A Review. *Industrial & Engineering Chemistry Research*, 49(17):7922–7950, 2010.

Bayanov, I. M. and Vanhaelst, R. The numerical simulation of vanadium RedOx flow batteries. *Journal of Mathematical Chemistry*, 49(9):2013–2031, 2011.

Bazant, M. Z. Phase-Field Theory of Ion Intercalation Kinetics. *Condensed Matter*, 4, 2012.

Bazant, M. Z. Theory of chemical kinetics and charge transfer based on nonequilibrium thermodynamics. *Accounts of Chemical Research*, 46(5):1144–1160, 2013.

Bazant, M. Z., Kilic, M. S., Storey, B. D., and Ajdari, A. Towards an understanding of

induced-charge electrokinetics at large applied voltages in concentrated solutions. *Advances in Colloid and Interface Science*, 152(1-2):48–88, 2009.

Benziger, J., Chia, E., Karnas, E., Moxley, J., Teuscher, C., and Kevrekidis, I. G. The stirred tank reactor polymer electrolyte membrane fuel cell. *AIChE Journal*, 50(8):1889–1900, 2004.

Bernardi, D. M. and Verbrugge, M. W. Mathematical model of a gas diffusion electrode bonded to a polymer electrolyte. *AIChE Journal*, 37(8):1151–1163, 1991.

Bernardi, D. M. and Verbrugge, M. W. A Mathematical Model of the Solid-Polymer-Electrolyte Fuel Cell. *Journal of The Electrochemical Society*, 139(9):2477, 1992.

Bertei, A. and Nicolella, C. Common inconsistencies in modeling gas transport in porous electrodes: The dusty-gas model and the Fick law. *Journal of Power Sources*, 279:133–137, 2015.

Bird, R. B., Stewart, W. E., and Lightfoot, E. N. *Fenómenos de transporte*. Reverté, Barcelona, 1st edition, 1964.

Blanc, C. and Rufer, A. Multiphysics and energetic modeling of a vanadium redox flow battery. *2008 IEEE International Conference on Sustainable Energy Technologies, ICSET 2008*, pages 696–701, 2008.

Bromberger, K., Kaunert, J., and Smolinka, T. A Model for All-Vanadium Redox Flow Batteries: Introducing Electrode-Compression Effects on Voltage Losses and Hydraulics. *Energy Technology*, 2(1):64–76, jan 2014.

Chen, C. L., Yeoh, H. K., and Chakrabarti, M. H. An enhancement to Vynnycky's model for the all-vanadium redox flow battery. *Electrochimica Acta*, 120:167–179, feb 2014.

Chen, H., Cong, T. N., Yang, W., Tan, C., Li, Y., and Ding, Y. Progress in electrical energy storage system: A critical review. *Progress in Natural Science*, 19(3):291–312, 2009.

Cho, J., Jeong, S., and Kim, Y. Commercial and research battery technologies for electrical energy storage applications. *Prog. Energy Combust. Sci.*, 48(0):84, 2015.

Cho, K. T., Tucker, M. C., and Weber, A. Z. A Review of Hydrogen/Halogen Flow Cells. *Energy Technology*, 4(6):655–678, 2016.

Darling, R. M., Weber, A. Z., Tucker, M. C., and Perry, M. L. The Influence of Electric Field on Crossover in Redox-Flow Batteries. *Journal of the Electrochemical Society*, 163(1): A5014–A5022, 2015.

Dewage, H. H., Yufit, V., and Brandon, N. P. Study of Loss Mechanisms Using Half-Cell Measurements in a Regenerative Hydrogen Vanadium Fuel Cell. *Journal of The Electrochemical Society*, 163(1):A5236–A5243, 2016.

Dickinson, E. J. F., Limon-Petersen, J. G., and Compton, R. G. The electroneutrality approximation in electrochemistry. *Journal of Solid State Electrochemistry*, 15(7-8):1335–1345, 2011.

Dowd, R. P., Lakhanpal, V. S., and Van Nguyen, T. Performance Evaluation of a Hydrogen-Vanadium Reversible Fuel Cell. *Journal of The Electrochemical Society*, 164(6):F564–F567, 2017a.

Dowd, R. P., Verma, A., Li, Y., Powers, D., Wycisk, R., Pintauro, P. N., and Van Nguyen, T. A Hydrogen-Vanadium Reversible Fuel Cell Crossover Study. *Journal of The Electrochemical Society*, 164(14):F1608–F1614, 2017b.

Ferguson, T. R. and Bazant, M. Z. Nonequilibrium Thermodynamics of Porous Electrodes. *Journal of the Electrochemical Society*, 159(12):A1967–A1985, 2012.

Ferreira, H. L., Garde, R., Fulli, G., Kling, W., and Lopes, J. P. Characterisation of electrical energy storage technologies. *Energy*, 53:288–298, 2013.

Fuller, T. F. Water and Thermal Management in Solid-Polymer-Electrolyte Fuel Cells. *Journal of The Electrochemical Society*, 140(5):1218, 1993.

Gallo, A., Simões-Moreira, J., Costa, H., Santos, M., and Moutinho dos Santos, E. Energy storage in the energy transition context: A technology review. *Renewable and Sustainable Energy Reviews*, 65:800–822, 2016.

Gandomi, Y. A., Aaron, D. S., Zawodzinski, T. A., and Mench, M. M. In Situ Potential Distribution Measurement and Validated Model for All-Vanadium Redox Flow Battery. *Journal of The Electrochemical Society*, 163(1):A5188–A5201, 2016.

Gileadi, E. *Electrode Kinetics for Chemists, Chemical Engineers and Materials Scientists*. John Wiley & Sons, Inc, New York, 1993. ISBN 978-0-471-18858-2. URL http://www.wiley.com/WileyCDA/WileyTitle/productCd-0471188581.html.

Hewa Dewage, H., Wu, B., Tsoi, A., Yufit, V., Offer, G., and Brandon, N. P. A novel regenerative hydrogen cerium fuel cell for energy storage applications. *J. Mater. Chem. A*, 3(18):9446–9450, 2015.

K, S. *Electrochemical Reaction Engineering K, Scott Academic Press Limited*. Academic Press Limited, 1991.

Knehr, K. and Kumbur, E. Open circuit voltage of vanadium redox flow batteries: Discrepancy between models and experiments. *Electrochemistry Communications*, 13(4):342–345, apr 2011.

Knehr, K., Agar, E., Dennison, C. R., Kalidindi, A. R., and Kumbur, E. C. A Transient Vanadium Flow Battery Model Incorporating Vanadium Crossover and Water Transport

through the Membrane. *Journal of the Electrochemical Society*, 159(9):A1446–A1459, aug 2012.

Knopf, D. A., Luo, B. P., Krieger, U. K., and Koop, T. Thermodynamic dissociation constant of the bisulfate ion from Raman and ion interaction modeling studies of aqueous sulfuric acid at low temperatures. *Journal of Physical Chemistry A*, 107(21):4322–4332, 2003.

Kontturi, K., Murtomäki, L., and Manzanares, J. A. *Ionic Transport Processes: In Electrochemistry and Membrane Science*. Oxford University Press Inc., New York, first edition, 2008. URL `http://www.amazon.com/Ionic-Transport-Processes-Electrochemistry-Membrane/dp/0199553814`.

Lei, Y., Zhang, B. W., Bai, B. F., and Zhao, T. S. A transient electrochemical model incorporating the Donnan effect for all-vanadium redox flow batteries. *Journal of Power Sources*, 299:202–211, dec 2015.

Leung, P., Li, X., Ponce de León, C., Berlouis, L., Low, C. T. J., and Walsh, F. C. Progress in redox flow batteries, remaining challenges and their applications in energy storage. *RSC Advances*, 2(27):10125, 2012.

Li, M. and Hikihara, T. A Coupled Dynamical Model of Redox Flow Battery Based on Chemical Reaction, Fluid Flow and Electrical Circuit. *Institute of Electronics, Information an Communication Engineers*, E91(7):1741–1747, 2008.

Li, S. E., Wang, B., Peng, H., and Hu, X. An electrochemistry-based impedance model for lithium-ion batteries. *Journal of Power Sources*, 258:9–18, 2014.

Li, X., Zhang, H., Mai, Z., Zhang, H., and Vankelecom, I. Ion exchange membranes for vanadium redox flow battery (VRB) applications. *Energy & Environmental Science*, 4(4): 1147, 2011.

Ma, X., Zhang, H., and Xing, F. A three-dimensional model for negative half cell of the vanadium redox flow battery. *Electrochimica Acta*, 58:238–246, dec 2011.

Maa, X., Zhangb, H., Xua, X., Jianga, S., Wua, J., Chigana, T., Wang, H., Zhaoa, H., and Chena, N. RKP Vanadium Flow Battery and its Application. *235th ECS Meeting*, (MA2019-01):Abstract 444, 2019.

Merei, G., Adler, S., Magnor, D., and Sauer, D. U. Multi-physics Model for the Aging Prediction of a Vanadium Redox Flow Battery System. *Electrochimica Acta*, 174:945–954, aug 2015.

Newman, J. Thermoelectric Effects in Electrochemical Systems. *Industrial & Engineering Chemistry Research*, 34:3208–3216, 1995.

Newman, J. S. and Thomas-Alyea, K. E. *Electrochemical Systems*. John Wiley & Sons, Inc., New York, 3rd edition, 2004. ISBN 0-471-47756-7.

Ontiveros, L. J. and Mercado, P. E. Modeling of a Vanadium Redox Flow Battery for power system dynamic studies. *International Journal of Hydrogen Energy*, 39(16):8720–8727, 2014.

Pavelka, M., Wandschneider, F., and Mazur, P. Thermodynamic derivation of open circuit voltage in vanadium redox flow batteries. *Journal of Power Sources*, 293:400–408, 2015.

Perry, M. L. and Weber, A. Z. Advanced Redox-Flow Batteries: A Perspective. *Journal of The Electrochemical Society*, 163(1):A5064–A5067, 2015.

Pino-Muñoz, C. A., Hewa Dewage, H., Yufit, V., and Brandon, N. P. A Unit Cell Model of a Regenerative Hydrogen-Vanadium Fuel Cell. *Journal of The Electrochemical Society*, 164 (14):F1717–F1732, 2017.

Pletcher, D. *A first course in Electrode Processes*. The Royal Society of Chemistry, second edi edition, 2009.

Ponce de León, C., Frías-Ferrer, A., González-García, J., Szánto, D., and Walsh, F. Redox flow cells for energy conversion. *Journal of Power Sources*, 160(1):716–732, 2006.

Pugach, M., Kondratenko, M., Briola, S., and Bischi, A. Zero dimensional dynamic model of vanadium redox flow battery cell incorporating all modes of vanadium ions crossover. *Applied Energy*, 226(June):560–569, 2018.

Pukrushpan, J. T., Stefanopoulou, a. G., and Peng, H. P. H. Modeling and control for PEM fuel cell stack system. *Proceedings of the 2002 American Control Conference IEEE Cat NoCH37301*, 4(12):3117–3122, 2002.

Rubio-Garcia, J., Kucernak, A., Zhao, D., Li, D. I., Fahy, K. F., Yufit, V., Brandon, N. P., and Gomez-Gonzalez, M. Hydrogen / manganese hybrid redox flow battery (in press). *J. Phys. Energy*, 2018.

Shah, A., Watt-Smith, M., and Walsh, F. A dynamic performance model for redox-flow batteries involving soluble species. *Electrochimica Acta*, 53(27):8087–8100, nov 2008.

Shah, A., Al-Fetlawi, H., and Walsh, F. Dynamic modelling of hydrogen evolution effects in the all-vanadium redox flow battery. *Electrochimica Acta*, 55(3):1125–1139, jan 2010a.

Shah, A., Al-Fetlawi, H., and Walsh, F. Dynamic modelling of hydrogen evolution effects in the all-vanadium redox flow battery. *Electrochimica Acta*, 55(3):1125–1139, 2010b.

Shah, A., Li, X., Wills, R. G. A., and Walsh, F. C. A Mathematical Model for the Soluble Lead-Acid Flow Battery. *Journal of The Electrochemical Society*, 157(5):A589, 2010c.

Shah, A., Tangirala, R., Singh, R., Wills, R., and Walsh, F. A Dynamic Unit Cell Model for the All-Vanadium Flow Battery. *Journal of The Electrochemical Society*, 158(6):A671, 2011.

Sharma, A., Vynnycky, M., Ling, C., Birgersson, E., and Han, M. The quasi-steady state of all-vanadium redox flow batteries: A scale analysis. *Electrochimica Acta*, 147:657–662, nov 2014.

Sharma, A., Ling, C., Birgersson, E., Vynnycky, M., and Han, M. Verified reduction of dimensionality for an all-vanadium redox flow battery model. *Journal of Power Sources*, 279:345–350, apr 2015.

Siegel, C. Review of computational heat and mass transfer modeling in polymer-electrolyte-membrane (PEM) fuel cells. *Energy*, 33(9):1331–1352, sep 2008.

Skyllas-Kazacos, M., Chakrabarti, M. H., Hajimolana, S. A., Mjalli, F. S., and Saleem, M. Progress in Flow Battery Research and Development. *Journal of The Electrochemical Society*, 158(8):R55, 2011.

Smith, R. B. and Bazant, M. Z. Multiphase Porous Electrode Theory. 164(11), 2017.

Soloveichik, G. L. Regenerative fuel cells for energy storage. *Proceedings of the IEEE*, 102 (6):964–975, 2014.

Sousa, R. and Gonzalez, E. R. Mathematical modeling of polymer electrolyte fuel cells. *Journal of Power Sources*, 147:32–45, 2005.

Springer, T. E., Wilson, M. S., and Gottesfeld, S. Polymer Electrolyte Fuel Cells. 140(12), 1993.

Springer, T., Zawodzinski, T., and Gottesfeld, S. Polymer electrolyte fuel cell model. *Journal of the Electrochemical Society*, 138(8):2334–2342, 1991.

Sun, C.-N., More, K. L., Veith, G. M., and Zawodzinski, T. a. Composition Dependence of the Pore Structure and Water Transport of Composite Catalyst Layers for Polymer Electrolyte Fuel Cells. *Journal of the Electrochemical Society*, 160(9):F1000–F1005, 2013.

Sun, C., Chen, J., Zhang, H., Han, X., and Luo, Q. Investigations on transfer of water and vanadium ions across Nafion membrane in an operating vanadium redox flow battery. *Journal of Power Sources*, 195(3):890–897, feb 2010.

Tang, A., Bao, J., and Skyllas-Kazacos, M. Dynamic modelling of the effects of ion diffusion and side reactions on the capacity loss for vanadium redox flow battery. *Journal of Power Sources*, 196(24):10737–10747, dec 2011.

Tang, A., McCann, J., Bao, J., and Skyllas-Kazacos, M. Investigation of the effect of shunt

current on battery efficiency and stack temperature in vanadium redox flow battery. *Journal of Power Sources*, 242:349–356, nov 2013.

Tang, A., Bao, J., and Skyllas-Kazacos, M. Studies on pressure losses and flow rate optimization in vanadium redox flow battery. *Journal of Power Sources*, 248:154–162, feb 2014.

Tang, A., Bao, J., and Skyllas-Kazacos, M. Thermal modelling of battery configuration and self-discharge reactions in vanadium redox flow battery. *Journal of Power Sources*, 216: 489–501, 2012.

Viswanathan, V., Crawford, A., Stephenson, D., Kim, S., Wang, W., Li, B., Coffey, G., Thomsen, E., Graff, G., Balducci, P., Kintner-Meyer, M., and Sprenkle, V. Cost and performance model for redox flow batteries. *Journal of Power Sources*, 247:1040–1051, feb 2014.

Vynnycky, M. Analysis of a model for the operation of a vanadium redox battery. *Energy*, 36(4):2242–2256, apr 2011.

Walsh, F. C. *A First Course in Electrochemical Engineering*. The Electrochemical Consultancy, 1993.

Wandschneider, F., Finke, D., Grosjean, S., Fischer, P., Pinkwart, K., Tübke, J., and Nirschl, H. Model of a vanadium redox flow battery with an anion exchange membrane and a Larminie-correction. *Journal of Power Sources*, 272:436–447, dec 2014.

Wang, W., Luo, Q., Li, B., Wei, X., Li, L., and Yang, Z. Recent Progress in Redox Flow Battery Research and Development. *Advanced Functional Materials*, 23(8):970–986, 2013.

Weber, A. Z. and Newman, J. Modeling transport in polymer-electrolyte fuel cells. *Chemical Reviews*, 104(10):4679–4726, 2004.

Weber, A. Z., Mench, M. M., Meyers, J. P., Ross, P. N., Gostick, J., and Liu, Q. Redox flow batteries: a review. *Journal of Applied Electrochemistry*, 41(10):1137–1164, 2011.

Wei, Z., Zhao, J., Skyllas-Kazacos, M., and Xiong, B. Dynamic thermal-hydraulic modeling and stack flow pattern analysis for all-vanadium redox flow battery. *Journal of Power Sources*, 260:89–99, aug 2014.

Wu, H.-W. A review of recent development: Transport and performance modeling of PEM fuel cells. *Applied Energy*, 165:81–106, mar 2016.

Xing, F., Zhang, H., and Ma, X. Shunt current loss of the vanadium redox flow battery. *Journal of Power Sources*, 196(24):10753–10757, dec 2011.

Xiong, B., Zhao, J., Tseng, K., Skyllas-Kazacos, M., Lim, T. M., and Zhang, Y. Thermal hydraulic behavior and efficiency analysis of an all-vanadium redox flow battery. *Journal of Power Sources*, 242:314–324, nov 2013.

Xiong, B., Zhao, J., Wei, Z., and Skyllas-Kazacos, M. Extended Kalman filter method for state of charge estimation ofvanadium redox flow battery using thermal-dependent electrical model. *Journal of Power Sources*, 262:50–61, sep 2014.

Xu, Q. and Zhao, T. Fundamental models for flow batteries. *Progress in Energy and Combustion Science*, 49:40–58, 2015.

Xu, W., Zhang, H., Xing, F., Zhang, H., Li, Y., Cao, J., and Li, X. The numerical simulation of dynamic performance in the vanadium flow battery. *Electrochimica Acta*, 118:51–57, feb 2014.

Yang, X.-G., Ye, Q., Cheng, P., and Zhao, T. S. Effects of the electric field on ion crossover in vanadium redox flow batteries. *Applied Energy*, 145:306–319, 2015.

Yang, Z., Zhang, J., Kintner-Meyer, M. C., Lu, X., Choi, D., Lemmon, J. P., and Liu, J. Electrochemical energy storage for green grid. *Chemical Reviews*, 111(5):3577–3613, 2011.

Ye, R., Henkensmeier, D., Yoon, S. J., Huang, Z., Kim, D. K., Chang, Z., Kim, S., and Chen, R. Redox Flow Batteries for Energy Storage: A Technology Review. *Journal of Electrochemical Energy Conversion and Storage*, 15(1):010801, 2017.

Yerramalla, S., Davari, A., Feliachi, A., and Biswas, T. Modeling and simulation of the dynamic behavior of a polymer electrolyte membrane fuel cell. *Journal of Power Sources*, 124(1):104–113, oct 2003.

Yi, J. S. and Nguyen, T. V. An Along-the-Channel Model for Proton Exchange Membrane Fuel Cells. *Journal of The Electrochemical Society*, 145(4):1149, 1998.

Yin, C., Gao, Y., Guo, S., and Tang, H. A coupled three dimensional model of vanadium redox flow battery for flow field designs. *Energy*, 74:886–895, 2014a.

Yin, C., Gao, Y., Guo, S., and Tang, H. A coupled three dimensional model of vanadium redox flow battery for flow field designs. *Energy*, 74:886–895, sep 2014b.

You, D., Zhang, H., and Chen, J. A simple model for the vanadium redox battery. *Electrochimica Acta*, 54(27):6827–6836, nov 2009.

You, D., Zhang, H., Sun, C., and Ma, X. Simulation of the self-discharge process in vanadium redox flow battery. *Journal of Power Sources*, 196(3):1578–1585, feb 2011.

Yu, V. and Chen, D. Dynamic Model of a Vanadium Redox Flow Battery for System Per-

formance Control. *Journal of Solar Energy Engineering*, 136(2):021005–1 – 0210057, 2014.

Yufit, V., Hale, B., Matian, M., Mazur, P., and Brandon, N. P. Development of a Regenerative Hydrogen-Vanadium Fuel Cell for Energy Storage Applications. *Journal of The Electrochemical Society*, 160(6):A856–A861, 2013.

Zhao, P., Zhang, H., Zhou, H., Chen, J., Gao, S., and Yi, B. Characteristics and performance of 10kW class all-vanadium redox-flow battery stack. *Journal of Power Sources*, 162(2): 1416–1420, nov 2006.

Zheng, Q., Li, X., Cheng, Y., Ning, G., Xing, F., and Zhang, H. Development and perspective in vanadium flow battery modeling. *Applied Energy*, 132:254–266, nov 2014a.

Zheng, Q., Xing, F., Li, X., Liu, T., Lai, Q., Ning, G., and Zhang, H. Investigation on the performance evaluation method of flow batteries. *Journal of Power Sources*, 266: 145–149, 2014b.

Zheng, Q., Zhang, H., Xing, F., Ma, X., Li, X., and Ning, G. A three-dimensional model for thermal analysis in a vanadium flow battery. *Applied Energy*, 113:1675–1685, jan 2014c.

Zheng, Q., Xing, F., Li, X., Ning, G., and Zhang, H. Flow field design and optimization based on the mass transport polarization regulation in a flow-through type vanadium flow battery. *Journal of Power Sources*, 324:402–411, 2016.

Chapter 3

A simplified base model for a redox flow battery: all-vanadium system

3.1 Introduction

Mathematical modelling is a crucial tool for design and control applications of Redox Flow Batteries (RFBs). This third chapter introduces a brief description of a modelling approach commonly used to simulate one of the most studied RFBs: an all-Vanadium Redox Flow Battery (VRFB). The operating principles and components description of a VRFB were explained in Chapter 2, along with a VRFB modelling overview. This chapter presents the implementation of a unit cell model for a VRFB, as described by the modelling framework previously reported in the literature (Gandomi et al., 2016; Knehr et al., 2012a; Pavelka et al., 2015; Shah et al., 2008, 2011b; Tang et al., 2011; Wei et al., 2014; Won et al., 2015; Yu and Chen, 2014a,b), stating the additional equations used to describe the concentration of protons in both electrodes and the equilibrium potential of the cell. The unit cell model is tested and compared with reported experimental data and simulations from reported one-dimensional (1D) and two-dimensional (2D) VRFB models. The development of this initial model provides the basis needed for proposing and implementing a unit cell model for a Regenerative Hydrogen-Vanadium Fuel Cell (RHVFC), which is presented in Chapter 4.

This chapter continues as follows, first, a description of the modelling approach is given, stating additional equations, assumptions and simplifications. Later, a model test is presented using reported data and simulations. The chapter ends with conclusions and an explanation of how this VRFB model is used as a starting point for the modelling of an RHVFC.

3.2 Zero-dimensional (0D) model of an all-vanadium redox flow battery

A schematic diagram of the VRFB along with the different domains considered in the unit cell model is presented in Figure 3.1. The model domains are (1) catholyte tank, (2) cathode, (3) membrane, (4) anode, and (5) anolyte tank. This zero-dimensional (0D) time-dependent model for a VRFB cell was developed considering rate reactions described by Faraday's law, and a number of assumptions and simplifications were considered which are listed below:

1. All domains are considered isothermal and to have the same temperature.

2. The catholyte and anolyte are considered incompressible, having constant density, viscosity and volume.

3. All physical properties, mass and charge-transfer properties are assumed isotropic
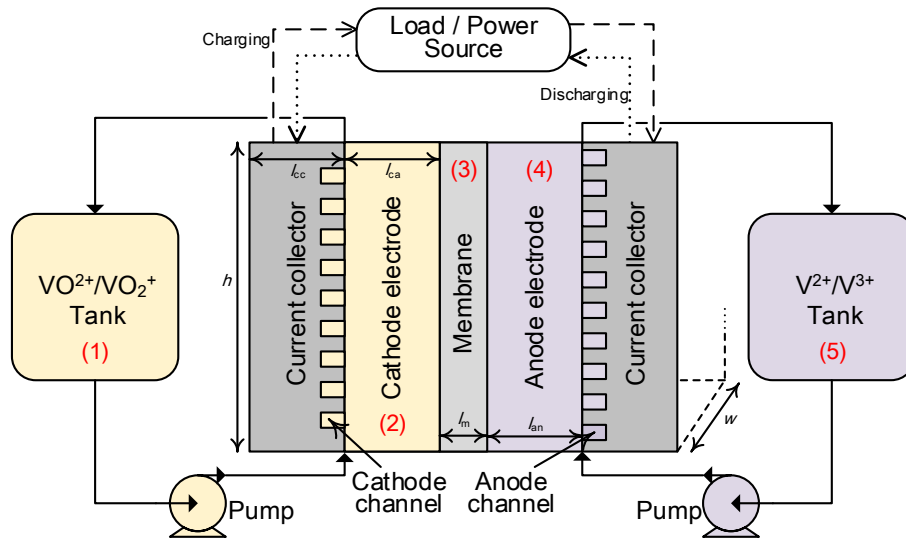
Figure 3.1: Schematic of the VRFB and model domains.

and homogeneous in all the domains.

4. The electrolytes must maintain electro–neutrality.

5. Gas evolution reactions in the electrodes are neglected.

6. Unit activity coefficients are assumed for all species.

7. Spatial concentration distribution in the catholyte tank, cathode, anode and anolyte tank are neglected.

8. The dilute solution approximation is considered.

9. Water crossover through the membrane is neglected.

10. Transport across the membrane is considered to be steady-state.

11. Full humidification of the membrane is assumed.

The mathematical description for the unit cell model, which responds to the simplifications and assumptions, was based on the modelling framework proposed for previously reported model for VRFBs (Gandomi et al., 2016; Knehr et al., 2012a; Pavelka et al., 2015; Shah et al., 2008, 2011b; Tang et al., 2011; Wei et al., 2014; Won et al., 2015; Yu and Chen, 2014a,b). These previously reported sets of equations and any additional equations needed for the model, as well as any modification to equations, are stated in the present chapter. The main components of the model are presented and discussed in two sections: electrodes and tanks, and cell potential.

3.2.1 Electrodes and tanks

The catholyte and anolyte solutions contain water, sulphuric acid species and vanadium species. Similar to previously reported models, only three species were considered in the

model for each electrode, namely VO^{2+}, VO_2^+ and H^+ for the catholyte, and V^{3+}, V^{2+} and H^+ for the anolyte. Considering a lumped parameter approach, conservation of species can be obtained for the vanadium species in the electrolytes at the electrodes as shown in Equations 3.1 to 3.4. At the anode side for V(II) and V(III) and at the cathode side for V(IV) and V(V). This approach considers recirculation between half-cells and electrolyte tanks, redox reactions, crossover of vanadium species and self-discharge reactions at each electrode. These self-discharge reactions were described in Equations 2.36 and 2.37 in Chapter 2. The third reaction in Equations 2.36 and 2.37 were neglected because they produce V(III) and V(IV), which will react with V(II) and V(V) giving the other proposed self-discharge reactions (Tang et al., 2011). Fick's first law was used to describe the diffusion flux from the half-cell of high concentration to the half-cell of low concentration, considering steady-state transport. Xu et al. (2014) used the same approach to obtain the mass balance of species, but did not consider recirculation effects.

$$\varepsilon_{ca} V_{ca} \frac{dc_{VO_2^+}}{dt} = Q_{ca}\big(c_{VO_2^+,T} - c_{VO_2^+}\big) + \frac{A_{ca} j}{F} - A_{ca}\left(\frac{D_{VO_2^+}^m c_{VO_2^+}}{l_m} + \frac{2 D_{V^{2+}}^m c_{V^{2+}}}{l_m} + \frac{D_{V^{3+}}^m c_{V^{3+}}}{l_m}\right) \tag{3.1}$$

$$\varepsilon_{ca} V_{ca} \frac{dc_{VO^{2+}}}{dt} = Q_{ca}\big(c_{VO^{2+},T} - c_{VO^{2+}}\big) - \frac{A_{ca} j}{F} - A_{ca}\left(\frac{D_{VO^{2+}}^m c_{VO^{2+}}}{l_m} - \frac{3 D_{V^{2+}}^m c_{V^{2+}}}{l_m} - \frac{2 D_{V^{3+}}^m c_{V^{3+}}}{l_m}\right) \tag{3.2}$$

$$\varepsilon_{an} V_{an} \frac{dc_{V^{2+}}}{dt} = Q_{an}\big(c_{V^{2+},T} - c_{V^{2+}}\big) + \frac{A_{an} j}{F} - A_{an}\left(\frac{D_{V^{2+}}^m c_{V^{2+}}}{l_m} + \frac{D_{VO^{2+}}^m c_{VO^{2+}}}{l_m} + \frac{2 D_{VO_2^+}^m c_{VO_2^+}}{l_m}\right) \tag{3.3}$$

$$\varepsilon_{an} V_{an} \frac{dc_{V^{3+}}}{dt} = Q_{an}\big(c_{V^{3+},T} - c_{V^{3+}}\big) - \frac{A_{an} j}{F} - A_{an}\left(\frac{D_{V^{3+}}^m c_{V^{3+}}}{l_m} - \frac{2 D_{VO^{2+}}^m c_{VO^{2+}}}{l_m} - \frac{3 D_{VO_2^+}^m c_{VO_2^+}}{l_m}\right) \tag{3.4}$$

In the above equations ε_k, V_k and A_k are the porosity, volume and cross-sectional area of the electrode k (k = {ca, an}). The terms c_i and $c_{i,T}$ are the concentration of species i (i = {VO_2^+, VO^{2+}, V^{2+}, V^{3+}}) in the electrode and in the electrolyte tank, respectively. The term Q_k is the electrolyte flow rate in the half-cell k, D_i^m is the Fickian diffusion coefficient of species i across the membrane and l_m is the membrane thickness.

The species conservation equations for H^+ at the cathode and anode were derived by initially stating the H^+ balance and then using the electro-neutrality condition to express each equation in terms of the vanadium concentrations, similar to what was proposed

by Xu et al. (2014). The electro-neutrality condition in each half-cell must be maintained and was represented by Equations 3.5 and 3.6 for the anode and the cathode, respectively. The derivation of the species conservation equations for H^+ at the cathode and anode are presented in Equations 3.7 and 3.8. Equation 3.7 includes the effect of the cathodic and anodic redox reactions, recirculation of electrolyte between the electrolytes tanks and half-cells, crossover of protons through the membrane due to diffusion, self-discharge reactions at each half-cell electrode, and a molar flux of protons to balance the charges ($\dot{n}_{H^+}^B$).

$$0 = 2\varepsilon V_{ca}\frac{dc_{VO^{2+}}}{dt} + \varepsilon V_{ca}\frac{dc_{VO_2^+}}{dt} + \varepsilon V_{ca}\frac{dc_{H^+}}{dt} \tag{3.5}$$

$$0 = 2\varepsilon V_{an}\frac{dc_{V^{2+}}}{dt} + 3\varepsilon V_{an}\frac{dc_{V^{3+}}}{dt} + \varepsilon V_{an}\frac{dc_{H^+}}{dt} \tag{3.6}$$

$$\varepsilon_{ca}V_{ca}\frac{dc_{H^+,ca}}{dt} = Q_{ca}\left(c_{H^+,T}^{ca} - c_{H^+,ca}\right) - \dot{n}_{H^+}^B - \frac{2A_{ca}D_{V^{2+}}^m c_{V^{2+}}}{l_m} - \frac{A_{ca}D_{H^+}^m c_{H^+}}{l_m} \pm \frac{2A_{ca}j}{F}$$

$$\varepsilon_{an}V_{an}\frac{dc_{H^+,an}}{dt} = Q_{an}\left(c_{H^+,T}^{an} - c_{H^+,an}\right) + \dot{n}_{H^+}^B - \frac{2A_{an}D_{VO^{2+}}^m c_{VO^{2+}}}{l_m} - \frac{4A_{an}D_{VO_2^+}^m c_{VO_2^+}}{l_m}$$
$$+ \frac{A_{an}D_{H^+}^m c_{H^+}}{l_m} \tag{3.7}$$

$$\varepsilon_{ca}V_{ca}\frac{dc_{H^+,ca}}{dt} = Q_{ca}\left(-2(c_{VO^{2+},T} - c_{VO^{2+}}) - (c_{VO_2^+,T} - c_{VO_2^+})\right) \pm \frac{A_{ca}j}{F}$$
$$- A_{ca}\left(\frac{4D_{V^{2+}}^m c_{V^{2+}}}{l_m} + \frac{3D_{V^{3+}}^m c_{V^{3+}}}{l_m} - \frac{2D_{VO^{2+}}^m c_{VO^{2+}}}{l_m} - \frac{D_{VO_2^+}^m c_{VO_2^+}}{l_m}\right)$$
$$\varepsilon_{an}V_{an}\frac{dc_{H^+,an}}{dt} = Q_{an}\left(-2(c_{V^{2+},T} - c_{V^{2+}}) - 3(c_{V^{3+},T} - c_{V^{3+}})\right) \pm \frac{A_{an}j}{F}$$
$$- A_{an}\left(-\frac{2D_{V^{2+}}^m c_{V^{2+}}}{l_m} - \frac{3D_{V^{3+}}^m c_{V^{3+}}}{l_m} + \frac{4D_{VO^{2+}}^m c_{VO^{2+}}}{l_m} + \frac{5D_{VO_2^+}^m c_{VO_2^+}}{l_m}\right) \tag{3.8}$$

The species conservation equations at each electrolyte tank were represented by Equation 3.9 for the five ionic species involved. Where V_T is the electrolyte tank volume.

$$V_T^k\frac{dc_{i,T}}{dt} = Q_k\left(c_i - c_{i,T}\right), \quad k = [ca, an], \quad i = \left[VO^{2+}, VO_2^+, V^{3+}, V^{2+}, H^+\right] \tag{3.9}$$

3.2.2 Cell potential

The cell potential during charge and discharge operation was estimated by considering the equilibrium potential, ohmic overpotentials and activation overpotentials for the operating conditions. In this model, the concentration overpotentials were not included in the kinetic expressions used for the cathode or the anode, nor were they included independently. The equilibrium potential was calculated by a Complete Nernst Equation (CNE) as shown in Equation 3.10. This equation proposed by Knehr et al. (2012b) modified the conventional Nernst equation by adding the membrane effect in the equilibrium potential. Both of these equations consider the concentration of protons at the cathode, and in the case of the CNE, the Donnan potential at both electrode/membrane interfaces is also considered. Equation 3.10 is the most used version of CNE in previously reported models, and therefore, it is used in this initial model. In the literature, a different version of the CNE has been recently proposed (Pavelka et al., 2015), which is not considered in this chapter but is discussed in Chapters 4.

$$E_{\text{eq}} = E^0 + \frac{RT}{F} \ln \left(\frac{c_{\text{V}^{2+}} c_{\text{VO}_2^+} c_{\text{H}^+,\text{ca}}^2}{c_{\text{V}^{3+}} c_{\text{VO}^{2+}}} \times \frac{c_{\text{H}^+,\text{ca}}}{c_{\text{H}^+,\text{an}}} \right) \tag{3.10}$$

The activation overpotential was calculated for the cathode and anode by a simplified Butler-Volmer kinetic approach, where the mass transport limitation effect was neglected by considering the concentrations of species at the surface and the bulk to be equal. This kinetic expression can be inverted to obtain the cathodic and anodic overpotentials (Shah et al., 2011b; Yu and Chen, 2014a). Equations 3.11 and 3.12 present the Butler-Volmer equations used for the anode and cathode, respectively. The exchange current density for the cathode was considered to only include the effect of V(IV) and V(V), while the effect of H^+ was neglected. This approach was selected since it is commonly used for describing the cathode kinetics, as previously discussed in Chapter 2. In Chapter 4 a more extensive discussion of the Butler-Volmer kinetics for the cathode is presented. Both kinetic equations consider a transfer coefficient of $\alpha_a = \alpha_c = 0.5$, which is normally used for these systems. An Arrhenius approach was used to estimate the kinetic rate constants at each electrode, taking into account a standard rate constant and the operating temperature by means of Equation 3.13 (Shah et al., 2011b; Yu and Chen, 2014a).

$$\eta_{\text{ac,an}} = \frac{2RT}{F} \sinh^{-1} \left(\frac{j}{2j_{0,\text{an}}} \right), \quad j_{0,\text{an}} = F k_{\text{an}} c_{\text{V}^{2+}}^{0.5} c_{\text{V}^{3+}}^{0.5} \tag{3.11}$$

$$\eta_{\text{ac,ca}} = \frac{2RT}{F} \sinh^{-1} \left(\frac{j}{2j_{0,\text{ca}}} \right), \quad j_{0,\text{ca}} = F k_{\text{ca}} c_{\text{VO}^{2+}}^{0.5} c_{\text{VO}_2^+}^{0.5} \tag{3.12}$$

$$k_{\mathrm{an}} = k_{\mathrm{an,ref}} \exp\left(\frac{FE^0_{\mathrm{an},T_{\mathrm{ref}}}}{R}\left[\frac{1}{T_{\mathrm{ref}}} - \frac{1}{T}\right]\right), \quad k_{\mathrm{ca}} = k_{\mathrm{ca,ref}} \exp\left(\frac{FE^0_{\mathrm{ca},T_{\mathrm{ref}}}}{R}\left[\frac{1}{T_{\mathrm{ref}}} - \frac{1}{T}\right]\right) \quad (3.13)$$

The overall ohmic overpotential was obtained by applying Ohm's law as shown in Equation 3.14, and adding the effect of current collectors, membrane, electrolytes and electrodes. An effective conductivity was utilised for electrolytes and electrodes as shown in Equation 3.15. The electrolyte conductivity was obtained using Equation 3.16 (Shah et al., 2008), accounting for the species considered at each electrode. The membrane conductivity was calculated taking into account the water content in the membrane (λ) and the temperature effect as shown in Equation 3.17.

$$E^{\mathrm{cc}}_{\mathrm{Ohm}} = j\frac{w_{\mathrm{cc}}}{\omega_{\mathrm{cc}}}, \quad E^{\mathrm{el}}_{\mathrm{Ohm}} = j\frac{w_{\mathrm{e}}}{\sigma^{\mathrm{eff}}_{\mathrm{el}}}, \quad E^{\mathrm{e}}_{\mathrm{Ohm}} = j\frac{w_{\mathrm{e}}}{\sigma^{\mathrm{eff}}_{\mathrm{e}}}, \quad E^{\mathrm{m}}_{\mathrm{Ohm}} = j\frac{w_{\mathrm{m}}}{\sigma_{\mathrm{m}}} \quad (3.14)$$

$$\sigma^{\mathrm{eff}}_{\mathrm{el}} = \varepsilon^{3/2}\sigma_{\mathrm{el}}, \quad \sigma^{\mathrm{eff}}_{\mathrm{e}} = (1-\varepsilon)^{3/2}\sigma_{\mathrm{e}} \quad (3.15)$$

$$\sigma_{\mathrm{el}} = \frac{F^2}{RT}\sum_{\mathrm{i}} z_{\mathrm{i}}^2 D_{\mathrm{i,el}} c_{\mathrm{i}} \quad (3.16)$$

$$\sigma_{\mathrm{m}} = (0.5139\lambda - 0.326)\exp\left(1268\left[\frac{1}{303} - \frac{1}{T}\right]\right) \quad (3.17)$$

3.3 Model implementation and test using literature data

The set of differential equations and additional relations were implemented and solved MATLAB® by means of an Ordinary Differential Equation (ODE) solver, namely `ode15s` function, with absolute and relative tolerance set at 1×10^{-6}. The unit cell model was tested using experimental and simulation results reported by Shah et al. (2011b) and You et al. (2009b). In the comparison with the work reported by Shah et al. (2011b), the experimental data (set 1) was obtained using a unit cell with two electrodes of carbon felt Sigratherm GFA5 electrodes ($0.1 \times 0.1 \times 0.004\,\mathrm{m}$) and a Nafion 115 cation exchange membrane ($0.15 \times 0.15\,\mathrm{m}$; dry thickness *ca.* $125\,\mu\mathrm{m}$). The electrolyte solution contained a total vanadium concentration of $1200\,\mathrm{mol\,m^{-3}}$ diluted in a H_2SO_4 solution at $4000\,\mathrm{mol\,m^{-3}}$, at a temperature of $297\,\mathrm{K}$. During charge and discharge, the cell was operated galvanostatically at a current density in the range of $200\text{-}1000\,\mathrm{A\,m^{-2}}$. In the comparison with the work reported by You et al. (2009b), the experimental data (set 2) was obtained using a unit cell with two electrodes of graphite felt Shanghai Xinxing Carbon Co. Ltd ($0.025 \times 0.02 \times 0.003\,\mathrm{m}$) and a Nafion 115 membrane of $125\,\mu\mathrm{m}$ of thickness. The elec-

trolyte contained a total vanadium concentration of $1500\,\mathrm{mol\,m^{-3}}$ in $\mathrm{H_2SO_4}$ $3000\,\mathrm{mol\,m^{-3}}$ and during charge and discharge the cell was operated galvanostatically at a current density of $400\,\mathrm{A\,m^{-2}}$.

Additionally, reported simulations by Chen et al. (2014) of a 1D model and Qiu et al. (2012) of a three-dimensional (3D) model, that were compared with the experimental and 2D-model results of You et al. (2009b), are included in this chapter. To implement the unit cell model, a series of known parameters including geometrical dimension, material properties and electrochemical parameters are needed, as well as the initial conditions at which the experimental data was obtained. Table 3.1 and 3.2 present the values of the known parameters and initial conditions, which were taken from the literature (Gandomi et al., 2016; Shah et al., 2011b; You et al., 2009b). In the case of the experimental data set 1, the applied current density used to test the unit cell model is different from the current density reported by Shah et al. (2011b). This decision was made based on the total operating time reported for the experimental cell potential and the evolution of species concentrations as explained in Appendix A. Electrode properties were assumed to be equal for the cathode and the anode, and the initial concentration of species was assumed to be equal in the electrodes and the electrolyte tanks.

The unit cell model was fitted to the experimental data set 1 and set 2 using a least-squares approach by means of the `lsqcurvefit` function of MATLAB. Two fitting parameters were considered: the specific surface area of the electrodes (S_k), and the electrode conductivity (σ_e). Table 3.3 presents the initial values considered for the fitting parameters along with their lower and upper bounds and fitted values for both sets of experimental data. Both fitting parameters (S_k and σ_e) were assumed to be equal for the cathode and the anode. Figure 3.2a shows the comparison of the unit cell model against the experimental and simulation results of cell potential reported by Shah et al. (2011b). Reasonable agreement between the output potential simulated by the unit cell model and the experimental potential behaviour during charge was found, while during discharge discrepancies were observed at low SOC, or from $50\,\mathrm{min}$ onwards. These discrepancies are most probably explained by the neglect of the mass-transport limitation effects in the cathodic and anodic kinetic equations. It is important to mention that the simulation results reported by Shah et al. (2011b), and also presented in Figure 3.2a displayed a better agreement with respect of the cell potential at the end-of-discharge even when similar kinetic equations were considered. It is possible that the different behaviour responded to differences in the simulated evolution of species concentration. During discharge, and hence as the SOC decreases, the cell potential will decrease faster until it reaches a mass-transport-limited region, where the potential will fall rapidly. The Root-Mean-Square Error (RMSE),

Table 3.1: Electrodes, membrane and current collector parameters for experimental data set 1 reported by Shah et al. (2011b) and experimental data set 2 reported by You et al. (2009b).

Parameter	Value set 1 / set 2	Unit	Source set 1 / set 2
h_e	0.1/0.025	m	Shah et al. (2011b)/You et al. (2009b)
w_e	0.1/0.02	m	Shah et al. (2011b)/You et al. (2009b)
l_e	0.004/0.003	m	Shah et al. (2011b)/You et al. (2009b)
l_m	1.25×10^{-4}	m	Shah et al. (2011b)/You et al. (2009b)
l_{cc}	0.005	m	Shah et al. (2011b)/You et al. (2009b)
ε_e	0.67/0.929	–	Shah et al. (2011b)/You et al. (2009b)
σ_{cc}	91000	$S\,m^{-1}$	Shah et al. (2011b)
$D_{VO^{2+}}^{el}$	3.9×10^{-10}	$m^2\,s^{-1}$	You et al. (2009b)
$D_{VO_2^+}^{el}$	3.9×10^{-10}	$m^2\,s^{-1}$	You et al. (2009b)
$D_{V^{3+}}^{el}$	2.4×10^{-10}	$m^2\,s^{-1}$	You et al. (2009b)
$D_{V^{2+}}^{el}$	2.4×10^{-10}	$m^2\,s^{-1}$	You et al. (2009b)
$D_{H^+}^{el}$	9.312×10^{-9}	$m^2\,s^{-1}$	You et al. (2009b)
$D_{VO^{2+}}^{m}$	6.83×10^{-12}	$m^2\,s^{-1}$	Yu and Chen (2014a)
$D_{VO_2^+}^{m}$	5.90×10^{-12}	$m^2\,s^{-1}$	Yu and Chen (2014a)
$D_{V^{3+}}^{m}$	3.22×10^{-12}	$m^2\,s^{-1}$	Yu and Chen (2014a)
$D_{V^{2+}}^{m}$	8.77×10^{-12}	$m^2\,s^{-1}$	Yu and Chen (2014a)
V_T	$2.23 \times 10^{-4}/3 \times 10^{-5}$	m^3	Shah et al. (2011b)/You et al. (2009b)
λ	22	–	Shah et al. (2011b)
ρ	1350	$kg\,m^{-3}$	Gandomi et al. (2016)
μ	4.928×10^{-3}	$Pa\,s$	You et al. (2009b)
E_{ca}^0	1.004	V	You et al. (2009b)
E_{an}^0	−0.255	V	You et al. (2009b)
$k_{ca,ref}$	6.8×10^{-7}	$m\,s^{-1}$	You et al. (2009b)
$k_{an,ref}$	1.7×10^{-7}	$m\,s^{-1}$	You et al. (2009b)
$\alpha_{a,ca}/\alpha_{c,ca}$	0.5	–	You et al. (2009b)
$\alpha_{a,an}/\alpha_{c,an}$	0.5	–	You et al. (2009b)

which has the same units as the dependent variable studied, and the Normalised Root-mean-Square-Error (NRMSE), which is dimensionless and presented as a percentage, are defined in Equation 3.18 and were used to assess the differences between the simulation results and experimental data. In this equation, the terms $\hat{y}_i$ and y_i represent the corresponding predicted and observed values for the dependent variable at data point i, and n represents the total number of data points that are compared. In general, NRMSE is used to compare data sets with different scales, where lower values indicate less residual variance. All NRMSEs presented in this work were normalised by the range of the mea-

Table 3.2: Operating and initial conditions for experimental data set 1 reported by Shah et al. (2011b) and experimental data set 2 reported by You et al. (2009b).

Parameter	Value set 1 / set 2	Unit	Source set 1 / set 2
T	297/298	K	Shah et al. (2011b)/You et al. (2009b)
Q_{ca}/Q_{an}	1×10^{-6}	$m^3\,s^{-1}$	Shah et al. (2011b)/You et al. (2009b)
j_{appl}	1250/400	$A\,m^{-2}$	Shah et al. (2011b)/You et al. (2009b)
$c^0_{VO^{2+}}$	1140/1430	$mol\,m^{-3}$	Shah et al. (2011b)/You et al. (2009b)
$c^0_{VO_2^+}$	1140/1430	$mol\,m^{-3}$	Shah et al. (2011b)/You et al. (2009b)
$c^0_{V^{3+}}$	60/70	$mol\,m^{-3}$	Shah et al. (2011b)/You et al. (2009b)
$c^0_{V^{2+}}$	60/70	$mol\,m^{-3}$	Shah et al. (2011b)/You et al. (2009b)
$c^0_{H^+,ca}$	4200/6000	$mol\,m^{-3}$	Shah et al. (2011b)/You et al. (2009b)
$c^0_{H^+,an}$	4200/4500	$mol\,m^{-3}$	Shah et al. (2011b)/You et al. (2009b)

Table 3.3: Fitting parameters for the unit cell model of a VRFB considering experimental data set 1 reported by Shah et al. (2011b) and experimental data set 2 reported by You et al. (2009b).

Fitting parameter	Unit	Lower bound	Upper bound	Initial guess set 1 / set 2	Fitted value set 1 / set 2
σ_e	$S\,m^{-1}$	100	1×10^4	1000	1982/1923
S_e	$m^2\,m^{-3}$	420	1×10^8	$420/1.62 \times 10^4$	2314/16494

sured data (y), *i.e.* maximum value minus minimum value ($y_{i,max} - y_{i,min}$). An NRMSE of 1.62% and 3.51% was observed during charge and discharge between the cell potential of the unit cell model and the experimental data set 1 when a value of 1982 S m^{-1} was considered for the electrode conductivity and a value of $2314\,m^2\,m^{-3}$ was considered for the specific surface area of the electrodes.

$$RMSE = \sqrt{\frac{\sum_i^n \hat{y}_i - y_i}{n}},$$
$$NRMSE = 100 \times \frac{RMSE}{y_{i,max} - y_{i,min}} \tag{3.18}$$

The evolution of V(II) and V(III) concentrations in the anode and anolyte tank during charge and discharge operation is shown in Figure 3.2b. Similar behaviour to the one described by Shah et al. (2011b) was observed for the evolution of species concentration in the electrodes and electrolytes tanks. The rate of depletion and accumulation for V^{3+} and V^{2+}, respectively, during the first minutes of operation of charge or discharge, was greater for the anode than for the anolyte tank. The rate of change in the species concentration reached a linear behaviour for both anode and anolyte tank. These linear regions were reached faster for the tanks than for the electrodes since the electrolyte volume in the
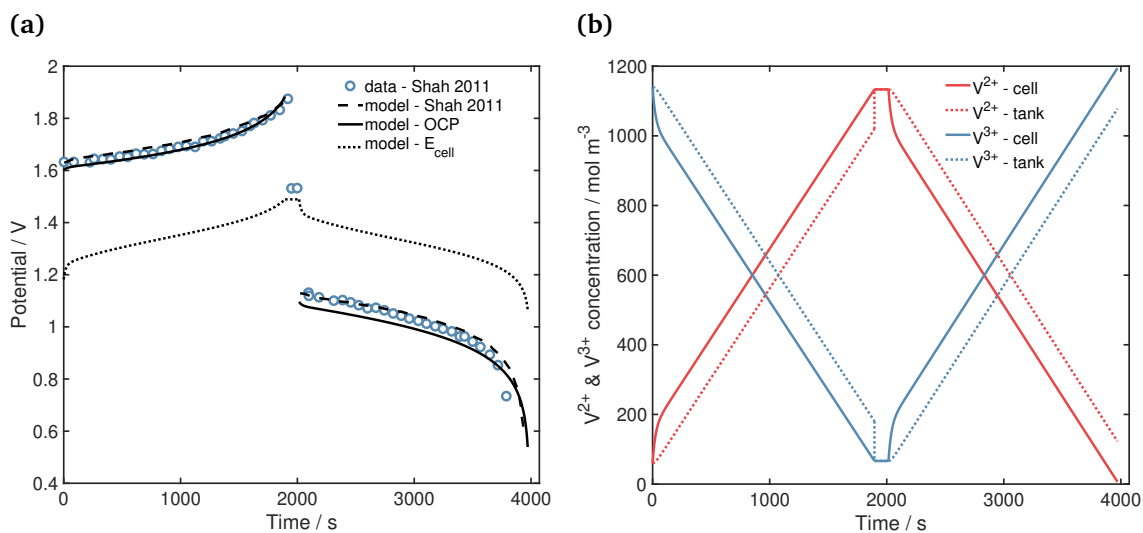
Figure 3.2: Unit cell model test: (a) Shows the comparison of cell potential against experimental and simulation results of Shah et al. (2011b); and (b) Shows the evolution of concentration for V^{2+} and V^{3+} at the anode and the anolyte tank.

tanks was much higher (Shah et al., 2011b).

Figure 3.3 presents the comparison of the unit cell model against experimental and simulations results of cell potential reported by You et al. (2009b). Figure 3.3 also includes the simulation results of cell potential reported by Chen et al. (2014) and Qiu et al. (2012). The calculated Open Circuit Potential (OCP), which was obtained by using the complete Nernst equation proposed by Knehr and Kumbur (2011), underestimated the expected equilibrium potential which should appear somewhere in between the cell potential of charge and discharge. Instead, the calculated OCP coincided with the discharge potential most probably due to unit activity assumptions for all ionic species. This mismatch in the expected OCP made it impossible to fit an appropriate cell potential by estimating the electrode overpotentials since any fitted parameters resulted in lower potentials when compared with the measured cell potential during charge and discharge. The cell potential simulation displayed in Figure 3.3 was obtained by favouring the fitting of the cell potential during charge only to be able to get the potential behaviour displayed by the cell, and therefore an important difference between the simulated and measured cell potential during discharge was observed. The NRMSE for the simulated results of the unit cell model in comparison to the experimental data set 2 was 1.49% during charge and 9.41% during discharge when a value of 1923 S m^{-1} was considered for the electrode conductivity and a value of $16\,494\,\text{m}^2\,\text{m}^{-3}$ was considered for the specific surface area of the electrodes. These parameter values were similar to the values presented by You et al. (2009b) of 1000 S m^{-1} for assumed electrode conductivity and $16\,200\,\text{m}^2\,\text{m}^{-3}$ for the fitted specific surface area.

The cell potential simulation reported by You et al. (2009b) using a 2D model and Qiu
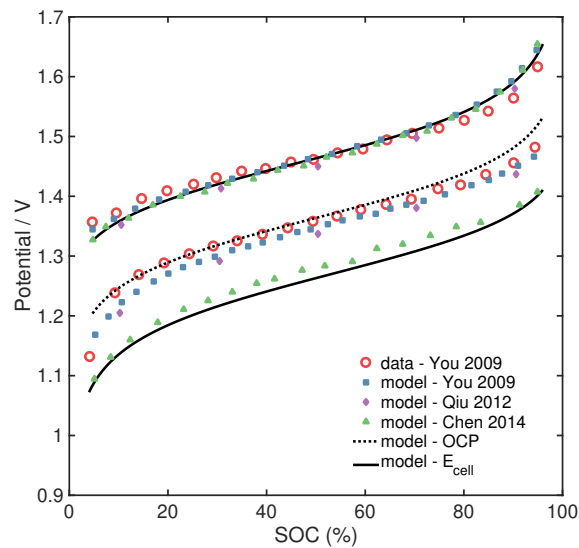
Figure 3.3: Comparison of cell potential from unit cell model against experimental and 2D simulation results reported by You et al. (2009b), 3D simulations reported by Qiu et al. (2012), and 1D simulations reported by Chen et al. (2014).

et al. (2012) using a 3D model showed a better agreement with the experimental data, as shown in Figure 3.3. It is important to mention that both of these works added an arbitrary potential of $140\,\text{mV}$ in order to fit the experimental data (Chen et al., 2014; Qiu et al., 2012; You et al., 2009b). This correction to the potential was said to account for unknown discrepancies such as the contact resistance between current collectors and porous electrodes, the connection from the load/power supply to the cell, the potential difference across the membrane due to different concentration of protons at each half-cell and the contribution of protons to the OCP (Knehr and Kumbur, 2011; Qiu et al., 2012; You et al., 2009b). It has been said that the complete Nernst equation, which includes the effect of the concentration of protons and the membrane in the equilibrium potential, represents approximately $80\,\%$ of this total potential correction, leaving a remaining discrepancy of $30 - 40$ mV (Chen et al., 2014). The unit cell model and the 1D model reported by Chen et al. (2014) did not consider any arbitrary potential correction and both models displayed similar results during charge and discharge. This decision was taken to visualise the sources of discrepancies between the simulations and the experimental data. Even when both of these models account for the concentration of protons and the Donnan potential in the OCP, the complete Nernst equation still underestimated the expected equilibrium potential. Additional effects that could affect the OCP are the chemical dissociation of sulphuric acid as the SOC changes, therefore changing the concentration of protons in the half-cells and the assumption of unity activity coefficients for all ionic species that is used to simplify the Nernst equation. Further discussion about the correct approach to estimate the equilibrium potential is presented in Chapter 4.

Figure 3.4 shows the integrated average of the activation overpotential reported by Chen

(a)

(b)
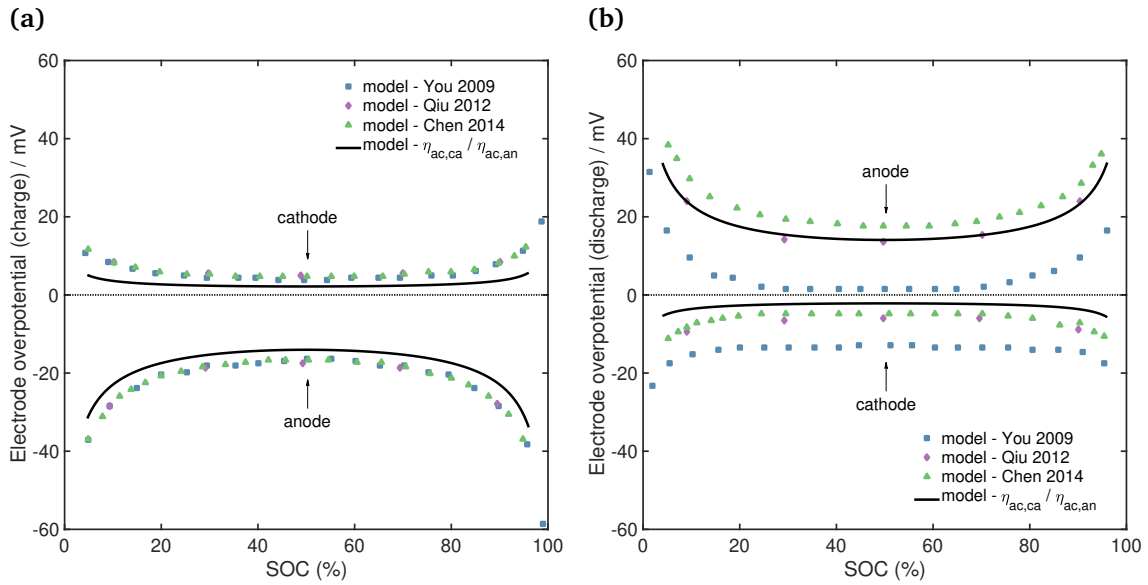
Figure 3.4: Overpotential estimation for the cathode and anode of different models during: (a) Charge; and (b) Discharge.

et al. (2014); Qiu et al. (2012); You et al. (2009b), along with the activation overpotential of the unit cell model for both electrodes. While the order of magnitude of the four overpotentials is similar, the behaviour was different for the overpotential reported by You et al. (2009b). If the polarity of the current density is reversed under the same operating condition, the overpotential of each half-cell as a function of SOC should change sign (Qiu et al., 2012). This is the behaviour observed in the 1D model, 3D model and the unit cell model. During charge and discharge, the behaviour and order of magnitude obtained by the unit model corresponded with the values reported by the 1D and 3D models, with main discrepancies at the limits of low and high SOC. These discrepancies seemed more important for the cathode, which could be related to mass-transport limitation effects. Since the unit cell model does not include as full a description of the electrodes as the 1D or 3D models, any statement on this matter remains speculative at this stage. Further discussion of the kinetic expression to represent the current density - overpotential relationship is given in Chapter 4.

3.4 Conclusions

This chapter introduces a simplified unit cell model based on the approaches of vanadium redox flow battery models reported in the literature. This model represented reasonably well the cell potential behaviour for two sets of experimental data reported by Shah et al. (2011b) (set 1) and You et al. (2009b) (set 2). The potential difference for set 1 was observed mainly at the end of charge and discharge, where the simplified Butler-Volmer equation used did not reproduce the experimentally observed the mass-transport limita-

tion effects. The cell potential reported by Shah et al. (2011b) presented a better fitting to the experimental data, which was explained by the higher rate of change of species concentration reported in their work. This allowed a lower SOC to be reached when compared with the unit cell model implemented here. Encouragingly, the analytical expression proposed in their work matched the behaviour described by the unit cell model. The potential difference for set 2 was mainly related to a poor estimation of the equilibrium potential. However, the shape of the simulated cell potential during charge and discharge agreed with the experimental data, which displayed a small mass-transport limitation at the end of discharge.

The unit cell model considered a Complete Nernst Equation (CNE) that accounts for the concentration of protons at the cathode and the Donnan potential at the electrode/membrane interfaces, assuming unity activity coefficients (Knehr and Kumbur, 2011). This equation is the most used version of a complete Nernst equation in recently reported models. It has been stated by Knehr and Kumbur (2011) that a difference of $131-140\,\text{mV}$ is observed between OCP experimental data and the simplified Nernst equation, which accounts for the redox reactions at each electrode and neglects the cathodic concentration of protons (Equation 2.39, SNE). The CNE is expected to eliminate this potential difference and represent more accurately the equilibrium potential as a function of SOC (Knehr and Kumbur, 2011). This CNE was used to calculate the equilibrium potential for two sets of experimental data reported by Shah et al. (2011b) (set 1) and You et al. (2009b) (set 2). The calculated OCP displayed slightly lower values of equilibrium potential for the experimental data set 1 with values between the cell potential of charge and discharge, while for the experimental data set 2 the calculated OCP coincided with the discharge cell potential making impossible to fit the cell potential. The OCP as expressed in Equation 3.10 only depends on the standard potential (E_{cell}^0 which is a function of temperature) and the state of charge of the battery, *i.e.* the concentration of ionic species at each electrode (c_i^k), while the operating conditions are not expected to have an effect on it. Experimental data set 1 and 2 were performed at the different initial concentration of vanadium and sulphuric acid, which could have an important effect in the potential correction obtained when using the CNE and considering the effect of concentration of protons and the Donnan potential. Even when the cathodic concentration of protons for the experimental set 2 was much higher, it was not enough to produce the expected potential correction and place the equilibrium potential in between the cell potential of charge and discharge. It is of interest to understand under what conditions the complete Nernst equation, as proposed by Knehr and Kumbur (2011), will represent accurately the equilibrium potential. The additional potential correction required to correctly describe the equilibrium potential may well be related to the assumption of unity activity coefficients. Recently, Pavelka et al. (2015) introduced a different expression of a complete Nernst Equation derived from thermody-

namics. This new CNE differs from the expression proposed by Knehr and Kumbur (2011). Further discussion about the correct description of a complete Nernst equation is presented in Chapter 4. It is critical to correctly estimate the equilibrium potential of the cell since a parametric fitting step is generally considered to simulate cell potential. This fitting step requires the estimation of ohmic and electrode overpotentials with respect to an equilibrium potential in order to match the measured cell potential. Additionally, the unit cell model considered a simplified Butler-Volmer equation, that accounted only for vanadium species concentrations. This equation neglects the effect of mass-transport limitations and the cathodic concentration of protons. Chapter 2 presented the general description of the rate of reaction for a single-step electrochemical reaction (Newman and Thomas-Alyea, 2004), which should involve the multiplication of all species involved in the reaction. Further discussion about the Butler-Volmer equation for the VO^{2+} / VO_2^+ reactions is presented in Chapter 4, where a complete Butler-Volmer equation is proposed.

Chapter 4 presents the development and implementation of a unit cell model for a Regenerative Hydrogen-Vanadium Fuel Cell (RHVFC). This model was based on the unit cell models studied in this chapter and Chapter 2. This next chapter includes a detailed explanation of the equations considered for the species conservation, equilibrium potential and electrode kinetics, as well as a simplified approach to account for a flow-by cell configuration. An initial test of the unit cell model is developed by means of experimental data of single-cycle charge-discharge potential from an in-house RHVFC.

Chapter references

Chen, C. L., Yeoh, H. K., and Chakrabarti, M. H. An enhancement to Vynnycky's model for the all-vanadium redox flow battery. *Electrochimica Acta*, 120:167–179, feb 2014.

Gandomi, Y. A., Aaron, D. S., Zawodzinski, T. A., and Mench, M. M. In Situ Potential Distribution Measurement and Validated Model for All-Vanadium Redox Flow Battery. *Journal of The Electrochemical Society*, 163(1):A5188–A5201, 2016.

Knehr, K. W., Agar, E., Dennison, C. R., Kalidindi, A. R., and Kumbur, E. C. A Transient Vanadium Flow Battery Model Incorporating Vanadium Crossover and Water Transport through the Membrane. *Journal of The Electrochemical Society*, 159(9):1446–1459, 2012a.

Knehr, K. and Kumbur, E. Open circuit voltage of vanadium redox flow batteries: Discrepancy between models and experiments. *Electrochemistry Communications*, 13(4): 342–345, apr 2011.

Knehr, K., Agar, E., Dennison, C. R., Kalidindi, A. R., and Kumbur, E. C. A Transient Vanadium Flow Battery Model Incorporating Vanadium Crossover and Water Transport

through the Membrane. *Journal of the Electrochemical Society*, 159(9):A1446–A1459, aug 2012b.

Newman, J. S. and Thomas-Alyea, K. E. *Electrochemical Systems*. John Wiley & Sons, Inc., New York, 3rd edition, 2004. ISBN 0-471-47756-7.

Pavelka, M., Wandschneider, F., and Mazur, P. Thermodynamic derivation of open circuit voltage in vanadium redox flow batteries. *Journal of Power Sources*, 293:400–408, 2015.

Qiu, G., Joshi, A. S., Dennison, C., Knehr, K., Kumbur, E., and Sun, Y. 3-D pore-scale resolved model for coupled species/charge/fluid transport in a vanadium redox flow battery. *Electrochimica Acta*, 64:46–64, mar 2012.

Shah, A., Watt-Smith, M., and Walsh, F. A dynamic performance model for redox-flow batteries involving soluble species. *Electrochimica Acta*, 53(27):8087–8100, nov 2008.

Shah, A., Tangirala, R., Singh, R., Wills, R., and Walsh, F. A Dynamic Unit Cell Model for the All-Vanadium Flow Battery. *Journal of The Electrochemical Society*, 158(6):A671, 2011.

Tang, A., Bao, J., and Skyllas-Kazacos, M. Dynamic modelling of the effects of ion diffusion and side reactions on the capacity loss for vanadium redox flow battery. *Journal of Power Sources*, 196(24):10737–10747, dec 2011.

Wei, Z., Zhao, J., Skyllas-Kazacos, M., and Xiong, B. Dynamic thermal-hydraulic modeling and stack flow pattern analysis for all-vanadium redox flow battery. *Journal of Power Sources*, 260:89–99, aug 2014.

Won, S., Oh, K., and Ju, H. Numerical analysis of vanadium crossover effects in all-vanadium redox flow batteries. *Electrochimica Acta*, 177:310–320, sep 2015.

Xu, W., Zhang, H., Xing, F., Zhang, H., Li, Y., Cao, J., and Li, X. The numerical simulation of dynamic performance in the vanadium flow battery. *Electrochimica Acta*, 118:51–57, feb 2014.

You, D., Zhang, H., and Chen, J. A simple model for the vanadium redox battery. *Electrochimica Acta*, 54(27):6827–6836, nov 2009.

Yu, V. and Chen, D. Dynamic Model of a Vanadium Redox Flow Battery for System Performance Control. *Journal of Solar Energy Engineering*, 136(2):021005–1 – 0210057, 2014a.

Yu, V. and Chen, D. Peak power prediction of a vanadium redox flow battery. *Journal of Power Sources*, 268:261–268, dec 2014b.

Chapter 4

Development of a unit cell model for the regenerative hydrogen-vanadium fuel cell

This chapter is based on the work:

C. A. Pino-Muñoz, H. Hewa Dewage, V. Yufit and N. P. Brandon, "A unit cell model of a regenerative hydrogen-vanadium fuel cell", Journal of The Electrochemical Society, 164 (14) F1717-F1732 (2017)(Pino-Muñoz et al., 2017).

4.1 Introduction

This chapter describes the development and testing of a simplified zero-dimensional unit cell model for a Regenerative Hydrogen Vanadium Fuel Cell (RHVFC). This zero-dimensional (0D) model was based on the physicochemical phenomena considering species conservation, transport mechanisms and electrochemical processes. The aim of this model is to provide a first approximation for the interplay of these various physicochemical phenomena occurring in an RHVFC, and to be a tool to rapidly evaluate the cell's performance so it can be of use in monitoring and designing tasks. Chapter 2 introduced the first proof of concept of an RHVFC and the motivation behind the study of such a system. This Chapter describes the RHVFC in detail along with a proposed unit cell model to simulate the potential dynamics of this cell.

The RHVFC was first proposed in 2013 by Yufit et al. (2013), reporting a proof of concept for this new battery alongside a performance study. This study showed that higher current densities or lower catholyte flow rates produce lower coulombic efficiencies, which could be explained by the mass transport limitations. Later, an in-depth analysis of the loss mechanisms of an RHVFC was reported by means of experimental studies (Hewa Dewage et al., 2015). The authors showed the occurrence of crossover of vanadium electrolyte, which could be adsorbed into the anode Pt catalyst. The authors also showed a negligible influence of the hydrogen flow rate on cell performance. These studies highlighted that better performance could be obtained if improved component materials and operating conditions were used. Modelling and simulation appear as an indispensable tool to support the design and optimisation of an RHVFC, saving time and reducing costs. To this end a 0D model or a lumped model is suitable, such a model can be based on a small set of differential algebraic equations, which can be fairly simple to integrate and can be accurate enough to describe the battery dynamics (Zheng et al., 2014a). Lumped models consider the time-dependent electrochemical phenomena, but assume a uniform spatial distribution of species concentrations. This approach has been used previously to model a VRFB (Shah et al., 2011b), considering mass conservation and the electrochemical process, and being able to capture the relation between performance and key properties (Zheng et al., 2014a), such as component properties and operating conditions. Additional effects were later included such as thermal processes (Tang et al., 2012a,b), self discharge (Skyllas-Kazacos and Goh, 2012; Tang et al., 2011; You et al., 2011), pump-

ing power and shunt current losses (Tang et al., 2013a; Xiong et al., 2013). Also, a PEMFC lumped model was developed by Pukrushpan et al. (2002), which allowed the evolution of component partial pressures and membrane humidity to be studied (Bavarian et al., 2010). Effects such as reactant starvation and flooding were later considered to describe the effect of water accumulation on the cell behaviour (McKay et al., 2005, 2008).

In a unit cell model, the cell potential is simulated by using an Open Circuit Potential (OCP) equation to calculate a reversible or equilibrium cell potential and simulating how far from equilibrium the system is. This enables simulation of the overpotentials of the system under particular operating conditions. Therefore, an important topic to be studied in this chapter is the redox reaction kinetics used to described the cathode and anode reactions, as well as the appropriate Nernst equations to estimate equilibrium potential (Pavelka et al., 2015). The redox reaction kinetics in PEMFCs are not fully understood since the oxygen and hydrogen reactions can be represented by different reaction paths with more than one step (Chen and Kucernak, 2004; Kucernak and Zalitis, 2016b; Shah et al., 2011a). A Butler-Volmer relation has been widely used to model the kinetics, which uses transfer coefficients with values of about 0.5 for both electrodes, and neglects the dependency on proton concentration and activity (Shah et al., 2011a; Weber and Newman, 2004). This assumption corresponds to the electro-neutrality condition assumed in the polymer electrolyte (Shah et al., 2011a; Weber and Newman, 2004), providing that the proton concentration is equal to the concentration of fixed charge sites in the polymer electrolyte. However, it has been reported that a Butler-Volmer type of expression does not represent correctly the relation between current density and overpotential for the hydrogen reaction (Chen and Kucernak, 2004; Kucernak and Zalitis, 2016b; Wang et al., 2006). The OCP has been considered to be dependent on the pressure of hydrogen, oxygen and liquid water (Weber and Newman, 2004). In VRFBs, the reaction kinetics are commonly modelled using the Butler-Volmer Equation (Zheng et al., 2014a), which neglects the effect of the concentration of protons in the positive side (cathode) (Gandomi et al., 2016; Knehr et al., 2012b; Shah et al., 2008; You et al., 2009b). This assumption is most probably a consequence of using an approach based on the one commonly used for PEMFCs, where the concentration of protons is around 1 M. This is not the case of VRFBs where the concentration of protons is higher than 5 M, and changes over the charge and discharge of the cell due to the electrochemical reactions. Therefore, the effect of the concentrations of protons in the kinetics could be more important and interesting to consider. Also, it has been recognised that when the transfer coefficients in the Butler-Volmer equation are equal to 0.5, the ability to fit polarisation data can be limited (Gandomi et al., 2016; Knehr et al., 2012b). In VRFBs, the impact of using the complete Nernst equation to describe the OCP has been stated by Knehr and Kumbur (2011), as shown in Equation 4.1. Where E_{OCP} is the open circuit potential, E_{cell}° is the standard cell potential, R is the universal gas

constant, T is the temperature, F is the Faraday constant, c_i is the bulk concentration of species i, and the superscript 'ca' and 'an' refers to positive and negative side, respectively. This equation has been used in different models to describe the equilibrium potential of the cell (Agar et al., 2013; Chen et al., 2014; Gandomi et al., 2016; Knehr et al., 2012b; Yang et al., 2015a).

$$E_{OCP} = E_{cell}^{\circ} + \frac{RT}{F}\ln\left(\frac{c_{VO_2^+}^{ca}\, c_{V^{2+}}^{an}\, (c_{H^+}^{ca})^2}{c_{VO^{2+}}^{ca}\, c_{V^{3+}}^{an}} \times \frac{c_{H^+}^{ca}}{c_{H^+}^{an}}\right) \tag{4.1}$$

This equation assumes that the activity coefficient (γ) for all species is equivalent to 1, and includes the effect of the cathode proton concentration and Donnan potential, which represents the potential jump at the electrolyte-membrane interfaces due to different proton concentrations in the anolyte and catholyte (Knehr and Kumbur, 2011). However, the inconsistency with thermodynamics of this equation has been stated by Pavelka et al. (2015), who have introduced an OCP equation for VRFBs derived from thermodynamic principles as shown Equation 4.2. Where a_i is the activity of species i. This new equation differs from the equation proposed by Knehr and Kumbur in the inclusion of the potential difference between catholyte and anolyte, which is the dialysis potential or potential across the entire membrane (Hamann et al., 2007; Kontturi et al., 2008; Pavelka et al., 2015). The relation proposed by Pavelka *et al.* underestimated the OCP data when unity activity coefficients are considered (Pavelka et al., 2015). To improve the agreement nonideal activity coefficients should be considered, which can be evaluated from experimental OCP data.

$$E_{OCP} = E_{cell}^{\circ} + \frac{RT}{F}\ln\left(\frac{a_{VO_2^+}^{ca}\, a_{V^{2+}}^{an}\, (a_{H^+}^{ca})^2}{a_{VO^{2+}}^{ca}\, a_{V^{3+}}^{an}\, a_{H_2O}^{ca}} \times \frac{a_{H^+}^{an}}{a_{H^+}^{ca}}\right) \tag{4.2}$$

This chapter continues as follows, first, a brief description of the hydrogen-vanadium cell is given followed by a detailed explanation of the proposed comprehensive model, stating equations, assumptions and simplifications. Later, the experimental methods describing the experimental set-up and a summary of the experimental data used in this chapter to do initial testing of the model are given. This is followed by a discussion of this model calibration and validation. The chapter ends with conclusions and future work in this area.

4.2 The regenerative hydrogen-vanadium fuel cell

An RHVFC uses an aqueous vanadium electrolyte, containing V(V) and V(IV), at the positive electrode and hydrogen at the negative electrode (Yufit et al., 2013). Figure 4.1

presents a schematic of a RHVFC. This cell is composed of a porous carbon layer for the positive electrode reaction (cathode electrode), membrane and catalysed porous carbon layer for the negative electrode reaction (catalyst layer plus gas diffusion layer). The catholyte solution is recirculated between the positive half-cell and the catholyte tank while passing through the flow channels (cathode channel) which are usually serpentine-like. Hydrogen is recirculated between the negative half-cell and the hydrogen tank and also uses a flow channel (anode channel) to get distributed to the electrode. Hydrogen evolution, which is an adverse reaction in VRFBs, is the main anodic process in the RHVFC. During discharge, V(V) is reduced to V(IV) and H_2 is oxidised, while the reverse process occurs during charge and H_2 is produced and stored. For the purpose of the work presented in this chapter, hydrogen is not recycled to a tank and electrolyte crossover is not pumped back to the catholyte tank in the experimental set-up, as it could be in a commercial set-up.
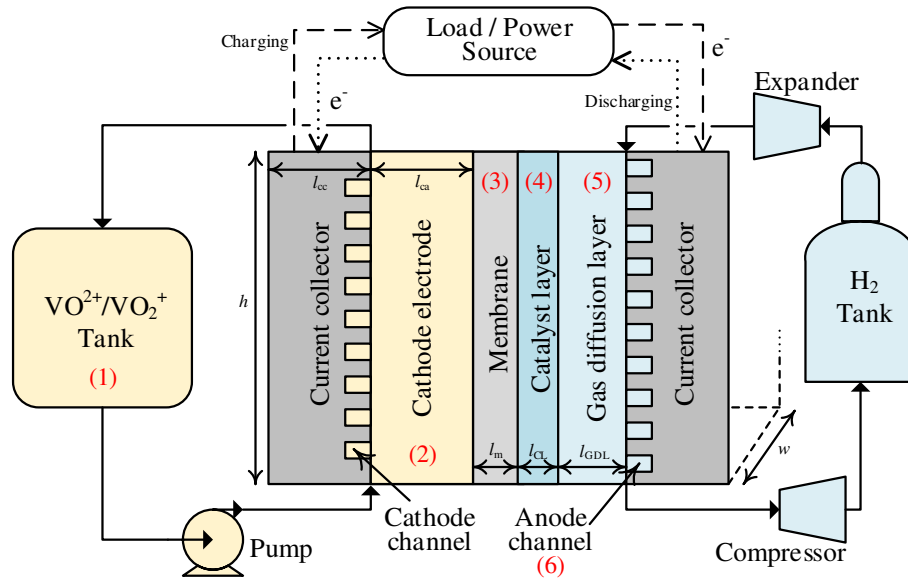
Figure 4.1: Schematic of the RHVFC and model domains.

The vanadium electron-transfer reaction takes place in the positive electrode, namely the cathode, while the hydrogen evolution/reduction reaction (HER/HOR) occurs in the catalyst layer (CL) of the negative electrode, namely the anode. The reduction-oxidation (redox) reactions that occur at the electrodes are presented in Equations 4.3 and 4.4, and the overall cell reaction in Equation 4.5 with a standard cell potential of $0.99\,\text{V}$. Where the charged species VO^{2+} and VO_2^+ represent the V(IV) and V(V) oxidation states, respectively. The term E^{Θ} is the standard potential with the subscripts 'ca' and 'an' referring to the positive and negative side respectively.

$$2VO_2^+ + 4H_3O^+ + 2e^- \underset{\text{charge}}{\overset{\text{discharge}}{\rightleftharpoons}} 2VO^{2+} + 6H_2O, \quad E_{\text{ca}}^{\Theta} = 0.99\,\text{V } \textit{vs. } \text{SHE} \qquad (4.3)$$

$$H_2 + 2H_2O \xrightleftharpoons[\text{charge}]{\text{discharge}} 2H_3O^+ + 2e^-, \quad E_{an}^{\ominus} = 0 \text{ V } \textit{vs. } \text{SHE} \tag{4.4}$$

$$2VO_2^+ + 2H_3O^+ + H_2 \xrightleftharpoons[\text{charge}]{\text{discharge}} 2VO^{2+} + 4H_2O, \quad E_{cell}^{\ominus} = 0.99 \text{ V } \textit{vs. } \text{SHE} \tag{4.5}$$
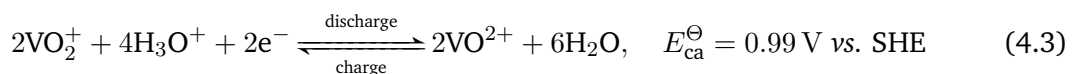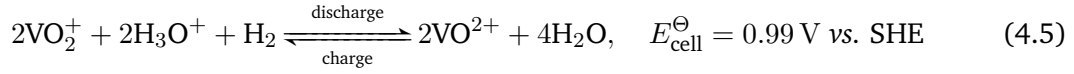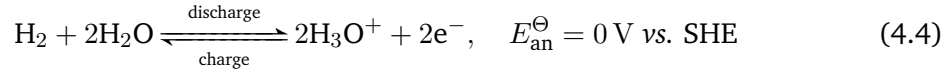
4.3 Zero-dimensional (0D) mathematical modelling of a RHVFC

The proposed mathematical description for a unit cell of the hydrogen-vanadium system was developed considering six domains: (1) catholyte tank, (2) cathode, (3) membrane, (4) catalyst layer (CL), (5) gas diffusion layer (GDL), and (6) the anode channel, which are shown in Figure 4.1. To develop the model a number of assumptions and simplifications were considered, which are listed below:

1. All domains are considered isothermal and having the same temperature.

2. The catholyte is considered incompressible, having a constant density, viscosity and volume.

3. All physical properties, mass and charge-transfer properties are assumed isotropic and homogeneous in all the domains.

4. The electrolytes must maintain electroneutrality, which is $\sum z_i c_i = 0$.

5. Unit activity coefficients are assumed for all species. However, an activity term is considered for the chemical dissociation of HSO_4^-, and a fitted global parameter representing the effect of the species activity coefficients is considered for the estimation of the Open Circuit Potential.

6. The dilute solution approximation is considered to model the liquid phase, namely the catholyte.

7. Spatial concentration distribution in the catholyte tank, cathode, CL and anode channel are neglected.

8. Transport across the membrane and GDL is considered to be steady-state.

9. Gas evolution reactions in the cathode are neglected.

10. Side reactions and self-discharge reactions involving vanadium ionic species at the cathode and the anode are neglected.

11. Dissociation of bi-sulphate ions is assumed to reach equilibrium instantaneously.

12. Full humidification of the membrane is assumed at the cathode/membrane interface.

13. The ionomer phase that is present in the CL has the same fixed charge concentration

as the ionomer in the membrane.

14. Protons are the only ionic species that can cross the membrane.

15. Water crossover from cathode to anode is considered, but any change of the catholyte volume is neglected.

16. Water only in the vapour phase can leave the CL and enters the anode channel or vice-versa, and also can leave the anode channel.

17. The gas phase at the anode side is treated as an ideal gas.

18. The cathode channel was not included as a model domain since the flow rate through it was assumed to by-pass the cathode porous electrode and to not participate in the vanadium reaction. Only a portion of the inlet flow rate was considered to enter the cathode.

19. The hydrogen tank was not considered as a model domain because the hydrogen flow was passed through the cell and not recirculated to a tank in the experimental set-up used in this work.

The set of equations proposed to described the RHVFC, which responds to these simplifications and assumptions, are based on the modelling framework propose for previous reported models for VRFBs (Gandomi et al., 2016; Knehr et al., 2012a; Pavelka et al., 2015; Shah et al., 2008, 2011b; Tang et al., 2011; Wei et al., 2014; Won et al., 2015; Yu and Chen, 2014a,b) and PEM fuel cells (Bertei and Nicolella, 2015; Ge et al., 2005; He et al., 2000; Kucernak and Zalitis, 2016a; Nam and Kaviany, 2003; Springer et al., 1991; Wu et al., 2009, 2010). The main components of the model are divided in three sections: cathode, anode and cell potential, which are discussed in the following sections.

4.3.1 Cathode side

The catholyte solution contains water, sulphuric acid species (H^+, HSO_4^- and SO_4^{2-}) and charged vanadium species (VO^{2+} and VO_2^+). These five ionic species were considered and their concentration evolution was modelled by species conservation equations. A correct estimation of the concentration of ionic species in the catholyte is of importance to maintain electro-neutrality and to calculate the equilibrium potential and overpotentials. To this end, the concentration of ionic species is considered to be affected by the redox reaction at the cathode according to Equation 4.3, the dissociation of bi-sulphate ions and the catholyte recirculation between the catholyte tank and the cathodic half-cell. In the case of protons, the concentration is also affected by the transport of protons through the membrane. The conservation of each ionic species in the cathode is represented by an ordinary differential equation (ODE) with respect to time, as presented in Equations 4.6 to 4.10. In a similar manner, the species conservation in the catholyte tank is represented

by ODEs, as given in Equation 4.11 for all species.

$$\varepsilon_{\text{ca}} V_{\text{ca}} \frac{dc_{\text{VO}^{2+}}}{dt} = Q_{\text{ca}}(c_{\text{VO}^{2+},\text{T}} - c_{\text{VO}^{2+}}) \mp \frac{A_{\text{ca}} j}{F} \tag{4.6}$$

$$\varepsilon_{\text{ca}} V_{\text{ca}} \frac{dc_{\text{VO}_2^+}}{dt} = Q_{\text{ca}}(c_{\text{VO}_2^+,\text{T}} - c_{\text{VO}_2^+}) \pm \frac{A_{\text{ca}} j}{F} \tag{4.7}$$

$$\varepsilon_{\text{ca}} V_{\text{ca}} \frac{dc_{\text{H}^+}}{dt} = Q_{\text{ca}}(c_{\text{H}^+,\text{T}} - c_{\text{H}^+}) \pm \frac{2 A_{\text{ca}} j}{F} \mp \frac{A_{\text{ca}} j}{F} + S_{\text{d}}^{\text{eq}} \tag{4.8}$$

$$\varepsilon_{\text{ca}} V_{\text{ca}} \frac{dc_{\text{SO}_4^{2-}}}{dt} = Q_{\text{ca}}(c_{\text{SO}_4^{2-},\text{T}} - c_{\text{SO}_4^{2-}}) + S_{\text{d}}^{\text{eq}} \tag{4.9}$$

$$\varepsilon_{\text{ca}} V_{\text{ca}} \frac{dc_{\text{HSO}_4^-}}{dt} = Q_{\text{ca}}(c_{\text{HSO}_4^-,\text{T}} - c_{\text{HSO}_4^-}) - S_{\text{d}}^{\text{eq}} \tag{4.10}$$

$$V_{\text{T}} \frac{dc_{\text{i},\text{T}}}{dt} = Q_{\text{ca}}(c_{\text{i}} - c_{\text{i},\text{T}}), \quad \text{i} = \left[\text{VO}^{2+}, \text{VO}_2^+, \text{H}^+, \text{SO}_4^{2-}, \text{HSO}_4^- \right] \tag{4.11}$$

The terms c_{i} and $c_{\text{i},\text{T}}$ denote the bulk concentration of species i in the electrolyte at the cathode and catholyte tank, respectively. The symbols ε_{ca}, V_{ca} and A_{ca} represent respectively the porosity, volume and cross-sectional area of the cathode. Where V_{ca} and A_{ca} can be obtained by considering the height, width and thickness of the cathode (h_{ca}, w_{ca} and l_{ca}). The term t is time, Q_{ca} is the flow rate of catholyte in the cathode, j is the applied current density, which refers to current per unit of cross-sectional area of electrode, and F is the Faraday constant. The term S_{d}^{eq} represents the change in concentration due to the dissociation of bi-sulphate ions, and V_{T} is the catholyte tank volume, which is assumed to remain constant.

The sulphuric acid dissociation was considered to follow a two-step process (Knopf et al., 2003), as shown in Equations 4.12 and 4.13. Where k_1 and k_2 represent the first and second dissociation constants, respectively. The first step of dissociation is assumed to be fully complete since it has been reported that it is essentially complete for concentrations up to $40 \, \text{mol kg}^{-1}$ at temperatures in the range of 273 to $323 \, \text{K}$ (Knopf et al., 2003). In chemical equilibrium, the second step of dissociation noticeably depends on temperature and can be described by the dissociation constant of bi-sulphate ions (k_2). This dissociation constant is defined by the activities (a_{i}) of the sulphuric acid species as presented in Equation 4.14. Where the species activities is related to their molar concentrations (c_{i}) and activity coefficients (γ_{i}) as shown in Equation 4.15. The standard molarity (c°) is considered to have a value of $1 \, \text{mol L}^{-1}$.

$$H_2SO_4 + H_2O \longrightarrow H_3O^+ + HSO_4^-, \quad k_1 \text{(strong acid)} \tag{4.12}$$

$$HSO_4^- + H_2O \longleftrightarrow H_3O^+ + SO_4^{2-}, \quad k_2 \tag{4.13}$$
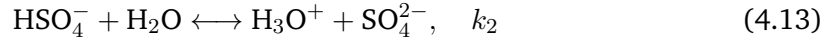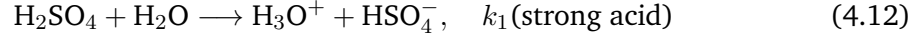
$$k_2(T) = \frac{c_{H^+} c_{SO_4^{2-}}}{c_{HSO_4^-} c^\circ} \frac{\gamma_{H^+} \gamma_{SO_4^{2-}}}{\gamma_{HSO_4^-}} = Q_M(T)\gamma(T) \tag{4.14}$$

$$a_i = \frac{\gamma_i c_i}{c^\circ} \tag{4.15}$$

The derivation of Equation 4.14 is similar to the one presented by Knopf et al. (2003), but the reference concentration has been changed from molality to molarity and includes a molar equilibrium dissociation quotient, $Q_M(T)$, and an activity coefficient product, $\gamma(T)$. In order to calculate the concentration change (S_d^{eq}) of H^+, HSO_4^- and SO_4^{2-} due to dissociation of bi-sulphate, an empirical model to estimate $Q_M(T)$ as a function of the H_2SO_4 concentration was used as presented in Equation 4.16. Figure 4.2 shows a comparison of the empirical model against the values of Q_M at $290\,K$ as a function of H_2SO_4 concentration. This model is based on experimental dissociation data reported by Knopf et al. (2003). For the purpose of this work, only experimental data at $290\,K$ was used. To calculate the change in the concentration of the sulphuric acid species due to the dissociation of HSO_4^-, Equation 4.16 was used to estimate Q_M based on the H_2SO_4 concentration. The chemical dissociation of HSO_4^- (presented in Equation 4.13) was used to describe the change in concentration of H^+, HSO_4^- and SO_4^{2-}, which is found by satisfying Equation 4.14 to return to chemical equilibrium.

$$Q_M = -0.118(c_{H_2SO_4})^2 + 1.672(c_{H_2SO_4}) - 0.720, \quad \text{at } 290\,K \tag{4.16}$$

The catholyte flow rate flows through the serpentine flow channels while it penetrates into the porous electrode. In order to simplify the flow distribution phenomena on the positive half-cell, a steady-state condition was assumed (Wei et al., 2014), which is that the pressure drop at the cathode and the flow channel is equal, *i.e.*, $\Delta p_{ca} = \Delta p_{CH}$. Using this assumption the flow rate in the flow channels and porous electrode were calculated. The portion of catholyte flow rate that flows through the flow channels was assumed to by-pass the reaction area (porous electrode), and only the portion of flow rate entering the cathode was incorporated in the conservation of ionic species as shown in Equations 4.6 to 4.10. Darcy's law as presented in Equation 4.17 was used to calculate the pressure drop through the porous electrode (Δp_{ca}) (Wei et al., 2014). The effective permeability of the cathode (κ) was determined by the Kozeny-Carman equation (Knehr et al., 2012b; Wei
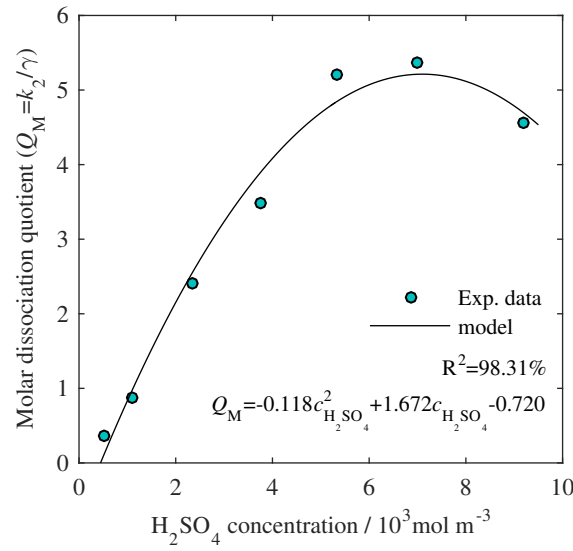
Figure 4.2: Dependency of Q_M with the molar concentration of H_2SO_4 at 290 K. Experimental data reported Knopf et al. (2003).

et al., 2014) as shown in Equation 4.18. In these equations, μ is the dynamic viscosity of the catholyte, which is considered constant at its reported value for a 50% state of charge (SOC) (Knehr et al., 2012b). L_{ca} is the cathode flow length, $A_{ca,f}$ is the flow area of electrode, d_f is the mean fibre diameter of the electrode, and K_{KC} is the Kozeny-Carman constant.

$$\Delta p_{ca} = \frac{\mu L_{ca} Q_{ca}}{\kappa A_{ca,f}} \tag{4.17}$$

$$\kappa = \frac{\varepsilon_{ca}^3 d_f^2}{K_{KC}(1 - \varepsilon_{ca})^2} \tag{4.18}$$

The pressure drop through the flow channels was calculated considering two sources: friction pressure drop and minor pressure drops. The minor pressure drops are caused by a sudden change in fluid direction or velocity (Wei et al., 2014). Equation 4.19 was used to calculate the pressure drop through the flow channels (Δp_{CH}) considering these two sources (Wei et al., 2014). Where the friction resistance coefficient (f_{CH}) was obtained as shown in Equation 4.20. The value 56.91 included in this equation was determined considering the specific geometry of the flow channels (Wei et al., 2014; White, 2011). $D_{h,ch}$ is the hydraulic diameter of the flow channels that is calculated considering its area and perimeter (A_{CH} and P_{CH}), K_f is the minor resistance coefficient, ρ is the density of the catholyte, Q_{ch} is the flow rate in the channel and Re_{D_h} is the Reynolds number based on the hydraulic diameter.

$$\Delta p_{CH} = \left(f_{CH} \frac{L_{CH}}{D_{h,CH}} + K_f \right) \frac{\rho}{2 A_{CH}^2} Q_{CH}^2 \tag{4.19}$$

$$f_{\text{CH}} = \frac{56.91}{Re_{D_{\text{h,CH}}}}, \quad Re_{D_{\text{h,CH}}} = \frac{\rho D_{\text{h,CH}} Q_{\text{CH}}}{\mu A_{\text{CH}}}, \quad D_{\text{h,CH}} = \frac{4A_{\text{CH}}}{P_{\text{CH}}} \quad (4.20)$$

This simplified steady-state pressure drop model allowed for the estimation of the effective flow rate that enters to the reaction area (cathode). Changes in the estimation of this flow rate are expected to affect the simulated cell potential by altering the residence time that the ionic species have to undergo electrochemical and chemical reactions.

4.3.2 Anode side

The anode side was modelled considering the CL, GDL and anode channel. Figure 4.3 shows a schematic of the molar flow rates of species($\dot{n}_{\text{i}}$) that are expected to be established for charge operation. The signal criteria adopted depends on the flow direction, as shown in Figure 4.3, where the direction of the arrows represents positive values of molar flow rates. At the CL, a molar flow rate of protons ($\dot{n}_{\text{H}^+,\text{m}}$) and dissolved water can arrive or leave due to transport through the membrane. Significant self-discharge of redox flow batteries due to the crossover of ionic species has been observed (Darling et al., 2015; Tucker et al., 2015), which increases with current density. Crossover fluxes of VO^{2+}, VO_2^+, HSO_4^- and SO_4^{2-} through the membrane have been neglected in this version of the model. The dissolved water is transported through the membrane by electro-osmotic drag ($\dot{n}_{\text{EO}}$) and diffusion ($\dot{n}_{\text{diff}}$). The diffusion flow rate is considered to always be from cathode to CL since full membrane humidification at the cathode-membrane interface is assumed. Dissolved water in the CL can be desorbed ($\dot{n}_{\text{des}}$) into liquid water, which can receive or lose material by condensation or evaporation ($\dot{n}_{\text{wv,CL}}$) depending on the vapour pressure at the CL and its saturation pressure. Hydrogen/protons is oxidised/reduced by means of the electron-transfer reaction ($\dot{n}_{\text{H}_2,\text{react}}$). Hydrogen can be transported from the CL through the GDL into the anode flow channels or vice-versa along with water vapour ($\dot{n}_{\text{H}_2,\text{GDL}}$ and $\dot{n}_{\text{v,GDL}}$). In the anode flow channels, pure hydrogen is entering ($\dot{n}_{\text{H}_2,\text{IN}}$), the phase change between vapour and liquid water is also considered ($\dot{n}_{\text{wv,CH}}$), and the outlet was only allowed to contain hydrogen and water vapour ($\dot{n}_{\text{H}_2,\text{OUT}}$ and $\dot{n}_{\text{v,OUT}}$).

The equations for the species conservation at the anodic half-cell are expressed by ODEs involving the molar flow rates due to transport and phase change that occur at the membrane, CL and GDL. Equations 4.21 to 4.25 present the conservation of protons, hydrogen, dissolved water, liquid water and vapour in the CL, and Equations 4.26 to 4.28 present the conservation of hydrogen, liquid water and vapour in the flow channels. In these equations, V_{CL} is the CL volume, ε_{m} is the volume fraction of electrolyte membrane in the CL, A_{CL} is the cross-sectional area of the CL, ε_{CL} is the porosity of the CL and s_{CL} is the liquid saturation in the CL. The term γ_{des} is the desorption rate, ξ_{drag} is the
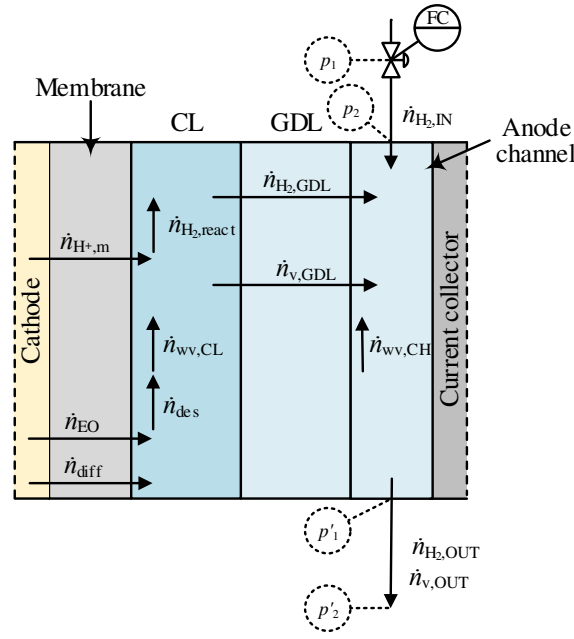
Figure 4.3: Schematic of molar flow rates at anode side.

electro-osmotic drag coefficient, $D_{dw,m}$ is the diffusion coefficient of dissolved water in the electrolyte membrane, l_m is the thickness of the membrane, ρ_w is the water density, M_w is the molar weight of water and $R_{w,CL}$ is the term that represents the phase change between vapour and liquid water in the CL. Also, V_{CH} is the anode channel volume, s_{CH} is the liquid saturation in the anode channel, $R_{w,CH}$ is the term that represents the phase change between vapour and liquid water in the anode channel.

The concentration of protons in the CL (Equation 4.21) is presented as a steady-state equation because of assumptions 4 and 14, which require that the concentration of protons in the CL to balance the fixed charge concentration in the polymer electrolyte of the membrane. This is $c_{H^+} + z_f c_f = 0$, where z_f and c_f is the charge number and concentration of the fixed charge in the polymer electrolyte. Water was considered to exist in three different phases depending on the domain (Wu et al., 2009, 2010), namely water vapour (v), liquid water (w) and dissolved water (dw). The transport of water through the polymer electrolyte was assumed to occur in the dissolved phase since the pore size of the polymer electrolyte is of the order of only $10\,\text{nm}$ and clusters of water tend to be localized and less connected (Wu et al., 2010). A diffusive approach is considered for the transport of dissolved water through the membrane as shown in Equation 4.23. This equation accounts for electro-osmotic drag due to transport of protons, with a electro-osmotic drag coefficient of $\xi_{drag} = 2.5\lambda/22$ (Springer et al., 1991). It also accounts for diffusion transport through the membrane and a desorption term.

$$V_{CL}\varepsilon_m \frac{dc_{H^+}}{dt} = \dot{n}_{H^+,m} \mp \frac{A_{CL}j}{F} = 0 \qquad (4.21)$$

$$V_{\text{CL}}\varepsilon_{\text{CL}}(1-s_{\text{CL}})\frac{dc_{\text{H}_2,\text{CL}}}{dt} = \pm\frac{A_{\text{CL}}j}{2F} - \dot{n}_{\text{H}_2,GDL} \tag{4.22}$$

$$V_{\text{CL}}\varepsilon_{\text{m}}\frac{dc_{\text{dw}}}{dt} = -V_{\text{CL}}\varepsilon_{\text{m}}\gamma_{\text{des}}(c_{\text{dw,CL}}-c_{\text{dw}}^{\text{eq}}) + \xi_{\text{drag}}\frac{A_{\text{CL}}j}{F} - A_{\text{m}}D_{\text{dw,m}}\frac{(c_{\text{dw,CL}}-c_{\text{dw,c-m}})}{l_{\text{m}}} \tag{4.23}$$

$$V_{\text{CL}}\varepsilon_{\text{CL}}\frac{\rho_{\text{w}}}{M_{\text{w}}}\frac{ds_{\text{CL}}}{dt} = V_{\text{CL}}\varepsilon_{\text{m}}\gamma_{\text{des}}(c_{\text{dw,CL}}-c_{\text{dw}}^{\text{eq}}) + R_{\text{w,CL}} \tag{4.24}$$

$$V_{\text{CL}}\varepsilon_{\text{CL}}(1-s_{\text{CL}})\frac{dc_{\text{v,CL}}}{dt} = -R_{\text{w,CL}} - \dot{n}_{\text{v,GDL}} \tag{4.25}$$

$$V_{\text{CH}}(1-s_{\text{CH}})\frac{dc_{\text{H}_2,\text{CH}}}{dt} = \dot{n}_{\text{H}_2,\text{GDL}} + \dot{n}_{\text{H}_2,\text{IN}} - \dot{n}_{\text{H}_2,\text{OUT}} \tag{4.26}$$

$$V_{\text{CH}}\frac{\rho_{\text{w}}}{M_{\text{w}}}\frac{ds_{\text{CH}}}{dt} = R_{\text{w,CH}} \tag{4.27}$$

$$V_{\text{CH}}(1-s_{\text{CH}})\frac{dc_{\text{v,CH}}}{dt} = -R_{\text{w,CH}} + \dot{n}_{\text{v,GDL}} - \dot{n}_{\text{v,OUT}} \tag{4.28}$$

The diffusion coefficient of dissolved water in the membrane is given by Equation 4.29. The desorption of dissolved water into liquid water at the CL was assumed to be proportional to the difference between the actual electrolyte membrane water content (λ) and the equilibrium water content (λ^{eq}) given in Equation 4.31. This equilibrium water content is determined by an empirical relationship obtained from experimental results of water uptake in CLs reported by Sun *et al.* (Sun et al., 2013). The term ρ_{dm} is the dry membrane density, EW is the equivalent molecular weight of the dry membrane, a_{v} is the activity of water vapour in the CL given in Equation 4.32, where $p_{\text{v}}^{\text{sat}}$ is the vapour saturation pressure.

$$D_{\text{dw,m}} = 4.1 \times 10^{-10}\left(\frac{\lambda}{25}\right)^{0.15}\left[1 + \tanh\left(\frac{\lambda - 2.5}{1.4}\right)\right] \tag{4.29}$$

$$c_{\text{dw}} = \lambda\frac{\rho_{\text{dm}}}{EW} \tag{4.30}$$

$$\lambda_{\text{CL}}^{\text{eq}} = 0.0514 + 10.987a_{\text{v}} - 13.164a_{\text{v}}^2 + 5.777a_{\text{v}}^3 \tag{4.31}$$

$$a_{\mathrm{v}} = \frac{c_{\mathrm{v,CL}} RT}{p_{\mathrm{v}}^{\mathrm{sat}}} \tag{4.32}$$

The desorption rate was also defined by an empirical relation that depends on the local electrolyte membrane hydration and is given in Equation 4.33 (Wu et al., 2010). The phase change between liquid and vapour for the water at the CL and anode flow channel is presented in a switching format between evaporation and condensation as shown in Equation 4.34. The mass-transfer rate for evaporation or condensation is related to the amount of reactant in the porous media and the driving force (He et al., 2000). The driving force is represented as the difference between the vapour pressure and its saturation pressure at the operating temperature. To avoid unrealistic values of vapour concentration or liquid saturation, Equation 4.34 was not considered and therefore evaporation was not possible when liquid water was not present or when the vapour pressure was lower than the saturation pressure at the operating temperature. In these equations, f_{V} is the volume fraction of water in the membrane, V_{w} water molar volume, V_{m} is the dry membrane molar volume, and l_{CL} is the thickness of the CL. V_{m} can be calculated by $V_{\mathrm{m}} = EW/\rho_{\mathrm{m}}$ (Ge et al., 2005). Also, k_{c} and k_{e} are the condensation and evaporation rate constants, y_{v} is the molar fraction of vapour in the gas phase, and p_{v} is the vapour pressure.

$$\gamma_{\mathrm{des}} = \frac{4.59 \times 10^{-5} f_{\mathrm{V}}}{l_{\mathrm{CL}}} \exp\left[2416\left(\frac{1}{303} - \frac{1}{T}\right)\right], \quad f_{\mathrm{V}} = \frac{\lambda V_{\mathrm{w}}}{V_{\mathrm{m}} + \lambda V_{\mathrm{w}}} \tag{4.33}$$

$$R_{\mathrm{w}} = \begin{cases} k_{\mathrm{c}} V \varepsilon (1-s) y_{\mathrm{v}} \frac{(p_{\mathrm{v}} - p_{\mathrm{v}}^{\mathrm{sat}})}{RT}, & \text{if } p_{\mathrm{v}} \geq p_{\mathrm{v}}^{\mathrm{sat}} \text{ (condensation)} \\ k_{\mathrm{e}} V \varepsilon s \frac{\rho_{\mathrm{w}}}{M_{\mathrm{w}}} (p_{\mathrm{v}} - p_{\mathrm{v}}^{\mathrm{sat}}), & \text{if } p_{\mathrm{v}} < p_{\mathrm{v}}^{\mathrm{sat}} \text{ (evaporation)} \end{cases} \tag{4.34}$$

The Dusty Gas Model (DGM), which considers both diffusion and pressure-driven convection (Mason and Malinauskas, 1983) was used to model the transport of hydrogen and vapour water through the GDL. In this work only steady-state transport was considered by Equation 4.35, which was used to describe the transport of the binary mixture (Bertei and Nicolella, 2015) (H_2 and v). In this model, the driving force for transport is the difference in molar fraction and pressure. The molar flow rate of species can be obtained by means of the following relation, $\dot{n}_{\mathrm{i,GDL}} = A_{\mathrm{GDL}} N_{\mathrm{i,GDL}}$, where A_{GDL} is the cross-sectional area of the GDL and N_{i} is the molar flux of species i. The effective binary diffusion coefficient ($D_{\mathrm{i,j}}^{\mathrm{eff}}$) is estimated from Chapman-Enskog kinetic theory assuming ideal gas behaviour holds (Bird et al., 1964) and is given in Equation 4.36. The effective Knudsen diffusion coefficient ($D_{\mathrm{Kn,i}}^{\mathrm{eff}}$) and the permeability of the porous material (K) are calculated using Equations 4.37 and 4.38 (Bertei and Nicolella, 2015). Both diffusion coefficients are corrected considering porosity and tortuosity (τ) of the porous media using a Bruggeman correlation (Jiao and Li, 2011; Nam and Kaviany, 2003), which is given by $\tau = \varepsilon^{-1/2}$. The

effect of liquid saturation over the transport parameters was neglected because of assumption 16, which results in no liquid water in the GDL. At the inlet of the anode channel pure dry hydrogen is entering, and at the outlet hydrogen and water vapour leave. Liquid water is not considered to leave the channel. The total mass flux (G) that enters and leaves the anode channel is estimated through an isothermal energy balance (Wilkes, 1999), given by Equation 4.39. This equation considers the fanning friction factor (f_F) for laminar flow, $f_F = 16/Re$, where Re is the Reynolds number. Figure 4.3 shows the two positions considered in each energy balance at the inlet (p_1 and p_2) and outlet (p'_1 and p'_2). After solving Equation 4.39 assuming laminar flow at the inlet and outlet, the Reynolds number was recalculated and a value of around 4.5 was obtained for inlet and outlet, which satisfied the previous assumption (*i.e.*, $Re < 2000$).

$$N_i = -\frac{p}{RT}\alpha_i^{-1}\nabla y_i - \frac{y_i}{RT}\left(\alpha_i^{-1}\left(1 + \frac{D_{Kn,j}^{eff}}{D_{i,j}^{eff}}\right) + \frac{Kp}{\mu}\right)\nabla p$$

$$\alpha_i = \frac{1}{D_{Kn,i}^{eff}} + \frac{y_j}{D_{i,j}^{eff}}\left(1 + \frac{y_i}{y_j}\left(\frac{M_i}{M_j}\right)^{0.5}\right), \quad i, j = [H_2, v/v, H_2] \tag{4.35}$$

$$D_{i,j}^{eff} = \frac{\varepsilon}{\tau}1.858 \times 10^{-7} T^{3/2} \frac{[(M_i + M_j)/M_i M_j]^{0.5}}{p\sigma_{ij}^2 \Omega_D} \tag{4.36}$$

$$D_{Kn,i}^{eff} = \frac{\varepsilon}{\tau}\frac{1}{3}d_p\left(\frac{8RT}{\pi M_i}\right)^{0.5} \tag{4.37}$$

$$K = \frac{\varepsilon}{\tau}\frac{d_p^2}{32} \tag{4.38}$$

$$G^2 = \frac{M}{RT}\frac{d}{4f_F L}(p_1^2 - p_2^2), \quad Re = \frac{\rho v_m d}{\mu} \tag{4.39}$$

In the above equations, K is the permeability, μ is the gas dynamic viscosity, M_i is the molecular weight of species i, σ_{ij} is the characteristic binary Lennard-Jones length, Ω_D is the diffusion collision integral, and d_p is the mean pore size. The parameters σ_{ij} and Ω_D are given by Equations 4.40 and 4.41, where σ_i and ϵ_i are the characteristic Lennard-Jones length and energy, ϵ_{ij} is the characteristic binary Lennard-Jones energy, and k_B is the Boltzmann constant. In Equation 4.39, M is the molecular weight of the gas, d is the pipe diameter, L is the pipe length, p_1 and p_2 are the pressure and the initial and final point, ρ is the gas density, and v_m is the mean velocity of the fluid.

$$\sigma_{ij} = \frac{(\sigma_i + \sigma_j)}{2} \tag{4.40}$$

$$\Omega_{\mathrm{D}} = \frac{1.06036}{(T^*)^{0.15610}} + \frac{0.19300}{\exp(0.47635T^*)} + \frac{1.03587}{\exp(1.52996T^*)} + \frac{1.76474}{\exp(3.89411T^*)} \quad (4.41)$$

where,

$$T^* = k_{\mathrm{B}}T/\epsilon_{\mathrm{ij}}, \quad \epsilon_{\mathrm{ij}} = (\epsilon_{\mathrm{i}}\epsilon_{\mathrm{j}})^{1/2} \quad (4.42)$$

4.3.3   Cell potential

The operating cell potential, E_{cell}, was estimated considering the open circuit potential (E_{OCP}), ohmic overpotential (η_{ohm}) and electrode overpotentials for the cathode and the anode ((η_{ca}) and (η_{an})) (Xu et al., 2014) as shown in Equation 4.43. Given an applied current density (j) for a galvanostatic operation, the overpotentials are added to the E_{OCP} for charge and are subtracted for discharge. The approach used for estimating the open circuit potential and the different overpotentials is presented in the following sections.

$$E_{\mathrm{cell}} = E_{\mathrm{OCP}} \pm \eta_{\mathrm{ohm}} \pm |\eta_{\mathrm{ca}}| \pm |\eta_{\mathrm{an}}| \quad (4.43)$$

Open circuit potential

The derivation of a "complete" Nernst equation to calculate the open circuit potential of the RHVFC is necessary to correctly estimate the cell potential and overpotentials. In this work, "complete" refers to an equation that includes the effect of the potential across the membrane in the OCP calculation. The derivation of such an equation is done to avoid any mistakes when writing the Nernst equation directly from the electrode redox reactions and adding the potential jump across the membrane. For VRFBs, there is lack of consensus about which is a correct version of the complete Nernst equation as was discussed in Section 5.1. The most used version of the complete Nernst equation for VRFBs has been said to not follow thermodynamic principles (Pavelka et al., 2015), however, it continues to be the most used version in the literature. The open circuit potential derivation for an RHVFC presented here follows the traditional approach of considering the equilibrium of the phases in contact inside the battery (Gileadi, 1993; Newman and Thomas-Alyea, 2004; Pavelka et al., 2015). Figure 4.4 presents a diagram of the species present at each phase in the RHVFC. The measured OCP is the difference in the electrochemical potential of electrons in the two terminals of a battery (Gileadi, 1993; Pavelka et al., 2015). This potential difference can be expressed as the addition of the potential differences between the phases as shown in Equation 4.44. Each one of these potential differences contributing

to the total cell potential can be expressed in terms of the electrochemical potential of the species i present at each phase. This can be done by using the equality of electrochemical potential of species i in two phases in contact, which can be expressed as $\tilde{\mu}_i^A = \tilde{\mu}_i^B$ for phases A and B in contact.
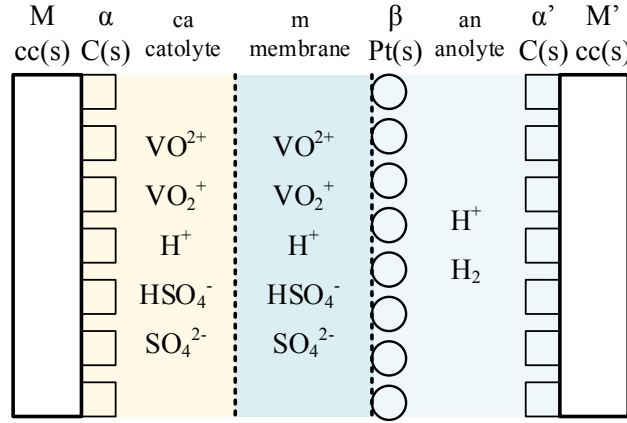
Figure 4.4: Diagram of species present in each phase of the RHVFC.

$$E_{\text{OCP}} = {}^M\Delta^\alpha\phi + {}^\alpha\Delta^{\text{ca}}\phi + {}^{\text{ca}}\Delta^m\phi + {}^m\Delta^\beta\phi + {}^\beta\Delta^{\text{an}}\phi + {}^{\text{an}}\Delta^{\alpha'}\phi + {}^{\alpha'}\Delta^{M'}\phi \tag{4.44}$$

The electrochemical potential of a species i ($\tilde{\mu}_i$) is given by Equation 4.45, which considers the chemical potential the species (μ_i) and the effect of potential (ϕ) on this charged species. The chemical potential of species i can be expressed in terms of the standard chemical potential (μ_i^Θ) and the activity of species i as shown in Equation 4.46. At equilibrium, each electrode reaction, which was presented in Equations 4.3 and 4.4, can be written in terms of the electrochemical potential of the species involved in the reaction as shown in Equations 4.47 and 4.48.

$$\tilde{\mu}_i = \mu_i + z_i F\phi \tag{4.45}$$

$$\mu_i = \mu_i^\Theta + RT\ln(a_i), \quad a_i = \gamma_i c_i \tag{4.46}$$

$$2\tilde{\mu}_{\text{VO}_2^+}^{\text{ca}} + 4\tilde{\mu}_{\text{H}^+}^{\text{ca}} + 2\tilde{\mu}_{\text{e}^-}^{\alpha} = 2\tilde{\mu}_{\text{VO}^{2+}}^{\text{ca}} + 2\tilde{\mu}_{\text{H}_2\text{O}}^{\text{ca}} \tag{4.47}$$

$$\tilde{\mu}_{\text{H}_2}^{\text{an}} = 2\tilde{\mu}_{\text{H}^+}^{\text{an}} + 2\tilde{\mu}_{\text{e}^-}^{\beta} \tag{4.48}$$

The potential difference of the battery, which is shown in Equation 4.49, was obtained by considering the equilibrium condition between the phases in contact and using Equation 4.45 to express the electrochemical potentials in the above equations. The superscripts M and M' represent the phase of the wires used to connect the voltmeter to the terminals of the battery, and in equilibrium with the current collectors. The difference of

potential of the electrolytes at the cathode and anode that is contained in Equation 4.49 was obtained by recognising that the cell is in steady-state condition (Pavelka et al., 2015). This condition leads to the equality of electrochemical potential of protons between both electrolytes as presented in Equation 4.50.

$$F(\phi^{\mathrm{M}} - \phi^{\mathrm{M'}}) = \mu_{\mathrm{VO}_2^+}^{\mathrm{ca}} + 2\mu_{\mathrm{H}^+}^{\mathrm{ca}} - \mu_{\mathrm{VO}^{2+}}^{\mathrm{ca}} - \mu_{\mathrm{H}_2\mathrm{O}}^{\mathrm{ca}} - \mu_{\mathrm{H}^+}^{\mathrm{an}} + \frac{1}{2}\mu_{\mathrm{H}_2}^{\mathrm{an}} + F(\phi^{\mathrm{ca}} - \phi^{\mathrm{an}}) \quad (4.49)$$

$$F(\phi^{\mathrm{ca}} - \phi^{\mathrm{an}}) = \mu_{\mathrm{H}^+}^{\mathrm{an}} - \mu_{\mathrm{H}^+}^{\mathrm{ca}} \quad (4.50)$$

An equivalent expression should be obtained by considering carefully the Donnan potential at the two electrolyte-membrane interfaces (Hamann et al., 2007; Kontturi et al., 2008). At equilibrium, the electrochemical potential of protons in the electrolyte and membrane must be the same. This was expressed for each interface as shown in Equation 4.51. Then, the potential across the entire membrane, namely the dialysis potential ($E_{\mathrm{Don}}^{\mathrm{m}}$), can be formed as shown in Equation 4.52. This potential across the entire membrane derived from thermodynamics differs from the relation presented by Knehr and Kumbur (2011) as has been stated by Pavelka et al. (2015).

$$\begin{aligned} -F(\phi^{\mathrm{m}} - \phi^{\mathrm{ca}}) &= \mu_{\mathrm{H}^+}^{\mathrm{m}} - \mu_{\mathrm{H}^+}^{\mathrm{ca}} \\ -F(\phi^{\mathrm{m}} - \phi^{\mathrm{an}}) &= \mu_{\mathrm{H}^+}^{\mathrm{m}} - \mu_{\mathrm{H}^+}^{\mathrm{an}} \end{aligned} \quad (4.51)$$

$$F E_{\mathrm{Don}}^{\mathrm{m}} = F(\phi^{\mathrm{ca}} - \phi^{\mathrm{an}}) = \mu_{\mathrm{H}^+}^{\mathrm{an}} - \mu_{\mathrm{H}^+}^{\mathrm{ca}} \quad (4.52)$$

To write the complete Nernst equation for the RHVFC as shown in Equation 4.53, Equation 4.52 was substituted in Equation 4.49 and the chemical potentials were expressed with respect to species activities by means of Equation 4.46. This equation assumes that the activity of water ($a_{\mathrm{H}_2\mathrm{O}}^{\mathrm{ca}}$) in the catholyte solution is equal to 1 and uses Henry's law for calculating hydrogen activity, which considers the activity of dissolved hydrogen equivalent to the change in the partial pressure of hydrogen (Kucernak and Zalitis, 2016b). The standard cell potential is defined by Equation 4.54 (Pavelka et al., 2015).

$$E_{\mathrm{OCP}} = E_{\mathrm{cell}}^{\Theta} + \frac{RT}{F}\ln\left(\frac{c_{\mathrm{VO}_2^+}^{\mathrm{ca}} c_{\mathrm{H}^+}^{\mathrm{ca}} (p_{\mathrm{H}_2}^{\mathrm{g}})^{0.5}}{c_{\mathrm{VO}^{2+}}^{\mathrm{ca}}} \times \frac{\gamma_{\mathrm{VO}_2^+}^{\mathrm{ca}} \gamma_{\mathrm{H}^+}^{\mathrm{ca}}}{\gamma_{\mathrm{VO}^{2+}}^{\mathrm{ca}}}\right) \quad (4.53)$$

$$E_{\mathrm{cell}}^{\Theta} = \frac{1}{F}\left(\mu_{\mathrm{VO}_2^+}^{\Theta,\mathrm{ca}} - \mu_{\mathrm{VO}^{2+}}^{\Theta,\mathrm{ca}} - \mu_{\mathrm{H}_2\mathrm{O}}^{\Theta,\mathrm{ca}}\right) = 0.99V \quad (4.54)$$

To further simplify Equation 4.53, and considering the difficulty in obtaining data of

activity coefficients, a global factor was considered ($F_\gamma = \gamma^{\text{ca}}_{\text{VO}_2^+} \gamma^{\text{ca}}_{\text{H+}} / \gamma^{\text{ca}}_{\text{VO}^{2+}}$). This factor can be obtained empirically by fitting Equation 4.53 to OCP data. An equivalent expression for the complete Nernst equation should be derived if the Nernst equation is considered in conjunction with the potential jump (Donnan potential) that appears at the two membrane-electrolyte interfaces due to the difference in concentration of protons (Pavelka et al., 2015). Figure 4.5a shows a comparison of the propose complete Nernst equation (CNE) and a Nernst equation (NE), which does not include the Donnan potential. The Nernst equation is shown in Equation 4.55. These equations were evaluated considering unity activity coefficients, a vanadium concentration of 0.75 M, and two initial concentrations of protons of 6.4 M and 4.4 M. It is clear that including the Donnan potential produces a lower OCP, which is related to the equilibrium state of the cell. This can be examined for a simple case of a membrane with different concentration of protons at each side. At equilibrium, the net transport of protons across the membrane must be zero. Since the concentration of protons at both sides of the membrane is different, being higher at the cathode, a negative concentration gradient is established if the cathode is considered to be at the left-hand side of the membrane. Therefore an opposite potential gradient must exist that can balance the transport due to diffusion, which will decrease the OCP. This concentration and ionic potential behaviour was observed by Yang et al. (2015b) for OCP conditions in an all-vanadium system at a 50% SOC. It is worth noticing that the values of OCP for the RHVFC calculated with the Nernst equation (solid line in Figure 4.5a) are expected to be lower than the OCP measured experimentally for the cell. Such a behaviour has been observed in the all-vanadium system and is usually attributed to the assumption of unity activity of species coefficients or the lack of the concentrations of protons in the OCP equation (Knehr and Kumbur, 2011). A lower acid concentration, and therefore a lower concentration of protons at the cathode produces a lower OCP. This effect is more important in the Nernst equation than in the complete Nernst equation since the concentration of protons in the cathode is considered to be to the power of two in the Nernst equation. In such a case, a bigger correction to fit the data would be needed, which is represented by the factor F_γ. This is discussed in the following section where Equation 4.53 is fitted to experimental data.

$$E^{\text{NE}}_{\text{OCP}} = E^{\circ}_{\text{cell}} + \frac{RT}{F} \ln \left(\frac{c^{\text{ca}}_{\text{VO}_2^+} (c^{\text{ca}}_{\text{H+}})^2 (p^{\text{g}}_{\text{H}_2})^{0.5}}{c^{\text{ca}}_{\text{VO}^{2+}} c^{\text{an}}_{\text{H+}}} \right) \tag{4.55}$$

In order to understand the Donnan potential effect, Figure 4.5b is used to explain the equilibrium state between the electrolyte solutions internal and external to the membrane. Figure 4.5b shows a physical representation of the ionic potential at a membrane/electrolyte interface for a cation-exchange membrane when co-ions and counter

(a)

(b)
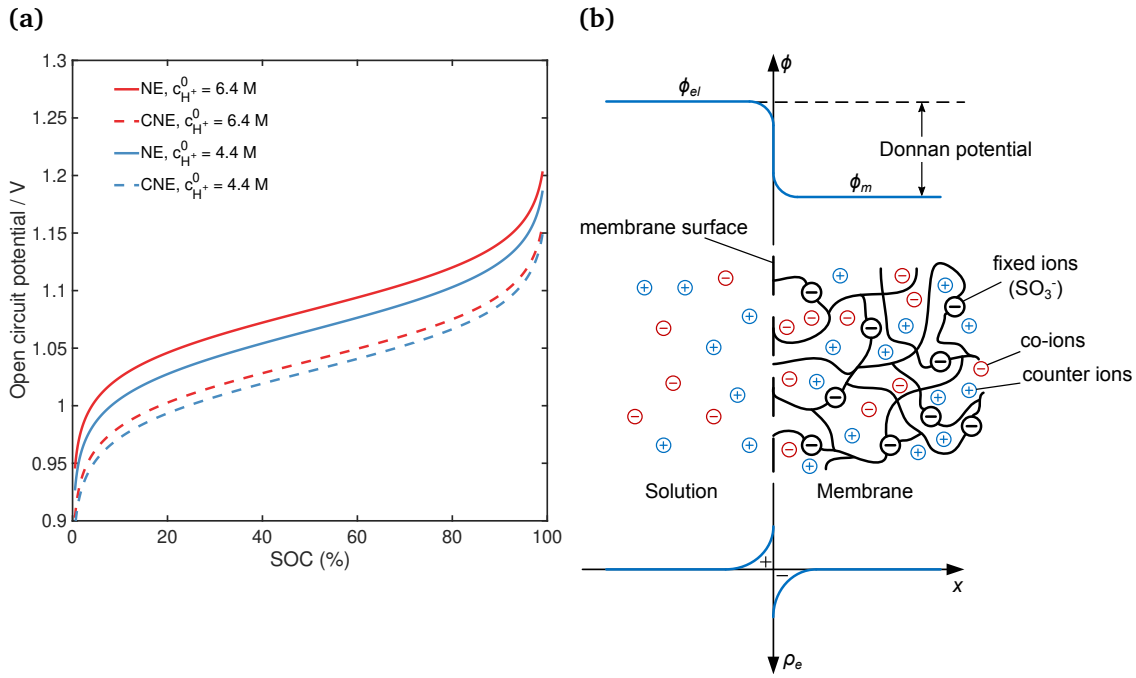
Figure 4.5: (a) Comparison of Nernst equation and the Complete Nernst equation for unity activity coefficients at vanadium concentration of 0.75 M. (b) Donnan potential at the surface of a cation exchange membrane.

ions are considered. The difference between the ionic potential in the membrane phase and in the external phase is called the Donnan potential ($E_{\mathrm{Don}}^{\mathrm{m/el}} = \phi^{\mathrm{m}} - \phi^{\mathrm{el}}$) (Hamann et al., 2007; Kontturi et al., 2008; Yang et al., 2015b). This Donnan potential is expected to fulfil the relation, $z_{\mathrm{f}}E_{\mathrm{Don}}^{\mathrm{m/el}} \geq 0$, according to Kontturi et al. (2008). That is, the Donnan potential is positive if the fixed groups in the membrane are positively charged, and negative otherwise. In Figure 4.5b, the membrane is negatively charged due to the fixed ions ($\mathrm{SO_3^-}$) and then the ionic potential in the membrane is expected to be lower than the ionic potential in the solution. The diffusion of ions gives rise to space charge layers at each side of the membrane surface, with a slight excess of negative charge near the membrane surface (right-hand side) and a slight excess of positive charge on the left hand side (Hamann et al., 2007). When the ion-exchange membrane separates solutions of different ionic activity, an interface equilibrium is established at each electrolyte/membrane interface, as shown in Equation 4.51 for the RHVFC.

Cathode overpotential

The electrode overpotential at the cathode is commonly modelled by a kinetic equation such as the Butler-Volmer equation (Newman and Thomas-Alyea, 2004; Zheng et al., 2014a), which neglects the effect of the concentration of protons in the cathode (Gandomi et al., 2016; Knehr et al., 2012a; Shah et al., 2008; You et al., 2009a). This simplification has been probably taken from PEM fuel cell models, where the concentration of proton is normally excluded from the kinetic equation. In PEM fuel cells, if electro-neutrality as-

sumed to be maintained in the polymer electrolyte membrane, then the concentration of protons will be around 1 M, and constant if an average fixed charge concentration is considered, *i.e.*, 1-1.2 M. It is expected then that the concentration of protons will only have a minor effect on the kinetics of a PEM fuel cells. This is not necessarily the same for the redox reaction at the cathode of an RHVFC, where the concentration of protons is approximately 5 times higher than the concentration of vanadium species and does not remain constant. Protons participate in the redox reaction and the dissociation of bi-sulphate at the cathode. In this work, the derivation of a more complete Butler-Volmer equation for the redox reaction between VO^{2+} and VO_2^+ is developed for the first time by considering the net rate of reaction and the equilibrium state, and following the general procedure presented by Newman and Thomas-Alyea (2004).

In the following analysis the activity of water is assumed to be constant and equal to 1. Unity activity coefficients for the ionic species are assumed, and therefore the derivation is written in terms of concentrations. This assumption responds to the difficulty in estimating individual activity coefficients. Equation 4.3 is rewritten as shown in Equation 4.56, from which the stoichiometric parameters (s_i, q_i and p_i) for each species are obtained and the number of electrons transferred (n) is 1. These values are presented in Table 4.1, and are used to express the rate of reaction (r) as shown in Equation 4.57. Where j^{BV} is the transfer current density, namely current per unit of surface of pore walls, k_a and k_c are the rate constants for the anodic and cathodic reaction, α_a and α_c are the transfer coefficient for the anodic and cathodic reaction. The transfer coefficients must add up to 1, *i.e.*, $\alpha_a + \alpha_c = 1$. The term c_i^s represents the surface concentration of species i at the pore walls, and E is the potential defined as the difference between the electrostatic potential of the electrode and the electrolyte, *i.e.*, $E = \phi_s - \phi_e$.

$$\text{VO}_2^+ + 2\text{H}^+ + e^- \underset{\text{anodic}}{\overset{\text{cathodic}}{\rightleftharpoons}} \text{VO}^{2+} + \text{H}_2\text{O} \tag{4.56}$$
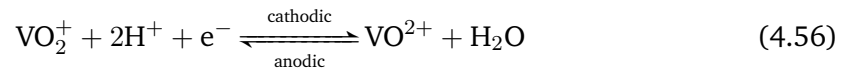
Table 4.1: Stoichiometric parameters of species in redox reaction at the cathode.

Species	q_i	p_i	s_i
VO^{2+}	0	1	1
VO_2^+	1	0	-1
H^+	2	0	-2

$$r = \frac{j^{BV}}{1F} = k_a \exp\left(\frac{\alpha_a 1F}{RT}E\right)(c_{VO^{2+}}^s)^1 - k_c \exp\left(\frac{-\alpha_c 1F}{RT}E\right)(c_{VO_2^+}^s)^1(c_{H^+}^s)^2 \tag{4.57}$$

At equilibrium, the potential takes a value of E_{eq} at which the net rate of reaction is zero, *i.e.*, the rate of the cathodic reaction equals the rate of the anodic reaction, and the concentrations of species are the same in the pore walls and further away. Thus, the bulk concentration of species i (c_i) and the surface concentration of species i (c_i^s) are equal. Considering the equilibrium state, Equation 4.57 can be rewritten as Equation 4.58 where the exchange current density ($j_{0,ca}^{BV}$), current per unit of surface area of pore walls, can be defined. This equation reveals that the equilibrium potential can be written as shown in Equation 4.59, which is a form of the Nernst equation for the redox reaction at the cathode. Using Equation 4.59 to eliminate the equilibrium potential in Equation 4.58 gives an explicit dependence of the exchange current density on the reactant and product concentrations as shown in Equation 4.60. Where the reaction rate constant is defined as $k_{ca} = k_a^{\alpha_c} k_c^{\alpha_a}$. The dependency of the reaction rate constant with temperature can be expressed by an Arrhenius approach, as shown in Equation 4.61, where $k_{ca,ref}$ is the reference rate constant, T_{ref} is the reference temperature and $E_{ca,T_{ref}}^{\Theta}$ is the standard potential of the reaction at the reference temperature.

$$\frac{j_{0,ca}^{BV}}{F} = k_a \exp\left(\frac{\alpha_a F}{RT} E_{eq}\right)(c_{VO^{2+}}) = k_c \exp\left(\frac{-\alpha_c 1 F}{RT} E_{eq}\right)(c_{VO_2^+})(c_{H^+})^2 \tag{4.58}$$

$$E_{eq} = \frac{RT}{F} \ln\left(\frac{k_c}{k_a}\right) + \frac{RT}{F} \ln\left(\frac{c_{VO_2^+} c_{H^+}^2}{c_{VO^{2+}}}\right) \tag{4.59}$$

$$j_{0,ca}^{BV} = k_a^{\alpha_c} k_c^{\alpha_a} c_{VO^{2+}}^{\alpha_c} c_{VO_2^+}^{\alpha_a} c_{H^+}^{2\alpha_c} \tag{4.60}$$

$$k_{ca} = k_{ca,ref} \exp\left(-\frac{F E_{ca,T_{ref}}^{\Theta}}{R}\left[\frac{1}{T_{ref}} - \frac{1}{T}\right]\right) \tag{4.61}$$

By defining the cathode overpotential as $\eta_{ca} = E - E_{eq}$ and using the definition of equilibrium potential given in Equation 4.59, Equation 4.57 can be modified to write the Butler-Volmer equation as shown in Equation 4.62. This kinetic equation includes all ionic species involved in the redox reaction (Bard and Faulkner, 2001; Newman and Thomas-Alyea, 2004) and the mass transfer effects by considering bulk and surface concentrations. The applied current density to the cell can be obtained according to $j = S_{ca} V_{ca} j^{BV}/A_{ca}$, where V_{ca} and A_A are the volume and cross-sectional area of the electrode, and S_{ca} is the specific surface area of the cathode, *i.e.*, surface area of pore walls per unit volume of total electrode.

$$j^{\text{BV}} = F j_{0,\text{ca}}^{\text{BV}} \left[\left(\frac{c_{\text{VO}_2^+}^{\text{s}}}{c_{\text{VO}_2^+}} \right) \left(\frac{c_{\text{H}^+}^{\text{s}}}{c_{\text{H}^+}} \right)^2 \exp \left(\frac{-\alpha_{\text{c}} F \eta_{\text{ca}}}{RT} \right) - \left(\frac{c_{\text{VO}^{2+}}^{\text{s}}}{c_{\text{VO}^{2+}}} \right) \exp \left(\frac{\alpha_{\text{a}} F \eta_{\text{ca}}}{RT} \right) \right] \quad (4.62)$$

In order to evaluate the surface concentrations, the rate of electrode reaction, *i.e.*, the flux of species due to consumption/production according to the Butler-Volmer equation, was assumed to match the rate at which electro-active species are brought to the surface by mass transfer (Bard and Faulkner, 2001). Figure 4.6 shows a schematic of the pore-scale used to represent the transport of species from the bulk to the electrode surface and vice-versa. For the sake of simplicity, a steady-state linear profile of concentration was used to describe the rate of mass transfer of species as shown in Equations 4.63, 4.64 and 4.65. The concentration gradients are evaluated along a Nernst diffusion layer (δ_0) (Bard and Faulkner, 2001; Gandomi et al., 2016; Knehr et al., 2012b; Shah et al., 2008), which is considered as the distance between the bulk and the surface of the electrode as shown in Figure 4.6. When high current densities are applied, the effect of mass transfer limitations in the kinetic equation becomes more important as the concentration gradient between the bulk and electrode surface increases and a limiting current density is reached. At this current density electro-active species are not brought to the surface of the electrode fast enough to match the redox reaction.
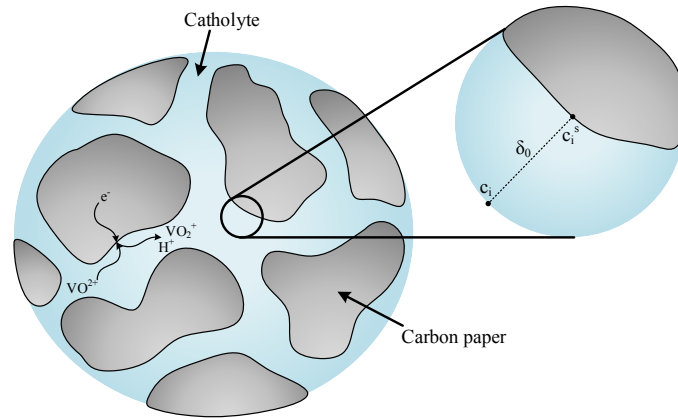
Figure 4.6: Diagram of pore transport in positive electrode.

$$-\frac{D_{\text{VO}^{2+}}}{\delta_0} (c_{\text{VO}^{2+}} - c_{\text{VO}^{2+}}^{\text{s}}) = \frac{j^{\text{BV}}}{F} \quad (4.63)$$

$$\frac{D_{\text{VO}_2^+}}{\delta_0} (c_{\text{VO}_2^+} - c_{\text{VO}_2^+}^{\text{s}}) = \frac{j^{\text{BV}}}{F} \quad (4.64)$$

$$\frac{D_{\text{H}^+}}{\delta_0} (c_{\text{H}^+} - c_{\text{H}^+}^{\text{s}}) = 2 \left(\frac{j^{\text{BV}}}{F} \right) \quad (4.65)$$

Figure 4.7 shows the behaviour of Butler-Volmer equation obtained by solving the system of 4 equations, including Equations 4.62, 4.63, 4.64, and 4.65, for a typical value of reaction rate constant of $3 \times 10^{-9} \, \mathrm{m \, s^{-1}}$. The cathode rate of reaction, namely the exchange current density, depends on the cathode overpotential (η_{ca}) and electrolyte SOC. For negative transfer current densities, as the SOC increases a mass transport limited region, where the overpotential increases steeply, is reached. Similar behaviour is observed for the opposite case with positive transfer current density. It is clear from Equation 4.62 that a change in the concentration of protons affects the kinetic behaviour of the redox reaction at the cathode. Figure 4.8 shows a comparison of the expected transfer current density (j^{BV}) as a function of the overpotential for a SOC of 1%, 50% and 99% when the concentration of protons is either considered or not, in the Butler–Volmer equation. A Butler-Volmer equation not including the effect of the concentration of protons can be obtained by setting equal to 1 all concentrations of protons in Equation 4.62. These curves should be compared qualitatively since the same values of parameters such as rate constants and transfer coefficients were used. When considering the effect of the concentration of protons, the rate of reaction is more sensitive to a change in overpotential for the same SOC, reaching a mass transport limiting region faster.

(a)

(b)
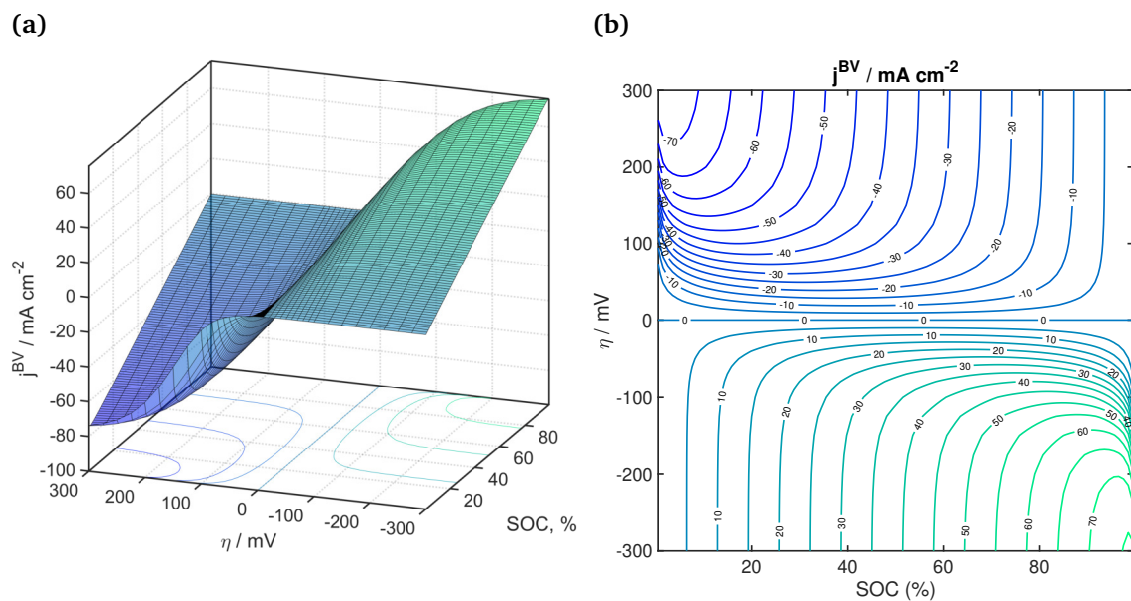
Figure 4.7: Cathode kinetics given by Buter-Volmer equation considering all ionic species involved in the redox reaction.

Anode overpotential

The overpotential for the anode (η_{an}) is approximated by a Tafel-Volmer (TV) approach, which describes the hydrogen evolution/oxidation reaction (HER/HOR). A Tafel-Volmer approach is used because it has been reported that the HER/HOR is not successfully repre-
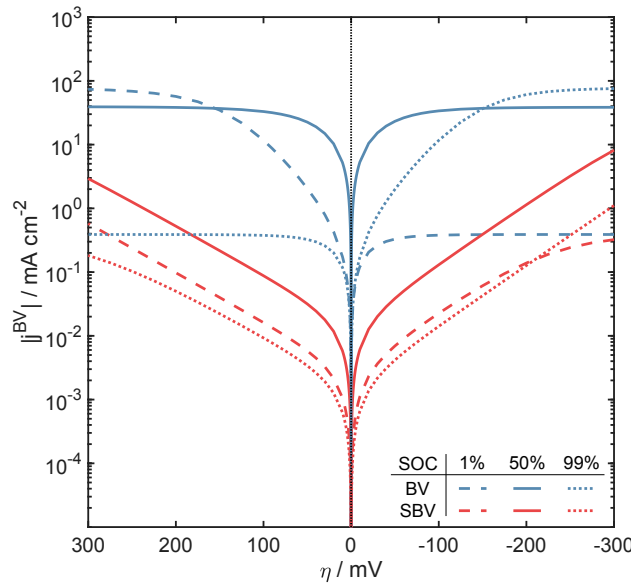
Figure 4.8: Comparison of Butler-Volmer equation including and neglecting concentration of protons effect. BV refers to Equation 4.62 and SBV version of the equation which does not includes the effect of the concentration of protons.

sented by a Butler-Volmer relation (Kucernak and Zalitis, 2016b). In the literature, kinetic models considering two pathways with three elementary steps, including a Tafel, Heyrovsky and Volmer step, are well established to consider in the overall rate expression. In this work, the kinetic expression proposed by Kucernak and Zalitis (2016b) is used to calculate the overpotential associated with the anode. The Tafel-Volmer elementary steps include adsorption/desorption of reactant and product, and the electron transfer reaction (Kucernak and Zalitis, 2016b) as shown in Equations 4.66 and 4.67. Where S is the surface adsorption site, $H_{2,surf}$ is the hydrogen molecule adjacent to the surface, k_{ad} and k_{des} are the adsorption and desorption rate constants of the Tafel reaction, and k_V and k_{-V} are the forward and backward rate constants of the Volmer reaction.

$$H_{2,surf} + 2S \underset{k_{des}}{\overset{k_{ad}}{\rightleftharpoons}} 2S - H_{ad} \tag{4.66}$$

$$S - H_{ad} \underset{k_{-V}}{\overset{k_V}{\rightleftharpoons}} S + H^+ - e^- \tag{4.67}$$
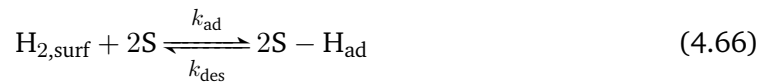
The TV kinetic model that has been introduced by Kucernak and Zalitis (2016b) is summarised in Equations 4.68 to 4.71. These equations describe the current density-overpotential relationship as being independent of pH, and only dependent on the hydrogen partial pressure and the kinetic rate constants under near mass-transport free conditions. The coverage of hydrogen on the electrode surface ($\theta_{H_{ad}}^{TV}$) is also a function of the hydrogen pressure and the overpotential as shown in Equation 4.69. Crossover of vanadium species is expected to reduce the electro-active area in the anode by means of ph-

ysisorption on the Pt catalyst competing with hydrogen adsorption, which could affect the current density of the cell. The loss in electro-active area could be included in the model by modifying the coverage of hydrogen on the electrode surface ($\theta_{H_{ad}}^{TV}$) and/or the roughness factor of the anode (R_{an}); however, such an effect is not considered in the present model. The effect of temperature was considered in Equation 4.71, which assumes that the reaction is controlled by a single activation energy (E_a) (Kucernak and Zalitis, 2016b). The parameters of the TV model reported at standard ambient temperature and pressure (SATP, $\varnothing$) conditions, namely a temperature of 298.15 K and an absolute pressure of 1 bar. The current density at standard conditions ($j^{TV,\varnothing}$) is obtained using Equations 4.68 to 4.70 and the applied current density can be obtained according to $j = R_{an}j^{TV}$, where R_{an} is the roughness factor of the CL and j^{TV} is the current density at operating conditions, *i.e.*, current per unit of electrochemically active area.

$$\frac{j^{TV}}{k_{des}} = FZ\big(\theta_{H_{ad}}^{TV}e^{\beta f\eta_{an}} - B\big(1 - \theta_{H_{ad}}^{TV}\big)e^{-(1-\beta)f\eta_{an}}\big) \tag{4.68}$$

$$\begin{aligned}\theta_{H_{ad}}^{TV} =& \big[4B^2 + Z\big(e^{\beta f\eta_{an}} + Be^{-(1-\beta)f\eta_{an}}\big) - \big[16B^2 + \big(Z(e^{\beta f\eta_{an}} + Be^{-(1-\beta)f\eta_{an}})\big)^2 \\ &+ 8BZ\big(Be^{\beta f\eta_{an}} + e^{-(1-\beta)f\eta_{an}}\big)\big]^{0.5}\big]/\big[4\big(B^2 - 1\big)\big]\end{aligned} \tag{4.69}$$

where,

$$B = \left(\frac{a_{H_2}k_{ad}}{k_{des}}\right)^{0.5}, \quad Z = \frac{k_V^{eq}}{k_{des}}, \quad f = \frac{F}{RT} \tag{4.70}$$

$$j^{TV} = (1 - s_{CL})j^{TV,\varnothing}\exp\left(-\frac{E_{an}}{R}\left(\frac{1}{T} - \frac{1}{298.15}\right)\right) \tag{4.71}$$

In the above equations, β is the transfer coefficient of the hydrogen redox reaction (Equation 4.4) and a_{H_2} is the activity of dissolved hydrogen and equivalent to the change in partial pressure of hydrogen (Kucernak and Zalitis, 2016b) according to $a_{H_2} = a_{H_2}^{\varnothing}(p_{H_2}/p_{H_2}^{\varnothing})$, where $a_{H_2}^{\varnothing}$ and $p_{H_2}^{\varnothing}$ are the standard state activity of hydrogen in solution and in the gas phase ($a_{H_2}^{\varnothing} = 1, p_{H_2}^{\varnothing} = 1$ bar).

Ohmic overpotential

The ohmic overpotential is calculated by adding the contribution of the different domains: current collectors (cc), catholyte (ca-el), cathode (ca), membrane (m), CL, polymer electrolyte in the CL (CL-m) and GDL. The ohmic overpotential contribution of each domain is described by means of Ohm's law (Shah et al., 2011b; Yu and Chen, 2014a) as shown

in Equations 4.72 and 4.73. Where l_k and σ_k are the thickness and conductivity of the domain k, and the superscript 'eff' denotes an effective property.

$$\eta_{ohm}^{cc} = j\frac{l_{cc}}{\sigma_{cc}}, \quad \eta_{ohm}^{m} = j\frac{l_m}{\sigma_m}, \quad \eta_{ohm}^{C} = jR_C \tag{4.72}$$

$$\eta_{ohm}^{k} = j\frac{l_k}{\sigma_k^{eff}}, \quad k = [\text{ca-el, ca, CL, CL-m, GDL}] \tag{4.73}$$

The Nafion membrane conductivity is described as a function of the water content (λ) and temperature through an empirical relation (Springer et al., 1991; Yu and Chen, 2014a), which is presented in Equation 4.74.

$$\sigma_m = (0.5139\lambda - 0.326)\exp\left(1268\left[\frac{1}{303} - \frac{1}{T}\right]\right) \tag{4.74}$$

The effect of the membrane uptake of sulphuric acid and vanadyl on membrane conductivity has been studied by Tang et al. (Tang et al., 2013b), who observed an enhancement or reduction of membrane conductivity depending on the acid and water content in the membrane. An increase in the concentration of protons due to acid presence in the membrane can enhance conductivity, while the mobility of protons significantly decreases with water loss (Tang et al., 2013b). When a Nafion membrane was equilibrated with an electrolyte solution of practical composition for VRFB operation, uptake of vanadyl and acid contributes to reduced membrane conductivity to some extent, and a complex equilibrium and partitioning competition between protons and vanadyl has been suggested (Tang et al., 2013b). Future studies should focus on the membrane-electrolyte equilibrium in the RHVFC to assess membrane conductivity, concentration and mobility of protons by means of a detailed transport model of water and ionic species through the membrane.

The electrolyte conductivity was estimated considering the concentration and charge of all ionic species in the electrolyte (Shah et al., 2008) as shown in Equation 4.75. A Bruggemann correction was applied to account for the porous electrode (Shah et al., 2008), allowing for the calculation of the effective conductivity of electrolytes and electrodes as shown in Equation 4.76. In these equations, z_i is the charge number of species i and $D_{i,el}$ is the diffusion coefficient of species i in the electrolyte.

$$\sigma_{ca-el} = \frac{F^2}{RT}\sum_i z_i^2 D_{i,el}c_i, \quad i = \left[VO^{2+}, VO_2^+, H^+, SO_4^{2-}, HSO_4^-\right] \tag{4.75}$$

$$\sigma_{ca-el}^{eff} = \varepsilon_{ca}^{3/2}\sigma_{ca-el}, \quad \sigma_{ca}^{eff} = (1 - \varepsilon_{ca})^{3/2}\sigma_{ca},$$
$$\sigma_{CL}^{eff} = (1 - \varepsilon_{CL} - \varepsilon_m)^{3/2}\sigma_{CL}, \quad \sigma_{CL-m}^{eff} = \varepsilon_m^{3/2}\sigma_{CL-m} \tag{4.76}$$

4.4 Model implementation

Before implementing the model a degree of freedom analysis was carried out to ensure that the model equations is a solvable set of equations, *i.e.*, the problem is well-defined. It may not be easy to evaluate this for a large or complicated steady-state or dynamic model (Seborg et al., 2011). In general, to have a finite, which is not necessarily unique, set of solutions the number of unknown variables (N_V) must equal the number of independent model equations (N_E), *i.e.*, all of the available degrees of freedom (N_F) must be utilised (Seborg et al., 2011). The number of degrees of freedom can be calculated as $N_F = N_V - N_E$. It is important to identify all the unknown quantities and specify which of them will be considered as known parameters (N_P). The result of the degree of freedom analysis is summarised in Table 4.2 and a detailed explanation of the analysis is given in Appendix B. The value of all the parameters (N_P) are given in Table 4.3 and 4.4. These parameter values were selected based on typical values used in reported models of VRFBs and PEMFCs. All model equations described in Section 4.3 were implemented and solved in MATLAB® by means of an Ordinary Differential Equation (ODE) solver, namely `ode15s` function, with absolute and relative tolerance set at 1×10^{-6}. The `ode15s` is a quasi-constant step size implementation of the numerical differentiation formulas (NFD's) in terms of backwards differences (Shampine and Reichelt, 1997).This function allows the stiff differential algebraic system of equations (DAEs) to be solved. The selection of the ODE solver from MATLAB was developed by first testing non-stiff ODE solvers, *e.g.*, `ode45`, which were not able to solve the problem. Later, stiff ODE solvers were tested such as `ode15s` and `ode23t`, recognising that `ode15s` was in general faster and robust to solve the set of equations. The events option of the ODE solver was used to incorporate the restriction associated with the water phase change given by Equation 4.34 (Golbert and Lewin, 2004). Figure 4.9 presents a flow diagram describing how the model was implemented for a single-cycle charge-discharge test, which in general consisted of four operating modes in series: (1) first OCP, (2) charge, (3) second OCP and (4) discharge. For the simulation of power curves and charge-discharge cycling, the implementation was analogous, but the operating modes were different. In the case of power curves only discharge and OCP steps were considered and for the case of cycling only charge and discharge steps. For the single-cycle charge-discharge presented in Figure 4.9, the experimental values used in the catholyte solution preparation including the total concentration of vanadium (c_V), concentration of sulphuric acid (c_{acid}) and catholyte solution volume (V_t, tank volume) were passed to a first process, which was usually a first OCP measurement, to calculate the initial concentration of species i ($c_i^1(t = 0)$). Also, the experimental data of applied current (I_{appl}, manipulated variable) of a single-cycle operating time was divided into four sets of data, which correspond to the different operating modes, by means of an initial process.

The results from these two processes along with experimental values of flow rates and the parameters and property values selected for the cell simulations were passed to a process that solved the ODE system of equations and gave back the evolution of the concentration of species i along the time of each operating mode. These results, along with the current set for each operating mode, were used in four processes that allow calculating the potential and overpotential required to then calculate the cell potential. The first process calculated the open circuit potential of the cell using the evolution of concentrations. The second process calculated the ohmic overpotential of the cell using the applied current. The third and fourth processes calculated the overpotential of the cathode and anode, respectively, using the evolution of concentration and the applied current. The OCP and the overpotentials were then used in a process that calculated the cell potential depending on the operating mode. Finally, the cell potential for each operating mode was reorganised to form a unique solution set (E_{calc}). The simulation of a potential curve of charge-discharge takes, in general, less than 5 minutes to run on an Intel Xeon E5-1620 v3,quad-core 3.5 GHz 64-bit workstation with 32 GB of RAM.

Table 4.2: Degrees of freedom analysis.

Number type	Value	Description
N_{P}	54	Electrochemical parameters, geometrical parameters, components properties, and physical constants
N_{V}	88	Concentrations, flow rates, source terms, and molar flux due to diffusive transport or phase change
N_{E}	81	Species conservation, transport parameters, thermodynamic and microstructural relations
N_{F}	7	Process is exactly specified by setting four manipulated variable: I_{appl}, Q_{V}, Q_{H_2} and p_{IN}, and choosing three fitting parameters: $k_{\text{ca,ref}}$, δ_0 and R_{C}

In this chapter the proposed model is used to simulate the cell potential of a $25\,\text{cm}^2$ area cell, whose experimental set-up is described in the following section. This is, however, only a preliminary testing of the model since the experimental set-up used here was not ideal, due to poor current collection, such that it was not possible to operate at practical current densities. Also, the experimental data were collected in different attempts of cell operation, and therefore at different cell conditions between measurements. A more detailed model application is presented later in Chapter 5.

Table 4.3: Electrochemical parameters for electrodes and constants.

Parameter	Value	Unit	Source
E_{ca}^0	0.99	V	Yufit et al. (2013)
E_{an}^0	0	V	Yufit et al. (2013)
k_{c}	100	s^{-1}	He et al. (2000)
k_{e}	100	$\mathrm{atm}^{-1}\,\mathrm{s}^{-1}$	He et al. (2000)
$\sigma_{\mathrm{H_2}}$	2.827	Å	Reid et al. (1977)
σ_{v}	2.641	Å	Reid et al. (1977)
$\epsilon_{\mathrm{H_2}}/k$	59.7	K	Reid et al. (1977)
ϵ_{v}/k	809.1	K	Reid et al. (1977)
α_{a}	0.55	–	Knehr et al. (2012b)
$Z^{\varnothing}$	0.42	–	Kucernak and Zalitis (2016b)
$B^{\varnothing}$	0.28	–	Kucernak and Zalitis (2016b)
$k_{\mathrm{des}}^{\varnothing}$	2.1×10^{-5}	$\mathrm{mol\,cm}^{-2}\,\mathrm{s}^{-1}$	Kucernak and Zalitis (2016b)
E_{a}	2.3×10^4	$\mathrm{kJ\,mol}^{-1}$	Kucernak and Zalitis (2016b)
β	0.52	–	Kucernak and Zalitis (2016b)
R	8.314	$\mathrm{J\,mol}^{-1}\,\mathrm{K}^{-1}$	–
F	96 485	$\mathrm{C\,mol}^{-1}$	–
M_{v}	0.018	$\mathrm{kg\,mol}^{-1}$	–
$M_{\mathrm{H_2}}$	0.0020	$\mathrm{kg\,mol}^{-1}$	–
P_{atm}	101 325	Pa	
T_{amb}	293	K	–

4.5 Experimental methods

Experimental data collection was performed following the procedures developed previously within our research group (Hewa Dewage, 2016) to operate a hybrid redox flow battery. A brief description of the equipment and data acquisition procedures used in this work are presented below, further detail can be found in the work developed by Hewa Dewage (2016).

4.5.1 Experimental set–up

The experimental set-up used for the acquisition of data is presented in Figure 4.10. An in-house manufactured cell having a cross-sectional area of $25\,\mathrm{cm}^2$ was used as a hydrogen-vanadium electrochemical reactor. A peristaltic pump was used to circulate a vanadium catholyte between the cell and a stirred catholyte tank, while hydrogen was

Table 4.4: Electrodes, membrane and current collector parameters.

Parameter	Value	Unit	Source
$h_{ca} = h_{an} = h_m = h_{cc}$	0.05	m	Dewage et al. (2016)
h_{ff}	0.082	m	Dewage et al. (2016)
h_{rib}	0.001	m	Dewage et al. (2016)
h_{ch}	0.001	m	Dewage et al. (2016)
$w_{ca} = w_{an} = w_m = w_{cc} = w_{ch}$	0.05	m	Dewage et al. (2016)
l_{ca}	0.0004	m	Dewage et al. (2016)
l_{an}	0.0002	m	Dewage et al. (2016)
l_m	1.83×10^{-4}	m	Fuel Cell Store (c)
l_{cc}	0.005	m	Dewage et al. (2016)
l_{ch}	0.001	m	Dewage et al. (2016)
ε_{ca}	0.88	–	Gandomi et al. (2016)
ε_{CL}	0.3	–	Wu et al. (2010)
ε_{GDL}	0.6	–	Wu et al. (2010)
ε_m	0.3	–	Wu et al. (2010)
σ_{ca}	482.4	$S\,m^{-1}$	Gandomi et al. (2016)
σ_{CL}	114	$S\,m^{-1}$	Wu et al. (2007)
σ_{GDL}	114	$S\,m^{-1}$	Wu et al. (2007)
σ_{cc}	1000	$S\,m^{-1}$	Knehr et al. (2012b)
r_p	50.3×10^{-6}	m	Knehr et al. (2012a)
d_f	17.6×10^{-6}	m	Gandomi et al. (2016)
d_p	1×10^{-5}	m	Estimated
S_{ca}	2.7×10^4	$m^2\,m^{-3}$	Carta et al. (1991)
R_{an}	200	$m^2\,m^{-2}$	Gasteiger et al. (2004)
$D_{VO^{2+}}$	3.9×10^{-10}	$m^2\,s^{-1}$	Gandomi et al. (2016)
$D_{VO_2^+}$	3.9×10^{-10}	$m^2\,s^{-1}$	Gandomi et al. (2016)
D_{H^+}	9.3×10^{-9}	$m^2\,s^{-1}$	Gandomi et al. (2016)
V_T	6×10^{-5}	m^3	Dewage et al. (2016)
ρ	1350	$kg\,m^{-3}$	Gandomi et al. (2016)
μ	0.005	$Pa\,s$	Gandomi et al. (2016)
ρ_m	2000	$kg\,m^{-3}$	Ge et al. (2005)
EW	1.1	$kg\,mol^{-1}$	Ge et al. (2005)
V_w	1.8×10^{-5}	$m^3\,mol^{-1}$	Ge et al. (2005)
c_f	1200	$mol\,m^{-3}$	Ge et al. (2005)
z_f	-1	–	–
K_{KC}	180	–	Gandomi et al. (2016)
K_f	1.1	–	–

passed through the anode side of the cell. A collector reservoir was connected to the
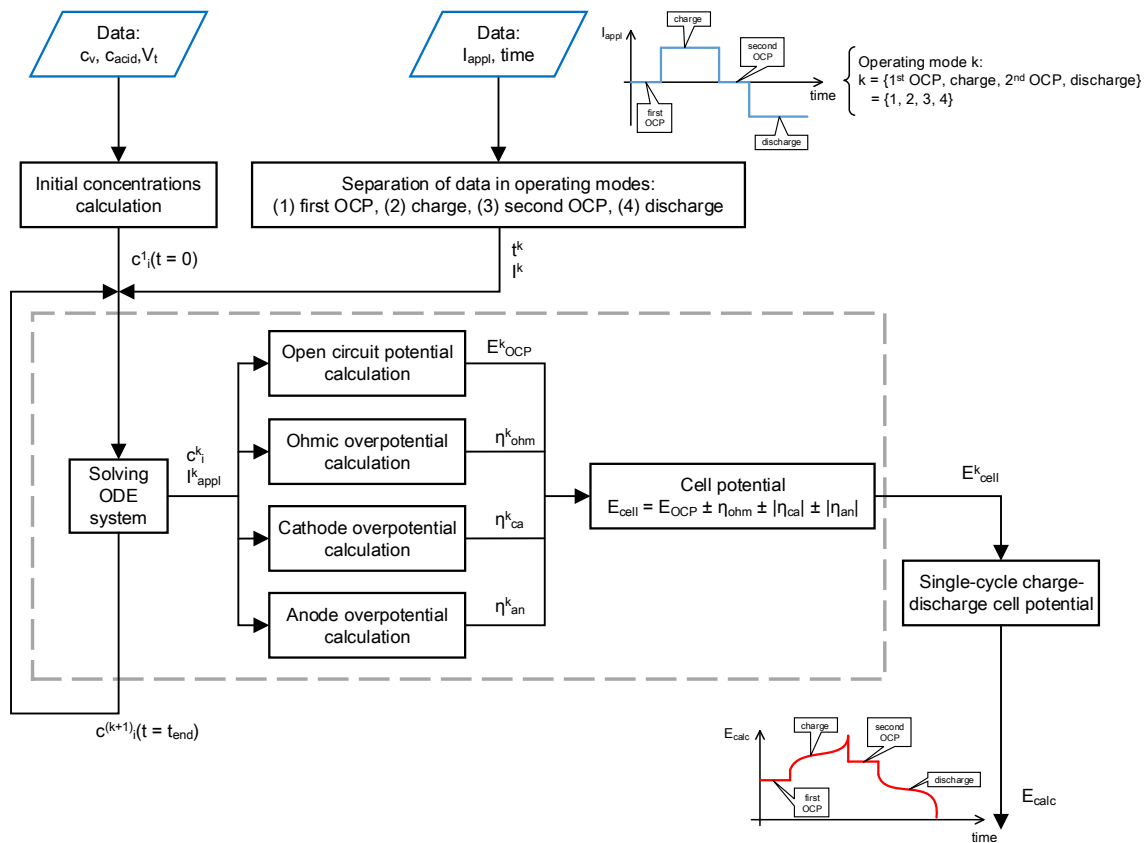
Figure 4.9: Model implementation flow diagram.

hydrogen outlet to collect any catholyte crossover.

The cell consisted of aluminium end plates, polypropylene insulating layers, graphite flow channel plates and the Membrane Electrode Assembly (MEA). The MEA contained a carbon electrode (SGL 10AA, $400\,\mu$m) and a platinised carbon paper electrode (Alfa Aesar Hydrogen Electrode, $200\,\mu$m, $0.5\,\mathrm{mg\,cm^{-2}}$ Pt loading), which were separated by a pre-hydrated Nafion 117 membrane. Multi-channel serpentine flow channel plates (SGL, BMA5 graphite plates) were used as current collectors and to distribute the vanadium electrolyte as well as the hydrogen gas. Figure 4.11 displays the cell assembly procedures of half-cell. The cell components were layered in sequence on top of an aluminium end plate, Figure 4.11(a) to Figure 4.11(e). Next the membrane was placed, Figure 4.11(f), and the inverse sequence was followed to complete the other half cell, Figure 4.11(e) to Figure 4.11(a). When all components were in place the cell was tightened up to $9\,\mathrm{N\,m}$. Figure 4.12 presents a diagram of the multi-channel serpentine flow plates with its characteristic dimensions, which are given in Table 4.4. Once the cell was fully assembled, it was placed at the centre of the experimental set-up, as shown in Figure 4.10. The hydrogen supply tubing was connected from the hydrogen valve, which was set at $1\,\mathrm{bar}$, to the hydrogen flow rate controllers which were connected to the hydrogen inlet on the anode side. The hydrogen outlet was connected to the collector reservoir and from there to the gas extraction hood. The catholyte supply tubing was connected from the stirred

catholyte tank to the vanadium inlet on the cathode side, passing through the peristaltic pump. The vanadium outlet was connected back to the catholyte tank. After all mechanical connections were made, a Bio-Logic potentiostat (VSP-300), running EC-Lab software, was connected to the cell. The working electrode was connected to the cathode side and the counter electrode, which was also used as a reference electrode, to the anode side.
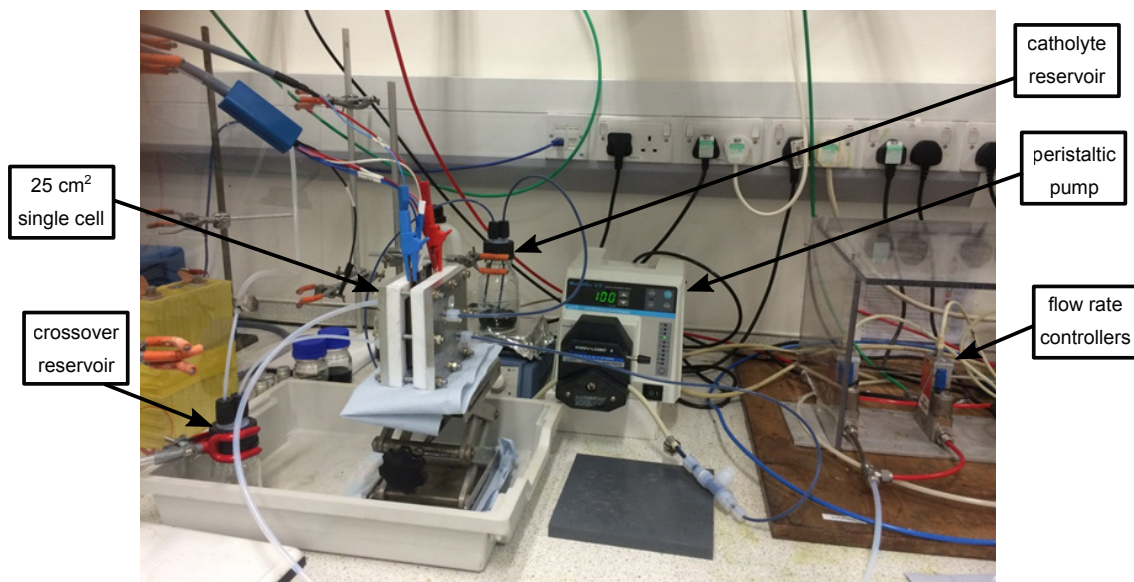
Figure 4.10: Experimental set-up of $25\,\mathrm{cm}^2$ area cell.
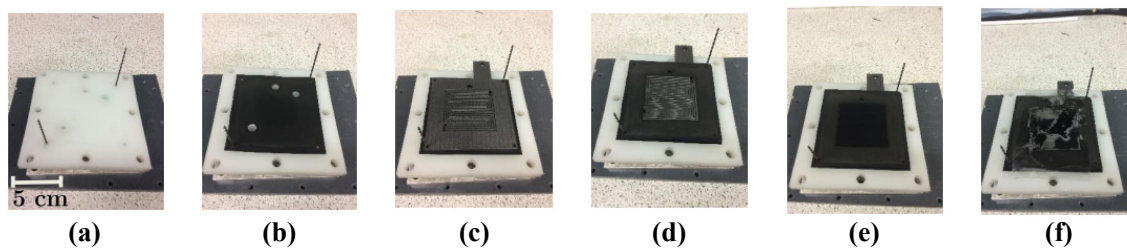
Figure 4.11: Cell assembly procedure (Hewa Dewage, 2016): (a) Aluminium end plate and polypropylene plate; (b) Full size gasket; (c) Graphite flow channel plate, (d) Partial gasket; (e) Carbon electrode; and (f) Nafion membrane.

The catholyte solution was prepared and placed in the catholyte tank by fully dissolving $14.1\,\mathrm{g}$ of vanadium sulphate hydrate (Sigma-Aldrich) in $60\,\mathrm{mL}$ of 5 M H_2SO_4 solution (Fluka Analytical). The initial vanadium concentrations in the catholyte was calculated to be around $1042\,\mathrm{mol\,m^{-3}}$ by considering the vanadium sulphate hydrate, $VOSO_4 \cdot xH_2O$, contained 3.5 molecules of water and therefore had a molecular weight (M) of $226\,\mathrm{g\,mol^{-1}}$. A correct estimation of the initial concentration of all ionic species in the catholyte is important to ensure the electro-neutrality condition is satisfied. To this end, the initial concentrations were calculated by taking into account the dissolution of vanadium sulphate hydrate and the dissociation of sulphuric acid. The sulphuric acid dissociation was assumed to reach chemical equilibrium as explained earlier in Sec-

(a)   **(b)**
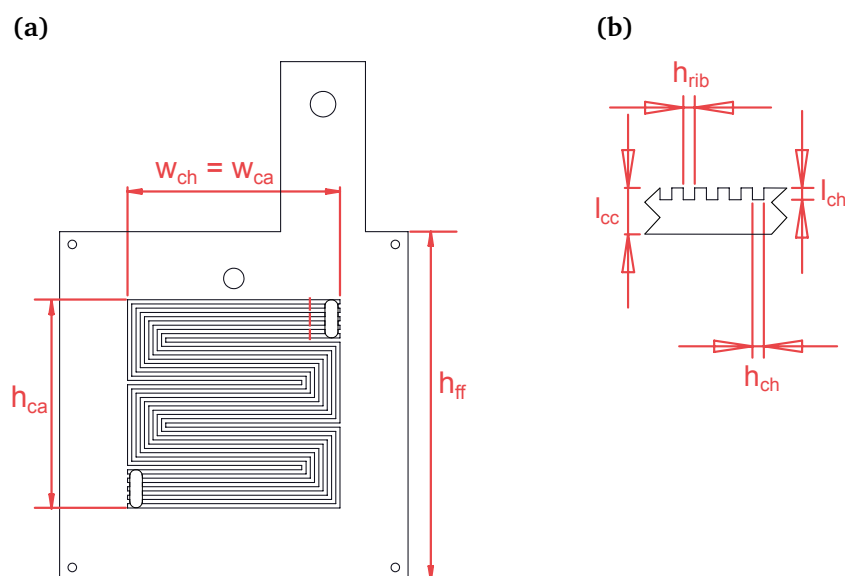
Figure 4.12: Multi-channel serpentine flow plate diagram for the $25\,\mathrm{cm}^2$ area RHVFC.

tion 4.3. The experimental data acquisition was performed at a constant current density and constant flow rate of catholyte and hydrogen. Several iterations of cell assembly and operation were carried out to obtain a leak-free cell and consistent experimental data.

4.5.2   Data acquisition

Experimental measurements of open circuit potential and single-cycle charge-discharge (ch-dch) potential were obtained using the experimental set-up previously described. OCP measurements were performed by operating the cell in a series of 10 steps of charge or discharge until an upper cut-off potential of $1.3\,\mathrm{V}$ or a lower cut-off potential of $0.4\,\mathrm{V}$ was reached, respectively. After assembly and conditioning of the cell, the OCP of the cell was initially monitored for $5\,\mathrm{min}$. Then after every charge or discharge step, the OCP was monitored for around $10\,\mathrm{min}$, allowing the cell to stabilise, *i.e.*, it returned to equilibrium. When the cut-off potential was reached, a final OCP was monitored for around $10\,\mathrm{min}$. Every charge or discharge step was designed to cover approximately one-tenth of the maximum experimental capacity (Q_{max}), which was theoretically estimated by Equation 2.29. Since the cell was operated in galvanostatic mode, the cell operating capacity (Q_{op}) over a period of operating time (t) can be obtained as $Q_{\mathrm{op}} = i \times t$, where i is the applied current. The state of charge (SOC) of the cell was calculated by comparing the operating capacity with the maximum experimental capacity, which was considered to be 100% SOC.

The single-cycle charge-discharge potential was measured in galvanostatic mode at different currents. After assembly and conditioning of the cell, the OCP was monitored for around $10\,\mathrm{min}$ prior charging operation. Then the cell was charged galvanostatically

until the cell potential reached the upper cut-off of $1.3\,\mathrm{V}$. After the charge, the OCP was monitored for around $10\,\mathrm{min}$, allowing the cell to return to equilibrium. Then the cell was discharged galvanostatically until the cell potential reached the lower cut-off potential of $0.4\,\mathrm{V}$. After discharge, the OCP was monitored again for around $10\,\mathrm{min}$.

Table 4.5 summarises the operating conditions of current density (j_{appl}), catholyte flow rate (Q_{V}), and hydrogen flow rate ($Q_{\mathrm{H_2}}$) used in the experimental tests in this chapter. Additionally, Table 4.5 includes a set of experimental tests taken from the work developed by Hewa Dewage (2016). This additional set of experiments included copper current collectors (Cu CC) between the polypropylene insulating plates and the graphite flow channel plates to improve current collection. The data sets presented in Table 4.5 were collected in several attempts of cell operation, and therefore, the cell was reassembled between measurements. Also, catholyte solutions were prepared several times to condition the cell before operation. The experimental data sets presented in this chapter are intended to be used in preliminary testing of the model. In the comparison of different cell operating condition, within these data sets, no strong conclusion should be drawn since these measurements were taken in an isolated manner and reassembling and reconditioning of the cell introduced experimental variance between data sets.

Table 4.5: Operating condition used for experimental tests.

Set	test[a]	$j_{\mathbf{appl}}/\ \mathrm{A\,m^{-2}}$	$Q_{\mathbf{V}}/\ 10^{-6}\,\mathrm{m^3\,s^{-1}}$	$Q_{\mathbf{H_2}}/\ 10^{-6}\,\mathrm{m^3\,s^{-1}}$	**Cu CC**
1	OCP	0	1.67	1.67	No
2	ch-dch	50	1.67	1.67	No
3	ch-dch	100	1.67	1.67	No
4	ch-dch	80	1.67	1.67	Yes
5	ch-dch	400	1.67	1.67	Yes
6	ch-dch	400	1.67	0.83	Yes
7	ch-dch	400	2.5	1.67	Yes
8	ch-dch	600	1.67	1.67	Yes

[a] Experimental test: OCP refers to open circuit potential test; and ch-dch refers to a test of a single charge-discharge cycle.

4.6 Model calibration

The model calibration was carried out in two stages. First, the complete Nernst equation was fitted to the experimental OCP data by means of Equation 4.53 so a relation was found between the factor (F_γ) and the SOC. Then, the model was calibrated by fitting the selected parameters to fit the cell potential measured during the operation of a single-cycle of charge-discharge. These fitting parameters, which are discussed in Subsection 4.6.2 are

considered for the results presented in this Chapter.

4.6.1 Open circuit potential

During OCP operation, the redox reaction and the acid dissociation cause a change in the concentration of all species in the catholyte. These effects are considered as shown in Equations 4.77 to 4.81, where the SOC is estimated depending on the capacity change of the cell for each charge or discharge step. The term c_V is the total concentration of vanadium and c_i^0 is the initial concentration of species i. The proton, bi-sulphate and sulphate concentrations were assumed to follow a complete first step of dissociation of sulphuric acid as shown in Equation 4.12, and the second step of dissociation as shown in Equation 4.13 according to a bi-sulphate dissociation constant (k_2) and an activity coefficient product (γ) as presented in Equation 4.14. For this purpose, the molar equilibrium dissociation quotient, $Q_M = k_2/\gamma$ presented in Figure 4.2 was used.

$$c_{VO^{2+}} = c_V \cdot (1 - SOC) \tag{4.77}$$

$$c_{VO_2^+} = c_V \cdot SOC \tag{4.78}$$

$$c_{H^+} = c_{H^+}^0 + c_V \cdot SOC + S_d^{eq} \tag{4.79}$$

$$c_{HSO_4^-} = c_{HSO_4^-}^0 - S_d^{eq} \tag{4.80}$$

$$c_{SO_4^{2-}} = c_{SO_4^{2-}}^0 + S_d^{eq} \tag{4.81}$$

Figure 4.13 shows the E_{OCP} estimated by Equation 4.53 compared to one data set of experimental OCP. This Figure includes three different estimations: (1) a the Nernst Equation (NE), with unity activity coefficients by means of Equation 4.55, (2) a Complete Nernst Equation (CNE) by means of Equation 4.53, with unity activity coefficients, and (3) a CNE considering non-ideal activity coefficients by means of a global factor (F_γ) that includes the activity coefficient effect.

In the case of VRFBs, the Nernst equation with unity activity coefficients underestimates the OCP data, and the Donnan potential across the membrane has been added in order to fit OCP data (Knehr and Kumbur, 2011). However, this potential difference should reduce the OCP when the catholyte concentration of protons is higher than the

(a)

(b)
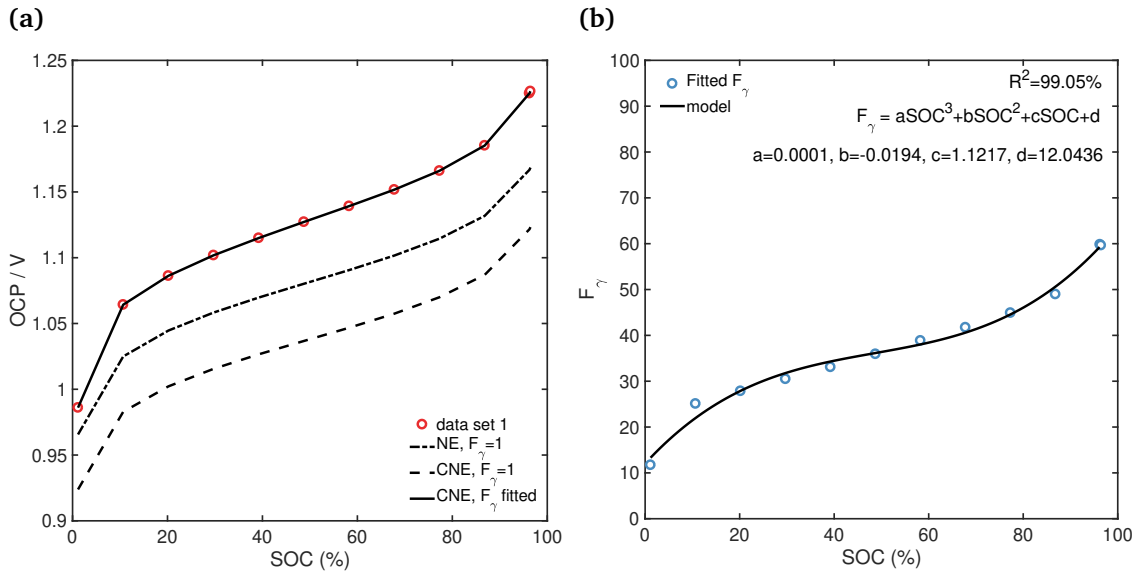
Figure 4.13: OCP at operating conditions presented in Table 4.5 for data set 1. (a) Shows a comparison of Nernst equation, and a complete Nernst equation (Equation 4.53) with unity activity coefficients and fitted values of a global factor (F_γ); and (b) Shows the fitted values of the global factor.

anolyte one because a steady-state condition must be maintained, *i.e.*, no net flux of protons across the membrane (Pavelka et al., 2015). This effect is observed in Figure 4.13a, where the complete Nernst equation with unity activity coefficients gives lower values of OCP in comparison to the Nernst equation estimation. The fitted values of F_γ are shown in Figure 4.13b along with an empirical model of its dependency with electrolyte SOC. This empirical model is later used when simulating the cell charge-discharge operation. The fitted values of this global factor vary from 10 to 60, which should be strongly related to the value of the activity of protons that have been reported to be of approximately 5 for a concentration of H_2SO_4 of $1\,\mathrm{mol\,kg^{-1}}$ and even higher for higher concentrations of H_2SO_4 (Knopf et al., 2003). The correct estimation of the OCP is key for the accuracy of model predictions and the estimation of overpotential contributions. OCP experimental measurements were performed four times considering two different fresh solutions. This analysis was repeated for each OCP experimental data set, which showed similar values for the fitted global factor.

4.6.2 Charge/Discharge cycles

The second step in the model calibration is to compare the model calculation against the experimental potential data of a single-cycle of charge-discharge. The fitting procedure was implemented in MATLAB® with absolute and relative tolerance set at 1×10^{-6}, using a non-linear least-squares solver (`lsqcurvefit` function) with upper (ub) and lower (lb) bounds for the fitting parameters (θ), as shown in Equation 4.82. In principle, any model parameter could be taken as a free fitting parameter, but its value should be main-

tained within the physically meaningful limits (Bessler, 2005). Common fitting parameters used in VRFB models are reaction rate constants, ionic or electronic conductivities, electrode specific surface areas, charge transfer coefficients, diffusion coefficients and permeabilities (Agar et al., 2013; Knehr et al., 2012b; Shah et al., 2008, 2011b; You et al., 2009b). It is also important to select realistic initial values of the fitting parameters to decrease the solution error since the solver algorithm does not necessarily find a global optimum or unique solution (Bessler, 2005). To this end, the fitting parameters were chosen to be the standard reaction rate constant for the cathode ($k_{ca,ref}$), the Nernst diffusion layer (δ_0) and an extra ohmic resistance (R_C). This extra ohmic resistance was included to account for any additional resistance, such as the contact resistance between current collectors and porous electrodes (Qiu et al., 2012; You et al., 2009b) and changes in the membrane conductivity due to uptake of ionic species (Tang et al., 2013b). The decision of including an additional resistance was based in previous measurements (Dewage et al., 2016) which showed a series resistance (R_S) of around $5\,\Omega\,cm^2$ at a catholyte flow rate of $1.67 \times 10^{-6}\,m^3\,s^{-1}$ using the same experimental set-up (cell, assembly, supplies, etc.) as the one used in this work without Cu current collectors, and a series resistance of around $0.8\,\Omega\,cm^2$ with Cu current collectors. The initial values, lower and upper bounds of the fitting parameters are summarised in Table 4.6. These values were selected based on the reported parameter from literature (Bourke et al., 2016; Knehr et al., 2012a) and experimental measurements (Dewage et al., 2016).

$$\min_{\theta} \|E_{cell}(\theta) - E_{data}\|_2^2 \quad \text{subject to} \quad lb \leq \theta \leq ub \tag{4.82}$$

Table 4.6: Fitting parameters of the unit cell model for a $25\,cm^2$ area RHVFC.

Parameter, θ	Unit	Cu CC	Lower bound	Upper bound	Initial guess	Fitted value
$k_{ca,ref}$	$m\,s^{-1}$	–	1×10^{-10}	1×10^{-6}	8.1×10^{-7}	1.2×10^{-7}
δ_0	m	–	$r_p/10$	$2r_p$	50.3×10^{-6}	84.8×10^{-6}
R_C	$\Omega\,cm^2$	No	3	6	5	3.6
		Yes	0.01	1	0.5	0.3

The fitting of the model was carried out against experimental data of one single-cycle of charge-discharge at a current density of $400\,A\,m^{-2}$. Figure 4.14 presents the model calibration against experimental charge and discharge potential curves at a current density of $400\,A\,m^{-2}$, for the cell with Cu current collectors. During the model fitting, it was noticed that the fitting error was mainly due to the differences at the final part of the discharge curve (SOC<20%), and therefore, a larger weighting factor was attributed to the charge

curve and the beginning of the discharge curve during the model fitting process to allow for a more balanced identification of fitting parameters. The fitted parameters obtained are presented in Table 4.6. Although the best fit could not remove all the discrepancies between the experimental data and the model simulation, a reasonably good agreement was observed with a total RMSE of 3.6% and 5.4% during charge and discharge, respectively. It can be seen that the error for the charge simulation is mainly produced by differences at extreme conditions and the high error for the discharge simulation is mainly due to the differences at low SOC, which are less critical in practical applications. It is worth noting that the rate of depletion of active species in the cathode is sensitive to the flow rate penetration into the cathode, which was calculated by a simplified model along with the assumption that only the fraction of catholyte flow rate through the cathode participate in the reaction. This may well be responsible for most of the differences during discharge. Additionally, the assumption of unity activity coefficients and neglected effects such as the transport of vanadium and H_2SO_4 species through the membrane into the CL and changes of water content in the catholyte could explain to some degree the difference between the model and experimental data. Self-discharge and gas evolving reactions are not considered in the model, which are expected to decrease the coulombic efficiency in the experimental case.
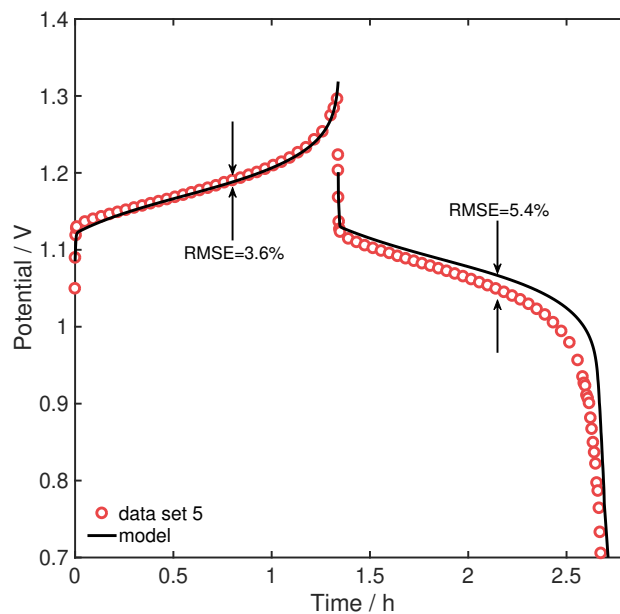
Figure 4.14: Model calibration against experimental data at a current density of $400\,\mathrm{A\,m^{-2}}$ and flow rate of catholyte and hydrogen of $1.67 \times 10^{-6}\,\mathrm{m^3\,s^{-1}}$ (data set 5).

After this calibration, simulations were carried out using the obtained fit parameters to validate the model under different current densities as reported in the next section. The only parameter refitted was R_C, depending if the tests were done with or without Cu current collectors. The potential simulations were performed following the actual operation of the cell, setting the initial SOC at a very small value (0.1%) in the cases

where a fresh catholyte solution was used or to an estimated value of initial SOC, usually between 0 and 5%, calculated based on the experimental data. The operating conditions used in the simulations are given in Table 4.5.

4.7 Model testing of charge/discharge cycles

After the model calibration, the fitted parameters $k_{\mathrm{ca,ref}}$, δ and R_{C} were used to simulate the cell performance at 80 and $600\,\mathrm{A\,m^{-2}}$, which correspond to data sets N°4 and N°8 from Table 4.5, respectively. The model demonstrated good accuracy in representing the performance of the cell at both current densities. Figure 4.15 shows the validation of the model by comparing the simulated cell potential and the experimental data at 80 and $600\,\mathrm{A\,m^{-2}}$, which produced a RMSE of 0.3% and 3.8% during charge and discharge at $8\,\mathrm{A\,m^{-2}}$ and a RMSE of 1.4% and 3.8% during charge and discharge at $600\,\mathrm{A\,m^{-2}}$. An increase in the discrepancy between the model and the experimental data occurs during discharge when a higher current density was used, which may respond to an overestimation of the average concentration of species in the cathode. In order to validate the model for a practical current density, systematic experimental data over a wide range of current densities including higher values ($>1500\,\mathrm{A\,m^{-1}}$) is required.

(a) **(b)**
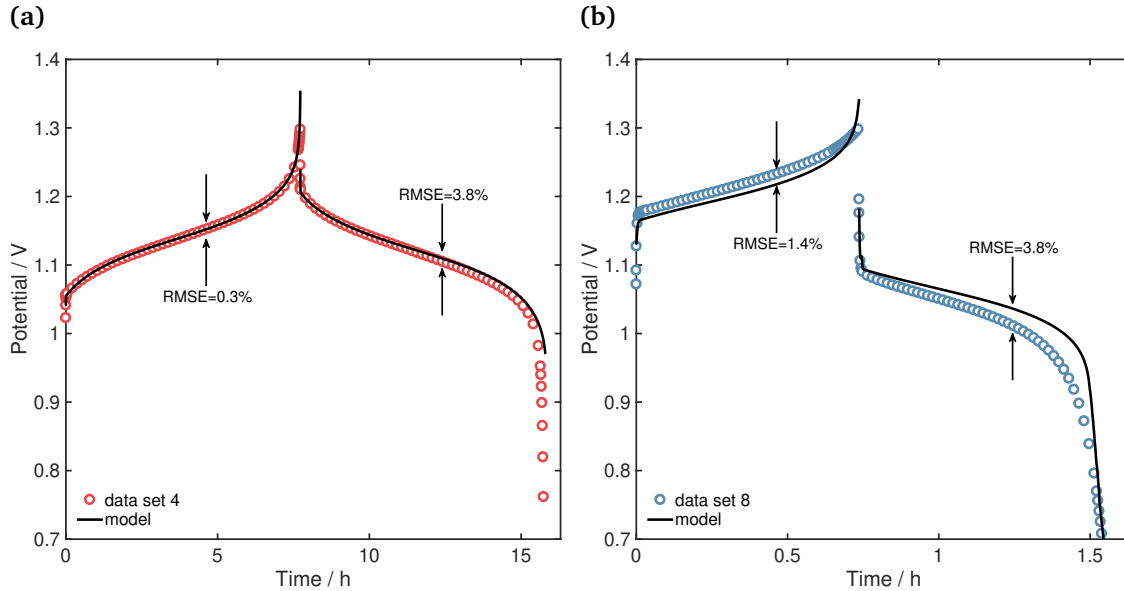
Figure 4.15: Model validation by using the same fitted parameters against experimental data at a flow rate of catholyte and hydrogen of $1.67 \times 10^{-6}\,\mathrm{m^3\,s^{-1}}$ and a current density of: (a) $80\,\mathrm{A\,m^{-2}}$ (data set 4); and (b) $600\,\mathrm{A\,m^{-2}}$ (data set 8).

The parameter R_{C} was refitted to be able to simulate the experimental data at 50 and $100\,\mathrm{A\,m^{-2}}$ of the cell without Cu current collectors, which correspond to data sets 2 and 3 from Table 4.5. The refitted R_{C} took the value $R_{\mathrm{C}}=3.6\,\Omega\,\mathrm{cm^2}$. The model demonstrated good agreement with the experimental data at both current densities. Figure 4.16a shows

the validation of the model by comparing the simulated cell performance and the experimental data at 50 and $100\,\mathrm{A\,m^{-2}}$, which produced a RMSE of 1.6% and 2.0% during charge and discharge at $50\,\mathrm{A\,m^{-2}}$ and a RMSE of 0.7% and 1.8% during charge and discharge at $100\,\mathrm{A\,m^{-2}}$. The effect of the extra ohmic resistance is evident, which produce an increase of approximately 60 mV of the potential curve at 100 $\mathrm{A\,m^{-2}}$ compared with the curve at 80 $\mathrm{A\,m^{-2}}$ over the linear range of performance.
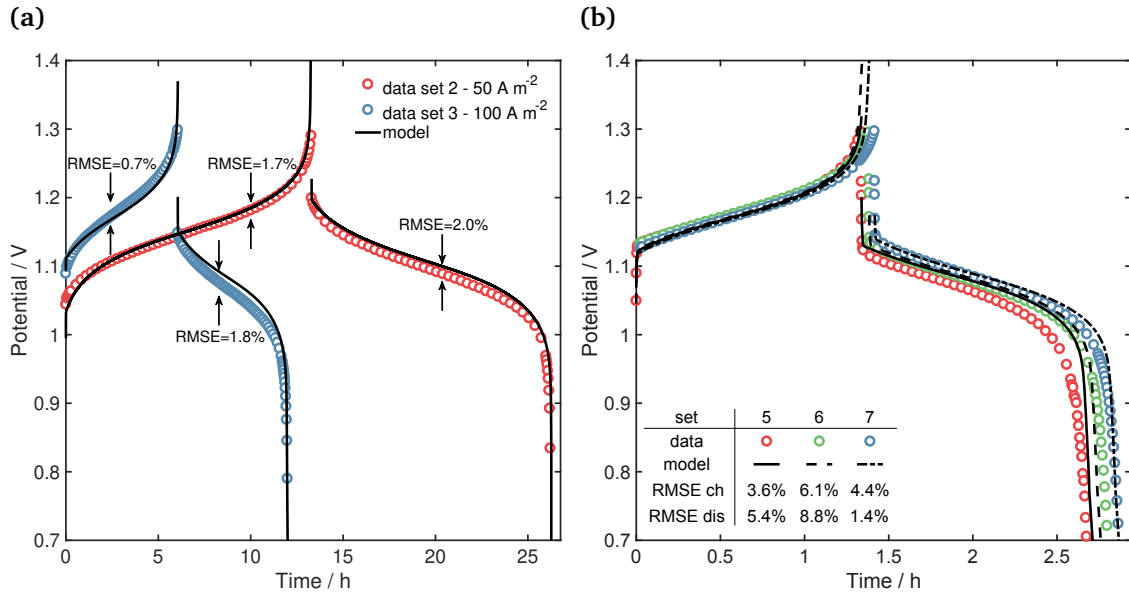
Figure 4.16: Model validation: (a) Using refitted R_C, against experimental data at a flow rate of catholyte and hydrogen of $1.67 \times 10^{-6}\,\mathrm{m^3\,s^{-1}}$ and a current density of $50\,\mathrm{A\,m^{-2}}$ (data set 2) and $100\,\mathrm{A\,m^{-2}}$ (data set 3); and (b) Using the same fitted parameters against experimental data at a current density of $400\,\mathrm{A\,m^{-2}}$ and flow rate of $1.67 \times 10^{-6}\,\mathrm{m^3\,s^{-1}}$ of catholyte and hydrogen (data set 5), $1.67 \times 10^{-6}\,\mathrm{m^3\,s^{-1}}$ of catholyte and $0.83 \times 10^{-6}\,\mathrm{m^3\,s^{-1}}$ of hydrogen (data set 6) and $2.5 \times 10^{-6}\,\mathrm{m^3\,s^{-1}}$ of catholyte and $1.67 \times 10^{-6}\,\mathrm{m^3\,s^{-1}}$ of hydrogen (data set 7).

On the other hand, testing of the model at different flow rates of catholyte and hydrogen is presented in Figure 4.16b, including data sets 5, 6 and 7 from Table 4.5. The model was able to simulate the performance of the cell when different flow rates were used, showing a similar change in the potential evolution as the one obtained in the experiments. The change in catholyte flow rate affects the flow rate penetration in the cathode, which has an effect on the evolution of species concentration and ultimately on the cell potential. For example, if a lower flow rate penetration into the cathode is allowed, shorter operation time is expected due to a reduction in the residence time of species. This is observed when comparing data set 5 and 7 in Figure 4.16.

4.8 Evolution of species concentration

The results of the evolution of species in the cathode and anode for the experimental data at a current density of $50\,\mathrm{A\,m^{-2}}$, which is data set 2 in Table 4.5, is presented in Figures 4.17 and 4.18. The concentration of vanadium species VO^{2+} and VO_2^+ based on Equations 4.6 and 4.7 and the concentration of sulphuric acid species based on Equations 4.8, 4.9 and 4.10 are presented in Figures 4.17a and 6.12, respectively. The species concentrations presented a linear rate of change, which is reached at around $70\,\mathrm{s}$ for the operating conditions used. An initial dynamic behaviour in the evolution of species concentration occurred during charge and discharge and can be observed in the zoomed figures included in Figure 4.17. The rate of change of the species concentrations depends on the stoichiometric coefficients and the number of electrons transferred in the redox reaction, along with the flow rate penetration to the cathode as can be seen in the species conservation equations. In the particular case of protons, during charge operation 2 moles of H^+ are produced in the catholyte with respect to 1 mole of VO^{2+} consumed and 1 mol of VO_2^+ produced, and it would be expected that the concentration of protons will increase with the same proportion. However, the concentration of protons in the catholyte is also affected by the transport through the membrane of 1 mole of protons that are needed to participate in the anode redox reaction, and the chemical dissociation of HSO_4^- that takes place in the catholyte. It can be seen in Figure 6.12 that the concentration of SO_4^{2-} and HSO_4^- changes during charge and discharge operation, which is related by the equilibrium condition for the HSO_4^- dissociation as presented in Equation 4.14.

(a)   **(b)**
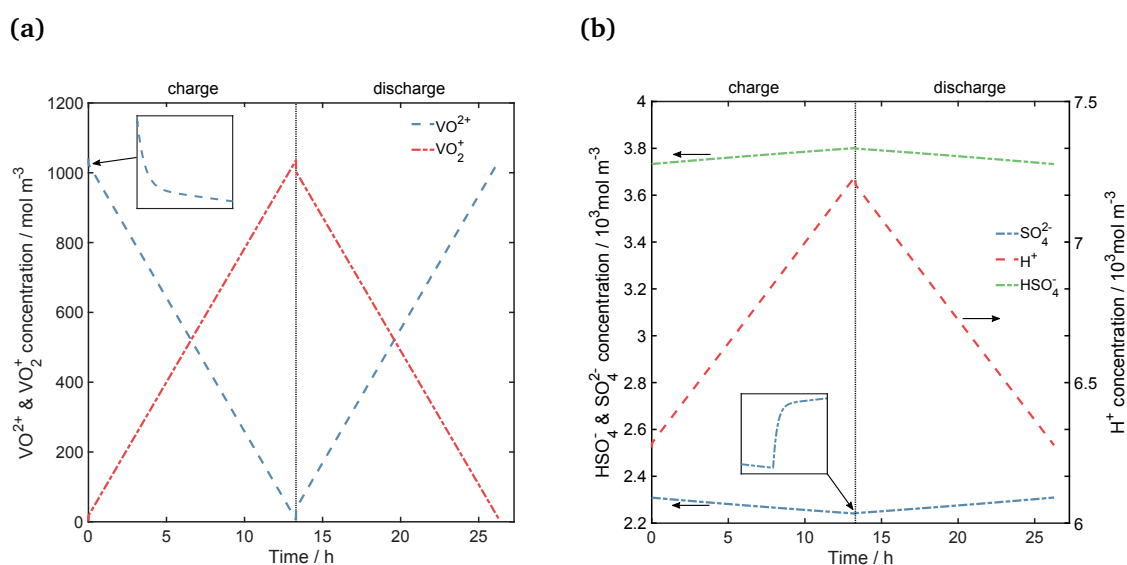
Figure 4.17: Evolution of species concentration against time in the cathode during charge and discharge at a current density of $50\,\mathrm{A\,m^{-2}}$ and a flow rate of catholyte and hydrogen of $1.67 \times 10^{-6}\,\mathrm{m^3\,s^{-1}}$ (data set 2): (a) Shows the vanadium species VO^{2+} and VO_2^+; and (b) Shows the sulphuric acid species H^+, SO_4^{2-} and HSO_4^-.

(a)

(b)
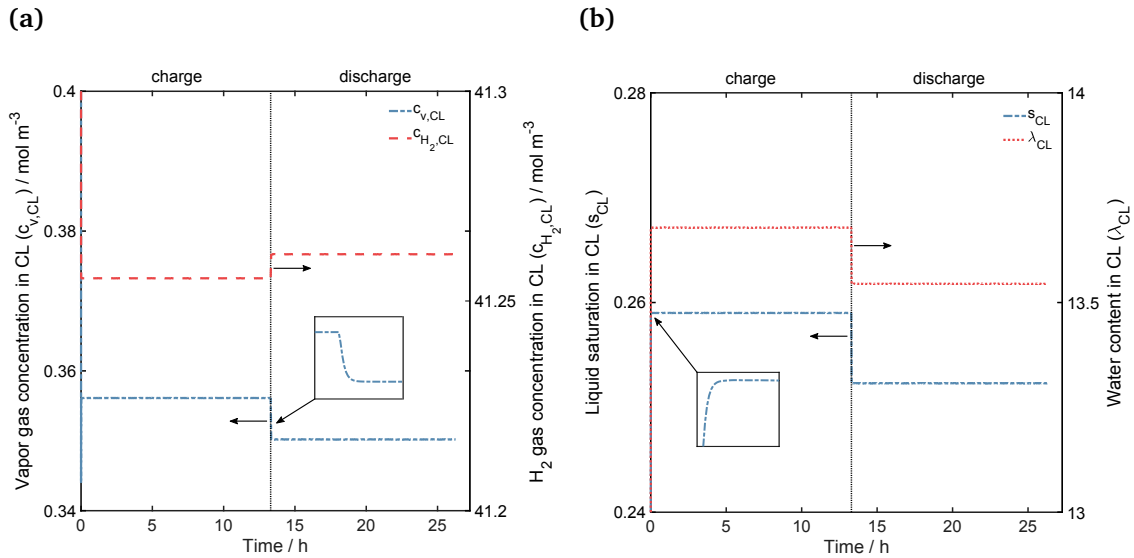
Figure 4.18: Evolution of species concentration against time in the CL during charge and discharge at a current density of $50\,\mathrm{A\,m^{-2}}$ and a flow rate of catholyte and hydrogen of $1.67 \times 10^{-6}\,\mathrm{m^3\,s^{-1}}$ (data set 2): (a) Shows vapour and hydrogen concentrations; and (b) Shows the liquid water saturation (s_{CL}) and water content in the polymer electrolyte (λ_{CL}).

The concentration of vapour and hydrogen-based on Equations 4.22 and 4.25 and the liquid water saturation and water content based on Equations 4.24 and 4.23 are presented in Figures 4.18a and 4.18b, respectively. All species concentrations in the anode CL presented a steady-state behaviour, which is reached in around $10\,\mathrm{s}$ for the operating conditions used. An initial transient behaviour was observed during charge and discharge in response to the water balance in the CL associated to water transport through the membrane and the phase change processes of liquid water desorption and evaporation/condensation between liquid and vapour water. This transient evolution of species can be observed in the zoomed figures included in Figure 4.18. It was observed that during discharge the liquid saturation slightly decreased with respect to its value during charge, possibly due to the change of direction of the electro-osmotic drag flux towards the cathode while the diffusion flux maintained its direction towards the anode. It is worth noting that the simulation results overestimated the amount of water loss from the catholyte tank with respect to the experimental observations. During the experimental operation of a single cycle of charge and discharge at a low current density, the total crossover solution collected from the outlet of the anode channel was marginal compared with the catholyte volume in the tank. The dark blue colour of this crossover solution suggested that vanadium species were also transported across the anode side and left the system. Tang et al. (2013b) have observed sulphuric acid and vanadium uptake in membranes after equilibration with solutions of sulphuric acid and vanadyl sulphate. They reported a reduction to some extent of the membrane conductivity, proton mobility and water content in the polymer electrolyte with a typical composition of VRFB feed, suggesting a complicated equilibrium and parti-

tioning competition between protons and vanadyl (Tang et al., 2013b). A detailed model of the simultaneous transport of species and water across the membrane was not explored in this study, but it highlights the need for such a study. Moreover, it is important to note that if different operating conditions were used as higher current densities, it is possible to produce flooding of the anode side.

4.9 Conclusions

This chapter introduced a first approximation of a time-dependent model for an RHVFC considering species conservation and electrochemical reaction processes. Well-established modelling approaches have been used to describe an RHVFC by means of coupling physicochemical phenomena used to simulate the performance of VRFBs and PEM fuel cells. Unlike reported VRFB models, a more strict derivation of an open circuit potential equation and a kinetic equation was developed in this work. A complete Nernst equation was derived from thermodynamics with special care in the inclusion of the Donnan potential across the electrolyte/membrane interfaces. The correct estimation of the open circuit potential is important since this equilibrium potential will be the baseline with respect to which the overpotential estimates will be calculated. In this sense, to correctly recognise the discrepancy of the complete Nernst equation with respect to the measured OCP allowed to ensure a correct estimation of the equilibrium potential when the cell is in charge-discharge operation. On the other hand, a complete Butler-Volmer kinetic equation was derived for the cathodic reaction, incorporating the concentration of protons effect which has been neglected in previous VRFB works. It is our belief that the decision of neglecting the concentration of protons was initially related to PEM fuel cells model that was taken as the basis to developed VRFB models. However, the level of concentration of protons is much higher in the catholyte of an RHVFC compared to the expected values in a PEM fuel cell. In order to maintain electroneutrality in a PEM fuel cell is commonly assumed that the concentration of protons is constant and equal to the opposite of the fixed charge concentration in the membrane. This is not the case in an RHVFC where the concentration of protons in the catholyte will change with the battery SOC, and in the membrane, a complex balance of all ionic species will occur. This is also the case of all-vanadium redox flow batteries. The model was calibrated considering experimental data of OCP and cell potential. The OCP data were fitted using a complete Nernst equation that was derived from thermodynamics, considering a global factor to account for the activity coefficients effect. The simulated cell potential, considering the overpotential of cathode and anode and the ohmic overpotential, was calibrated against a single-cycle charge-discharge potential test, showing a good degree of accuracy in predicting the cell performance. The discrepancy between experimental data and the model simulations at

the end of charge and discharge operation is most likely explained by the use of a simplified model to estimate the catholyte flow rate penetration into the cathode domain, which may predict a slower rate of change of active species concentration. The discrepancies at extreme conditions (10% > SOC or SOC > 90%) could be explained by the use of unity activity coefficients in the kinetic relations, *i.e.*, Butler-Volmer relation for the cathode and Tafel-Volmer relation for the anode. Moreover, self-discharge, gas evolving reactions and crossover of ionic species through the membrane have been neglected in the proposed model, which may well affect the performance of the cell. The model is capable of representing the potential dynamics observed in an RHVFC at moderate current densities, considering the range of operating conditions used to validate it in this chapter. However, the use of the model to predict performance at conditions beyond the validation range implemented in this paper might not produce meaningful results and significant further experimental data would be required.

The model presented in this chapter can be used as a first approximation, allowing simulation of the system and providing a foundation for further development of physical-based models for regenerative fuel cells. In addition, the electrochemical approaches used in the model may serve as reference for studying similar systems, such as all-vanadium and hydrogen-based hybrid RFBs, which may benefit from the complete Butler-Volmer equation for the cathode considering VO^{2+}, VO_2^+ and H^+, the complete Nernst equation and the kinetic approach for the HER/HOR used in this study. The low-complexity modelling approach used in this work has enhanced the understanding of the system performance by coupling physical and electrochemical processes occurring in the RHVFC, enabling identification of the key phenomena and highlighting areas requiring future in-depth study. It was made clear the need for the incorporation to the present model the transport across the membrane of ionic species and their interaction at the anode CL. The following Chapter presents extensive experimental data of an hydrogen-vanadium system, which is used to characterise the performance of this novel cell. This experimental data is used to calibrate and validate the unit cell model for a wider range of current densities and catholyte flow rates. To this end, a crossover model of ionic species through the membrane is introduced and incorporated to the present model, permitting the simulation of cycling operation.

Chapter references

Agar, E., Knehr, K. W., Chen, D., Hickner, M. A., and Kumbur, E. C. Species transport mechanisms governing capacity loss in vanadium flow batteries: Comparing Nafion® and sulfonated Radel membranes. *Electrochimica Acta*, 98:66–74, may 2013.

Bard, A. J. and Faulkner, L. R. *ELECTROCHEMICAL METHODS: Fundamentals and ap-

plications. 2001. ISBN 0471043729. doi: 10.1146/annurev.matsci.30.1.117. URL `http://tocs.ulb.tu-darmstadt.de/95069577.pdf`.

Bavarian, M., Soroush, M., Kevrekidis, I. G., and Benziger, J. B. Mathematical Modeling, Steady-State and Dynamic Behavior, and Control of Fuel Cells: A Review. *Industrial & Engineering Chemistry Research*, 49(17):7922–7950, 2010.

Bertei, A. and Nicolella, C. Common inconsistencies in modeling gas transport in porous electrodes: The dusty-gas model and the Fick law. *Journal of Power Sources*, 279:133–137, 2015.

Bessler, W. G. A new computational approach for SOFC impedance from detailed electrochemical reaction-diffusion models. *Solid State Ionics*, 176(11-12):997–1011, 2005.

Bird, R. B., Stewart, W. E., and Lightfoot, E. N. *Fenómenos de transporte*. Reverté, Barcelona, 1st edition, 1964.

Bourke, A., Miller, M. A., Lynch, R. P., Gao, X., Landon, J., Wainright, J. S., Savinell, R. F., and Buckley, D. N. Electrode Kinetics of Vanadium Flow Batteries: Contrasting Responses of V ^{II} -V ^{III} and V ^{IV} -V ^{V} to Electrochemical Pretreatment of Carbon. *Journal of The Electrochemical Society*, 163(1):A5097–A5105, 2016.

Carta, R., Palmas, S., Polcaro, A. M., and Tola, G. Behaviour of a carbon felt flow by electrodes Part I: Mass transfer characteristics. *Journal of Applied Electrochemistry*, 21 (9):793–798, 1991.

Chen, C. L., Yeoh, H. K., and Chakrabarti, M. H. An enhancement to Vynnycky's model for the all-vanadium redox flow battery. *Electrochimica Acta*, 120:167–179, feb 2014.

Chen, S. and Kucernak, A. Electrocatalysis under Conditions of High Mass Transport Rate: Investigation of hydrogen Oxidation on Single Submicron Pt Particles Supported on Carbon. *The Journal of Physical Chemistry B*, 108(10):3262–3276, 2004.

Darling, R. M., Weber, A. Z., Tucker, M. C., and Perry, M. L. The Influence of Electric Field on Crossover in Redox-Flow Batteries. *Journal of the Electrochemical Society*, 163(1): A5014–A5022, 2015.

Dewage, H. H., Yufit, V., and Brandon, N. P. Study of Loss Mechanisms Using Half-Cell Measurements in a Regenerative Hydrogen Vanadium Fuel Cell. *Journal of The Electrochemical Society*, 163(1):A5236–A5243, 2016.

Fuel Cell Store. Properties of Nafion ® PFSA Membrane: 115, 117 and 1110. URL `http://www.fuelcellstore.com/nafion-117`.

Gandomi, Y. A., Aaron, D. S., Zawodzinski, T. A., and Mench, M. M. In Situ Potential

Distribution Measurement and Validated Model for All-Vanadium Redox Flow Battery. *Journal of The Electrochemical Society*, 163(1):A5188–A5201, 2016.

Gasteiger, H. A., Panels, J. E., and Yan, S. G. Dependence of PEM fuel cell performance on catalyst loading. *Journal of Power Sources*, 127(1-2):162–171, 2004.

Ge, S., Li, X., Yi, B., and Hsing, I.-M. Absorption, Desorption, and Transport of Water in Polymer Electrolyte Membranes for Fuel Cells. *Journal of The Electrochemical Society*, 152(6):A1149, 2005.

Gileadi, E. *Electrode Kinetics for Chemists, Chemical Engineers and Materials Scientists*. John Wiley & Sons, Inc, New York, 1993. ISBN 978-0-471-18858-2. URL `http://www.wiley.com/WileyCDA/WileyTitle/productCd-0471188581.html`.

Golbert, J. and Lewin, D. R. Model-based control of fuel cells: (1) Regulatory control. *Journal of Power Sources*, 135(1-2):135–151, 2004.

Hamann, C. H., Hamnett, A., and Vielstich, W. *Electrochemistry*. WILEY-VCH Verlag GmbH & Co. KGaA, Weinheim, second edition, 2007. ISBN 3-540-08986-1. doi: 10.1007/BFb0047025. URL `http://www.springerlink.com/index/10.1007/BFb0047025`.

He, W., Yi, J. S., and Nguyen, T. V. Two-phase flow model of the cathode of PEM fuel cells using interdigitated flow fields. *AIChE Journal*, 46(10):2053, 2000.

Hewa Dewage, H. *Investigation of Hydrogen based Redox Flow Batteries*. PhD thesis, Imperial College London, 2016.

Hewa Dewage, H., Wu, B., Tsoi, A., Yufit, V., Offer, G., and Brandon, N. P. A novel regenerative hydrogen cerium fuel cell for energy storage applications. *J. Mater. Chem. A*, 3(18):9446–9450, 2015.

Jiao, K. and Li, X. Water transport in polymer electrolyte membrane fuel cells. *Progress in Energy and Combustion Science*, 37(3):221–291, 2011.

Knehr, K. W., Agar, E., Dennison, C. R., Kalidindi, A. R., and Kumbur, E. C. A Transient Vanadium Flow Battery Model Incorporating Vanadium Crossover and Water Transport through the Membrane. *Journal of The Electrochemical Society*, 159(9):1446–1459, 2012a.

Knehr, K. and Kumbur, E. Open circuit voltage of vanadium redox flow batteries: Discrepancy between models and experiments. *Electrochemistry Communications*, 13(4): 342–345, apr 2011.

Knehr, K., Agar, E., Dennison, C. R., Kalidindi, A. R., and Kumbur, E. C. A Transient Vanadium Flow Battery Model Incorporating Vanadium Crossover and Water Transport

through the Membrane. *Journal of the Electrochemical Society*, 159(9):A1446–A1459, aug 2012b.

Knopf, D. A., Luo, B. P., Krieger, U. K., and Koop, T. Thermodynamic dissociation constant of the bisulfate ion from Raman and ion interaction modeling studies of aqueous sulfuric acid at low temperatures. *Journal of Physical Chemistry A*, 107(21):4322–4332, 2003.

Kontturi, K., Murtomäki, L., and Manzanares, J. A. *Ionic Transport Processes: In Electrochemistry and Membrane Science*. Oxford University Press Inc., New York, first edition, 2008. URL http://www.amazon.com/Ionic-Transport-Processes-Electrochemistry-Membrane/dp/0199533814.

Kucernak, A. R. and Zalitis, C. General Models for the Electrochemical Hydrogen Oxidation and Hydrogen Evolution Reactions: Theoretical Derivation and Experimental Results under Near Mass-Transport Free Conditions. *Journal of Physical Chemistry C*, 120(20):10721–10745, 2016a.

Kucernak, A. R. J. and Zalitis, C. M. General Models for the Electrochemical Hydrogen Oxidation and Hydrogen Evolution Reactions Theoretical Derivation and Experimental Results Under Near Mass-Transport Free Conditions. *The Journal of Physical Chemistry C*, page acs.jpcc.6b00011, 2016b.

Mason, E. and Malinauskas, A. *Gas transport in porous media: The Dusty-Gas Model*. Elsevier, Amsterdam - Oxford - New York, 1983.

McKay, D. a., Ott, W. T., and Stefanopoulou, a. G. Modeling, Parameter Identification, and Validation of Reactant and Water Dynamics for a Fuel Cell Stack. *International Mechanical Engineering Congress & Exposition*, 2005(April):1177–1186, 2005.

McKay, D. A., Siegel, J. B., Ott, W., and Stefanopoulou, A. G. Parameterization and prediction of temporal fuel cell voltage behavior during flooding and drying conditions. *Journal of Power Sources*, 178(1):207–222, 2008.

Nam, J. H. and Kaviany, M. Effective diffusivity and water-saturation distribution in single- and two-layer PEMFC diffusion medium. *International Journal of Heat and Mass Transfer*, 46(24):4595–4611, nov 2003.

Newman, J. S. and Thomas-Alyea, K. E. *Electrochemical Systems*. John Wiley & Sons, Inc., New York, 3rd edition, 2004. ISBN 0-471-47756-7.

Pavelka, M., Wandschneider, F., and Mazur, P. Thermodynamic derivation of open circuit voltage in vanadium redox flow batteries. *Journal of Power Sources*, 293:400–408, 2015.

Pino-Muñoz, C. A., Hewa Dewage, H., Yufit, V., and Brandon, N. P. A Unit Cell Model of a

Regenerative Hydrogen-Vanadium Fuel Cell. *Journal of The Electrochemical Society*, 164 (14):F1717–F1732, 2017.

Pukrushpan, J. T., Stefanopoulou, a. G., and Peng, H. P. H. Modeling and control for PEM fuel cell stack system. *Proceedings of the 2002 American Control Conference IEEE Cat NoCH37301*, 4(12):3117–3122, 2002.

Qiu, G., Joshi, A. S., Dennison, C., Knehr, K., Kumbur, E., and Sun, Y. 3-D pore-scale resolved model for coupled species/charge/fluid transport in a vanadium redox flow battery. *Electrochimica Acta*, 64:46–64, mar 2012.

Reid, R. C., Prausnitz, J. M., and Sherwood, T. K. *The Properties of Gases and Liquids*. McGraw-Hill, New York, 1977.

Seborg, D. E., Edgar, T. F., Mellichamp, D. A., and Doyle, F. J. *Process Dynamics and Control*. John Wiley & Sons, Inc., third edition, 2011. ISBN 2013436106. doi: 10. 1360/zd-2013-43-6-1064.

Shah, A. A., Luo, K. H., Ralph, T. R., and Walsh, F. C. Recent trends and developments in polymer electrolyte membrane fuel cell modelling. *Electrochimica Acta*, 56(11):3731–3757, 2011a.

Shah, A., Watt-Smith, M., and Walsh, F. A dynamic performance model for redox-flow batteries involving soluble species. *Electrochimica Acta*, 53(27):8087–8100, nov 2008.

Shah, A., Tangirala, R., Singh, R., Wills, R., and Walsh, F. A Dynamic Unit Cell Model for the All-Vanadium Flow Battery. *Journal of The Electrochemical Society*, 158(6):A671, 2011b.

Shampine, L. and Reichelt, M. Ode_Suite. *Journal of Scientific Computing*, 18:1–22, 1997.

Skyllas-Kazacos, M. and Goh, L. Modeling of vanadium ion diffusion across the ion exchange membrane in the vanadium redox battery. *Journal of Membrane Science*, 399-400:43–48, may 2012.

Springer, T., Zawodzinski, T., and Gottesfeld, S. Polymer electrolyte fuel cell model. *Journal of the Electrochemical Society*, 138(8):2334–2342, 1991.

Sun, C.-N., More, K. L., Veith, G. M., and Zawodzinski, T. a. Composition Dependence of the Pore Structure and Water Transport of Composite Catalyst Layers for Polymer Electrolyte Fuel Cells. *Journal of the Electrochemical Society*, 160(9):F1000–F1005, 2013.

Tang, A., Bao, J., and Skyllas-Kazacos, M. Dynamic modelling of the effects of ion diffusion and side reactions on the capacity loss for vanadium redox flow battery. *Journal of Power Sources*, 196(24):10737–10747, dec 2011.

Tang, A., Bao, J., and Skyllas-Kazacos, M. Thermal modelling of battery configuration and self-discharge reactions in vanadium redox flow battery. *Journal of Power Sources*, 216: 489–501, oct 2012a.

Tang, A., Ting, S., Bao, J., and Skyllas-Kazacos, M. Thermal modelling and simulation of the all-vanadium redox flow battery. *Journal of Power Sources*, 203:165–176, 2012b.

Tang, A., McCann, J., Bao, J., and Skyllas-Kazacos, M. Investigation of the effect of shunt current on battery efficiency and stack temperature in vanadium redox flow battery. *Journal of Power Sources*, 242:349–356, nov 2013a.

Tang, Z., Svoboda, R., Lawton, J. S., Aaron, D. S., Papandrew, A. B., and Zawodzinski, T. A. Composition and Conductivity of Membranes Equilibrated with Solutions of Sulfuric Acid and Vanadyl Sulfate. *Journal of The Electrochemical Society*, 160(9):F1040–F1047, 2013b.

Tucker, M. C., Cho, K. T., Spingler, F. B., Weber, A. Z., and Lin, G. Impact of membrane characteristics on the performance and cycling of the Br2-H2 redox flow cell. *Journal of Power Sources*, 284:212–221, 2015.

Wang, J. X., Springer, T. E., and Adzic, R. R. Dual-Pathway Kinetic Equation for the Hydrogen Oxidation Reaction on Pt Electrodes. *Journal of The Electrochemical Society*, 153(9):A1732, 2006.

Weber, A. Z. and Newman, J. Modeling transport in polymer-electrolyte fuel cells. *Chemical Reviews*, 104(10):4679–4726, 2004.

Wei, Z., Zhao, J., Skyllas-Kazacos, M., and Xiong, B. Dynamic thermal-hydraulic modeling and stack flow pattern analysis for all-vanadium redox flow battery. *Journal of Power Sources*, 260:89–99, aug 2014.

White, F. *Fluid Mechanics*. McGraw-Hill, New York, 7th edition, 2011.

Wilkes, J. O. *Fluid mechanics for chemical engineers*. Prentice Hall PTR, 1st edition, 1999.

Won, S., Oh, K., and Ju, H. Numerical analysis of vanadium crossover effects in all-vanadium redox flow batteries. *Electrochimica Acta*, 177:310–320, sep 2015.

Wu, H., Li, X., and Berg, P. Numerical analysis of dynamic processes in fully humidified PEM fuel cells. *International Journal of Hydrogen Energy*, 32(12):2022–2031, aug 2007.

Wu, H., Li, X., and Berg, P. On the modeling of water transport in polymer electrolyte membrane fuel cells. *Electrochimica Acta*, 54(27):6913–6927, 2009.

Wu, H., Berg, P., and Li, X. Modeling of PEMFC Transients with Finite-Rate Phase-Transfer Processes. *Journal of The Electrochemical Society*, 157(1):B1, 2010.

Xiong, B., Zhao, J., Tseng, K., Skyllas-Kazacos, M., Lim, T. M., and Zhang, Y. Thermal hydraulic behavior and efficiency analysis of an all-vanadium redox flow battery. *Journal of Power Sources*, 242:314–324, nov 2013.

Xu, W., Zhang, H., Xing, F., Zhang, H., Li, Y., Cao, J., and Li, X. The numerical simulation of dynamic performance in the vanadium flow battery. *Electrochimica Acta*, 118:51–57, feb 2014.

Yang, W., He, Y., and Li, Y. Performance Modeling of a Vanadium Redox Flow Battery during Discharging. *Electrochimica Acta*, 155:279–287, feb 2015a.

Yang, X.-G., Ye, Q., Cheng, P., and Zhao, T. S. Effects of the electric field on ion crossover in vanadium redox flow batteries. *Applied Energy*, 145:306–319, 2015b.

You, D., Zhang, H., and Chen, J. Theoretical analysis of the effects of operational and designed parameters on the performance of a flow-through porous electrode. *Journal of Electroanalytical Chemistry*, 625(2):165–171, jan 2009a.

You, D., Zhang, H., and Chen, J. A simple model for the vanadium redox battery. *Electrochimica Acta*, 54(27):6827–6836, nov 2009b.

You, D., Zhang, H., Sun, C., and Ma, X. Simulation of the self-discharge process in vanadium redox flow battery. *Journal of Power Sources*, 196(3):1578–1585, feb 2011.

Yu, V. and Chen, D. Dynamic Model of a Vanadium Redox Flow Battery for System Performance Control. *Journal of Solar Energy Engineering*, 136(2):021005–1 – 0210057, 2014a.

Yu, V. and Chen, D. Peak power prediction of a vanadium redox flow battery. *Journal of Power Sources*, 268:261–268, dec 2014b.

Yufit, V., Hale, B., Matian, M., Mazur, P., and Brandon, N. P. Development of a Regenerative Hydrogen-Vanadium Fuel Cell for Energy Storage Applications. *Journal of The Electrochemical Society*, 160(6):A856–A861, 2013.

Zheng, Q., Li, X., Cheng, Y., Ning, G., Xing, F., and Zhang, H. Development and perspective in vanadium flow battery modeling. *Applied Energy*, 132:254–266, nov 2014.

Chapter 5

Characterization of the regenerative hydrogen-vanadium fuel cell using a unit cell model

This chapter is based on the work:

C. A. Pino-Muñoz, B. K. Chakrabarti, V. Yufit and N. P. Brandon,"Characterisation of a regenerative hydrogen-vanadium fuel cell using an experimentally validated unit cell model", Journal of The Electrochemical Society, 166 (14) A1-A14 (2019) (Pino-Muñoz et al., 2019).

5.1 Introduction

In this fifth chapter, a characterisation of the performance of the RHVFC based on extensive experimental data obtained from an improved cell design is presented. Additionally, performance simulations by means of a unit cell model, introduced in the previous chapter, are considered. In redox flow batteries, the cell performance is evaluated by considering the power output of the cell for a particular operating condition, but also by assessing the cycle life of the battery and how the performance could vary over time. A performance decay could be closely related to the crossover of ionic species through the membrane which causes a capacity loss, and possible degradation of membrane and electrode materials, increasing their overpotential. Thus, the unit cell model was modified to include the crossover molar flux of all ionic species and water thought the membrane. This model was then calibrated using data of one single-cycle charge-discharge test at different flow rate conditions. Afterwards, a parametric sensitivity analysis of the target model output, namely the cell potential, with respect to the selected fitting parameters was performed. The model was then tested using the additional experimental measurements of polarisation, power curve and cycling analyses. Finally, the change in the model response with respect to a change of component property values was investigated by considering an operating base case.

5.2 Additional model considerations

The time-dependent unit cell model introduced in Chapter 4 was modified to facilitate the simulation of continuous operation of an RHVFC. While the previous model validation against single-cycle charge-discharge potential data was satisfactory, when continuous cycling operation was simulated the capacity loss due to crossover of ionic species and water through the membrane produces an irreconcilable mismatch over time between the experimental data and simulations. This crossover effect changes the concentration of species, as well as the volume of solution in the catholyte tank, reducing the operating charge or discharge time per cycle since the set cut-off potential is reached faster as the cycle number increases. Therefore, the voltage and energy efficiency and the available capacity per cycle is reduced, even when the coulombic efficiency of the cell may be maintained.

A mathematical description of the ionic species crossover through the membrane is fundamental to simulate practical operating conditions and to estimate capacity loss over time. This is of relevance to assess when rebalance or possible regeneration of electrolytes is required in order to keep the battery performance within acceptable target values of efficiencies and electrolyte utilisation. The modified unit cell model includes the same domains considered for Chapter 4 (Figure 4.1). These domains are the vanadium electrolyte tank, cathode, membrane, catalyst layer (CL), gas diffusion layer (GDL), and anode channel. The following additional model assumptions were considered in the modified unit cell model:

1. The electrolytes and the membrane must maintain electro-neutrality:

$$
\begin{aligned}
\sum z_i c_i &= 0, \quad \text{for electrolytes,} \\
\sum z_i c_i + z_f c_f &= 0, \quad \text{for the membrane}
\end{aligned}
\tag{5.1}
$$

2. Water balance at the cathode, considering the transport of water through the membrane directly affects the catholyte tank volume.

3. Protons are the dominant charge carriers crossing the membrane.

4. Constant concentration of ionic species was assumed at the anode catalyst layer.

The species conservation equations for the cathode, which were presented in Equation 4.6 to 4.10, were modified to incorporate the crossover molar flux of species through the membrane ($N_{i,m}$). These conservation equations are presented in a general form in Equation 5.2, which includes the effect on the concentration of catholyte recirculation between cell and tank, the electron transfer reaction, the HSO_4^- dissociation, and the membrane crossover. Table 6.5 summarises the source terms for vanadium species (VO^{2+} and VO_2^+) and sulphuric acid species (H^+, HSO_4^- and SO_4^{2-}) at the cathode. Any change in the water concentration at the cathode was assumed to affect instantaneously the volume of solution in the catholyte tank. The change in catholyte tank volume over time indirectly affect the concentration of ionic species in the catholyte tank as shown in Equation 5.3. Equation 5.4 introduces the balance of water, considering the electron transfer reaction, diffusion through the membrane and electro-osmotic drag. In this equation, ρ_w and M_w are the water density and the water molar weight. The diffusion coefficient for dissolved water in the membrane was calculated as shown in Equation 4.29 considering the mean water content of the membrane.

$$
\varepsilon_{ca} V_{ca} \frac{dc_i}{dt} = Q_{ca}(c_{i,T} - c_i) + S_i + N_{i,m}
\tag{5.2}
$$

$$
V_T \frac{dc_{i,T}}{dt} = Q_{ca}(c_i - c_{i,T})
\tag{5.3}
$$

$$\frac{\rho_{\mathrm{w}}}{M_{\mathrm{w}}}\frac{dV_{\mathrm{T}}}{dt} = \mp\frac{A_{\mathrm{ca}}j}{F} + A_{\mathrm{m}}D_{\mathrm{dw,m}}\frac{(c_{\mathrm{dw,CL}} - c_{\mathrm{dw,c\text{-}m}})}{l_{\mathrm{m}}} \mp \xi_{\mathrm{drag}}\frac{A_{\mathrm{ca}}j}{F} \tag{5.4}$$

Table 5.1: Source for species in the positive electrode.

Species	Source term (S_i)
VO^{2+}	$\mp\frac{A_{\mathrm{ca}}j}{F}$
VO_2^+	$\pm\frac{A_{\mathrm{ca}}j}{F}$
H^+	$\pm 2\frac{A_{\mathrm{ca}}j}{F} - S_{\mathrm{d}}^{\mathrm{eq}}$
HSO_4^-	$S_{\mathrm{d}}^{\mathrm{eq}}$
SO_4^{2-}	$-S_{\mathrm{d}}^{\mathrm{eq}}$

In order to estimate the flux of dissolved water due to diffusion, the dissolved water concentration at the interface between cathode and Nafion membrane was assumed to reach equilibrium. Experimental data of water content (λ) presented by Tang et al. (2013b) of a Nafion membrane equilibrated in sulphuric acid is shown in Figure 5.1a as a function of the water activity. It can be observed that water content increases with water activity, displaying two distinctive regions. When the water activity is less than 0.8, where water content is roughly linearly dependent on water activity, and when the water activity is greater than 0.8, an important increase of water uptake occurs (Tang et al., 2013b). This dependence of water content in the Nafion membrane is similar to the known dependence of water content in Nafion membranes upon equilibration with water vapour (Tang et al., 2013b). The relation of between water activity and sulphuric acid concentration for aqueous sulphuric acid solutions reported by Staples (1981) was used to estimate the water activity at the interface between the cathode and the Nafion membrane. This relation shows how the water concentration and water activity decrease as the acid concentration increases in aqueous sulphuric acid solutions. On the other hand, the concentration of water at the interface between the Nafion membrane and the catalyst layer was estimated by means of the water balance presented previously in Equation 4.23.

The crossover molar flux of ionic species through the membrane was obtained according to the modelling approach reported by Darling et al. (2015). Where the crossover molar flux of ionic species i, ($N_{i,m}$), was mathematically represented by the Nernst-Planck equation (Newman and Thomas-Alyea, 2004), which is shown in Equation 5.5. This approach considers the transport of ionic species due to diffusive, migration and convective fluxes. The ion mobility was eliminated as an independent parameter in Equation 5.5 by means of the Nernst-Einstein equation, which is shown in Equation 5.6. In these equations, c_i, $D_{i,m}$, z_i, and $\mu_{i,m}$ are the concentration, diffusion coefficient, charge number and mobility of species i in the membrane, ϕ is the potential in the solution, and v is the bulk

(a)

(b)
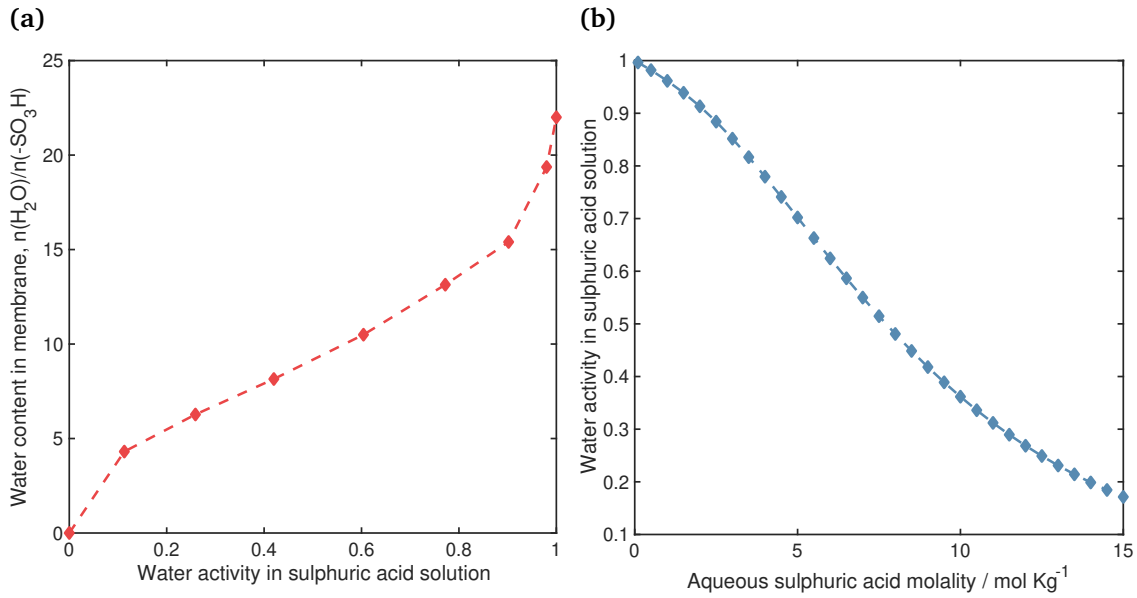
Figure 5.1: (a) Water content in Nafion membrane, namely $\lambda = n(\text{H}_2\text{O})/n(-\text{SO}_3\text{H})$, upon equilibration with aqueous sulphuric acid solutions as given by Tang et al. (2013b); and (b) Water activity in the membrane with respect to sulphuric acid concentration as given by Staples (1981).

velocity. The superscript term "m" refers to the membrane, and all transport properties were assumed constant throughout the membrane.

$$N_{\text{i,m}} = c_{\text{i}}^{\text{m}} v - D_{\text{i,m}} \nabla c_{\text{i}}^{\text{m}} - z_{\text{i}} \mu_{\text{i,m}} F c_{\text{i}}^{\text{m}} \nabla \phi \tag{5.5}$$

$$\mu_{\text{i,m}} = \frac{D_{\text{i,m}}}{RT} \tag{5.6}$$

Following the approach of Darling et al. (2015), it was assumed that protons were the main charge carriers when crossing the membrane. The bulk velocity along the membrane was estimated by considering the electro-osmotic and diffusive flow of water ($N_{\text{w,m}}$) through the membrane by means of Equation 5.7. For the sake of simplicity, the transport of water was assumed to reach a steady-state condition, following the approach developed in Chapter 4. Additionally, the migration flux term in Equation 5.5 can be simplified by considering Ohm's law in the membrane and the membrane conductivity as shown in Equation 5.8. By substituting Equations 5.7 and 5.8 in Equation 5.5, it was possible to express the molar flux equation in terms of the applied current density (j), as shown in Equation 5.9. This equation was expressed in terms of the one-dimensional coordinate (x) through the thickness of the membrane, with x going from 0 to l_{m} from the interface between the cathode and the membrane to the interface between the membrane and the catalyst layer, and neglecting any variation in the other direction. The concentration of the ionic species at each side of the membrane were specified as the concentration at the cathode (c_{i}^{ca}) and at the catalyst layer (c_{i}^{CL}). In these equations, σ_{m} is the membrane

conductivity, ξ_{drag} is the electro-osmotic drag coefficient, $\bar{c}_{\text{w}}$ is the mean concentration of water in the membrane ($c_{\text{w}} = \lambda\rho_{\text{dm}}/EW$, where λ is the water content, ρ_{dm} is the dry membrane density and EW is the equivalent molecular weight of the dry membrane), j is the applied current density, l_{m} is the membrane thickness, and D_{w} is the diffusion coefficient of water in the membrane.

$$N_{\text{w,m}} = \bar{c}_{\text{w}}v = \frac{\xi_{\text{drag}}j}{F} - D_{\text{w}}\frac{(c_{\text{w}}^{\text{CL}} - c_{\text{w}}^{\text{ca}})}{l_{\text{m}}} \tag{5.7}$$

$$j = -\sigma_{\text{m}}\nabla\phi \tag{5.8}$$

$$N_{\text{i,m}} = \left(\frac{\xi_{\text{drag}}j}{\bar{c}_{\text{w}}F} - D_{\text{w}}\frac{(c_{\text{w}}^{\text{CL}} - c_{\text{w}}^{\text{ca}})}{\bar{c}_{\text{w}}l_{\text{m}}}\right)c_{\text{i}}^{\text{m}} - D_{\text{i,m}}\frac{\text{d}c_{\text{i}}^{\text{m}}}{\text{d}x} + z_{\text{i}}\mu_{\text{i,m}}Fc_{\text{i}}^{\text{m}}\frac{j}{\sigma_{\text{m}}} \tag{5.9}$$

In order to simplify the notation, Equation 5.9 was rearranged into the boundary value problem presented in Equation 5.10, whose Dirichlet boundary conditions for the dimensionless concentration presented in Equation 5.11. This boundary value problem considers a constant term (ζ), and the dimensionless variables for concentration (θ), coordinate x ($\tilde{x}$) and crossover molar flux through the membrane ($\tilde{N}_{\text{i,m}}$). These dimensionless variables are defined in Equation 5.12.

$$\tilde{N}_{\text{i,m}} = -\frac{\text{d}\theta}{\text{d}\tilde{x}} + \zeta\theta, \tag{5.10}$$

$$\text{BCs:} \quad \theta(\tilde{x} = 0) = 1; \quad \theta(x = 1) = \frac{c_{\text{i}}^{\text{CL}}}{c_{\text{i}}^{\text{ca}}} \tag{5.11}$$

$$\tilde{x} = \frac{x}{l_{\text{m}}}, \quad \theta = \frac{c_{\text{i}}^{\text{m}}}{c_{\text{i}}^{\text{ca}}}, \quad \tilde{N}_{\text{i,m}} = \frac{N_{\text{i,m}}l_{\text{m}}}{D_{\text{i,m}}c_{\text{i}}^{\text{ca}}}, \quad \text{and}$$
$$\zeta = \left(\frac{z_{\text{i}}F}{\sigma_{\text{m}}RT} + \frac{\xi_{\text{drag}}}{\bar{c}_{\text{w}}D_{\text{i,m}}F}\right)jl_{\text{m}} - \frac{D_{\text{w}}}{D_{\text{i,m}}}\frac{(c_{\text{w}}^{\text{CL}} - c_{\text{w}}^{\text{ca}})}{\bar{c}_{\text{w}}} \tag{5.12}$$

Performing the integration of Equation 5.10 for a constant value of applied current density subject to the specified boundary conditions, an expression for the ionic molar flux of species i through the membrane was obtained as shown in Equation 5.13. This integration was possible since the crossover molar flux is constant over x, when considering steady-state conservation for species in the membrane, *i.e.*, $\nabla \cdot N_{\text{i,m}} = 0$, in a one-dimensional approach. The expressions for the crossover molar flux of species were incorporated in the respective conservation equations (Equation 5.2) for vanadium species, bi-sulphate and sulphate in the cathode. It is a common assumption in models of all-vanadium systems to consider that the concentrations of all vanadium species at the op-

posite electrode are equal to zero due to self-discharge reactions at each electrode (Tang et al., 2011). These self-discharge reactions are assumed to take place instantaneously when vanadium species reach the opposite electrode and become in contact with other vanadium species (Darling et al., 2015; Pugach et al., 2018). In this work, possible side (Dowd et al., 2017b) and self-discharge reactions were neglected, and therefore, the presence of ionic species at the anode catalyst layer was allowed. This consideration coincides with what was observed after operating the cell and disassembling the Membrane Electrode Assembly (MEA), where a catholyte-like solution was found between the surface of the membrane and anode CL. For the sake of simplicity, a constant value of the concentration of ionic species was considered at the anode CL (c_i^{CL}), allowing for ionic transport through the membrane, which depends on the operating mode (charge or discharge), towards both electrodes (cathode or anode). Figure 5.2a shows the estimated total crossover flux for V(IV) through the membrane at different values of applied current density. These fluxes were calculated using Equation 5.13 and considering a fixed concentration of V(IV) at the cathode and anode CL of 500 and $250\,\mathrm{mol\,m^{-3}}$, respectively. The molar fluxes have been multiplied by Faraday's constant to facilitate their comparison with the applied current densities. The molar fluxes corresponding to only diffusion, migration and electro-osmosis transport are also displayed in Figure 5.2a.

$$N_{i,m} = \frac{D_{i,m} c_i^{ca}}{l_m} \left(\frac{\zeta(e^\zeta - c_i^{CL}/c_i^{ca})}{e^\zeta - 1} \right) \tag{5.13}$$

(a)

(b)
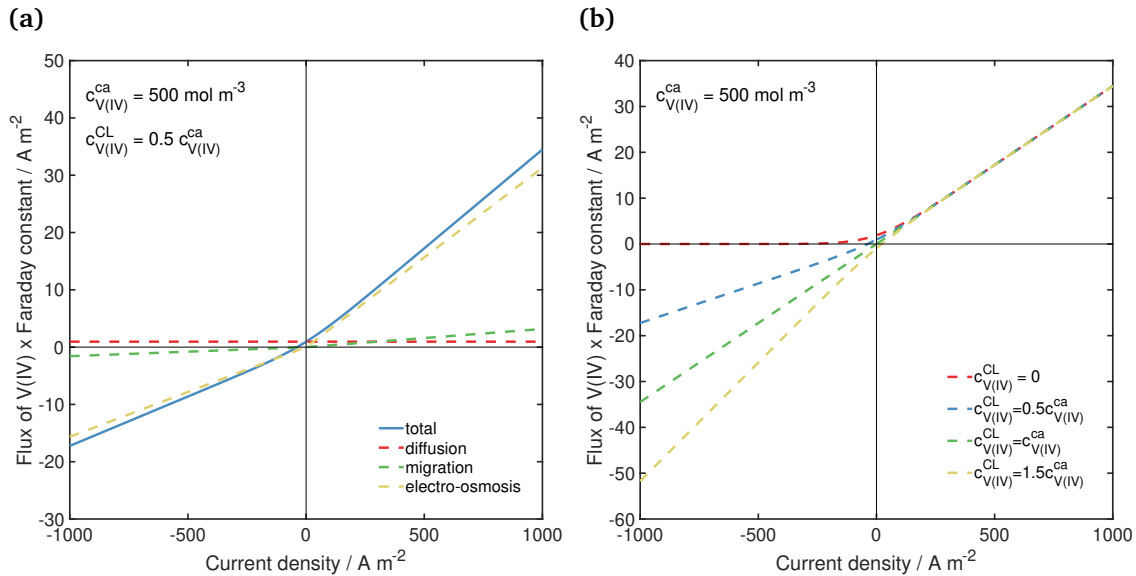
Figure 5.2: Crossover flux of V(IV): (a) Total, diffusion, migration and electro-osmotic crossover flux as a function of the applied current density; and (b) Total crossover flux for different values of V(IV) concentration at the anode CL.

The electro-osmotic flux is larger than the migration flux due to the selected values for transport parameters. The crossover flux due to diffusive transport is independent of

the current density value or direction, and in the cases displayed only depends on the concentration of V(IV) at either side of the membrane. While the crossover flux due to migration and electro-osmotic transport are affected by the applied current density value and direction. During charge, both fluxes increase the crossover flux of V(IV) towards the anode CL. However, during discharge the crossover flux due to diffusion maintains its direction from higher concentration to lower concentration (*i.e.*, in this case from cathode to anode) while the crossover flux due to migration and electro-osmotic drag follow the direction of the applied current density (*i.e.*, from anode to cathode), flipping the direction of the total crossover flux of V(IV). The behaviour of the other ionic species was analogous to the one shown in Figure 5.2 for V(IV), but different in magnitude depending on the selected transport parameters for the different ionic species. Figure 5.2b displays the total crossover flux of V(IV) for a concentration at the cathode of $500\,\mathrm{mol\,m^{-3}}$ and different concentrations at the anode CL. During charge, and at large applied current densities, the total crossover flux of V(IV) reaches virtually the same value for all different anode CL concentrations of V(IV). The discrepancies between these four cases only depend on the diffusion term which is much smaller than the other fluxes. At low current densities, the crossover flux due to migration and electro-osmotic drag are much smaller than the diffusion transport allowing for seeing the discrepancy between the four cases with different concentration of V(IV) at the anode CL. During discharge and at high densities of applied current, the effect of these different V(IV) concentrations on the crossover molar flux from the anode to the cathode becomes clear. The total crossover flux for zero concentration of species at the opposite half-cell (red segmented line) corresponds to the crossover behaviour used recently in all-vanadium systems to model the crossover of vanadium species through Nafion membranes (Darling et al., 2015; Pugach et al., 2018).

5.3 Experimental methods

Experimental data collection was developed by means of a commercial PEM fuel cell adapted for operation as a hybrid hydrogen-vanadium flow battery. A brief description of the equipment and data acquisition procedures used in this work are presented below.

5.3.1 Experimental set-up

The experimental set-up used for the acquisition of data is presented in Figure 5.3. A single cell (Scribner Associates) having an electrode cross-sectional area of $5\,\mathrm{cm^2}$, with height and width of $2.24 \times 10^{-2}\,\mathrm{m}$, was used as hydrogen-vanadium electrochemical reactor. Hydrogen was passed through the anode side at a constant flow rate, while a small glass reservoir was connected to the hydrogen outlet to collect any vanadium electrolyte

crossover. A peristaltic pump (Cole Parmer) was used to recirculate the vanadium electrolyte between the cell and the stirred catholyte tank also at a constant flow rate. This single cell is commercially sold for PEM fuel cell applications, however, its components were modified in order to allow for the operation of a hybrid hydrogen-vanadium system. The cell consisted of anodised aluminium end plates, gold-plated copper current collectors, graphite flow fields and the Membrane Electrode Assembly (MEA). The MEA contained a Freudenberg H23 carbon paper as a cathodic electrode with a thickness of $210\,\mu m$ and an SGL 29BC platinised carbon paper as an anodic electrode with a thickness of $235\,\mu m$ and Pt loading of $0.3\,mg\,cm^{-2}$. These electrodes were separated by a Nafion 115 membrane with a thickness of $127\,\mu m$. For all the experiments, the cathodic electrode was heat-treated at $500\,°C$ for $6\,h$ before use. A single-channel serpentine graphite flow field distributed the vanadium electrolyte, as well as the hydrogen gas, into the cathodic and anodic half-cell, respectively. This experimental set-up displayed a better current collection with respect to the previous experimental set-up used in Chapter 4, mainly due to the use of gold-plated copper current collectors. The cell assembly and connection procedures were analogous to the procedures described in Section 4.5. Once all components were in place, the cell was tightened up to $4\,N\,m$, and then inlet and outlet connections for the vanadium electrolyte and hydrogen, along with the electrical connections of the worker, counter and reference electrodes to a Bio-Logic potentiostat (VSP-300) running EC-Lab software, were made.
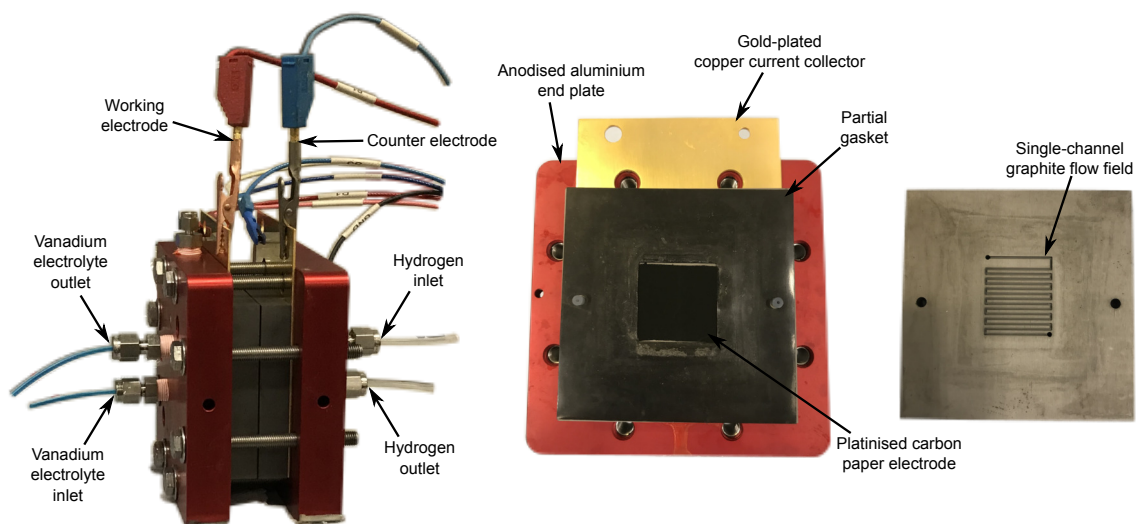
Figure 5.3: RHVFC with an area of $5\,cm^2$ and its components, inlet and outlet connections for vanadium electrolyte and hydrogen, and electrical connections.

For all experiments considered in this chapter, the vanadium electrolyte solution was prepared following the same procedure. An amount of $10.8\,g$ of vanadium sulphate hydrate (Sigma-Aldrich) were dissolved in $60\,mL$ of 5 M H_2SO_4 solution (Fluka Analytical) to produce a vanadium electrolyte solution of $800\,mol\,m^{-3}$ of V(IV). This initial vanadium concentration was calculated by considering the vanadium sulphate hydrate,

$VOSO_4 \cdot xH_2O$, contained 3.5 molecules of water and therefore had a molecular weight (M) of $226 \, g \, mol^{-1}$. The initial concentrations of sulphuric acid species were calculated by taking into account the dissolution of vanadium sulphate hydrate and the dissociation of sulphuric acid. This dissociation was considered to be in a complete first step to form HSO_4^- and H^+, and the second step of HSO_4^- dissociation to form SO_4^{2-} and H^+ controlled by a dissociation constant (k_2), as explained in the previous chapter. The vanadium electrolyte solution was then placed in a stirred catholyte tank and recirculated between the cathodic half-cell and the catholyte tank, at the same time hydrogen was passed through the anodic half-cell, to condition the cell for operation. This is to remove the air contained in the cathodic and anodic half-cells, by filling up the serpentine flow fields and electrodes with vanadium electrolyte solution and hydrogen, respectively. The experimental data acquisition was performed at a constant flow rate of vanadium electrolyte and hydrogen. Several iterations of cell assembly and operation were carried out to obtain a leak-free cell and to obtain consistent experimental data.

5.3.2 Data acquisition

Experimental measurements of Open Circuit Potential (OCP), single-cycle charge-discharge (ch-dch) potential, polarisation and power curves, and cycling operation were obtained using the experimental set-up previously described. These experiments were performed in collaboration with Dr. Barun Chakrabarti at Imperial College, while the data analysis and interpretation were done independently. A summary of the operating conditions used in the experimental tests is presented in Table 5.2, along with the tag "set" going from 1 to 23 to identify each test. The flow rate of vanadium electrolyte was set to 50 or $100 \, mL \, min^{-1}$ (0.83 or $1.67 \times 10^{-6} \, m^3 \, s^{-1}$), and the hydrogen flow rate to 100 or $30 \, mL \, min^{-1}$ (1.67 or $0.5 \times 10^{-6} \, m^3 \, s^{-1}$). For all experimental tests, the cell was allowed to reach an upper cut-off potential of $1.4 \, V$ during charge and lower cut-off potential of $0.4 \, V$ during discharge.

Two open circuit potential measurements were performed (sets 13 and 14) by operating the cell in a series of steps of galvanostatic charge until the upper cut-off potential was reached, and then operating the cell in a series of steps of galvanostatic discharge until the lower cut-off potential was reached. After assembly and conditioning of the cell, the OCP of the cell was initially monitored for about $15 \, min$. Then, after every charge or discharge step, the OCP was also monitored, to allow the cell to stabilise, *i.e.*, to return to equilibrium. When the cut-off potentials were reached, a final OCP measurement was recorded. Every charge or discharge step in galvanostatic operating mode covered a portion of the maximum experimental capacity (Q_{max}), which was calculated considering the operating time and the applied current. This maximum experimental capacity was theoretically estimated by Equation 2.29, and was considered to represent 100% State Of Charge (SOC)

Table 5.2: Experimental data sets measured in the $5\,\mathrm{cm}^2$ area RHVFC.

Set	test[a]	$j_{\mathbf{appl}}$[b] $\mathrm{A\,m^{-2}}$	$Q_{\mathbf{V}}$ $\mathrm{mL\,min^{-1}}$	$Q_{\mathbf{H_2}}$ $\mathrm{mL\,min^{-1}}$
1	1$^{\mathrm{st}}$ ch	100	100	100
2	EIS	0	100	100
3 - 9	ch-dch	100, 200, 300, 400, 500, 1000, 1500	100	100
10	PC	40:120:3880, 4040, 4200, 4360	100	100
11	1$^{\mathrm{st}}$ ch	100	50	100
12	EIS	0	50	100
13 & 14	OCP	0	50	100
15 - 21	ch-dch	100, 200, 300, 400, 500, 1000, 1500	50	100
22	PC	40:120:3880, 4040, 4200, 4360	50	100
23	Cycling	700	50	30

[a] OCP: open circuit potential, ch-dch: charge-discharge, EIS: electrochemical impedance spectroscopy, PC: polarisation/power curve.
[b] $j_1 : \Delta j : j_2$ refers to current densities from j_1 to j_2 with increments of Δj.

of the cell.

Two Electrochemical Impedance Spectroscopy (EIS) tests were carried out at OCP conditions and a SOC of 100% for two flow rates of vanadium electrolyte (set 2 and 12). These EIS measurements were performed after the first galvanostatic charge (set 1 and 11) of freshly prepared solution of vanadium electrolyte at an applied current density of $100\,\mathrm{A\,m^{-2}}$. These two EIS measurements were carried out at galvanostatic mode with an AC current R.M.S value of $5\,\mathrm{mA}$ over a frequency range between $100\,\mathrm{mHz}$ to $1\,\mathrm{MHz}$, and considering 6 points per decade of frequency.

Two series of single-cycle charge-discharge cell potential tests were performed at constant current densities ranging from $100-1500\,\mathrm{A\,m^{-2}}$ for two flow rates of vanadium electrolyte (sets 3-9 and 15-21). OCP measurements were performed after the galvanostatic charge or discharge operation during each test. Polarisation and power characteristic curves (sets 10 and 22) were obtained at an initial SOC of 100% and for two flow rates of vanadium electrolyte. The selection of 100% SOC as initial SOC was made to enable comparison with the performance results previously reported in the literature (Dowd et al., 2017a; Yufit et al., 2013). These curves were obtained by performing a series of galvanostatic discharge steps at a constant current density ranging from 40 to $4200\,\mathrm{A\,m^{-2}}$ followed by a short OCP rest period after each discharge step. Finally, a cycling test of 51 continuous charge-discharge cycles (set 23) was performed over the course of 16 days at a constant current density of $700\,\mathrm{A\,m^{-2}}$, a flow rate of vanadium electrolyte of $50\,\mathrm{mL\,min^{-1}}$ and a hydrogen flow rate of $30\,\mathrm{mL\,min^{-1}}$. The cell was allowed to return shortly to OCP

before each charge or discharge operation.

An X-ray CT test and data analysis were carried out by Dr. Oluwadamilola Taiwo at Imperial College. Averaged microstructural parameters for the vanadium electrode were obtained by imaging a sample of Freudenberg H23 carbon paper using a laboratory X-ray CT system (Phoenix Nanotom S, GE Measurement and Control, MA, USA). A Freudenberg H23 sample of dimensions $834\,\mu\text{m} \times 1585\,\mu\text{m} \times 179\,\mu\text{m}$ was scanned at a resolution of $1\,\mu\text{m}$. Tomographic reconstruction of the acquired projection images was performed, followed by image pre-processing and segmentation of the resulting reconstructed volume that was carried out using commercial image processing software (Avizo) and an open source software (TaufactorCooper et al. (2016), ImageJ and Fiji). Figure 5.4 shows two views of the 3D porous electrode reconstructed from X-ray CT. Averaged values of microstructural parameters of porosity, fibre diameter, pore diameter, and specific surface were estimated and are summarised in Table 5.3. These averaged values were later used in the unit cell model as known property values of the electrode or bound values for the fitting parameters.

(a)   **(b)**
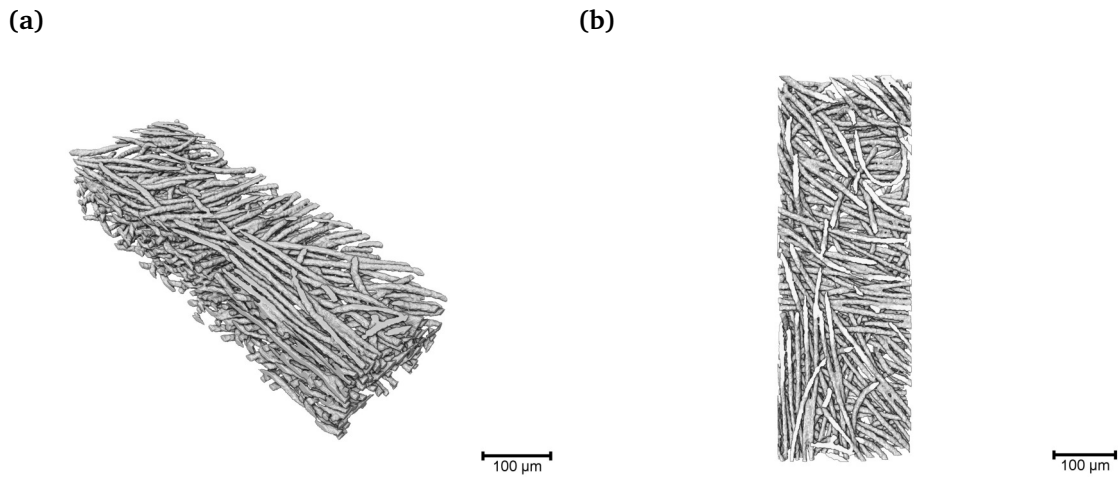
Figure 5.4: 3D image reconstructed from X-ray CT for Freudenberg H23 carbon paper: (a) Front view; and (b) Top view.

Table 5.3: Averaged microstructural parameters for Freudenberg H23 carbon paper.

Parameter	Value	Unit	Source
d_f^{ca}	7.92×10^{-6}	m	Experimentally determined - ImageJ, Fiji
d_p^{ca}	21.01×10^{-6}	m	Experimentally determined - ImageJ, Fiji
ε_{ca}	$0.79/0.79$	–	Experimentally determined - Avizo/TauFactor
$S_{\text{ca}}^{\text{geo}}$	$4.29/1.44 \times 10^5$	$\text{m}^2\,\text{m}^{-3}$	Experimentally determined - Avizo/TauFactor

5.4 Model calibration

The calibration of the modified unit cell model was developed in two stages, following the same approach described in Chapter 4. Firstly, the OCP data were used to calibrate the complete Nernst equation (Equation 4.53). Secondly, one set of experimental data of the single-cycle charge-discharge potential was used to fit selected model parameters for two different flow rates of vanadium electrolyte. A number of properties are required to inform the unit cell model, only additional properties are included in this chapter, any property value not included here can be found in Chapter 4. All physical property values are based on mean values reported in the literature for all-vanadium RFBs or PEM fuel cells.

5.4.1 Open circuit potential

The relation between open circuit potential and state of charge for the RHVFC was obtained in order to describe the equilibrium potential and is presented in Equation 4.53. Following the analysis developed in the previous chapter, the SOC of the cell (SOC_e) was calculated by comparing the experimental capacity increase at each galvanostatic charge or discharge step with respect to the theoretical maximum capacity of the solution (Q_{max}), which is given in Equation 2.29. Equation 5.14 presents the experimental SOC as a function of the initial SOC ($SOC(t_i)$), the time period ($t_f - t_i$) and the applied current (I_{appl}). This maximum capacity for our experimental set-up was of approximately $4342\,\mathrm{A\,s}$. Equation 5.15 presents the SOC of the cell calculated as a function of the concentration of reactants and products in the cathodic side.

$$SOC_e = SOC(t_i) + \frac{(t_f - t_i)I_{appl}}{Q_{max}} \tag{5.14}$$

$$SOC = \frac{c_{VO_2^+}}{c_{VO_2^+} + c_{VO^{2+}}} \tag{5.15}$$

During charge and discharge operation, changes in the concentration of all ionic species in the vanadium electrolyte occur due to the electron-transfer reaction, transport through the membrane, and acid dissociation(Knehr and Kumbur, 2011; Pino-Muñoz et al., 2017). The evolution of the concentration of species with respect to SOC was obtained as presented in Equation 4.77 to 4.81. Equation 5.16 presents the complete Nernst equation as a function of SOC_e, where $c_{H^+}^{0,ca}$ is the initial concentration of protons at the cathode, c_V is the total vanadium concentration, and S_d^{eq} is the change in concentration of sulphuric acid species due to the dissociation of bi-sulphate ions. In this equation, the partial pressure of hydrogen was considered constant since the system quickly reached a

steady-state condition at the anode side (Pino-Muñoz et al., 2017), and the global factor was fitted to match the experimental data. A comparison of the estimated E_{OCP} and experimental data of OCP for the $5\,\text{cm}^2$ area RHVFC is presented in Figure 5.5.

$$E_{\text{OCP}} = E_{\text{cell}}^{\circ} + \frac{RT}{F}\ln\left(\frac{SOC_{\text{e}}}{1 - SOC_{\text{e}}}\right) + \frac{RT}{2F}\ln\left(p_{\text{H}_2}^{\text{g}}\right) + \frac{RT}{F}\ln\left(c_{\text{H}^+}^{0,\text{ca}} + c_{\text{V}} \cdot SOC_{\text{e}} + S_d^{\text{eq}}\right)$$
$$+ \frac{RT}{F}\ln\left(F_{\gamma}\right)$$
$$(5.16)$$
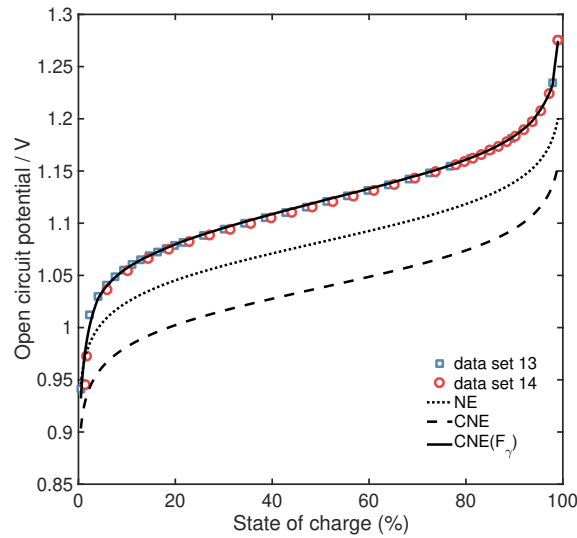
Figure 5.5: Comparison of experimental data of OCP with a Nernst Equation (NE), a Complete Nernst Equation (CNE) assuming unity activity coefficients for all species, and a CNE with a fitted global factor (F_{γ}), at a flow rate of vanadium electrolyte and hydrogen of 50 and $100\,\text{mL}\,\text{min}^{-1}$, respectively.

Figure 5.5 shows three different equations to estimate OCP, namely a complete Nernst equation (CNE) with a fitted global factor (F_{γ}), a complete Nernst equation assuming unity activity coefficients for all ionic species ($F_{\gamma} = 1$), and a Nernst Equation (NE) that does not include the potential difference between the electrolytes, namely the dialysis potential. As expected, the experimental data of OCP at different conditions of the flow rate of vanadium electrolyte displayed the same behaviour with respect to SOC, since at each OCP step the cell was allowed to reach equilibrium. The Nernst equation considerably underestimates the experimental OCP. The addition of the Donnan potential across both interfaces of the membrane (*i.e.*, the dialysis potential) acts to decrease the estimated OCP, which is even much lower than the experimental OCP. This decrease in potential is more significant for the RHVFC than is expected for a VRFB since the difference of concentration of protons between cathode and anode is higher in the case of the RHVFC, e.g., about $4\,\text{M}$ of difference. The concentration of protons in the anode of the RHVFC was considered to be equal to the fixed charge concentration in the membrane ($c_{\text{f}} = 1.2\,\text{M}$) to hold

electro-neutrality, while the concentration of protons in the cathode was higher than $5\,\mathrm{M}$ (initial sulphuric acid concentration). Effects that are usually neglected when modelling the OCP of RFBs, such as non-unity activity coefficients for the active ionic species, were represented by the global factor (F_γ).

5.4.2   Charge-discharge cycles

The first galvanostatic charge and EIS response of the RHVFC at two different flow rate of vanadium electrolyte are presented in Figure 5.6. The total capacity measured during this first charge (Figure 5.6a) was of 4598.6 and $4339.1\,\mathrm{A\,s}$ for a flow rate of vanadium electrolyte of 100 and $50\,\mathrm{mL\,min}^{-1}$, respectively. Table 5.4 summarises the initial vanadium concentration and expected and measured capacities for each operating condition. To calibrate the unit cell model, first, the electronic conductivity for the electrodes was estimated to be of about $500\,\mathrm{S\,m}^{-1}$ and the ionic conductivity of the membrane was calculated as a function of mean water content (Pino-Muñoz et al., 2017). Then, the electronic conductivity of the current collectors (σ_{cc}), including the flow fields plates, was estimated to be approximately $5000\,\mathrm{S\,m}^{-1}$, such that the cell series resistance was consistent with the series resistance (R_{s}) obtained from the initial EIS measurements (data sets 2 and 12). This series resistance includes the effect of contact resistance. Figure 5.6b presents the typical EIS response of the cell represented by a Nyquist plot, and obtained at OCP condition with a SOC of 100%. The measured series resistance corresponds to the sum of all the ohmic resistances of the cell, including electronic and ionic resistances, which also accounts for the current collectors (Yufit et al., 2013). Two depressed semi-circles are distinguished in the Nyquist plots, suggesting that at least two different processes were present when the cell was operated. The high-frequency process was attributed to charge transfer resistances, while the low-frequency process to diffusion in the porous media. Each one of these processes could reflect contributions from one or both electrodes, however, considering the fast kinetics of the hydrogen electrode and the high flow stoichiometry of hydrogen used, it would be reasonable to attribute the charge transfer resistances to the vanadium half-cell electrode kinetics (Yufit et al., 2013). An experimental value of the cell series resistance of approximately $0.50\,\Omega\,\mathrm{cm}^2$ was set to be a fixed parameter for all simulations. Changes in the simulated cell series resistance (R_{S}) were attributed to changes in the mean water content of the membrane (λ), which affects the membrane ionic conductivity (σ_{m}), the contact resistances between cell components, and possible degradation of the electrodes and membranes. It is expected that during charge, transport of water through the membrane by diffusion and electro-osmotic drag occurs towards the anode, and during discharge, the electro-osmotic drag flux changes direction towards the cathode while the diffusion flux maintains its direction towards the anode. This change in flux direction affects the mean water content of the membrane, which presents higher

values during charge than discharge operation. A higher mean water content in the membrane will increase the membrane conductivity and therefore reduce the total cell series resistance.

Table 5.4: Experimental and theoretical maximum capacity.

Q_V / mL min^{-1}	m / g	c_V / mol m^{-3}	Q_{max} / A s	Q_{max}^{exp} / A s	EU (%)
100	10.92	805	4660.2	4598.6	98.7
50	10.44	770	4457.6	4339.1	97.3

To quantify the relative contribution of the different processes present in the EIS responses, the equivalent circuit proposed by Yufit et al. (2013), and shown in Figure 5.6d, was fitted to both EIS data sets. The fitting procedure was developed considering the impedance modulus of the EIS data, $|Z|$, as a weighting factor. In the equivalent circuit, L represents the inductance behaviour and R_S the sum of the electronic and ionic resistances of all the cell components, including the current collectors. The resistance R_{CT} in parallel with the constant phase element CPE_{CT} emulate the charge transfer resistance of the vanadium electron-transfer reaction. While the last element, comprising another resistance R_{Diff} in parallel with the constant phase element CPE_{Diff}, was associated with the diffusion processes in the porous media. Equation 5.17 presents the cell impedance calculated in terms of the equivalent circuit components, where each fractional term on the right-hand side of the equation represents the impedance of a resistor and a constant phase element in parallel with characteristic time calculated as $\tau = \sqrt[n]{RQ}$. Where Q is a capacitance-like parameter and the exponent n usually has a value between 0 and 1, where 0, 1, and 0.5 represent a pure resistor, an ideal capacitor and a Warburg diffusion impedance, respectively (Yufit et al., 2013). The equivalent circuit, containing the elements discussed above, was fitted to the experimental data with an EC-lab software using a Levenberg-Marquardt algorithm. The equivalent circuit model predictions are included in Figure5.6b. Table 5.5 presents the fitted parameters of the equivalent circuit for the two flow rates of vanadium electrolyte (Q_V).

$$Z_{cell} = Lj\omega + R_S + \frac{R_{CT}}{1 + R_{CT}Q_{CT}(j\omega)^{n_{CT}}} + \frac{R_{Diff}}{1 + R_{Diff}Q_{Diff}(j\omega)^{n_{Diff}}} \tag{5.17}$$

The values of the different resistances are shown in Figure 5.6c. An increase in the flow rate of vanadium electrolyte from 50 to 100 mL min^{-1} produced a considerable decrease of 80.1% in the charge transfer resistance (R_{CT}) and a drop of 5.4% in the diffusion related resistance (R_{Diff}). Yufit et al. (2013) observed similar trends, but the change in R_{CT} ($\sim 25\%$ at 0% SOC and $\sim 9\%$ at 100% SOC) when increasing the flow rate of vana-

(a)

(b)

(c)

(d)
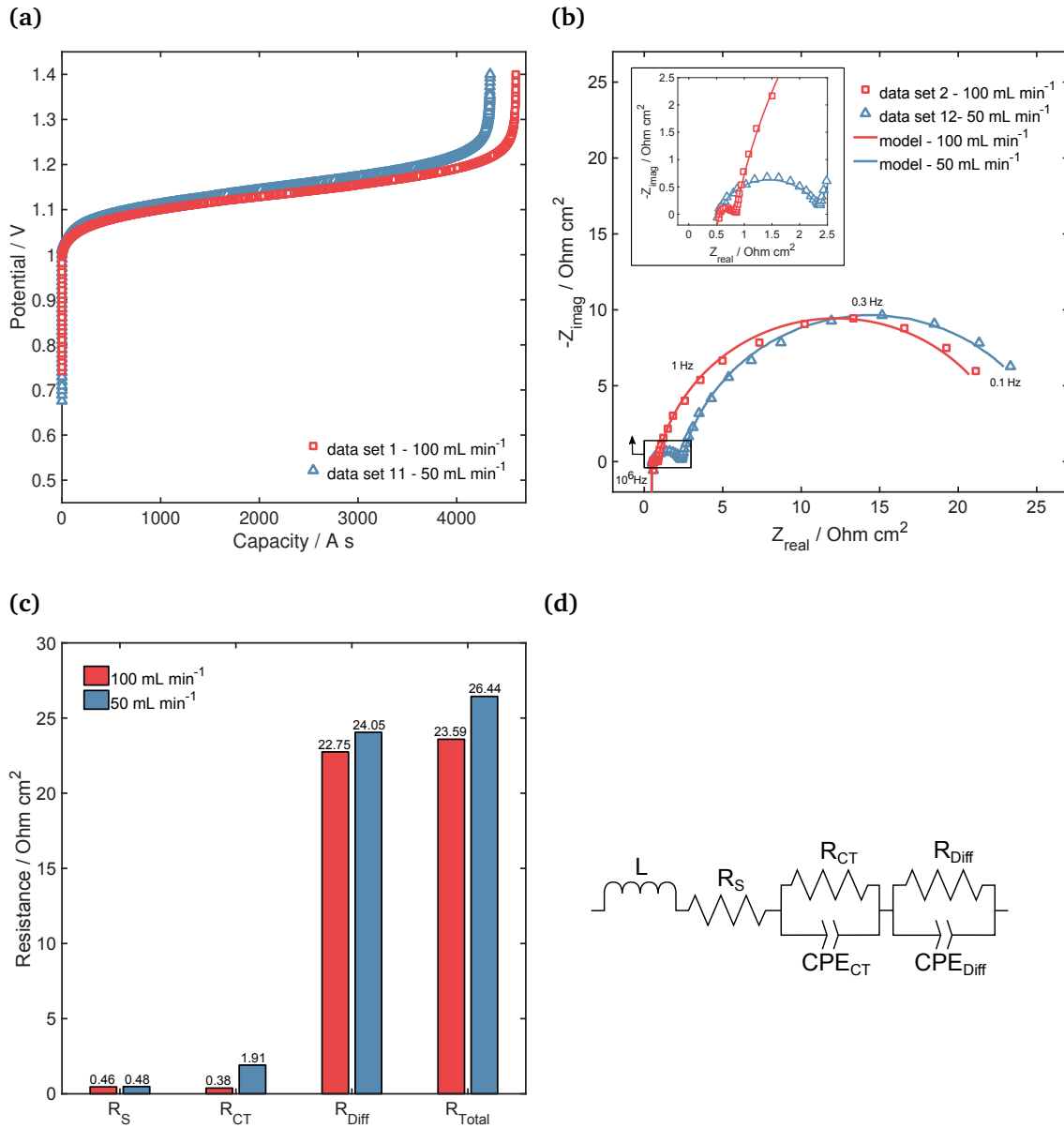
Figure 5.6: First galvanostaic charge and EIS response for the $5\,\mathrm{cm}^2$ RHVFC at a hydrogen flow rate of $100\,\mathrm{mL\,min}^{-1}$, and a flow rate of vanadium electrolyte of 100 and $50\,\mathrm{mL\,min}^{-1}$: (a) Galvanostatic charge at a current density of 100 A m^{-2}; (b) Nyquist representation of the cell EIS response at open circuit conditions and at SOC of 100%; (c) Estimated equivalent circuit parameters of resistance: series resistance (R_S), charge transfer resistance (R_{CT}), diffusion process resistance (R_{Diff}), and total cell resistance (R_{Total}); and (d) Equivalent circuit used to fit EIS experimental data.

Table 5.5: Fitted parameters of the equivalent circuit model of the $5\,\mathrm{cm}^2$ RHVFC at OCP conditions and 100% SOC, and a flow rate of hydrogen of $100\,\mathrm{mL\,min}^{-1}$.

Q_V	L	R_S	R_{CT}	Q_{CT}	n_{CT}	R_{Diff}	Q_{Diff}	n_{Diff}	τ_{CT}	τ_{Diff}
mL min^{-1}	nH	Ω	Ω	$\Omega^{-1}\mathrm{s}^n$	–	Ω	$\Omega^{-1}\mathrm{s}^n$	–	ms	ms
100	14.90	0.092	0.076	0.93×10^{-3}	0.72	4.55	0.10	0.88	0.0017	409
50	14.65	0.095	0.38	0.77×10^{-3}	0.74	4.81	0.10	0.86	0.017	427

dium electrolyte from 30 to $70\,\mathrm{mL\,min}^{-1}$ was not as significant as the one observed here, however, a different carbon electrode for the cathode was used. Dewage et al. (2016) ob-

served an almost constant charge transfer resistance for the EIS response of the whole cell, whereas for the EIS response of the vanadium half-cell a decrease of 13% was observed when the flow rate of vanadium electrolyte was increased from 50 to $200\,\mathrm{mL\,min^{-1}}$, also using a different cathode. In both of these works (Dewage et al., 2016; Yufit et al., 2013), a cathode with five times more cross-sectional area ($25\,\mathrm{cm^2}$), serpentine flow fields with a higher number of flow channels (5 channels) and a higher cell compression ($9\,\mathrm{N\,m}$) were used in comparison to those used in this work. These differences illustrate the sensitivity of the measured performance to the electrode/cell characteristics. In this work, the series, charge transfer and diffusion resistances were used to assist the model fitting procedure.

The fitting procedure of the single-cycle charge-discharge tests was developed in MAT-LAB® with absolute and relative tolerance set at 1×10^{-6}, using a non-linear least-squares solver (`lsqcurvefit` function) with upper (ub) and lower (lb) bounds for the fitting parameters (θ), as shown in Equation 4.82. Two sets of experimental data of single-cycle charge-discharge potential (set 7 and 19) obtained during galvanostatic operation at a current density of $500\,\mathrm{A\,m^{-2}}$ and two values of flow rates of the vanadium electrolyte, namely $100\,\mathrm{mL\,min^{-1}}$ and $50\,\mathrm{mL\,min^{-1}}$ were considered to calibrate the set of selected fitting parameters. The cell was assembled more than once during the experimental measurements, considering newly prepared components for the electrodes and the membrane, and therefore, different "cells" were considered to be obtained. Table 5.6 summarises the geometric and material properties for the cathode and anode electrodes, membrane, current collectors and single serpentine flow channel (Figure 5.7), considered in the unit cell model. An additional resistance (R), was taken into account to match the cell potential at the beginning of charge. This resistance was considered to be different for the operation at different flow rates of vanadium electrolyte with the value of R set to $0.94\,\Omega\,\mathrm{cm^2}$ and $0.34\,\Omega\,\mathrm{cm^2}$ for the operation at 50 and $100\,\mathrm{mL\,min^{-1}}$, respectively.
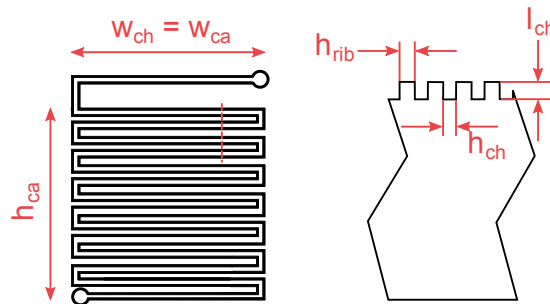
Figure 5.7: Single serpentine flow channel diagram for the $5\,\mathrm{cm^2}$ area RHVFC.

The fitting parameters were chosen to be the standard reaction rate constant of the vanadium electrode ($k_{\mathrm{ca,ref}}$, θ_1) and the active specific surface area of the vanadium electrode ($S_{\mathrm{ca}}^{\mathrm{ac}}$, θ_2). A grouped parameter ($K_{\mathrm{ca}} = S_{\mathrm{ca}}^{\mathrm{ac}} k_{\mathrm{ca,ref}}$, θ_{12}) for the vanadium electrode is

Table 5.6: Geometric and material properties for cell components of the $5\,\text{cm}^2$ area RHVFC.

Parameter	Value	Unit	Source
h_{ca}	0.024	m	Experimental set-up
w_{ca}	0.024	m	Experimental set-up
l_{ca}	210×10^{-6}	m	Fuel Cell Store (b)
l_{an}	235×10^{-6}	m	Fuel Cell Store (a)
l_{m}	127×10^{-6}	m	Fuel Cell Store (c)
l_{cc}	0.0127	m	Scribner Associates
h_{ch}	7.87×10^{-4}	m	Scribner Associates (Figure 5.7)
h_{rib}	8.64×10^{-4}	m	Scribner Associates (Figure 5.7)
l_{ch}	1.02×10^{-3}	m	Scribner Associates (Figure 5.7)
σ_{e}	500	$\text{S}\,\text{m}^{-1}$	Estimated
σ_{cc}	5000	$\text{S}\,\text{m}^{-1}$	Estimated (Figure 5.6b)
R_{an}	200	$\text{m}^2\,\text{m}^{-2}$	Assumed

also considered as an electrode parameter since the uncertainty on both parameters was considered, and a grouped parameter could ease the comparison between different electrode performances. Also selected as fitting parameters were the thickness of the Nernst diffusion layer at the vanadium electrode (δ^{ca}, θ_3), and the desorption rate constant of the Tafel reaction for the hydrogen electron-transfer reaction at standard conditions ($k_{\text{des}}^{\varnothing}$, θ_4). The grouped parameter (K_{ca}) included the effect of the electrode kinetics and the active specific surface area of the vanadium electrode. Although, a value for the total geometric specific surface area of the vanadium electrode ($S_{\text{ca}}^{\text{geo}}$, Table 5.3) was obtained by means of image analysis, its value is expected to be different to the actual value of the active specific surface area, which is related to the electrode active sites available for reaction (Kim et al., 2015). The heat treatment of the vanadium electrode affects the electrode kinetics as well as its total active area due to expected changes in the electrode wettability (Kim et al., 2015). An alternative option would have been to set the active specific area equal to the measured specific surface area ($S_{\text{ca}}^{\text{ac}} = S_{\text{ca}}^{\text{geo}}$) and only considered as a fitting parameter the standard rate constant of the electrode. A grouped parameter for the anode was not considered since the anode kinetic expression (Equation 4.68 to 4.71) is more complex and a simple substitution was not possible. Instead, an assumed value was considered for the roughness factor of the anode (R_{an}) and only the desorption rate constants of the Tafel reaction at standard conditions ($k_{\text{des}}^{\varnothing}$) were varied during the fitting. Upper and lower bounds were selected for each fitting parameter along with initial estimated guesses, which are summarised in Table 5.7.

Table 5.7: Fitting parameters of the unit cell model for a $5\,\mathrm{cm}^2$ area RHVFC.

Parameter	Unit	Lower bound	Upper bound	Initial guess	Fitted value $100\,\mathrm{mL\,min}^{-1}$	Fitted value $50\,\mathrm{mL\,min}^{-1}$
$k_{\mathrm{ca,ref}}$ (θ_1)	$\mathrm{m\,s}^{-1}$	1.0×10^{-12}	1.0×10^{-6}	$3.0 \times 10^{-9\,\mathrm{a}}$	1.19×10^{-10}	4.36×10^{-11}
$S_{\mathrm{ca}}^{\mathrm{ac}}$ (θ_2)	$\mathrm{m}^2\,\mathrm{m}^{-3}$	1×10^4	$S_{\mathrm{ca}}^{\mathrm{geo}}$	$3.0 \times 10^{4\,\mathrm{b}}$	4.09×10^5	4.11×10^5
K_{ca} (θ_{12})	s^{-1}	1×10^{-8}	0.429	9×10^{-5}	4.89×10^{-5}	1.79×10^{-5}
δ^{ca} (θ_3)	m	1×10^{-6}	$3 d_{\mathrm{p}}^{\mathrm{ca}}$	$d_{\mathrm{p}}^{\mathrm{ca}}/2$	1.25×10^{-5}	1.21×10^{-5}
$k_{\mathrm{des}}^{\varnothing}$ (θ_4)	$\mathrm{mol\,cm}^{-2}\,\mathrm{s}^{-1}$	1×10^{-7}	1×10^{-3}	$2.1 \times 10^{-5\,\mathrm{c}}$	2.08×10^{-5}	2.01×10^{-5}

[a] Knehr et al. (2012b)
[b] Gandomi et al. (2016)
[c] Kucernak and Zalitis (2016b)

It is important to mention that the fitting parameters were calibrated separately for the two flow rates of vanadium electrolyte. This decision was made based on the different EIS spectra obtained after the cell was first reassembled (Figure 5.6b), especially when considering the charge transfer process. The calibration results of cell potential as a function of time are presented in Figure 5.8a, including the predicted OCP by the complete Nernst equation (Equation 4.53), and parity plots for the measured and simulated cell potential with confidence intervals of 95% are presented in Figure 5.8b and 5.8c. These parity plots only include the data points considered in the fitting procedure, which was decided to favour the charge operation and the beginning discharge until a potential of approximately 0.9-1.0 V. This decision was made to capture most of the potential behaviour correctly and recognising the challenge of reproducing exactly the potential behaviour at very low or high SOC discharge. It can be observed in Figure 5.8b ans 5.8c that at potentials over $1.3\,\mathrm{V}$ the discrepancies between the observed and predicted cell potential are more significant, but still within an acceptable margin (of about $0.5\,\mathrm{V}$). However, during discharge and for potentials lower than about 0.9-1.0 V the discrepancies were more important and it was not possible to reconcile through the fitting procedure. Nonetheless, a good agreement was found between experimental data and modelled potentials, with Normalised Root-Mean-Square Errors (NRMSEs, Equation 3.18) of 0.8% and 10.6% for charge and discharge operation at a flow rate of vanadium electrolyte of $100\,\mathrm{mL\,min}^{-1}$, and NRMSEs of 0.9% and 11.9% for charge and discharge at a flow rate of vanadium electrolyte of $50\,\mathrm{mL\,min}^{-1}$. The fitted value of $k_{\mathrm{ca,ref}}$, $S_{\mathrm{ca}}^{\mathrm{ac}}$, δ^{ca} and $k_{\mathrm{des}}^{\varnothing}$ are summarised in Table 5.7. The values obtained for the fitted parameters were later used to simulate other operating conditions, while no additional fitting procedure was reconsidered.

5.4.3 Model parametric sensitivity

A parametric sensitivity analysis was performed considering only well fitted points of the different single-cycle charge-discharge curves (data set 3 to 9 and 15 to 21), *i.e.*, $e = |y -$

(a)

(b)

(c)
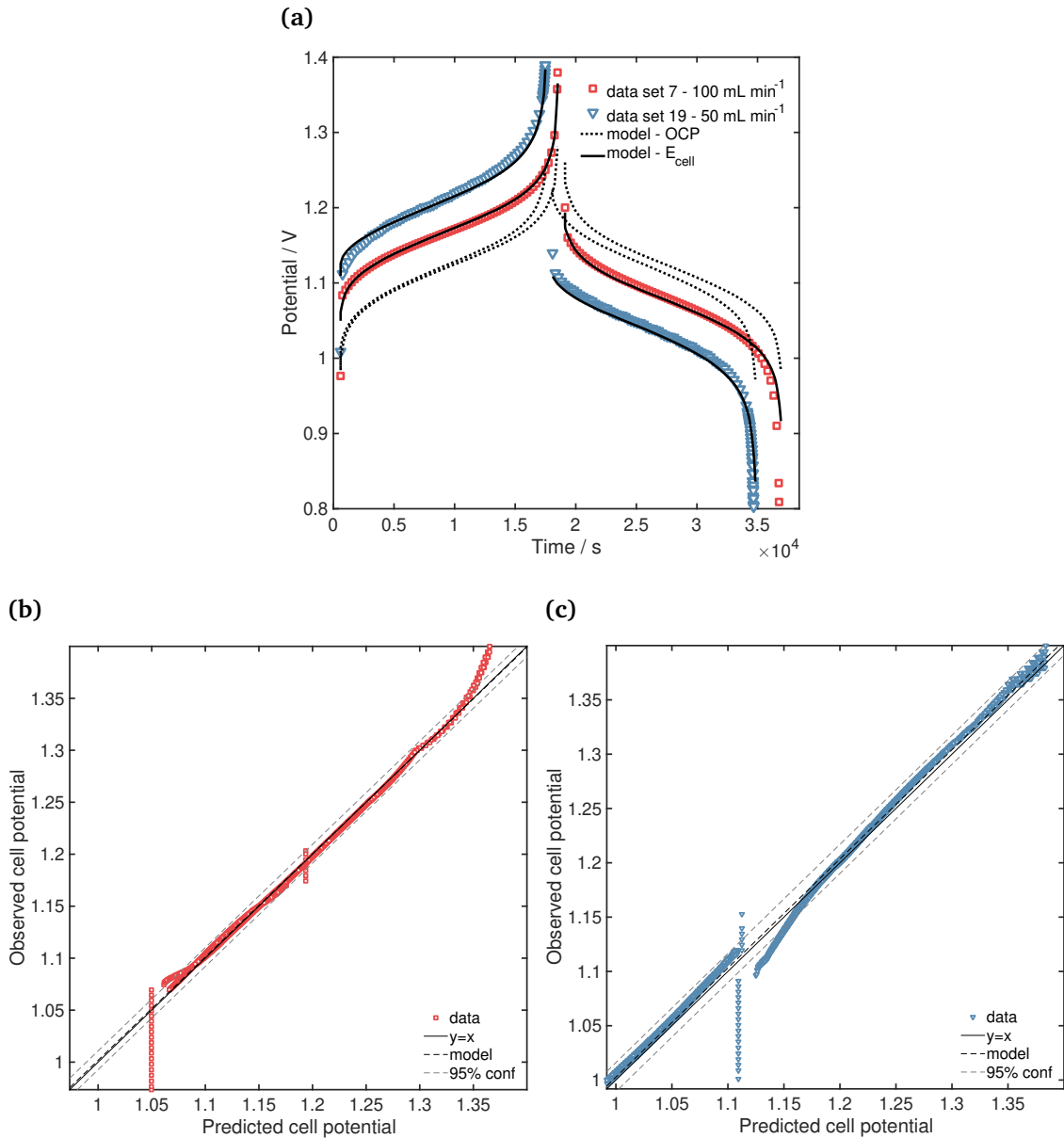
Figure 5.8: Single-cycle charge-discharge potential at a current density of $500\,\text{A m}^{-2}$, a hydrogen flow rate of $100\,\text{mL min}^{-1}$, and a flow rate of vanadium electrolyte of 100 and $50\,\text{mL min}^{-1}$: (a) Model calibration result. OCP refers to open circuit potential, and E_{cell} refers to the cell potential; (b) Parity plot with confidence intervals for a Q_V of $100\,\text{mL min}^{-1}$, set data 7; and (c) Parity plot with confidence intervals for a Q_V of $50\,\text{mL min}^{-1}$, set data 10.

$y_{\text{mod}}|/y < 0.025$ (Araya et al., 2007; Sacher et al., 2011). The average absolute sensitivity of the cell potential ($|G_i^{\text{ave}}|$) with respect to the fitting parameters (θ) were assessed for the different applied current densities during charge and discharge by means of Equation 5.18. These average absolute sensitivities were obtained considering the sensitivity coefficient (G_i) as a function of time (Sacher et al., 2011). This coefficient describes the small change of the output cell potential, E_{cell}, with respect to a small change in the fitting parameters, $\theta = [k_{\text{ca,ref}}, S_{\text{ca}}^{\text{ac}}, \delta^{\text{ca}}, k_{\text{des}}^{\varnothing}]$, at a given time during charge or discharge operation. These sensitivity coefficients were calculated using a central finite difference approximation as shown in Equation 5.19. Also, the normalised sensitivity coefficients (G_i^{nor}) were obtained

by means of Equation 5.20, after running simulations considering perturbations for each fitting parameter (Araya et al., 2007; Huerta-Pérez and Pérez-Correa, 2018).

$$|G_i^{ave}| = \int_0^{t_{max}} \frac{1}{t_{max}} \left| \frac{\theta_i}{E_{cell}^{max}} \cdot G_i(t) \right| dt \tag{5.18}$$

where,

$$G_i(t) = \frac{\partial E_{cell}(t)}{\partial \theta_i} = \frac{E_{cell}(t, \theta_i + \Delta\theta_i) - E_{cell}(t, \theta_i - \Delta\theta_i)}{2\Delta\theta_i} \tag{5.19}$$

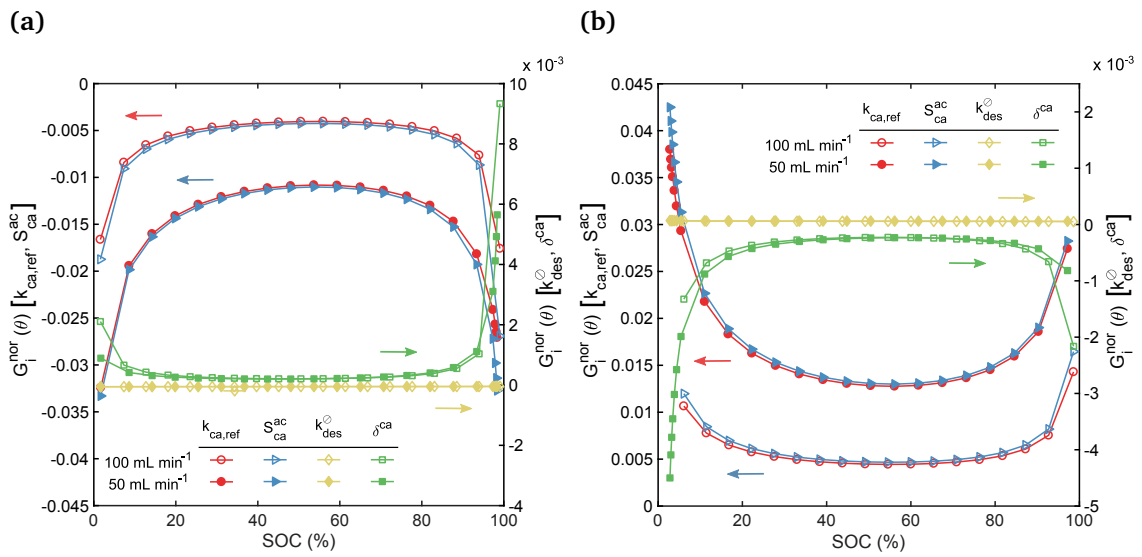$$G_i^{nor}(t) = \frac{\theta_i}{E_{cell}(t)} \cdot G_i(t) \tag{5.20}$$

Figure 5.9: Normalised sensitivity coefficient of fitting parameters as a function of SOC at a current density of $500\,A\,m^{-2}$ during: (a) Charge; and (b) Discharge.
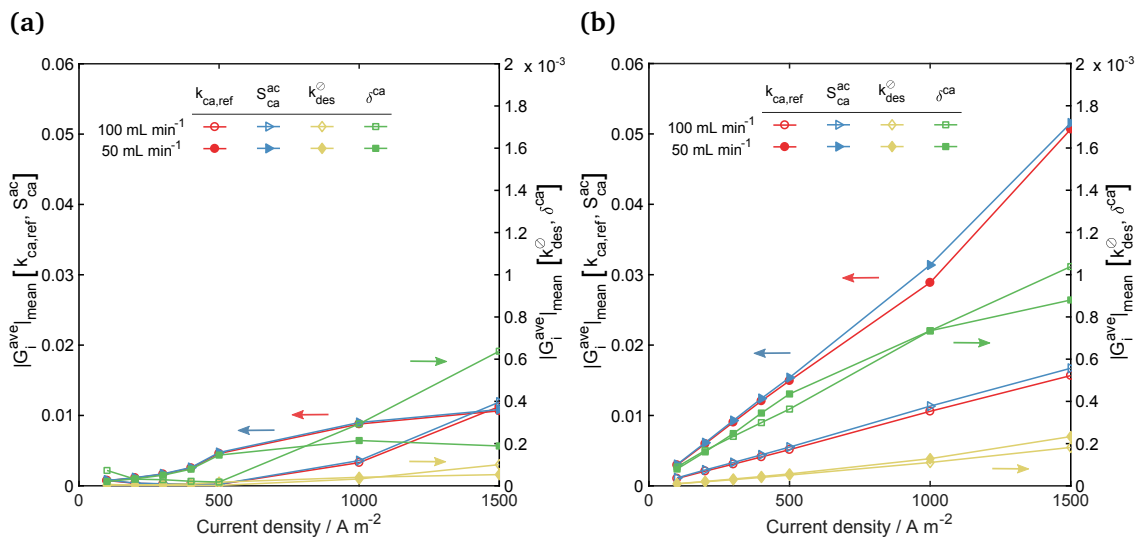

Figure 5.10: Average absolute sensitivity of fitting parameters along variations of current density during discharge operation during: (a) Charge; and (b) Discharge.

Figure 5.9 presents the normalised sensitivity coefficients as a function of SOC for the charge and discharge potentials at a current density of $500\,\mathrm{A\,m^{-2}}$ and the two flow rates of vanadium electrolyte, set 7 and 19. The cell potential during discharge increased with $k_{\mathrm{ca,ref}}$, $S_{\mathrm{ca}}^{\mathrm{ac}}$ and $k_{\mathrm{des}}^{\varnothing}$, and a stronger effect was observed at the low flow rate of the vanadium electrolyte for both fitting parameters. While the cell potential during discharge decreased with δ^{ca}, different flow rates of vanadium electrolyte presented a similar effect. At lower and higher SOCs the effect of $k_{\mathrm{ca,ref}}$, $S_{\mathrm{ca}}^{\mathrm{ac}}$ and δ^{ca} increases significantly with respect to the values at the intermediate region of SOC. These parameters are involved in the kinetic relation for the cathode (Equations 4.62 to 4.65), and a change in the parameters tends to have a higher effect in the extreme regions of SOC where the resulting overpotential is expected to be higher. The effect of $k_{\mathrm{ca,ref}}$ and $S_{\mathrm{ca}}^{\mathrm{ac}}$ was virtually the same for most of the SOC range, and only at very high or very low SOC did the effect of the active specific area for the electron-transfer reaction seem to have a higher impact on the cell potential. As expected a faster cathodic parameter K_{ca} will produce an increase in cell potential during discharge, i.e., a lower overpotential, while a thicker diffusion layer, δ^{ca}, will cause a decrease in the cell potential during discharge, i.e., a higher overpotential. Similar results with parameters having the opposite effect were obtained for the charging operation. Figure 5.10 shows the average absolute sensitivity as a function of the applied current density during charge and discharge operation. The effect of the fitting parameters on the cell potential during charge or discharge increased as the current density increased, with higher average absolute sensitivities during discharge. The average absolute sensitivity of the cell potential during discharge varied between 3×10^{-3} and 0.052 for $k_{\mathrm{ca,ref}}$ and $S_{\mathrm{ca}}^{\mathrm{ac}}$, 1.0×10^{-5} and 2.3×10^{-4} for $k_{\mathrm{des}}^{\varnothing}$, and 8.0×10^{-5} and 1.0×10^{-3} for δ^{ca}. The cell potential was consistently more sensitive to the cathodic kinetic parameters across the current densities, and at high current densities δ^{ca} became more significant.

5.5 RHVFC performance

5.5.1 Single-cycle charge-discharge cell potential

The performance of the RHVFC during the galvanostatic single-cycle charge-discharge operation was studied to evaluate the dependency of the cell polarisation with respect to the operating conditions tested. Using the previously fitted parameters, model predictions were compared to experimental data of single-cycle charge-discharge potentials at different current densities of 100, 200, 300, 400, 1000 and $1500\,\mathrm{A\,m^{-2}}$, and two values of the flow rate of vanadium electrolyte of 100 and $50\,\mathrm{mL\,min^{-1}}$. Figure 5.11 shows the model prediction of OCP and cell potential for a current density of 300, 500 and $1000\,\mathrm{A\,m^{-2}}$. A reasonably good agreement was found for all the current densities tested with NRM-

SEs (Table 5.8) for charge/discharge within the range of 0.77-14.19% / 2.92-26.99% and 2.11-11.40% / 3.55-18.10% obtained for a flow rate of vanadium electrolyte of 100 and $50\,\mathrm{mL\,min^{-1}}$, respectively. The discrepancies between model predictions and experimental data were more evident at the lower flow rate of the vanadium electrolyte during discharge, and at high current densities during charge. This could be related to an increase in the mass-transport effects at the cathodic side when using a lower flow rate of vanadium electrolyte due to a decreased transport of active ionic species to and from the porous electrode. The unit cell model only incorporates the mass-transport effects within the electrode pores, *i.e.*, the difference between concentration of ionic species in the bulk and at the electrode surface, while any effect due to transport of species from the serpentine flow channel to the electrode was not accounted for in the unit cell model, which considers a zero-dimensional approach. An increase in applied current density produces a faster depletion/generation of reactant/product species of the electron-transfer reaction at the cathode leading to increase mass-transport effects which could limit the cell performance and which were neglected in the unit cell model.

(a) **(b)**
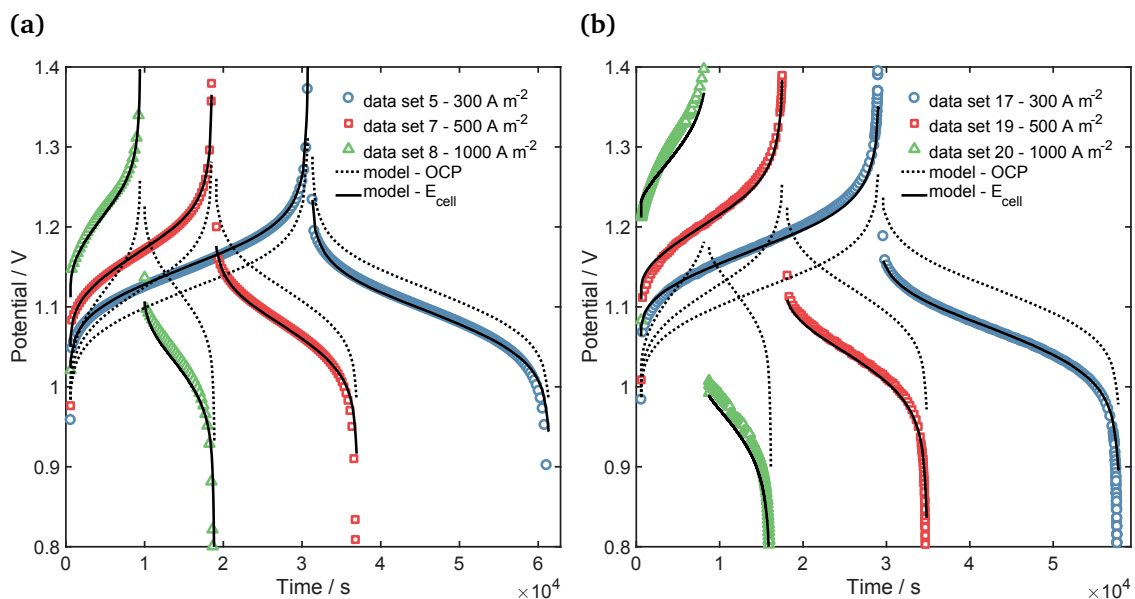
Figure 5.11: Comparison of experimental data of single-cycle charge-discharge potential with model testing at a current density of 300, 500 and $1000\,\mathrm{A\,m^{-2}}$ and a flow rate of hydrogen of $100\,\mathrm{mL\,min^{-1}}$ and vanadium electrolyte of: a) $100\,\mathrm{mL\,min^{-1}}$; and b) $50\,\mathrm{mL\,min^{-1}}$.

As observed in Figure 5.11, increasing the applied current density during the galvanostatic tests increases the total overpotential, which accounts for electrode and ohmic overpotentials. This produces a shorter time of operation, either for charge or discharge, since the cut-off potentials are reached sooner. When comparing tests at the same operating conditions of current density and different flow rates, an increase in the total overpotential is observed at the lower flow rate of vanadium electrolyte. This overpotential difference

Table 5.8: Normalised Root-Mean-Square Errors for galvanostatic single-cycle charge-discharge tests.

Set	$j_{\mathbf{appl}}$	NRMSEs - charge		NRMSEs - discharge	
	$\mathrm{A\,m^{-2}}$	$100\ \mathrm{mL\,min^{-1}}$	$50\ \mathrm{mL\,min^{-1}}$	$100\ \mathrm{mL\,min^{-1}}$	$50\ \mathrm{mL\,min^{-1}}$
3 & 15	100	1.00	3.69	2.92	3.55
4 & 16	200	0.77	3.37	4.06	14.40
5 & 17	300	0.99	2.72	5.24	17.47
6 & 18	400	0.99	2.22	9.11	18.10
7 & 19	500	1.023	2.11	13.53	18.04
8 & 20	1000	2.38	5.30	16.50	12.82
9 & 21	1500	14.19	11.40	26.99	10.34

increases with the applied current density. It is important to mention that the overpotential difference observed between different flow rates of vanadium electrolyte at the same applied current density (Figure 5.11) does not only includes the effect of flow rate, but also other effects since the cell characteristic were not exactly the same every time the cell was reassembled. The total overpotential was primarily affected by the cathode overpotential and ohmic overpotential, while the anode overpotential presented very small values due to the fast kinetics of the HER/HOR. This anode overpotential was estimated by Equation 4.68 considering only the effect of the change of hydrogen partial pressure in the CL, which was virtually constant with a value of $ca.1.0\,\mathrm{Pa}$. Figure 5.12a presents the evolution of the cathodic overpotential as a function of the SOC for the single-cycle charge-discharge operation at an applied current density of 500 and $1000\,\mathrm{A\,m^{-2}}$.

It is possible to observe that galvanostatic operation at a lower flow rate of vanadium electrolyte produces consistently higher cathodic overpotential when comparing the same SOC. As the current density increases the total change in SOC decreases, therefore, a lower capacity is accessed during operation of either charge or discharge. In particular, for the operation at $1000\,\mathrm{A\,m^{-2}}$ and the lower flow rate of vanadium electrolyte the SOC reached at the end of the charge operation is about 90%. Operation of the cell at very low ($< 5\%$) or very high ($> 95\%$) SOC, displayed a significant change in overpotential for a small change in SOC. This behaviour affected directly the prediction of cell potential, producing an important mismatch particularly at the end of discharge, namely low SOCs. In order to predict the cell potential accurately when operating at very low or high SOC, a model able to estimate with higher accuracy the evolution of the concentration of ionic species at extreme SOC conditions is required. Effects that are reasonably neglected for operation in an intermediate range of operation, $e.g.,$ $20\% < SOC < 80\%$, may well become more important at these extreme conditions and their inclusion may be required, such as the
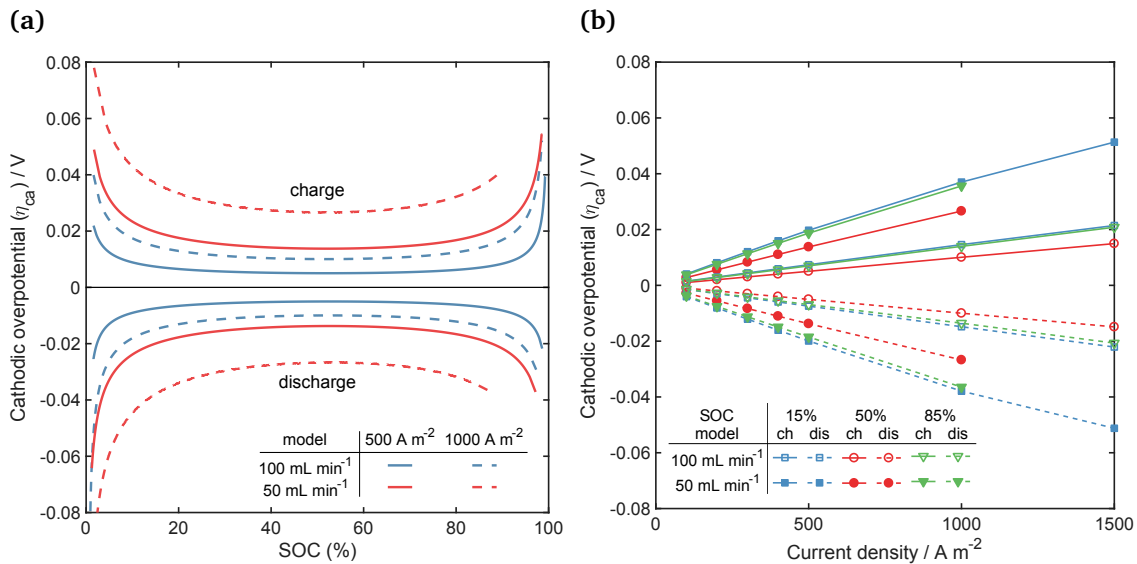
(a)

(b)

Figure 5.12: Cathodic overpotential (η_{ca}) during single-cycle charge-discharge operation at a flow rate of hydrogen of 100 mL min^{-1} and a flow rate of vanadium electrolyte of 100 and 50 mL min^{-1}: (a) η_{ca} as a function of SOC for an applied current density of 500 and 1000 A m^{-2}; and (b) η_{ca} as a function of the applied current density for a SOC of 15%, 50% and 85%.

non-ideal species behaviour and a concentrated solution theory for the transport of multiple species. Figure 5.12b presents the cathodic overpotential as a function of the applied current density for 3 values of SOC (15%, 50% and 85%). The cathodic overpotential at each SOC increased almost linearly with current density, displaying higher absolute values at low and high SOC which were virtually identical.

The change in ohmic overpotential also contributes to the cumulative change in total overpotential, where the membrane ohmic overpotential should contribute significantly. Figure 5.13 presents the mean membrane behaviour as a function of the applied current density at different flow rates of vanadium electrolyte. The mean water content of the membrane varied within a small range, namely $10.1 < \lambda < 11.4$ (Figure 5.13a), increasing during charge operation as the applied current density increased, and decreasing during discharge operation as the applied current density decreased. This behaviour corresponds with the transport phenomena considered for the transport of water through the membrane, which includes electro-osmotic drag and diffusive molar flux. The electro-osmotic drag produced a significant increase in the transport of water through the membrane as the current increased. During charge, the H^+ molar flux is established from the cathodic to the anodic half-cell, and therefore, the transport of water occurs also towards the anode increasing the mean water content of the membrane. During discharge, the opposite behaviour is established decreasing the mean water content of the membrane. As expected, the membrane resistance (R_m) presents an inversely proportional behaviour to the water content, changing within a small range of $0.24 < R_m < 0.27$ (Figure 5.13b). This change in membrane resistance produced a linear increase of membrane ohmic drop with current

density from approximately 2.4 to $38.4\,\mathrm{mV}$. The transport of water through the membrane was considered to affect directly the catholyte tank volume, which is presented in Figure 5.13c, decreasing during charge and increasing during discharge, with a net loss of catholyte solution during a single-cycle charge-discharge operation when comparing the initial catholyte volume to its value at the end of discharge.

(a)

(b)

(c)
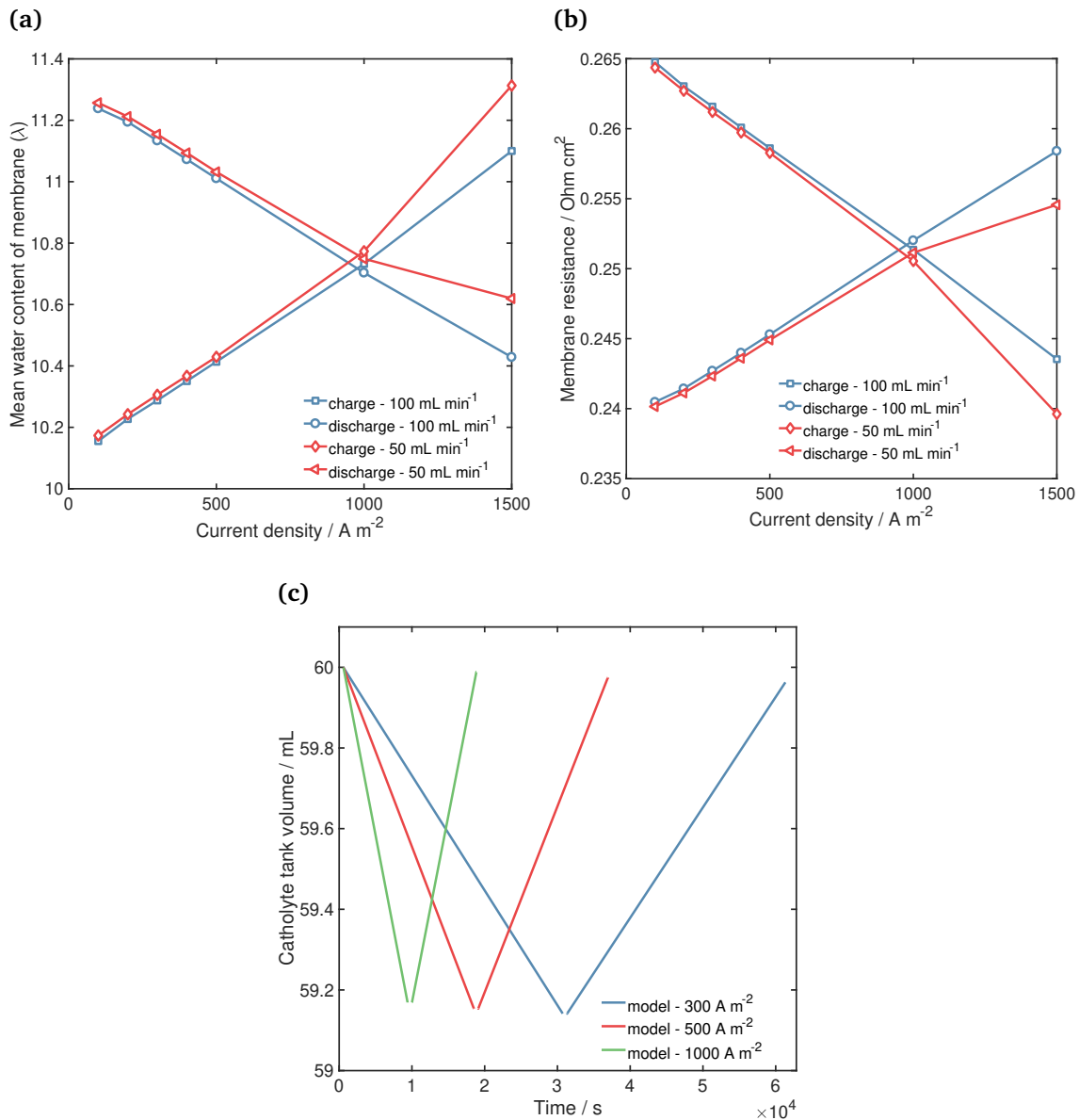
Figure 5.13: (a) Mean water content along variation of current density; (b) Mean membrane resistance along variation of current density; and (c) Evolution catholyte tank volume during charge and discharge at an applied current density of 300, 500 and $1000\,\mathrm{A\,m^{-2}}$ and a flow rate of hydrogen and vanadium electrolyte of $100\,\mathrm{mL\,min^{-1}}$.

Figures 5.14a, 5.14b and 5.14c present the evolution of species concentration in the cathode for different applied current densities at a flow rate of vanadium electrolyte of $100\,\mathrm{mL\,min^{-1}}$ for VO^{2+}, VO_2^+ and H^+, respectively. The evolution over time of the different concentrations was as expected, during charge depletion of VO^{2+} and accumulation of VO_2^+ and H^+ ocurred, while during discharge the opposite occurred. The effect of the

transfer current density was also observed in the surface concentration for VO^{2+}, VO_2^+ and H^+, which are also included in Figures 5.14a, 5.14a and 5.14c. During charge, the surface concentration of VO^{2+} was lower than its bulk concentration, while during discharge the opposite occurred. In the case of VO_2^+ and H^+, their surface concentrations were higher than their bulk concentration during charge and lower than their bulk concentration during discharge. Therefore, VO_2^+ and H^+ were produced at the electrolyte/electrode interface and their transport occurred from the electrode surface to the bulk during charge, while VO^{2+} was consumed at the electrolyte/electrode interface and its transport occurred from the bulk to the electrode surface. Figure 5.14d shows the difference in concentrations between their value at the electrode surface and the bulk, *i.e.*, $\Delta c = c^s - c^b$, as a function of applied current density and at a flow rate of vanadium electrolyte and hydrogen of $100\,\mathrm{mL\,min^{-1}}$. Similar trends were observed at a flow rate of vanadium electrolyte of $50\,\mathrm{mL\,min^{-1}}$. The concentration difference depended linearly on the applied current density, showing a small value for protons than for the vanadium species as expected from the pore transport equations (Equation 4.63, 4.64 and 4.65).

Figure 5.15 displays the dependency on SOC of the crossover fluxes of vanadium species, which were multiplied by Faraday's constant. During discharge, the transport of species happened from anode to cathode, while during charge the opposite occurred. This was expected from the analysis presented in Section 5.2, where it was observed that for the transport parameters used in this model the crossover flux of ionic species was primarily affected by the electro-osmotic drag, followed by the migration, and both of these fluxes follow the current direction. The dependency of the crossover fluxes with SOC was related to a change in the concentration of ionic species. During charge, it is possible to observe that for very low values of concentration of ionic species at the cathode, the total crossover flux was directed towards the cathode until a certain value of concentration was reached when the crossover flux change its direction towards the anode, which was maintained for most of the charge operation. Low values of concentration of ionic species at the cathode were expected to reduce the migration and electro-osmosis crossover fluxes, while increasing the concentration difference between both membrane ends, increasing the diffusive crossover flux with direction towards the cathode. This behaviour was directly related to the concentration values set at the anodic CL that for the simulation presented in this chapter were of $c_{VO^{2+}}^{CL} = 0.7c_V$ and $c_{VO_2^+}^{CL} = 0.4c_V$ in order to obtain the best possible fitting of the cycling data.

Commonly, four figures of merit are used to indicate the performance of charge-discharge tests in electrochemical cells (Tang et al., 2014; Zhao et al., 2006; Zheng et al., 2014b). These figures of merit are the coulombic (η_C), voltage (η_V), and energy (η_E) efficiencies, and the electrolyte utilisation (EU), previously defined in Chapter 2. Fig-

(a)

(b)

(c)

(d)
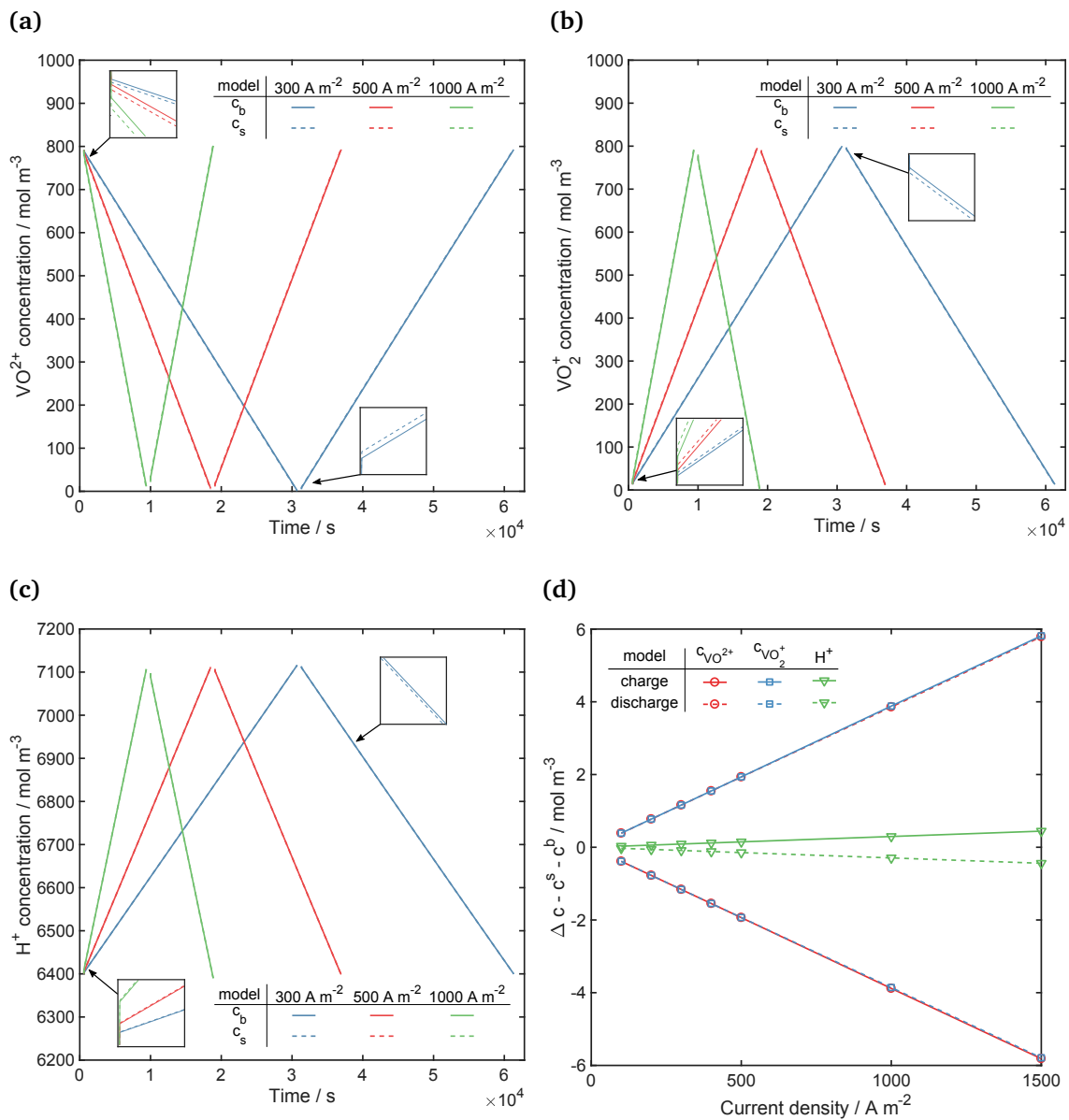
Figure 5.14: Evolution of species concentration against time in the cathode during charge and discharge at an applied current density of 300, 500 and $1000\,\mathrm{A\,m^{-2}}$ and a flow rate of vanadium electrolyte and hydrogen of $100\,\mathrm{mL\,min^{-1}}$: (a) $\mathrm{VO^{2+}}$; (b) $\mathrm{VO_2^+}$; and (c) $\mathrm{H^+}$. (d) Concentration difference at electrode surface and bulk as a function of the applied current density.

ures 5.16a and 5.16b present the coulombic, energy and voltage efficiencies, and the electrolyte utilisation during discharge, respectively. The performance features of the RHVFC were consistently better at the highest flow rate of the vanadium electrolyte of $100\,\mathrm{mL\,min^{-1}}$, when compared to the performance at a flow $50\,\mathrm{mL\,min^{-1}}$. The coulombic efficiencies at a flow rate of vanadium electrolyte of $100\,\mathrm{mL\,min^{-1}}$ were over 99%, with a lowest value of 98.2% at an applied current density of $1500\,\mathrm{A\,m^{-2}}$. This suggests that the rate of self-discharge of the cell due to the crossover of ionic species was not important for the experimental current densities and single-cycle test times used. At the lower flow rate, a moderate decrease in coulombic efficiency at high current densities was observed. This coulombic efficiency drop could be related to the fact that the system displayed a mass-
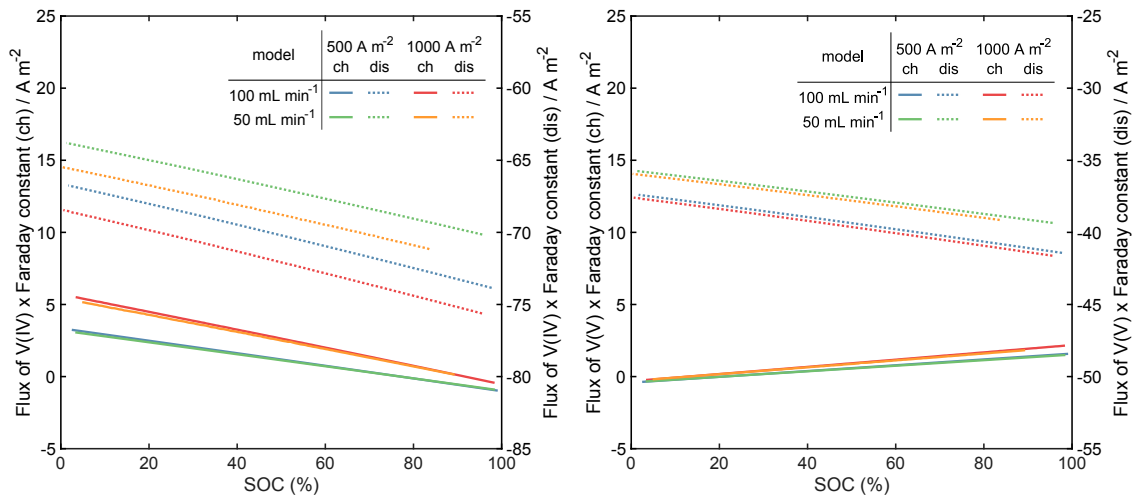
Figure 5.15: Crossover flux during charge and discharge as a function of SOC for an applied current density of 500 and 1000 $A\,m^{-2}$ and a flow rate of hydrogen of 100 $mL\,min^{-1}$ and vanadium electrolyte of 100 and 50 $mL\,min^{-1}$: a) V(IV); and b) V(V).

transport limited behaviour quite early on when using a flow rate of vanadium electrolyte of 50 $mL\,min^{-1}$.
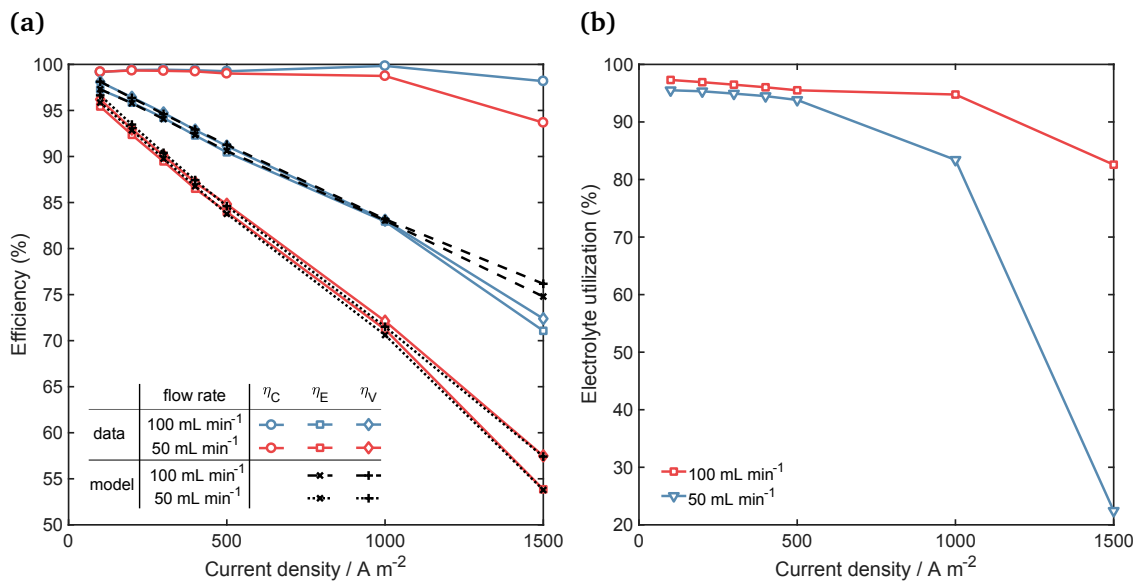
Figure 5.16: Figures of merit for cell tests along variations of applied current density at a flow rate of vanadium electrolyte of 100 and 50 $mL\,min^{-1}$, and a hydrogen flow rate of 100 $mL\,min^{-1}$: (a) Coulombic, energy and voltage efficiency during single-cycle charge-discharge operation; and (b) Experimental electrolyte utilisation during discharge operation.

The voltage efficiency showed a virtually linear trend with respect to current density for both flow rates. The voltage efficiency decreased as the applied current density increased. For the high flow rate, the lowest current density of 100 $A\,m^{-2}$ reached a voltage efficiency of 98.1%, while the highest current density of 1500 $A\,m^{-2}$ resulted in a value of only 72.4%. The voltage efficiency was lower for the low flow rate of vanadium electrolyte, with a value of 57.5% at a current density of 1500 $A\,m^{-2}$. This difference in voltage effi-

ciency tends to rise with the increase in the applied current density. An increase in overpotential was observed in the measured potential at the low flow rate of vanadium electrolyte and high current densities, as can be observed in Figure 5.11. This increased overpotential could be explained by poor mass-transport conditions at the cathodic half-cell along with additional overpotentials that could appear at the anodic half-cell in relation to the water management in the CL. The simulated voltage and energy efficiencies for all the current densities tested is also included in Figure 5.16a. No significant discrepancy was observed between the observed and predicted values, and only a mismatch at the highest current density was displayed. The electrolyte utilisation during discharge at low current densities, *e.g.*, $<500\,\mathrm{A\,m^{-2}}$, were very similar, with a mean value of 95.6%, for the high and low flow rates of vanadium electrolyte. A consistently lower electrolyte utilisation during discharge at a flow rate of vanadium electrolyte of $50\,\mathrm{mL\,min^{-1}}$ was observed. For this flow rate a minimum value of electrolyte utilisation of 22.4% at a current density of $1500\,\mathrm{A\,m^{-2}}$ was observed, while the value rose to 82.6% at the higher flow rate of vanadium electrolyte of $100\,\mathrm{mL\,min^{-1}}$. It is worth mentioning that the operating time and current density used at each galvanostatic single-cycle charge-discharge test were inputs of the models, and as such, the coulombic efficiency and electrolyte utilisation matched perfectly with the experimental values obtained. The model predicted the voltage and energy efficiencies well, only showing minor discrepancies at the higher current densities.

5.5.2 Effect of cell component properties

The implementation of the unit cell model required a number of component properties, whose values were assumed as known. These properties were extracted from the literature published for VRFBs and PEM fuel cells and can be found in Table 5.6 or Chapter 4. Also required by the model are the operating conditions used in every experiment, such as the initial concentration of vanadium and sulphuric acid species, vanadium electrolyte volume in the tank, the inlet pressure of hydrogen, flow rates of vanadium electrolyte and hydrogen, temperature, and applied current density. The effect of material property values and operating conditions on the cell potential was assessed by means of a relative sensitivity factor. An analysis of the influence of some of the properties (P) on the output cell potential was carried out by consecutively changing their standard value (P_i^0) by 5% and 10% to a modified value P_i^+. This change in the parameter value resulted in a relative change in the variable of interest, which in this case is the cell potential, $\partial E_{\mathrm{cell}} = (E_{\mathrm{cell}}^+ - E_{\mathrm{cell}}^0)/E_{\mathrm{cell}}^0$. A factor ($f_{\mathrm{rel}}$) was obtained to quantify the relative sensitivity of the cell potential (simulation target) with respect to changes in the standard values of components properties and operating conditions. Equation 5.21 was used to obtain these relative factors in a similar fashion to G_i^{nor}, Equation 5.20 . A value of $f_{\mathrm{rel,\,i}} = 1$ indicates direct proportionality between the model parameter and the simulation target (Vogler et al., 2009). This analysis

can also provide guidelines to determine for which parameters an independent validation is important (Vogler et al., 2009), for example parameters with values of $f_{\text{rel, i}} > 0.1$. It is important to consider that in reality a change in a particular property most probably will affect the value of other properties, when considering, for example, microstructural properties (Bertei et al., 2014). As such, the analysis is intended as a numerical exercise to evaluate the relative importance of each individual property on the target output of the model. Figure 5.17 reports the relative sensitivity of the cell potential with respect to a relative change in the value of properties during discharge operation at a current density of $500\,\text{A}^2\,\text{m}^{-1}$. As expected, the cell potential during discharge increased, i.e., showed a lower total overpotential, as the kinetic rate constants ($k_{\text{ca,ref}}$ and $k_{\text{des}}^{\varnothing}$), the active specific area of the electrodes ($S_{\text{ca}}^{\text{ac}}$ and R_{an}), and the component conductivities (σ_{k}) increased. A similar effect was observed for the cathode thickness (l_{ca}), the porosity of the cathode (ε_{ca}) and the volume fraction of polymer electrolyte in the membrane (ε_{m}). On the other hand, the cell potential during discharge decreased, i.e., it showed a higher total overpotential, as the porosity of the GDL (ε_{GDL}), the thickness of the membrane and GDL (l_{m} and l_{GDL}), and the cathodic transfer coefficient of the cathode kinetics (α_{c}) increased. Similarly, the cell potential during charge was affected by the properties, but in general, the opposite effect was observed.

$$f_{\text{rel, i}} = \frac{P_{\text{i}}}{E_{\text{cell}}(t)}\frac{\partial E_{\text{cell}}(t)}{\partial P_{\text{i}}} = \frac{P_{\text{i}}^0}{E_{\text{cell}}^0(t)}\frac{(E_{\text{cell}}^+(t) - E_{\text{cell}}^0(t))}{P_{\text{i}}^+ - P_{\text{i}}^0} \tag{5.21}$$
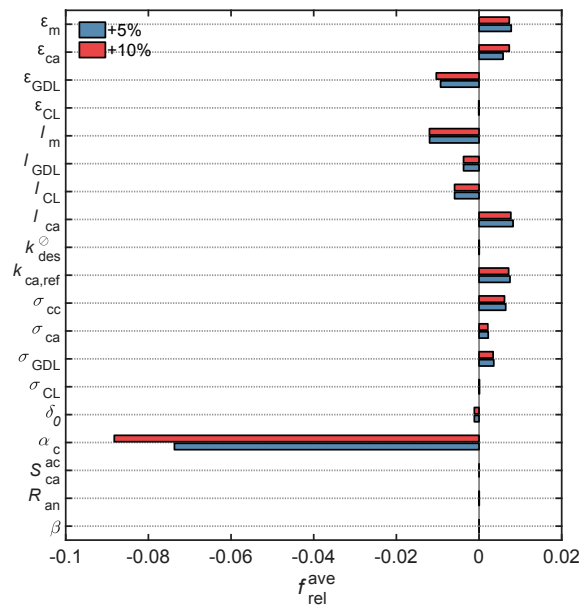
Figure 5.17: Average relative sensitivity of the model prediction of cell potential during discharge operation at a current density of $500\,\text{A}\,\text{m}^{-2}$ with respect to a relative change of 5% and 10% of component property values.

Most of these trends seemed obvious when considering the effect of each property in

the ohmic, cathodic or anodic overpotential (Pino-Muñoz et al., 2017), but interestingly only a subgroup of properties affect the potential response considerably. Among these properties, the transfer coefficient of the kinetic relation for the cathode and its porosity, and the membrane thickness, have a major influence on the discharge cell potential (Figure 5.18).
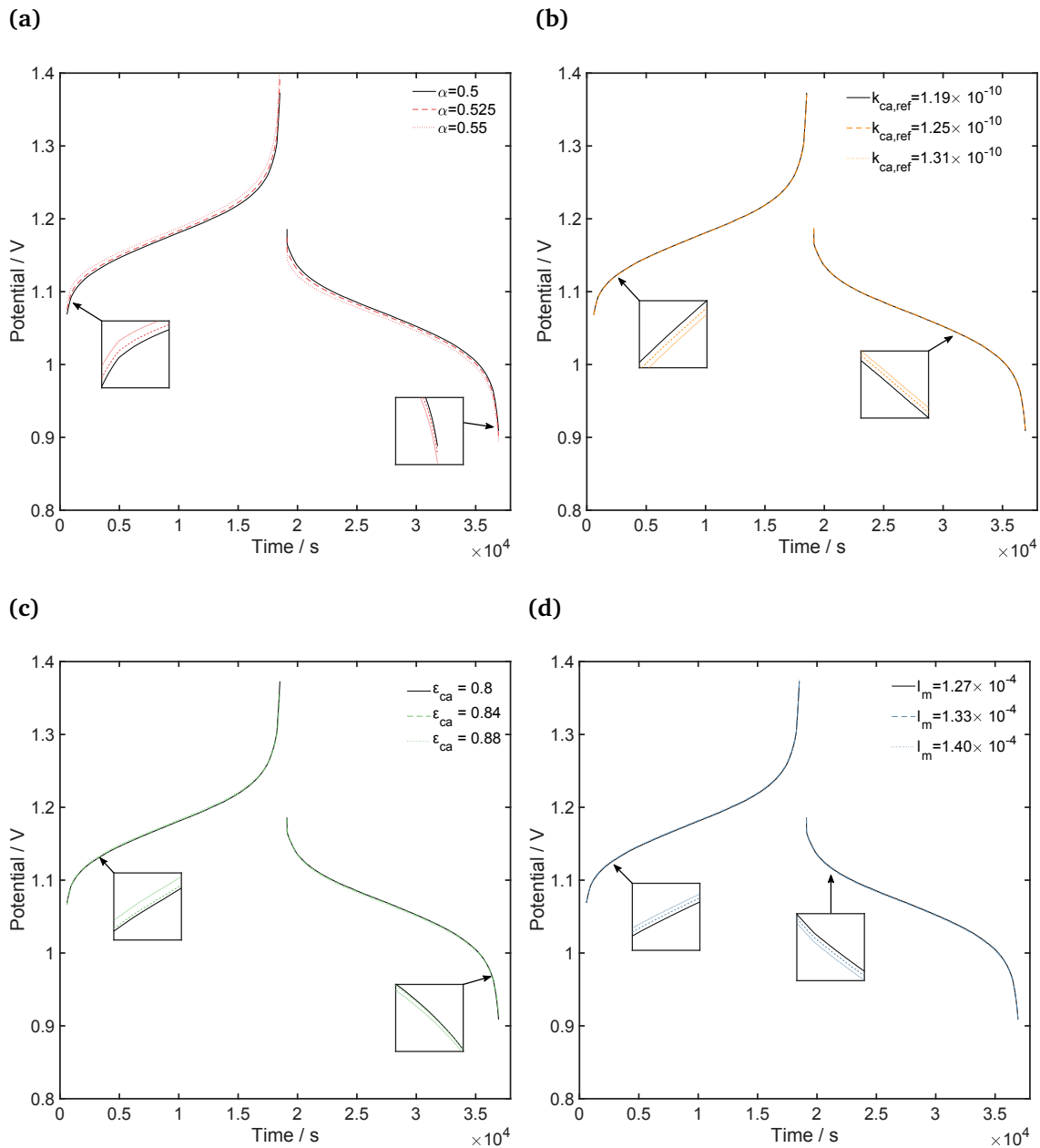
Figure 5.18: Effect on cell potential for a relative change of 5% and 10% of: (a) Transfer coefficient of cathode; (b) Standard reaction rate constant of cathode; (c) Cathode porosity; and (d) Membrane thickness.

The effect of the porosity of the cathode is mostly related to how this property affects the effective conductivity of the cathode, while the transfer coefficient of the cathodic reaction affects the cathode overpotential response. The effect of the membrane thickness is directly related to the crossover of ionic species and water. This study suggests that care

should be taken when selecting the values of porosity and transfer coefficient to reduce the uncertainty of these parameters. Thus, it is recommended to conduct a kinetic study of the relationship between current density and overpotential for the cathode, namely a Butler-Volmer relation (Equation 4.62), at more practical concentrations of vanadium and sulphuric acid such as the ones used in this work (0.8 M of vanadium sulphate hydrate dissolved in 5 M H_2SO_4). On the other hand, it is important to consider a more detailed description of the species and water transport through the membrane and the anode, to understand the dominant phenomena involved and its effect on the cell performance.

5.5.3 Polarisation and power curves

Polarisation curves using the unit cell model were obtained for a wider range of current density values and the two flow rates of vanadium electrolyte. Figure 5.19 presents the experimental polarisation and power curves obtained for the 5 cm^2 RHVFC at an initial SOC of 100%. During discharge at the low flow rate of $50\,mL\,min^{-1}$, mass-transport effects were observed from around $500\,A\,m^{-2}$ with a limiting current density over $3652\,A\,m^{-2}$ and peak power density of 1930 $W\,m^{-2}$. When a high flow rate of vanadium electrolyte of $100\,mL\,min^{-1}$ was used, there was a significant increase in performance, with a peak power density of $2840\,W\,m^{-2}$ and a limiting current density over $4200\,A\,m^{-2}$. This higher performance could be attributed to an improved transport of active species to and from the porous electrode. Dowd et al. (2017a) reported similar performance with a cell of $9\,cm^2$ flow field area at an initial SOC of 90% with a membrane electrode assembly consisting of a carbon paper cathode, a Pt coated carbon paper anode and an N115 membrane. A peak power density of $1680\,W\,m^{-2}$ at a current density of $2700\,A\,m^{-2}$ and a limiting current density above $3500\,A\,m^{-2}$ for a flow rate of vanadium electrolyte of $12\,mL\,min^{-1}$ was reported. Model predictions of polarisation curves are also included in Figure 5.19, indicating the validated range of the current density, in which single-cycle charge-discharge tests were available. At high current densities, the model differed from the experimental data, displaying slightly lower performances than the ones experimentally obtained. This behaviour occurred approximately from $2500\,A\,m^{-2}$ at the low and high flow rates of the vanadium electrolyte. It is worth mentioning that the model was calibrated with experimental data of a single-cycle charge-discharge potential at current densities in the range of 100 to $1500\,A\,m^{-2}$. For the single-cycle charge-discharge tests only current densities up to 1500 A m^{-2} were used since for the experimental set-up employed in this work higher current densities produced lower electrolyte utilisations, which was more significant at lower flow rates of vanadium electrolyte (Figure 5.16). The mismatch at high current densities could be explained by additional transport phenomena that may well have appeared during operation at high current densities. These additional phenomena could be related to anodic mass-transport limitations related to transport of water across the mem-

brane and the anode, and the intensified crossover of ionic species. Additional data of charge-discharge operation at higher current densities ($>1500\,\mathrm{A\,m^{-2}}$) is required to study these phenomena, as well as to calibrate or modify the model for a wider range of current densities. Figure 5.20 presents the detailed overpotential contributions to the total cell polarisation along variations of the applied current density. Here, the anodic overpotential was negligible when compared with the cathodic overpotential contribution, and as the applied current density increased the ohmic overpotential became more significant, while the region controlled by mass-transport limitations was not clearly reached in this study either for the model simulations nor the experimental data. It is important to mention that the total ohmic overpotential was considered different for the operation at different flow rates of vanadium electrolyte of 100 and $50\,\mathrm{mL\,min^{-1}}$ since the experimental set-ups were considered to be different. This is, the cell components, namely electrodes and membrane, were prepared independently, and the cell was reassembled at each one of these operating conditions. Also, even when the initial cell resistance measured from EIS was virtually equal for both flow rates of vanadium electrolyte, an additional resistance was added to the fitting procedure to match the cell polarisation at the beginning of charge.
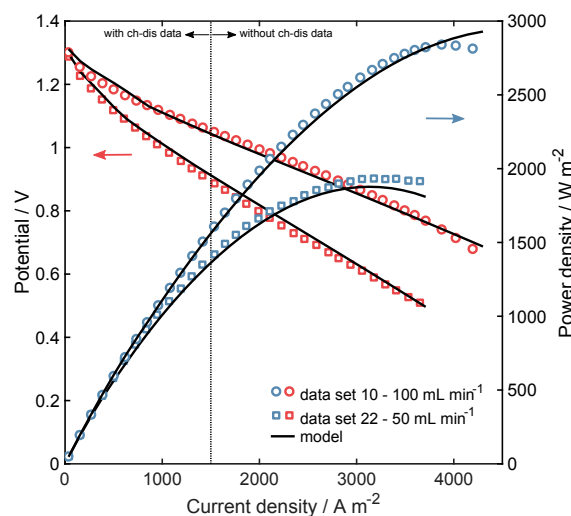
Figure 5.19: Comparison of model predictions with polarisation data at an initial SOC of 100%, a flow rate of vanadium electrolyte of 50 and $100\,\mathrm{mL\,min^{-1}}$, and hydrogen flow rate of $100\,\mathrm{mL\,min^{-1}}$. Two current density ($j$) regions: a validated region ($j \leq 1500\,\mathrm{A\,m^{-2}}$), where the model was fitted to charge-discharge (ch-dis) data, and a more uncertain region ($j > 1500\,\mathrm{A\,m^{-2}}$), where charge-discharge data were not available.

On the other hand, Figure 5.21 shows the evolution of the concentration of vanadium species and SOC as a function of the applied current density during the polarisation test at a flow rate of vanadium electrolyte of $100\,\mathrm{mL\,min^{-1}}$. Similar behaviour was observed for the polarisation test obtained at the lower flow rate of vanadium electrolyte. This polarisation test was obtained by running a series of OCP steps, each one of them followed by a discharge step. The mean values of concentrations and SOC in the cathodic half-
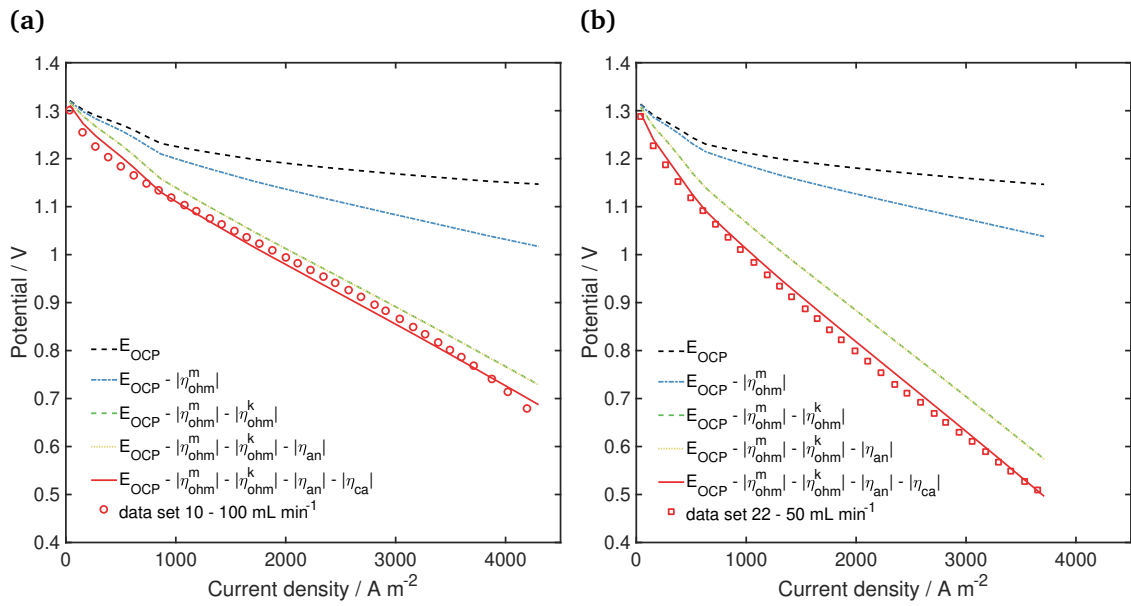
Figure 5.20: Detailed overpotential contributions in the RHVFC at an initial SOC of 100%, a flow rate of hydrogen 100 mL min^{-1} and a flow rate of vanadium electrolyte of: a) 100 mL min^{-1}; and b) 50 mL min^{-1}. Where, E_{OCP} is the open circuit potential, η_{ohm}^{m} is the ohmic overpotential of the membrane, η_{ohm}^{k} is the ohmic overpotential of all other components, and η_{an} and η_{ca} are the anodic and cathodic overpotentials.
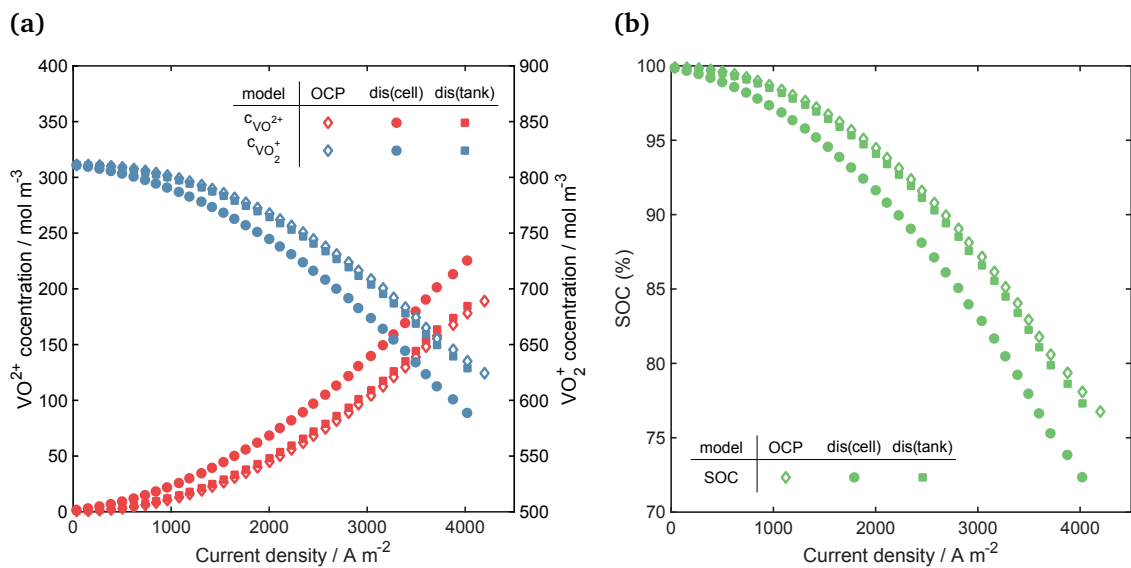
Figure 5.21: Simulated mean behaviour as a function of the applied current density during polarisation test (data set 10) at a flow rate of vanadium electrolyte of 100 mL min^{-1}: a) Concentration of VO^{2+} and VO_2^+; and b) SOC.

cell and catholyte tank for the discharge steps are displayed in Figure 5.21. As expected, during the OCP steps the system return to equilibrium fairly quickly, displaying the same values of concentrations for ionic species in the cathodic half-cell and catholyte tank, and therefore, the same SOC. It is important to realise that the mean SOC at OCP conditions changed from 100% to 76.6% during the polarisation test, while the mean SOC during discharge operation changed from 100% to 72.2% for the cathodic half-cell and from 100% to 77.1% for the catholyte tank. Care must be taken when referring to Figure 5.19 as

the characteristic plot of polarisation and power density at a particular SOC. Unlike PEM fuel cells, which can reach a steady-state operating condition and whose characteristic curves reflect a unique SOC, the operation of redox flow batteries is inherently transient which produces a changing SOC. In order to achieve a constant SOC during an RFB polarisation test, different experimental modifications for laboratory-scale testing has been implemented and assessed (Gandomi et al., 2018), including cell-in-series and symmetric cell operation, among others. A different strategy sometimes taken is to consider a charge step after each discharge step to return a SOC of about 100%, so that, all discharge steps start from the same condition. Since the simulation of polarisation and power curve behaviour was obtained by considering the exactly the same steps of zero current and OCP step time and discharge current and discharge step time, the evolution of concentration over time is predicted by the model.

5.5.4 Cycling cell operation

To quantify the loss of capacity and the figures of merit of the cell over the continuous operation, a cycling test (set 23) was performed comprising 51 continuous cycles of charge-discharge at a constant current density of $700\,\mathrm{A\,m^{-2}}$. A short period at OCP operation before each charge or discharge step was allowed for each single-cycle. This permitted the OCP to be tracked along the cycling test which is a qualitative estimation of the SOC of the cell when fully charged or discharged. A simulation of the cycling operation by means of the unit cell model was compared to the observed experimental data. Figure 5.22a presents the comparison of the experimental cell potential data for the cycles 2, 15, 30 and 45 and the model testing. The experimental data showed a capacity change from 4485 to $4205\,\mathrm{A\,s}$ over 51 cycles with a virtually linear trend. This total capacity change represented a capacity loss of $\sim 5.6\,\mathrm{A\,s}$ per cycle or $\sim 0.12\%$ per cycle, which responds to the crossover of vanadium (VO^{2+} and VO_2^+) and sulphuric acid (H^+, SO_4^{2-} and HSO_4^-) species, as well as liquid water, into the anode side. Indeed, during the cycling test, it was possible to observe a solution of blue colour slowly accumulating in the crossover reservoir connected at the hydrogen outlet. This accumulation confirmed the loss of solution to the anodic side. Figure 5.22a includes the model simulation of the cycling operation for the 4 cycles presented. A reasonably good agreement was found for the simulated potentials, with NRMSEs for charge and discharge in the range of 1.5-12.6% and 24.8-30.4%. The main discrepancies were found at the tails of the charge and discharge cell potential, which is most probably related to discrepancies in the expected concentration of ionic species. It was clear that a small variation in the concentration of ionic species, and therefore in the cell capacity, at the end of charge or discharge produces a mismatch in the cell potential. At discharge, for example, if the ionic concentrations are slightly higher, the potential does not reach the region where the potential falls rapidly, *i.e.*, mass-transport

controlled region. The opposite situation occurs if the concentrations are slightly lower towards the end of charge. In this work, the simulations were run at exactly the same operating conditions of current density and time as in the experimental operation of the cell. It is clear that if the operating time were slightly longer during the simulations, the potential would have fallen sharply as expected.
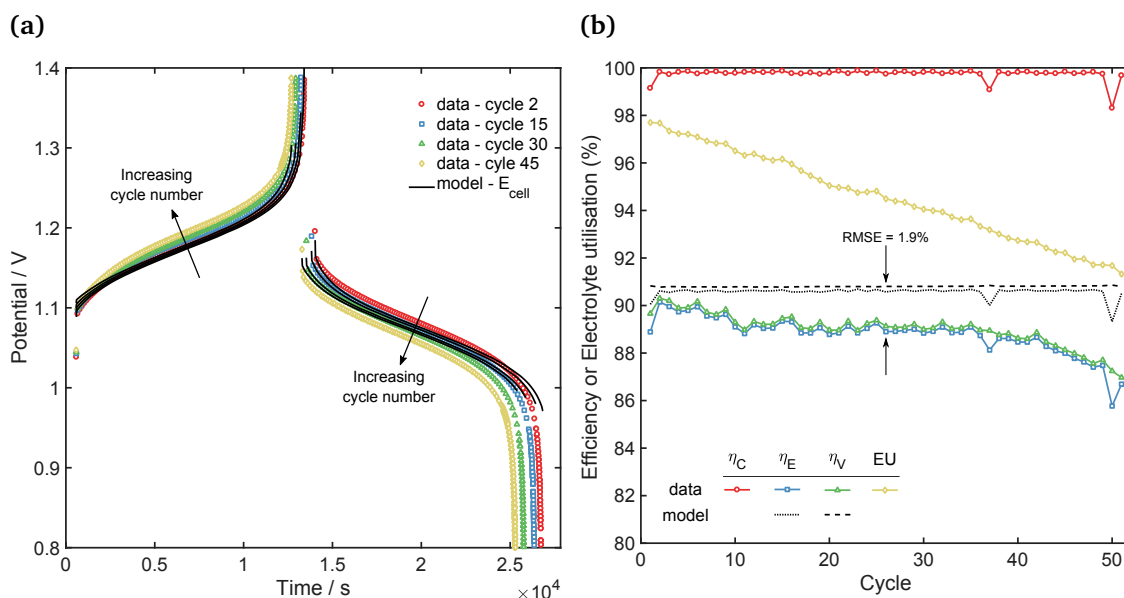
(a)   **(b)**

Figure 5.22: Cycling test at a current density of $700 \, \mathrm{A \, m^{-2}}$, a flow rate of vanadium electrolyte of $50 \, \mathrm{mL \, min^{-1}}$, and hydrogen flow rate of $30 \, \mathrm{mL \, min^{-1}}$ (data set 23). (a) Comparison of Charge-discharge potential data for cycles 2, 15, 30 and 45 with model cycling test; and (b) Figures of merit for cycling test along 51 continuous cycles of charge-discharge operation.

Figure 5.22b shows the variation of the experimental electrolyte utilisation and coulombic, energy and voltage efficiency, as a function of cycle number. The experimental data showed an electrolyte utilisation that varied almost linearly from 97.7% to 91.3% over 51 cycles. This decrease in the electrolyte utilisation is directly related to the loss in capacity due to crossover of ionic species and liquid water, as well as to an increase of cell resistances, and therefore, an increase of the total cell polarisation which caused the cut-off potentials to be reached earlier than estimated. This increase in cell polarisation can be observed clearly in Figure 5.22a, when number of cycles increases from 2 to 45. The coulombic efficiency showed a stable trend over the course of 16 days of the cycling test, with a mean value of 99.8%. It can be observed that three cycles, namely cycle 1, 37 and 50, presented a coulombic efficiency away from the mean. This was attributed to experimental anomalies during the cycling test: a noise in the current signal during the charge of cycles 37 and 50, and an initial higher potential during charge for cycle 1 due to membrane electrolyte uptake. The voltage efficiency presented a maximum and minimum value of 90.3% and 87.0%, with a slow decreasing trend over time. This decrease in voltage efficiency was also reflected in the energy efficiency and is related to the in-

crease of the total cell polarisation. The coulombic and voltage efficiencies were slightly higher than those reported for all-vanadium systems at similar current densities (300-1000 $A^2 m^{-1}$) (Kim et al., 2010; Li et al., 2011a), and the capacity loss was smaller for the hydrogen-vanadium system. The model estimation of voltage and energy efficiencies was higher than those expected experimentally, with an RMSE of 1.9% when considering all 51 cycles. This discrepancy is related to a slight mismatch in the concentration of species at the end of charge and discharge operation as was explained above. It is important to recognise the need for a detailed experimental and modelling study of crossover of ionic species and water, as well as possible side reactions at the anodic side, in a hybrid system such as the RHVFC. A higher-dimensional continuum model could be considered to simulate the crossover phenomena in more detail. This model could enable a better understanding of the mechanisms responsible for cell degradation through extended periods of operation, to weigh their relative importance, and to discern design strategies to improve cell performance. To correctly describe mass-transport limitation effects a spatially distributed approach of a continuum or pore-level model may well be required. These distributed models could allow the study of the interaction of the flow fields and the porous electrode. Such effects are out of the scope of this chapter but will be studied in the following chapter. Additionally, an extra overpotential, possibly related to mass-transport limitations, has been observed in the anodic side of the RHVFC at high current densities. This additional overpotential could be explained by the effect of crossover of vanadium and sulphuric acid species to the anodic catalyst layer or water management issues (flooding or drying). Moreover, Dowd et al. (2017b) proposed side reactions involving vanadium ionic species that could occur at the anodic side of an RHVFC. These side reactions, if present, will affect the performance of the cell. In order to successfully identify, quantify and describe these effects an extensive experimental study is required, as well as a detailed crossover model for an RHVFC.

5.6   Conclusions

In this chapter the characterisation of a $5\,cm^2$ area RHVFC was presented, characterisation that was based on extensive experimental measurements taken at different flow rates of the vanadium electrolyte and densities of the applied current. The polarisation performance of the cell had a maximum peak power density of $2840\,W\,m^{-2}$ and a limiting current density over $4200\,A\,m^{-2}$, for a flow rate of vanadium electrolyte and hydrogen of $100\,mL\,min^{-1}$. The cycling performance of the cell displayed a capacity loss of $5.6\,A\,s$ per cycle, which was reflected in the virtually linear decrease in the discharge electrolyte utilisation. This loss in capacity was related to the crossover of ionic species and liquid water into the anodic side and could also be related to possible self-discharge or side reaction

involving vanadium species. The coulombic efficiency was very stable on cycling, while the voltage efficiency slowly decreased. This decrease in voltage efficiency was related to the increase in cell polarisation over the 51 continuous cycles of charge-discharge.

A unit cell model including crossover flux of ionic species through the membrane was calibrated against single-cycle charge-discharge potentials. A good agreement was found between model simulations and experimental data, while the discrepancies increased at a lower flow rate of vanadium electrolyte and a higher current density. Simulations for polarisation and power curves were obtained, with good agreement within the range of current densities validated with single-cycle charge-discharge tests. The cell potential was more sensitive to changes in the transfer coefficient of the cathodic reaction, the cathode porosity and the membrane thickness, which are directly related to the cathodic overpotential from the Butler-Volmer equation, the cathodic ohmic overpotential, and the crossover effects. A kinetic study of the cathodic reaction is recommended at practical concentration levels of vanadium and sulphuric acid species, to reduce the uncertainty of the kinetic parameters such as transfer coefficients and standard rate constants. It is also necessary to obtain good estimations of microstructural parameters such as porosity and specific surface areas of electrodes. At the very least, it is important to differentiate between the geometrical specific surface area, *i.e.*, the total area available, and the active specific surface area, *i.e.*, a fraction of the total area that is used for the redox reaction.

It is important to highlight the need for reliable and detailed experimental data at high current densities to test and extend the range of validity of the model. Since different processes could dominate at lower or higher current densities, as well as at lower or higher SOCs, it is imperative to carry out extensive model validation over a wider range of conditions. At the same time, this validation could help to recognise phenomena that need to be included in the model description or processes that could be neglected. Specifically, the anodic overpotential at high current densities and the effect of crossover of vanadium and sulphuric acid species into the CL must be assessed in order to unambiguously elucidate and describe all the relevant phenomena involved in an RHVFC. Chapter 6 introduces the formulation of a one-dimensional continuum model to describe the transport of ionic species through the membrane in the RHVFC to improve the understanding of the crossover mechanisms and their impact on cell performance.

Chapter references

Araya, M. M., Arrieta, J. J., Pérez-Correa, J. R., Biegler, L. T., and Jorquera, H. Fast and reliable calibration of solid substrate fermentation kinetic models using advanced non-linear programming techniques. *Electronic Journal of Biotechnology*, 10(1), 2007.

Bertei, A., Mertens, J., and Nicolella, C. Electrochemical simulation of planar solid oxide fuel cells with detailed microstructural modeling. *Electrochimica Acta*, 146:151–163, 2014.

Cooper, S. J., Bertei, A., Shearing, P. R., Kilner, J. A., and Brandon, N. P. TauFactor: An open-source application for calculating tortuosity factors from tomographic data. *SoftwareX*, 5:203–210, 2016.

Darling, R. M., Weber, A. Z., Tucker, M. C., and Perry, M. L. The Influence of Electric Field on Crossover in Redox-Flow Batteries. *Journal of the Electrochemical Society*, 163(1): A5014–A5022, 2015.

Dewage, H. H., Yufit, V., and Brandon, N. P. Study of Loss Mechanisms Using Half-Cell Measurements in a Regenerative Hydrogen Vanadium Fuel Cell. *Journal of The Electrochemical Society*, 163(1):A5236–A5243, 2016.

Dowd, R. P., Lakhanpal, V. S., and Van Nguyen, T. Performance Evaluation of a Hydrogen-Vanadium Reversible Fuel Cell. *Journal of The Electrochemical Society*, 164(6):F564–F567, 2017a.

Dowd, R. P., Verma, A., Li, Y., Powers, D., Wycisk, R., Pintauro, P. N., and Van Nguyen, T. A Hydrogen-Vanadium Reversible Fuel Cell Crossover Study. *Journal of The Electrochemical Society*, 164(14):F1608–F1614, 2017b.

Fuel Cell Store. 0.3 mg/cm2 40% Platinum on Vulcan Carbon Paper Electrode, a. URL http://www.fuelcellstore.com/fuel-cell-components/gas-diffusion-electrode/platinum-electrodes/03-ptc-paper-electrode.

Fuel Cell Store. FREUDENBERG Gas Diffusion Layers for PEMFC and DMFC, b. URL http://www.fuelcellstore.com/freudenberg-h2315.

Fuel Cell Store. Properties of Nafion ® PFSA Membrane: 115, 117 and 1110, c. URL http://www.fuelcellstore.com/nafion-117.

Gandomi, Y. A., Aaron, D. S., Houser, J. R., Daugherty, M. C., Clement, J. T., Pezeshki, A. M., Ertugrul, T. Y., Moseley, D. P., and Mench, M. M. Critical ReviewExperimental Diagnostics and Material Characterization Techniques Used on Redox Flow Batteries. *Journal of The Electrochemical Society*, 165(5):A970–A1010, 2018.

Gandomi, Y. A., Aaron, D. S., Zawodzinski, T. A., and Mench, M. M. In Situ Potential Distribution Measurement and Validated Model for All-Vanadium Redox Flow Battery. *Journal of The Electrochemical Society*, 163(1):A5188–A5201, 2016.

Huerta-Pérez, F. and Pérez-Correa, J. R. Optimizing ethanol recovery in a spinning cone column. *Journal of the Taiwan Institute of Chemical Engineers*, 83:1–9, 2018.

Kim, K. J., Park, M. S., Kim, Y. J., Kim, J. H., Dou, S. X., and Skyllas-Kazacos, M. A technology review of electrodes and reaction mechanisms in vanadium redox flow batteries. *Journal of Materials Chemistry A*, 3(33):16913–16933, 2015.

Kim, S., Yan, J., Schwenzer, B., Zhang, J., Li, L., Liu, J., Yang, Z. G., and Hickner, M. A. Cycling performance and efficiency of sulfonated poly(sulfone) membranes in vanadium redox flow batteries. *Electrochemistry Communications*, 12(11):1650–1653, nov 2010.

Knehr, K. and Kumbur, E. Open circuit voltage of vanadium redox flow batteries: Discrepancy between models and experiments. *Electrochemistry Communications*, 13(4): 342–345, apr 2011.

Knehr, K., Agar, E., Dennison, C. R., Kalidindi, A. R., and Kumbur, E. C. A Transient Vanadium Flow Battery Model Incorporating Vanadium Crossover and Water Transport through the Membrane. *Journal of the Electrochemical Society*, 159(9):A1446–A1459, aug 2012.

Kucernak, A. R. J. and Zalitis, C. M. General Models for the Electrochemical Hydrogen Oxidation and Hydrogen Evolution Reactions Theoretical Derivation and Experimental Results Under Near Mass-Transport Free Conditions. *The Journal of Physical Chemistry C*, page acs.jpcc.6b00011, 2016.

Li, L., Kim, S., Wang, W., Vijayakumar, M., Nie, Z., Chen, B., Zhang, J., Xia, G., Hu, J., Graff, G., Liu, J., and Yang, Z. A stable vanadium redox-flow battery with high energy density for large-scale energy storage. *Advanced Energy Materials*, 1(3):394–400, 2011.

Newman, J. S. and Thomas-Alyea, K. E. *Electrochemical Systems*. John Wiley & Sons, Inc., New York, 3rd edition, 2004. ISBN 0-471-47756-7.

Pino-Muñoz, C. A., Hewa Dewage, H., Yufit, V., and Brandon, N. P. A Unit Cell Model of a Regenerative Hydrogen-Vanadium Fuel Cell. *Journal of The Electrochemical Society*, 164 (14):F1717–F1732, 2017.

Pino-Muñoz, C. A., Chakrabarti, B. K., Yufit, V., and Brandon, N. P. Characterisation of a Regenerative Hydrogen-Vanadium Fuel Cell Using an Experimentally Validated Unit Cell Model. *Journal of the Electrochemical Society*, 166(14):A1–A14, 2019.

Pugach, M., Kondratenko, M., Briola, S., and Bischi, A. Zero dimensional dynamic model of vanadium redox flow battery cell incorporating all modes of vanadium ions crossover. *Applied Energy*, 226(June):560–569, 2018.

Sacher, J., Saa, P., Cárcamo, M., López, J., Gelmi, C. A., and Pérez-Correa, R. Improved calibration of a solid substrate fermentation model. *Electronic Journal of Biotechnology*, 14(5), 2011.

Scribner Associates. 5 cm 2 Graphite Flow Field with REF Channel.

Staples, B. R. Activity and osmotic coefficients of aqueous sulfuric acid at 298.15 K. *Journal of Physical and Chemical Reference Data*, 10(3):779–798, 1981.

Tang, A., Bao, J., and Skyllas-Kazacos, M. Dynamic modelling of the effects of ion diffusion and side reactions on the capacity loss for vanadium redox flow battery. *Journal of Power Sources*, 196(24):10737–10747, dec 2011.

Tang, A., Bao, J., and Skyllas-Kazacos, M. Studies on pressure losses and flow rate optimization in vanadium redox flow battery. *Journal of Power Sources*, 248:154–162, feb 2014.

Tang, Z., Svoboda, R., Lawton, J. S., Aaron, D. S., Papandrew, A. B., and Zawodzinski, T. A. Composition and Conductivity of Membranes Equilibrated with Solutions of Sulfuric Acid and Vanadyl Sulfate. *Journal of The Electrochemical Society*, 160(9):F1040–F1047, 2013.

Vogler, M., Bieberle-hütter, A., Gauckler, L., Warnatz, J., and Bessler, W. G. Ni/YSZ Patterned Anode Modelling Study of Surface Reactions, Diffusion, and Spillover at a Modelling Study of Surface Reactions, Diffusion, and Spillover at a Ni/YSZ Patterned Anode. *J. Electrochem. Soc*, 156(5):663–672, 2009.

Yufit, V., Hale, B., Matian, M., Mazur, P., and Brandon, N. P. Development of a Regenerative Hydrogen-Vanadium Fuel Cell for Energy Storage Applications. *Journal of The Electrochemical Society*, 160(6):A856–A861, 2013.

Zhao, P., Zhang, H., Zhou, H., Chen, J., Gao, S., and Yi, B. Characteristics and performance of 10kW class all-vanadium redox-flow battery stack. *Journal of Power Sources*, 162(2): 1416–1420, nov 2006.

Zheng, Q., Xing, F., Li, X., Liu, T., Lai, Q., Ning, G., and Zhang, H. Investigation on the performance evaluation method of flow batteries. *Journal of Power Sources*, 266: 145–149, 2014.

Chapter 6

Poisson-Nernst-Planck model of ionic crossover through the membrane of a regenerative hydrogen-vanadium fuel cell

6.1 Introduction

Recently, ionic transport across cation-exchange membranes used in all-Vanadium Redox Flow Batteries (VRFBs) have been studied in order to rationalise the phenomena controlling the cell capacity loss during continuous cycling operation. Most of the reported VRFB models have only considered proton transport through the membrane, which are normally considered to be the main charge carriers. In lumped or unit cell models, transport through the ion-exchange membrane of other species present, namely vanadium and sulphuric acid species, have been considered to be steady-state or transient diffusion with fixed ionic concentrations at each half-cell. These concentrations at each side of the membrane are usually set by means of a lumped or continuum model for cathodic and anodic electrodes. Only recently, VRFB models have started incorporating transport through the membrane driven by diffusion, migration and convection mechanisms, as well as the effect of the Donnan potential that appears across the electrode-membrane interfaces (Knehr et al., 2012a; Lei et al., 2015; Yang et al., 2015b). Similarly to VRFBs, the Regenerative Hydrogen-Vanadium Fuel Cell (RHVFC) also displays crossover of ionic species and water through the membrane, degrading the performance of the cell. This crossover flow is collected in a reservoir connected to the anodic outlet when the continuous operation of the cell is performed. Chapter 5 introduced a unit cell model, which incorporated the ionic crossover through the membrane in a lumped fashion, to simulate the cell potential during single-cycle and cycling. This unit cell model was capable of reproducing satisfactorily the single-cycle data, but only to some extent the cycling data. In this chapter, a Poisson-Nernst-Planck (PNP) model implemented in a one-dimensional (1D) macro-homogeneous approach is used to describe the transport of ionic species in the RHVFC. The aim of this study is to understand the phenomena involved in multiple ion transport across a perfluorinated sulfonated cation exchange membrane such as Nafion and to apply the model to an RHVFC case to analyse and differentiate the dominant phenomena controlling the capacity loss. A half-cell problem, where only cathode, membrane and Catalyst Layer (CL) are considered, is used for the mathematical description of the cell is introduced. This 1D model relaxes the commonly used assumption of electro-neutrality in order to allow the formation of a space charge region at the electrode-membrane interface. The expected concentration and potential profiles, as well as the total and individual species crossover fluxes, are investigated. The effect of the current density and the State Of Charge (SOC) of the cell is studied at Steady-State (SS), and then evolution over time of the observed result for a single-cycle of charge-discharge is studied by means of a Time-Dependent (TD) model. Throughout this chapter, some concepts, which were mentioned in previous chapters, are repeated in order to allow for a clear and self-consistent explanation of the model.

6.2 Poisson-Nernst-Planck model for the RHVFC

The proposed model of a half-cell of the RHVFC was developed considering three components, namely the cathodic electrode (ca), the Nafion membrane (m) and the catalyst layer, which are schematised in Figure 6.1. The half-cell is studied by means of a 1D macro-homogeneous approach along the x-coordinate, which is considered to be the dominant direction of the current density. Figure 6.2 presents the mathematical modelling domain, where the boundary at $x = x_0$ represent the interface between the current collector and the cathode, or between the flow channel and the cathode; the boundary set at $x = x_2$ represents the interface between the membrane and the CL; $x = x_1$ is the interface between the cathode and the membrane. The model considers the transport of five species, namely VO^{2+}, VO_2^+, H^+, HSO_4^- and SO_4^{2-}, across the cathode and membrane. Since transport across the catalyst layer is not modelled, it is not treated as a separate domain.
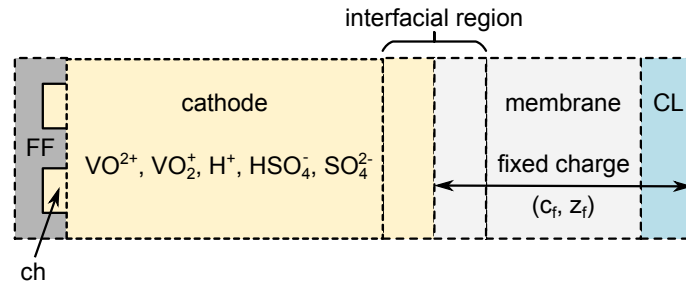
Figure 6.1: Schematic diagram of the component layers in a half-cell representation of a RHVFC. The term FF refers to flow field plate, ch refers to flow channel, and CL refers to catalyst layer.
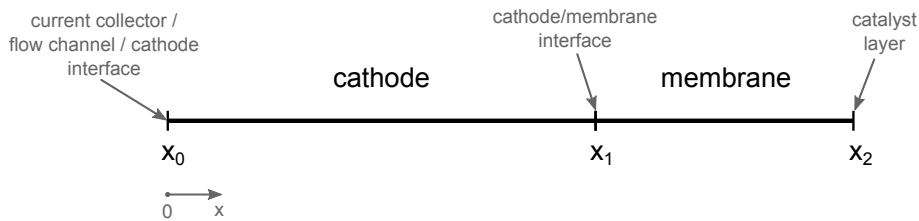
Figure 6.2: 1D modelling domain along the x-coordinate, with $l_{ca} = x_1 - x_0$ and $l_m = x_2 - x_1$ representing the thickness of the cathode and membrane, respectively.

To develop the 1D PNP model of the half-cell the following assumptions and simplifications were considered:

1. All domains are considered isothermal and having the same temperature.

2. The catholyte is considered incompressible, having constant density and viscosity.

3. All physical properties, mass and charge-transfer properties are assumed isotropic and homogeneous.

4. Variations of ionic concentrations, electronic and ionic potential, and pressure are

neglected in the y- and z-coordinates.

5. Unit activity coefficients are assumed for all species.

6. The dilute solution approximation is adopted for the species transport in the cathode and membrane.

7. Gas evolution, side reactions and self-discharge reactions are neglected.

Considering the concentration levels used at RHVFC experimental tests, *e.g.*, 1 M of vanadium and 5 M of sulphuric acid, Assumptions 5 and 6 are strong assumptions and they may well generate irreconcilable inaccuracies. However, in this first model implementation the decision of keeping these assumptions was made based on the lack of literature data of activity coefficients or corrected diffusivities for the ionic species, and to avoid the need for an extra set of equations to estimate correction factors. The set of governing equations, describing the conservation of mass, momentum, species and charge were expressed following the differential form of the conservation law as shown in Equation 6.1. This conservation law enables the mathematical accounting of a quantity over a control volume, where the rate of accumulation in the volume is equal to the net influx plus the net generation. The flux density is usually divided into a convective and a diffusive contribution. In Equation 6.1, b is the quantity concentration in units of [#/volume], t is the time, F is the flux density in units of [#/(area·time)], S is the production (or consumption) rate density in units of [#/(volume·time)], Λ is the generalised diffusion coefficient in units of [length^2/time], and Γ is the driving force vector in units of [length/time].

$$\frac{\partial b}{\partial t} + \nabla \cdot F = S$$
$$\frac{\partial b}{\partial t} + \nabla \cdot (\Gamma b) = \nabla \cdot (\Lambda \nabla b) + S$$

(6.1)

6.2.1 Conservation of mass and momentum

The flow of electrolyte through the porous electrode and membrane can be described by the governing equations representing the conservation of mass and momentum, which are presented in Equations 6.2 and 6.3, respectively. In these equations, ρ and μ is the density and viscosity of the electrolyte, v is the velocity, S_{mass} and S_{mom} are the source terms of mass and momentum, respectively. Equation 6.4 presents the momentum source term, S_{mom}, for the cathode and the membrane. In the cathode, the electrolyte flow is driven primarily by the pressure gradient (Gandomi et al., 2016; Knehr et al., 2012a; Newman and Thomas-Alyea, 2004), while in the membrane the electrolyte flow is driven by pressure gradient as well as electro-osmotic convection caused by the gradient of ionic potential across the membrane ($\nabla \phi_{\text{e}}$) and the effective diffusion potential ($\nabla \phi_{\text{diff}}$) (Knehr

et al., 2012a; Kontturi et al., 2008; Lei et al., 2015), which results from the viscous drag due to ion diffusion. The term $F(\nabla\phi_e + \nabla\phi_{\text{diff}})$ represents the body force acting on the mobile ions(Knehr et al., 2012a). In Equation 6.4, p is the pressure, κ_p is the hydraulic permeability, κ_ϕ is the electro-kinetic permeability, z_f and c_f are the charge and concentration of the fixed sulphonic acid groups present in the ionic exchange membrane, such as Nafion, and F is Faraday's constant.

$$\frac{\partial\rho}{\partial t} + \nabla\cdot(\rho v) = S_{\text{mass}} \tag{6.2}$$

$$\frac{\partial\rho v}{\partial t} + \nabla\cdot(\rho v v) = \nabla\cdot(\mu\nabla v) + S_{\text{mom}} \tag{6.3}$$

$$
\begin{aligned}
S_{\text{mom}}^{\text{ca}} &= -\nabla p - \frac{\mu}{\kappa_p^{\text{ca}}}v \quad \text{(cathode)} \\[2mm]
S_{\text{mom}}^{\text{m}} &= -\nabla p - \frac{\mu}{\kappa_p^{\text{m}}}v - \frac{\kappa_\phi^{\text{m}}}{\kappa_p^{\text{m}}}F(-z_f c_f)(\nabla\phi_e + \nabla\phi_{\text{diff}}) \quad \text{(membrane)}
\end{aligned}
\tag{6.4}
$$

Equation 6.2 is reduced to the continuity equation (Equation 6.5) because the electrolyte density is considered constant, while the mass source term is assumed equal to zero. This assumption is taken because, in the reactions involved, namely the cathodic charge-transfer reaction and the bi-sulphate dissociation, the consumption of reactants is accompanied by the production of products which in total have the same mass as the reactants consumed, as shown in Equations 4.3 and 4.13. The conservation of momentum is reduced into Darcy's and Schlogl's equation for the cathode and the membrane, respectively, as shown in Equations 6.6 and 6.7. In the electrolyte, momentum transport is expected to be much faster than the transport of ionic species, and therefore, steady-state transport of momentum can be assumed. Also in these porous media, the permeability is very low and the momentum source term is much higher in magnitude, and therefore, the other terms in the equation can be neglected. The hydraulic permeability in the cathode is estimated by the Kozeny-Carman Equation 6.8, considering the mean fibre diameter (d_f), the cathodic porosity (ε), and the Kozeny-Carman constant (C_{KC}). The effective diffusion potential in the membrane is calculated by Equation 6.9, considering the concentration gradient and the effective conductivity of the membrane (σ^{m}).

$$\nabla\cdot v = 0 \tag{6.5}$$

$$v = -\frac{\kappa_p^{\text{ca}}}{\mu}\nabla p \quad \text{(cathode)} \tag{6.6}$$

$$v = -\frac{\kappa_p^m}{\mu}\nabla p - \frac{\kappa_\phi^m}{\mu}F(-z_f c_f)\big(\nabla\phi_e + \nabla\phi_{\text{diff}}\big) \quad \text{(membrane)} \tag{6.7}$$

$$\kappa_p^{ca} = \frac{d_f^2}{C_{KC}}\frac{\varepsilon^3}{(1-\varepsilon)^2} \tag{6.8}$$

$$\nabla\phi_{\text{diff}} = \frac{F\sum z_k D_k^m \nabla c_k}{\sigma^m}, \quad \sigma^m = \frac{F^2}{RT}\sum z_k^2 D_k^m c_k \tag{6.9}$$

6.2.2 Conservation of species

The transport equations in dilute solution are adopted to describe the flow through the cathode and membrane of vanadium species (VO^{2+} and VO_2^+) and sulphuric acid (H^+, HSO_4^- and SO_4^{2-}) species as presented by the conservation of species in Equation 6.10. Where c_k is the concentration of species k, N_k is the flux density of the charged species, and S_k is the source term. The term c_k represents the amount of the species averaged over the volume of pores, *i.e.*, the pore-phase concentration, which is continuous within the porous media. In this work, all the concentration of species are determined through Equation 6.10, and unlike most of the VRFB reported models, the electro-neutrality condition, which assumes that there is no charge separation anywhere in the solution (Dickinson et al., 2011), is not enforced. As mentioned in Chapter 2, the electro-neutrality condition was proposed in order to facilitate the derivation of analytical solutions for the Nernst-Planck equations. This seems unnecessary, or at least not required as an a priori assumption, for numerical solutions as no clear computational advantage of using the electro-neutrality approximation has been perceived (Dickinson et al., 2011; Vøllestad et al., 2013). Even when the electro-neutrality condition renders accurate results, implementing the Poisson's equation (Gauss's Law) instead can allow for more realistic potential and concentration profiles in regions were charge separation is expected to be present, by considering the effect of charge separation on the ionic potential, and allow for more complete physical interpretations of the model results (Dickinson et al., 2011). For these reasons, the modest computational cost (at least in a 1D approach) of solving Poisson's equation along with Nernst-Planck equations (Equation 6.11) and the increase of generality, Poisson's equation was implemented as an extra differential equation instead of imposing the strict algebraic constraint of electro-neutrality ($\sum_k z_k c_k = 0$). The flux density of species, considering the dilute-solution approximation, is calculated by the Nernst-Planck equation as shown in Equation 6.11. This equation includes the superficial molar flux of species k due to convection, diffusion and migration (from left to right in the right-hand side), which is averaged over the cross-sectional area of the electrode - including solid-phase and pore-phase. The diffusive flux in Equation 6.11 considers the effective

diffusivity D_k^{eff}, which accounts for the effect of the porosity and the tortuosity (τ) on the diffusivity of species k (D_k), and is estimated by means of the Bruggemann correlation, $\tau = \varepsilon^{-1/2}$ (Equation 6.12). The ionic mobility (μ_k) is calculated using the Nernst-Einstein relation (Equation 5.6), which is used to eliminate the ionic mobility as an independent variable from Equation 6.11. The terms R and T are the universal gas constant and the temperature, respectively.

$$\frac{\partial \varepsilon c_k}{\partial t} + \nabla \cdot N_k = S_k, \quad k = \left[\text{VO}^{2+}, \text{VO}_2^+, \text{H}^+, \text{SO}_4^{2-}, \text{HSO}_4^- \right] \tag{6.10}$$

$$N_k = v c_k - D_k^{\text{eff}} \nabla c_k - z_k \mu_k c_k F \nabla \phi_e \tag{6.11}$$

$$D_k^{\text{eff}} = \frac{\varepsilon}{\tau} D_k = \varepsilon^{3/2} D_k \tag{6.12}$$

$$\mu_k = \frac{D_k^{\text{eff}}}{RT} \tag{6.13}$$

The source terms represent the consumption or production of species k due to the cathodic charge-transfer reaction presented in Equation 6.14 occurring in the cathode domain, and the chemical dissociation of bisulphate presented in Equation 6.16 occurring in the cathode and membrane domain. Additionally, the anodic charge-transfer reaction, namely HOR / HER, presented in Equation 6.15, occurring at the catalyst layer, which in the present model is considered to occur at the membrane/catalyst layer interface at $x = x_2$. Table 6.2.2 summarises the source terms considered in each component. The cathodic charge-transfer reaction takes place at the interface between the solid electrode and the pore-phase, where the transfer current density (j_{BV}) is proportional to the rate of reaction, $r = j_{\text{BV}}/(nF)$, in units of mol per m^2 of active surface area. The specific surface area (a), *i.e.*, m^2 of active surface area per m^3 of electrode, is used to obtain the volumetric rate of reaction. Therefore, the source term from the charge-transfer reaction at the cathode, which is intrinsically a heterogeneous reaction, is included in the model as a homogeneous source term along with the dissociation of HSO_4^-. The anodic charge-transfer reaction takes place over the interfacial area between the catalyst and the electrolyte phase, where the transfer current density (j_{TV}) is also proportional to the rate of reaction, and the roughness factor (R_{CL}), *i.e.* m^2 of active surface area per m^2 of cross-sectional area of electrode. Therefore, the charge-transfer at the anodic catalyst layer was included in the model as a heterogeneous source term.
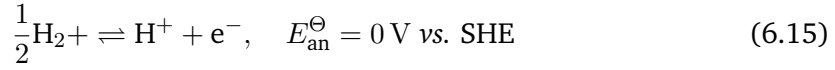
$$\text{VO}^{2+} + \text{H}_2\text{O} \rightleftharpoons \text{VO}_2^+ + 2\text{H}^+ + \text{e}^-, \quad E_{\text{ca}}^{\ominus} = 0.99\,\text{V} \textit{ vs. } \text{SHE} \tag{6.14}$$

$$\frac{1}{2}H_2+ \rightleftharpoons H^+ + e^-, \quad E_{an}^\Theta = 0 \text{ V } \textit{vs. } \text{SHE} \tag{6.15}$$

$$HSO_4^- \rightleftharpoons H^+ + SO_4^{2-} \tag{6.16}$$

Table 6.1: Source for species in the cathode and membrane.

Species	Cathode	Membrane	Catalyst layer
$S_{VO^{2+}}$	$-aj_{BV}/F$	–	–
$S_{VO_2^+}$	aj_{BV}/F	–	–
S_{H^+}	$2aj_{BV}/F - S_d$	$-S_d$	$j_{TV}R_{CL}/F$
$S_{HSO_4^-}$	S_d	S_d	–
$S_{SO_4^{2-}}$	$-S_d$	$-S_d$	–

The kinetic expressions used to obtain the transfer current density for the charge-transfer reactions at the cathode and catalyst layer were explained in detail in Chapter 4. These kinetics relations depend on the concentration of species and the overpotential (η). For the cathodic kinetics expression, the difference between the concentration of species at the surface and the bulk is considered by Fickian diffusion at steady-state conditions over a Nernst diffusion layer (δ_0), as shown in Equation 6.17. In a macro-homogeneous modelling approach the overpotential is given by Equation 6.18, where ϕ_s is the electronic potential and E_{eq} is the equilibrium potential, which is given for the cathode and the anode by Equations 6.19 and 6.20, respectively. At an equilibrium condition, the cell is assumed to be at a constant concentration, and therefore, the concentration of species in the bulk is equal to their surface concentration.

$$-\frac{D_{VO^{2+}}}{\delta_0}(c_{VO^{2+}} - c_{VO^{2+}}^s) = \frac{j_{BV}}{F}$$
$$\frac{D_{VO_2^+}}{\delta_0}(c_{VO_2^+} - c_{VO_2^+}^s) = \frac{j_{BV}}{F} \tag{6.17}$$
$$\frac{D_{H^+}}{\delta_0}(c_{H^+} - c_{H^+}^s) = 2\left(\frac{j_{BV}}{F}\right)$$

$$\eta = \phi_s - \phi_e - E_{eq} \tag{6.18}$$

$$E_{eq,ca} = E_{ca}^\circ + \frac{RT}{F}\ln\left(\frac{c_{VO_2^+}c_{H^+}^2}{c_{VO^{2+}}}\right) \tag{6.19}$$

$$E_{\text{eq,an}} = E_{\text{an}}^{\circ} + \frac{RT}{F} \ln \left(\frac{c_{\text{H}^+}^{\text{CL}}}{p_{\text{H}_2}^{1/2}} \right) \tag{6.20}$$

The dissociation of H_2SO_4 affects the concentration of H^+, HSO_4^- and SO_4^{2-}, and it is assumed to occur in two steps, considering the first step to be fast and the second step to be rate-limiting. The reaction source term associated with this second dissociation step was described following the relation presented in Equation 6.21, which has been recently adopted in most of the VRFB modelling literature (Knehr et al., 2012a). In this equation, k_d and β_d are the dissociation reaction coefficient and the degree of dissociation of HSO_4^-, respectively. The degree of dissociation of HSO_4^- changes from the cathode to the membrane due to the presence of a fixed charge, which suppresses this chemical dissociation (Yang et al., 2015b).

$$S_d = k_d \left(\frac{c_{\text{H}^+} - c_{\text{HSO}_4^-}}{c_{\text{H}^+} + c_{\text{HSO}_4^-}} - \beta_d \right), \quad 0 < \beta_d < 1 \tag{6.21}$$

6.2.3 Conservation of charge and Poisson equation

As it was mentioned before, the electro-neutrality condition was not enforced in the cathode or the membrane, and therefore, the charge conservation for the ionic and electronic current is given by Equation 6.22, where the term aj_{BV} represents the source term of ionic and electronic charge ($S_{\text{e/s}}$). In this equation, ρ_{sol} is the charge density of the solution, and j_e and j_s are the ionic (or liquid) and electronic (or solid) current densities, respectively. These current densities are defined in Equations 6.23 and 6.24. An accumulation of space charge due to the accumulation of ionic species was allowed, while no accumulation of electronic charge was considered. Therefore, the ionic charge leaving the pore-phase (electrolyte) plus the rate of change of the solution space charge must equal the electronic charge entering the solid-phase (electrode). It can be seen in Equation 6.23 that the ionic current density must include the transport of species due to convection, diffusion and migration. The convective flux contribution to the ionic current density is usually neglected due to the electro-neutrality condition, but that is not the case here.

$$\varepsilon \frac{\partial \rho_{\text{sol}}}{\partial t} + \nabla \cdot j_e = -\nabla \cdot j_s = aj_{\text{BV}} \tag{6.22}$$

$$j_e = F \sum_k z_k N_k = F \sum_k z_k c_k v - F \sum_k z_k D_k^{\text{eff}} \nabla c_k - \sigma_e^{\text{eff}} \nabla \phi_e \tag{6.23}$$

$$j_s = -\sigma_s^{\text{eff}} \nabla \phi_s \tag{6.24}$$

The effective ionic and electronic conductivity, including the porosity and tortuosity effect, are given by Equations 6.25 and 6.26, respectively.

$$\sigma_e^{\text{eff}} = F^2 \sum_k z_k^2 \mu_k c_k \tag{6.25}$$

$$\sigma_s^{\text{eff}} = (1 - \varepsilon)^{3/2} \sigma_s \tag{6.26}$$

Since the electro-neutrality condition was eliminated from the set of equations, the five equations for conservation of species contains six unknowns, namely five concentrations, c_k, and the ionic potential, ϕ_e. It is necessary to relate the migration transport of species, which is driven by potential differences, with the degree of charge separation present in the electrolyte (Dickinson et al., 2011). This can be done by considering Gauss's law and that the only charge carries in the solution are the dissociated ionic species, leading to Poisson's equation as shown in Equation 6.27. This equation relates the electric field to the charge separation in the electrolyte and represents the electrostatic repulsion, while other chemical interactions affecting the membrane selectivity need to be accounted for in the effective diffusivities of the ionic species (Kodým et al., 2016), such as non-ideal solution behaviour. At the membrane, the electric field is induced by the charge density in the solution, *i.e.*, density of ionic species (ρ_{sol}), as well as by the charge density due to the fixed functional groups in the ionic-exchange membrane, ρ_{fix}. Equation 6.28 was used to calculate the charge density in the cathode and membrane. Equation 6.27 does not consider a time derivative, and therefore, it sets an analytical constraint in the solution of the coupled system of equations, causing the concentrations and potential to vary spatially and temporally (Kee et al., 2013).

$$\nabla^2 \phi_e + \frac{\rho_e}{\epsilon_0 \epsilon_r} = 0 \tag{6.27}$$

$$\rho_e = \rho_{\text{sol}} = F \sum_k z_k c_k, \quad \text{(cathode)}$$

$$\rho_e = \rho_{\text{sol}} + \rho_{\text{fix}} = F \sum_k z_k c_k + F z_f c_f, \quad \text{(membrane)} \tag{6.28}$$

In the above equations, ρ_e is the charge density, ϵ_0 is the permittivity of free space, and ϵ_r is the relative permittivity of the medium. The grouped permittivity term, $\epsilon_e = \epsilon_0 \epsilon_r$, represents the permittivity or dielectric constant of the medium, namely the electrolyte.

In Chapter 4, the Donnan potential was introduced and considered in the open circuit equation. It was shown how this jump in potential appears at the interfaces between

the electrode and the Nafion membrane when the electrochemical potential equality at equilibrium condition is considered for the different phases in contact inside the battery. The Donnan potential is defined as the difference between the ionic potential in the membrane phase and in the external phase, namely the electrolyte solution in the cathode ($\Delta\phi_D = \phi^m - \phi^{ca}$) (Hamann et al., 2007; Kontturi et al., 2008; Yang et al., 2015b). Also, it was mentioned that the Donnan potential is expected to fulfil the relation, $z_f\Delta\phi_D \geq 0$, according (Kontturi et al., 2008). Therefore for a Nafion membrane, the ionic potential on the membrane side of the interface is expected to be higher than the ionic potential on the cathodic side of the interface, $\phi^m > \phi_{ca}$. Equation 6.29 presents the relation between the concentration at the membrane and the cathode and the Donnan potential. At the cathode-membrane interface a Donnan Exclusion Region (DER), where exclusion of co-ions is expected, is formed and is responsible for the perm-selectivity of the ionic-exchange membrane (Kodým et al., 2016; Kontturi et al., 2008). The ions in solution inside the membrane are termed counter-ions if they have an opposite sign with respect to the fixed charge groups, in this case positively charged ions (VO^{2+}, VO_2^+ and H^+), or are named co-ions if they have similar charge, in this case negatively charged ions (HSO_4^- and SO_4^{2-}). The Nafion cation-exchange membrane contains negatively charged (or anionic) groups ($-SO_3^-$), which repel electrostatically anions and attract cations so that their fixed charge is compensated (Kontturi et al., 2008). In between the two electro-neutral phases (cathode and membrane) an interfacial region where charge separation is present and the potential and concentration of species vary continuously due to Donnan exclusion is formed (Kodým et al., 2016; Kontturi et al., 2008). Therefore, the Donnan potential, *i.e.*, jump in ionic potential, takes place in a non-electro-neutral or electrified interfacial region, which is known as the electrical double layer. As mentioned in Chapter 2 the electrical double layer extends over a region with a thickness approximately given by the Debye length, which is typically of the order of nanometers for electrochemical systems. Far from this interface or in the bulk of the membrane and the cathode, the charge density and the resultant electric field are expected to be zero (Kontturi et al., 2008).

$$c_k^m = c_k^{ca} \exp\left(\frac{-z_k F \Delta\phi_D}{RT}\right) \tag{6.29}$$

6.2.4   Boundary conditions

The 1D PNP model was developed considering a single-domain approach, which solves a single set of governing equations throughout the modelling domain (Yang et al., 2015b). This means that boundary conditions (Figure 6.2) are only considered at each end of the modelling domain, *i.e.*, at $x = x_0$ (ch or cc) and $x = x_2$ (CL), and not at the cathode/membrane interface, *i.e.*, at $x = x_1$ (ca-m), for all governing equations, except for

the equation used to solve for the electronic potential, which was not defined in the membrane.

Boundary conditions for the conservation momentum

The velocity across the cathode and membrane in the x-coordinate direction is constant, from Equation 6.5, and unknown. During the experiments, the velocity of the electrolyte is set at the inlet of the cathodic flow channel, which has been assumed to be a flow-by configuration with a serpentine design. The electrolyte flows along the flow channel in the y- and z- coordinate direction, while some of this flow penetrates the cathodic electrode. Therefore, the velocity in the x-coordinate direction was allowed to be an output of the model, when a pressure difference is set across the cathode and membrane. Equations 6.30 and 6.31 represent the Dirichlet boundary conditions for pressure, where the anode side was considered to be at atmospheric pressure and the cathode channel was set to a higher value of pressure ($p_{ch} > p_{atm}$), producing a positive velocity in the direction from cathode to anode.

$$p = p_{ch}, \quad \text{at } x = x_0 \tag{6.30}$$

$$p = p_{atm}, \quad \text{at } x = x_2 \tag{6.31}$$

Boundary conditions for the conservation of species

At the flow channel-cathode interface ($x = x_0$) the concentration of species is specified by using a Dirichlet boundary condition, Equation 6.32, to set the concentration equal to the concentration in the catholyte tank. The concentration of species in the flow channel was not modelled, but it was assumed equal to the catholyte tank concentration, so that, any gain/loss of species into/from the flow channel was assumed to affect directly the concentration of species in the catholyte tank. At the membrane-catalyst layer interface ($x = x_2$) the concentration of species is unknown, and therefore a Newman boundary condition for the diffusive flux was implemented, Equation 6.33. A zero diffusive flux was set for all ionic species except for protons, which undergoes the charge-transfer reaction at the catalyst layer, and therefore, the diffusive flux was set equal to the heterogeneous reaction source term at the boundary.

$$c_k = c_k^T, \quad \text{at } x = x_0 \tag{6.32}$$

$$\left.\begin{array}{r} -D_{\mathrm{H^+}}^{\mathrm{eff}} \nabla c_{\mathrm{H^+}} = S_{\mathrm{H^+}}^{\mathrm{CL}} \\ -D_{\mathrm{k \neq H^+}}^{\mathrm{eff}} \nabla c_{\mathrm{k \neq H^+}} = 0 \end{array}\right\} \quad \text{at } x = x_2 \tag{6.33}$$

The recirculation of the electrolyte through the catholyte tank during charge and discharge operation modifies the concentration of species in the catholyte tank, *i.e.*, the Dirichlet boundary condition of concentration at the flow channel-cathode interface. Also, the open boundary considered at the membrane-catalyst layer interface for the electrolyte flow through the membrane affects the total volume of electrolyte in the tank. The evolution of the concentration of species and electrolyte volume in the catholyte tank was modelled using Ordinary Differential Equations (ODEs) as shown in Equations 6.34 and 6.35, where the initial concentration of species in the catholyte tank depends on the solution preparation and the initial SOC.

$$V_{\mathrm{T}} \frac{\mathrm{d}c_{\mathrm{k}}^{\mathrm{T}}}{\mathrm{d}t} = -A_{\mathrm{ca}} N_{\mathrm{k}}|_{x=x_0}, \quad c_{\mathrm{k}}^{\mathrm{T}}(t=0) = c_{\mathrm{k}}^{\mathrm{T,0}} \tag{6.34}$$

$$\frac{\mathrm{d}V_{\mathrm{T}}}{\mathrm{d}t} = -A_{\mathrm{ca}} v|_{x=x_0}, \quad V_{\mathrm{T}}(t=0) = V_{\mathrm{T,0}} \tag{6.35}$$

Boundary conditions for the conservation of charge

The operation of the battery was considered to be in galvanostatic mode, *i.e.*, constant applied current density (j_{appl}). This was set as a Newman boundary condition at the current collector/cathode interface as shown in Equation 6.36. At the cathode-membrane interface ($x = x_1$) a zero flux Newman condition was set (Equation 6.37) since the membrane is not electronically conductive. For the anodic side, which is only represented in the model as a boundary, the electronic potential was set to zero and represents a reference potential (Equation 6.38).

$$-\sigma_{\mathrm{s}}^{\mathrm{eff}} \nabla \phi_{\mathrm{s}} = j_{\mathrm{appl}}, \quad \text{at } x = x_0 \tag{6.36}$$

$$\nabla \phi_{\mathrm{s}} = 0, \quad \text{at } x = x_1 \tag{6.37}$$

$$\phi_{\mathrm{s}} = 0, \quad \text{at } x = x_2 \tag{6.38}$$

The flux of ionic current across the boundaries of the modelling domains was allowed since the electrolyte can enter or leave at the flow channel-cathode interface and the membrane-catalyst layer interface, and therefore, the boundary condition for the ionic

potential is required. At the flow channel-cathode interface, a zero flux Newman boundary condition was set as shown in Equation 6.39, while at the membrane-catalyst layer interface the ionic potential was specified by a Dirichlet boundary condition as shown in Equation 6.40. This ionic potential is calculated by solving Equation 6.41, which assumes that all the current applied to the cell in galvanostatic mode is converted into transfer current density (j_{TV}) due to the charge-transfer reaction at the boundary. The charge-transfer reaction takes into account the effect of concentration of protons through the equilibrium potential (Equation 6.20) and the effect of the hydrogen partial pressure through the activity of hydrogen, Equation 4.68. The partial pressure of hydrogen was set to atmospheric pressure for all simulations.

$$\nabla \phi_{\mathrm{e}} = 0, \quad \text{at } x = x_0 \tag{6.39}$$

$$\phi_{\mathrm{e}} = \phi_{\mathrm{e}}^{\mathrm{CL}}, \quad \text{at } x = x_2 \tag{6.40}$$

$$j_{\mathrm{TV}} R_{\mathrm{CL}} + j_{\mathrm{appl}} = 0 \tag{6.41}$$

6.2.5 Model implementation

The 1D PNP model consists of 18 dependent variables: five molar concentration of species (bulk), c_{k}, hydraulic pressure, p, electronic potential, ϕ_{s}, and ionic potential, ϕ_{e}, throughout the 1D domain; and three molar concentration of species in the electrode surface, $c_{\mathrm{k}}^{\mathrm{s}}$, five concentration of species in the catholyte tank, $c_{\mathrm{k}}^{\mathrm{T}}$, the volume of electrolyte in the cathode tank, V_{T}, and the ionic potential at the catalyst later, $\phi_{\mathrm{e}}^{\mathrm{CL}}$. The set of formulated governing equations considers six balance equations in the 1D domain, Equation 6.10 and 6.2, one charge balance, Equation 6.22, and one Poisson's equation, Equation 6.27. Additionally, three analytical equations are considered for the pore-phase transport, Equations 4.63, 4.64 and 4.65, six ODE are considered, Equation 6.34 and 6.35, along with the analytical equation at the catalyst layer, Equation 6.41. This set of equations was solved in COMSOL Multiphysics$^{\mathrm{TM}}$. COMSOL Multiphysics$^{\mathrm{TM}}$ is a finite element analysis (FEA) software that uses finite element method (FEM) theory to discretise a mathematical model, *e.g.*, a set of partial differential equations (PDEs), into a numerical model or a discrete approximation. The FEM is characterised by a variational formulation or weak formulation of the mathematical model which is obtained by employing a test function and integrating the PDE over the domain. The discretisation strategy includes the creation of finite element meshes, the definition of basis functions, and the mapping of such functions onto the elements of the mesh. In the discretisation, the PDE solution is expressed as a linear com-

bination of a set of basis functions and once the boundary conditions are imposed a system of equations, according to $\mathbf{Ax} = \mathbf{b}$, is obtained, where $\mathbf{A}$ is the system or stiffness matrix, and $\mathbf{x}$ is the vector of unknowns. Numerical solution algorithms are then applied, considering direct or iterative solvers. The mathematics module of COMSOL Multiphysics™ was used to implement an Equation-Based Model (EBM), where the Partial Differential Equation (PDE) interface was used to define equations using the General Form PDE, and the ODE and Differential Algebraic Equation (DAE) interface was used to define equations using the Domain and Boundary ODEs and DAEs. The boundary conditions were implemented by the Zero flux, Dirichlet and Flux/Source option. Table 6.2 summarises the interfaces and options used to implement the model in COMSOL Multiphysics™. The 1D PNP model was solved initially considering a (pseudo) Steady-State (SS) approach, where all equations in Table 6.2 except for the two last equations, namely Equations 6.35 and 6.34, were considered. Later, a Time-Dependent (TD) approach was implemented and solved by adding these two equations, which allow the changes in concentration of species and electrolyte volume at the catholyte tank to be tracked. All simulations were performed with relative tolerance set to 1×10^{-4}. Steady-state and transient problems were solved as a fully coupled problem using a Newton-Raphson method and the Multifrontal Massively Parallel sparse direct Solver (MUMPS).

Table 6.2: Modules, interface and options used in COMSOL Multiphysics™.

Variable to solve for	Eq.	Module	Interface	Option
	6.5			General Form PDE
Pressure (p)	6.30	Mathematics	PDE	Dirichlet
	6.31			Dirichlet
	6.10			General Form PDE
Concentrations (c_k)	6.32	Mathematics	PDE	Dirichlet
	6.33			Flux/Source
	6.22			General Form PDE
Electronic potential (ϕ_s)	6.36	Mathematics	PDE	Flux/Source
	6.37			Zero Flux
	6.27			General Form PDE
Ionic potential (ϕ_e)	6.39	Mathematics	PDE	Zero flux
	6.40			Dirichlet
Surface concentrations (c_k^s)	6.17	Mathematics	ODE and DAE	Domain ODEs and DAEs
Ionic potential at CL (ϕ_e^{CL})	6.41	Mathematics	ODE and DAE	Boundary ODEs and DAEs
Tank volume (V_T)	6.35	Mathematics	ODE and DAE	Boundary ODEs and DAEs
Tank concentrations (c_k^T)	6.34	Mathematics	ODE and DAE	Boundary ODEs and DAEs

An electroneutrality condition was enforced as initial condition across both domains, cathode and membrane, as shown in Equation 6.42. In order to start with a non-constant

profile of the concentration of species across the modelling domain, an interfacial region in the cathode and membrane was considered, as shown in Figure 6.1. The thickness of these interfacial regions was set to $\delta_D = 5\,\text{nm}$, considering that the expected Debye's length is of *ca.* $2.8\,\text{nm}$ for a concentration of $1000\,\text{mol}\,\text{m}^{-3}$ and the relative permittivity of water, $\epsilon_r = 78.46$. This allowed an initial profile of concentration to be set as shown in Equation 6.43, where a linear change of concentration was established initially in the interfacial regions. At the cathode, the initial tank concentration was set for all species, while in the membrane the concentration of all species was set equal to the fixed charge concentration (c_f). This decision was taken for the sake of simplicity and considering that the concentration of species at the membrane side of the cathode-membrane interface are unknowns. However, considering Equation 6.29 it is expected a priori positive jumps in concentration for cations, $\Delta c_+ = c_+^m - c_+^{ca} > 0$, and negative jumps in concentration for anions, $\Delta c_- = c_-^m - c_-^{ca} < 0$. These concentration jumps are obtained once the model is solved and the charge carriers in the solution at each side of the cathode-membrane interface are accommodated. During the model testing, it was seen that considering the initial profile of concentrations (c_k^0) given in Equation 6.43, instead of a constant concentration across the whole modelling domain or a constant concentration at each phase, namely cathode and membrane, ensuring the convergence of the system of equations.

$$\sum_k z_k c_k = 0, \quad \text{for } x_0 \leq x \leq x_1$$
$$\sum_k z_k c_k + z_f c_f = 0, \quad \text{for } x_1 < x \leq x_2 \tag{6.42}$$

$$c_k^0 = \begin{cases} c_k^{T,0}, & \text{for } x < l_{ca} - \delta_D \\ mx - b, & \text{for } l_{ca} - \delta_D > x > l_{ca} + \delta_D \\ c_f, & \text{for } x > l_{ca} + \delta_D \end{cases} \tag{6.43}$$

$$m = \frac{c_f - c_k^{T,0}}{2\delta_D}, \quad b = c_k^{T,0} - \frac{c_f - c_k^{T,0}}{2\delta_D}(l_{ca} - \delta_D) \tag{6.44}$$

A structured mesh size was used for the modelling domain, considering 100 elements in the interfacial regions of thickness δ_D, 840 elements in the remaining cathode of thickness $l_{ca} - \delta_D$, and 508 elements in the remaining membrane of thickness $l_m - \delta_D$. Table 6.3 summarises the operating condition used when simulating the steady-state and time-dependent problem. The electrolyte solution was considered to be of 0.8 M V(IV) in 5 M of H_2SO_4. Several geometric, transport and kinetic properties, of the cell components, were required to implement the model. Table 6.4 summarises the value of the input prop-

erties used in the 1D PNP model for the 5 cm^2 cross-sectional area RHVFC. Any property not included in this table can be found in the previous Chapters 4 and 5. The relative permittivity of the environment could change with temperature and electrolyte composition, however, such an effect was neglected in this work and instead the permittivity of water (ϵ_r) was used. In the following sections, the simulation results of the time-dependent 1D PNP model and the steady-state simulation results are presented.

Table 6.3: Simulated operating conditions.

Approach	Current density / $\pm A\,m^{-2}$	SOC / SOC($t = 0$) (%)
Steady-state	2, 20:10:4660	1:1:99
Time dependent	250, 500, 1000, 1500, 2000	1 (ch) and 99 (dis)

Table 6.4: Geometric and transport properties.

Parameter	Value	Unit	Source
k_d	1×10^4	s^{-1}	(Knehr et al., 2012b)
β_d^{ca}	0.25	–	(Knehr et al., 2012b)
β_d^m	0.05	–	–
κ_p^m	1.58×10^{-18}	m^2	Lei et al. (2015)
κ_ϕ^m	1.13×10^{-20}	m^2	Lei et al. (2015)
ϵ_0	8.8542×10^{-12}	$F\,m^{-1}$	–
ϵ_r	78.46	$F\,m^{-1}$	–
ε_m	0.2	m^2	Yang et al. (2015b)
δ_D	5×10^{-9}	m	Estimated

6.3 Electronic potential during galvanostatic charge and discharge

Using the 1D PNP model the cell behaviour under galvanostatic charge and discharge at five applied current densities (Table 6.3) was studied. The initial SOC in the electrolyte tank was set to 1% and 99% for galvanostatic charge and discharge, respectively. The 1D PNP model along with the ODEs for the electrolyte tank was able to simulate the cell potential behaviour during charge and discharge. The electronic potential at the current collector/electrode interface along the charge and discharge time is presented in Figure 6.3. In this figure, no other ohmic overpotential from the additional components (*e.g.,* anodic gas diffusion layer, flow fields and current collectors) were considered, and therefore, it does not represent the total cell potential. As expected, increasing the applied current

density produces an increase in the electronic potential at the current collector/electrode interface during charge and a decrease during discharge. This effect was related to an increase in the electrode overpotential as the charge or discharge current increases (*i.e.*, the absolute value of the applied current increases), producing a decrease in the total time of charge or discharge since the mass-transport limitation effects are displayed faster. At the beginning of the charge operation, an increase in the overpotential of the electrode was observed at high values of applied current density. In this region ($\sim t < 300$ s), the electronic potential at $x = 0$ displayed a fast decrease from an initial high value of potential and then continued increasing as expected with respect to time. Such potential behaviour has been observed in experimental measurements of single-cycle charge-discharge as the current density is increased, and it was related to mass-transport limitation effects that could appear at the beginning of charge when high current density values are used due to a fast initial depletion of reactants. Figure 6.4a presents the electronic potential at the current collector/electrode interface during galvanostatic charge at a current density of 500 A m^{-2} and at different values of diffusion coefficient for VO^{2+}. It was assumed equal diffusion coefficients for VO^{2+} and VO$_2^+$. At low values of the diffusion coefficient, the initial mass-transport limitation region was observed. Additionally, higher overpotentials were also observed, producing lower operating times to reach a cut-off potential, *e.g.*, 1.4 V for the charge. It is important to reduce the uncertainty of the diffusion coefficient for vanadium species, which could depend on temperature and composition when simulating the cell performance at the practical level of concentration of vanadium and sulphuric acid (*e.g.*, 1 M VOSO$_4$ and 5 M H$_2$SO$_4$) used in RHVFCs. Figure 6.4b presents the concentration profiles for VO^{2+} across the thickness of the electrode at four initial SOCs of 1.0%, 1.25%, 2.0% and 3.0% (which are marked on the inset of Figure 6.4a) for two values of diffusion coefficients for VO^{2+} ($0.75 \times D_{\text{VO}^{2+}}^{\text{el}}$ and $D_{\text{VO}^{2+}}^{\text{el}}$). In general, the increase in mass-transport limitation effects at the beginning of charge was observed at SOCs lower than 3.0%. There was an initial increase in the concentration of the reactant, *i.e.*, VO^{2+} during charge operation, close to the membrane while a decrease in its concentration close to the current collector. As the SOC slightly increased from 1.0% to 3.0% the concentration profile transitioned to a decreasing profile from the current collector to the membrane. At higher values of diffusion coefficient for VO^{2+}, the depletion of VO^{2+} due to the charge-transfer reaction occurring predominantly close to the current collector could be counteracted by its transport from the membrane to the current collector. As the diffusion coefficient decreased this effect was less intense and an increase of potential at the beginning of the charge operation was displayed. It is important to mention that at even lower diffusion coefficients and very low SOC, *e.g.*, SOC $< 2\%$, the numerical approximation did not successfully represent the profile of the concentration of VO^{2+} across the electrode producing negative values for its concentration, therefore, such

initial results were disregarded. To verify the model for such initial conditions, namely low diffusion coefficients or high applied current densities, is necessary and it is considered as an important part of the future work.
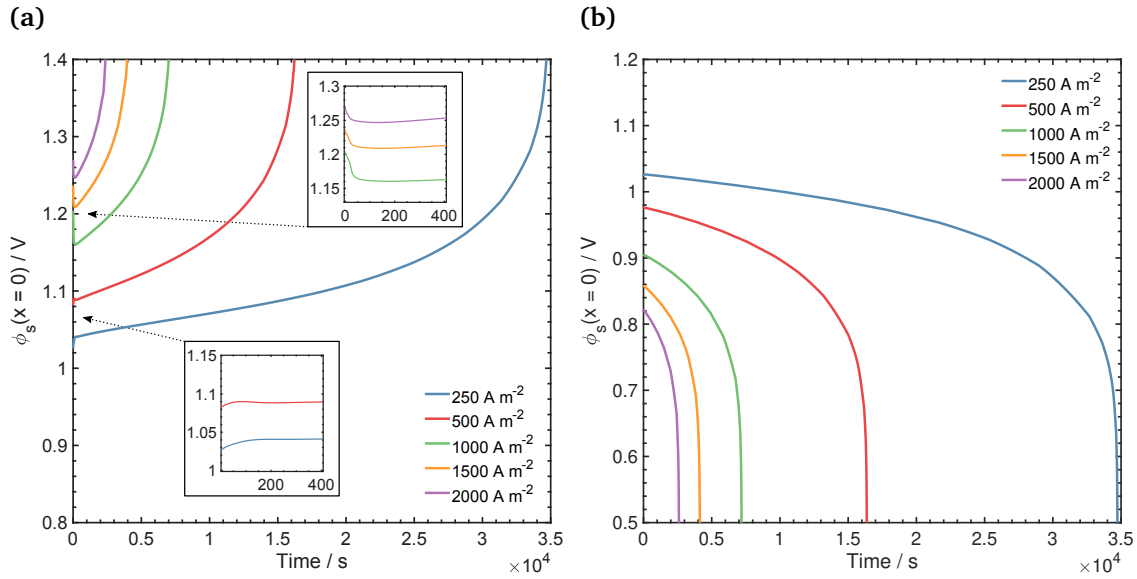
(a)

(b)

Figure 6.3: Electronic potential at the current collector / electrode interface (x = 0) as a function of time during galvanostatic operation: (a) Charge; and (b) Discharge.
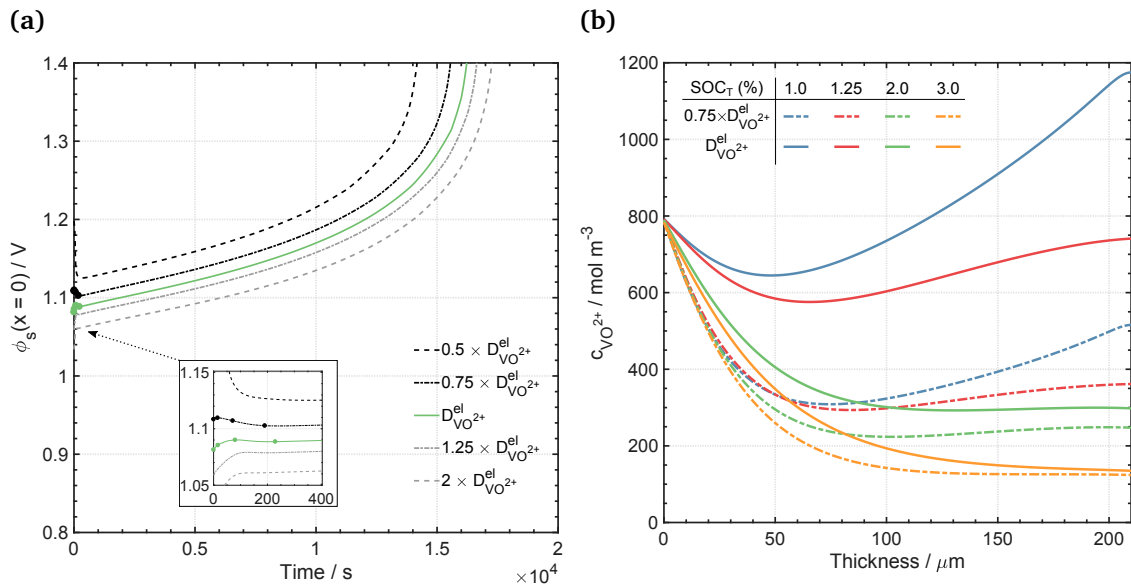
(a)

(b)

Figure 6.4: Electronic potential at the current collector / electrode interface during galvanostatic charge at a current density of 500 $A\,m^{-2}$ and different values for the diffusion coefficient of VO^{2+} and VO_2^+. These diffusion coefficients were set to $D_{VO^{2+}}^{el} = D_{VO_2^+}^{el} = 3.9 \times 10^{-10}$.

Figure 6.5 presents the normalised electronic potential and the cathodic overpotential distribution in the electrode during the galvanostatic charge at an applied current density of 250, 500 and 1000 $A\,m^{-2}$. Two times, which correspond to a SOC in the electrolyte tank of 25% and 75%, during the cell operation are displayed. The SOCs

were calculated using the concentration of species in the electrolyte tank, *i.e.*, $SOC(\%) = 100 \times c_{\mathrm{VO}_2^+}^{\mathrm{T}}/(c_{\mathrm{VO}^{2+}}^{\mathrm{T}} + c_{\mathrm{VO}_2^+}^{\mathrm{T}})$. The electronic potential values were normalised by considering the total potential drop across the electrode, *i.e.*, $\Phi = (\phi_{\mathrm{s}} - \phi_{\mathrm{s}}^{\min})/(\phi_{\mathrm{s}}^{\max} - \phi_{\mathrm{s}}^{\min})$, to allow for better visualisation of the electronic potential profiles due to the small gradients across the electrode. It is possible to observe that the charge-transfer reaction occurs mostly close to the current collector ($x = 0$) for most of the SOC range, and as the applied current density increased, the cathodic overpotential and the gradient of electronic potential also increased, while the used electrode thickness for the charge-transfer reaction decreased. This indicated that the transport of protons across of the membrane was not a limiting process, considering the high concentration of H$^+$ in the solution, while the transport of vanadium species (VO^{2+} and VO$_2^+$) was considered to be limiting process. This is discussed in more detail below by means of a simple scaling analysis. Higher positive values of cathodic overpotential were observed during charge, when the forward or anodic direction of the charge-transfer reaction took place (Equation 6.14), in response to higher positive current densities. Similar trends were displayed during discharge, where higher negative values of cathodic overpotential were observed for higher negative current densities, *i.e.*, the backward or cathodic direction of the charge-transfer reaction took place (Equation 6.14). This was in accordance with the formulation of the rate of reaction (Butler-Volmer kinetics). The cathodic overpotential profile across the used electrode thickness predicted by the model became more linear with higher values as the SOC increases as well as with higher applied current densities. This could be related to the faster depletion of reactants, and therefore, lower used electrode thicknesses, which could require higher rates of reaction in order to maintain galvanostatic operation at the applied current density.

The electronic potential gradient also increased with current density during discharge, displaying positive values of the gradient across the electrode. Figure 6.6a presents the distribution across the electrode of the electronic (j_{s}) and ionic (j_{e}) current density for a time when the SOC in the electrolyte tank was of 25% and 75% during galvanostatic discharge. For the kinetic and transport conditions considered in the model, the charge-transfer reaction occurred in some fraction of the electrode for the most part as it was seen in Figure 6.5. The used thickness of the electrode varies with the SOC, being thinner as the SOC increased during charge and thinner as the SOC decreased during discharge, which corresponded to fewer reactant species being present in the electrolyte. This was confirmed by the profile of concentration difference in the pore-phase ($\Delta c = c_{\mathrm{k}}^{s} - c_{\mathrm{k}}$) as shown in Figure 6.6b. As expected for discharge operation, the surface concentration of VO$_2^+$ and H$^+$ were lower than their concentration in the bulk of the pore-phase, while the opposite was observed for VO^{2+}. During charge operation, similar profiles were found but reactants and products were inverted since the charge-transfer reaction occurred in the
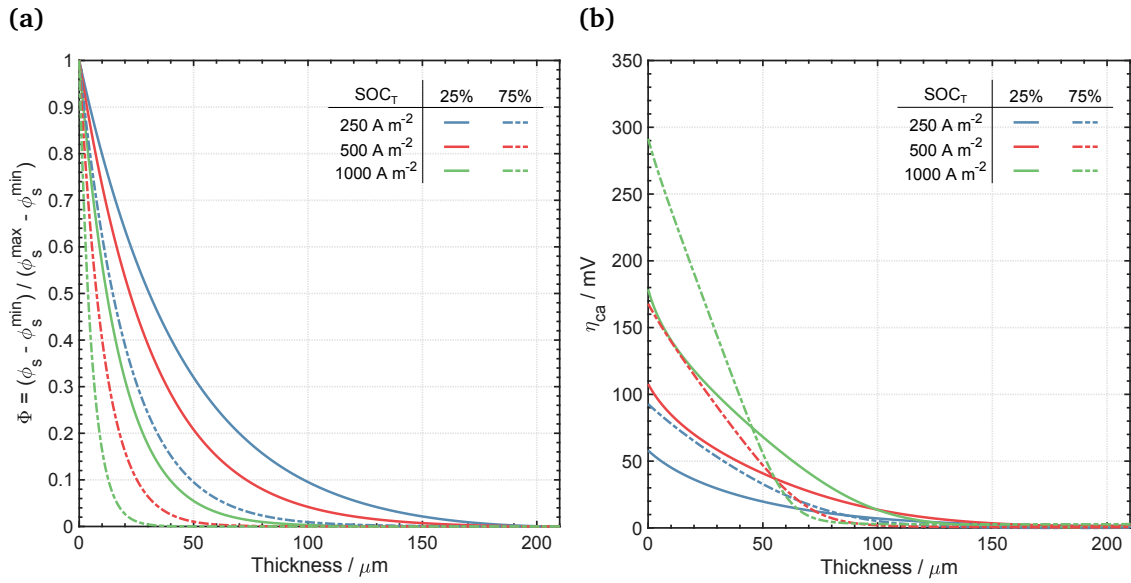
(a)

(b)

Figure 6.5: Distribution in the electrode for galvanostatic charge at a current density of 250, 500 and 1000 $\mathrm{A\,m^{-2}}$ and at a SOC of 25% and 75% in the electrolyte tank: (a) Normalised electronic potential and (b) Cathodic overpotential.

opposite direction. Once the electronic current density reached a zero value within the thickness of the electrode, the ionic current density remained constant in the remaining electrode thickness, as to be expected by the conservation equations.
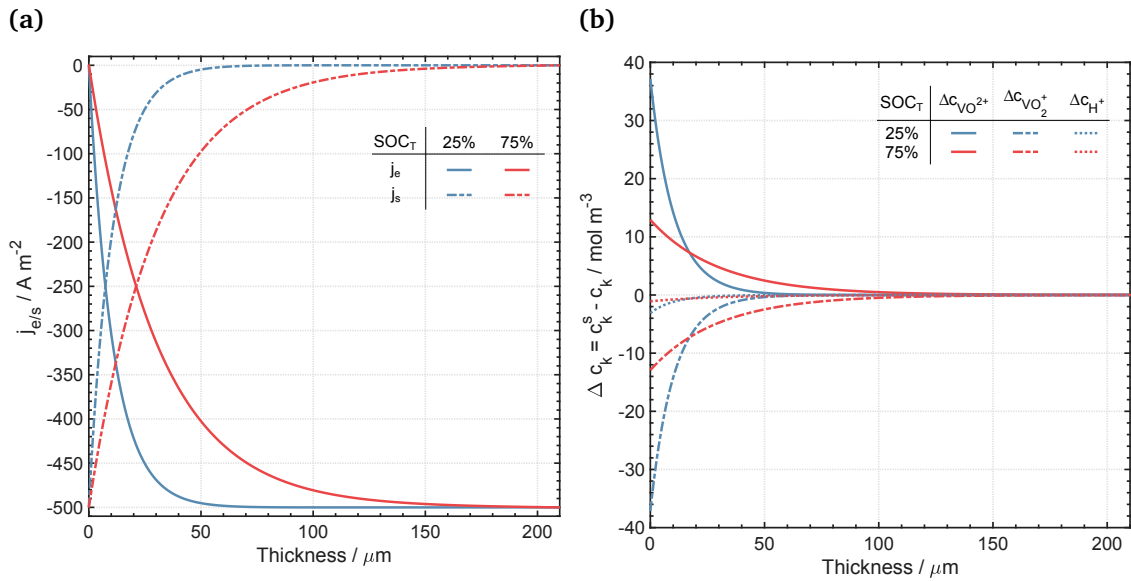
(a)

(b)

Figure 6.6: Distributions in the electrode for galvanostatic discharge at an applied current density of 500 $\mathrm{A\,m^{-2}}$ and at a SOC of 25% and 75% in the electrolyte tank of: (a) Electronic (j_s) and ionic (j_e) current densities; and (b) Concentration difference in the pore-phase, $\Delta c = c_\mathrm{k}^s - c_\mathrm{k}$.

In order to understand the limiting transport process that dominates the electrode behaviour, a scaling analysis of the conservation of species (Equation 6.10) and the conservation of electronic charge in the electrode (Equation 6.22) was developed. The non-dimensional variables presented in Equation 6.45 were used for this analysis, where char-

acteristic concentrations ($c_k(x = 0)$), length (l_{ca}) and thermal potential (RT/F) were defined. Equations 6.46 and 6.47 present the non-dimensional equations for the conservation of species and charge in the electrode, where the characteristic time scales (τ) for the transport mechanisms of species, including convection (C), diffusion (D) and migration (M), and the Damköhler number for the transport of electrons (Da_s) are considered.

$$\tilde{c}_k = \frac{c_k}{c_k(x=0)}, \quad \tilde{x} = \frac{x}{l_{ca}}, \quad \tilde{\phi}_e = \frac{\phi_e F}{RT}, \quad \tilde{\phi}_s = \frac{\phi_s F}{RT}, \quad \tilde{\eta} = \frac{\eta F}{RT} \tag{6.45}$$

$$\frac{\partial \varepsilon \tilde{c}_k}{\partial t} + \frac{\partial}{\partial \tilde{x}}\left(\frac{1}{\tau_C}\tilde{c}_k - \frac{1}{\tau_D}\frac{\partial \tilde{c}_k}{\partial \tilde{x}} - \frac{1}{\tau_M}\tilde{c}_k\frac{\partial \tilde{\phi}_e}{\partial \tilde{x}} \right) = \frac{1}{\tau_{CT}}\left(\frac{\tilde{c}_{VO^{2+}}}{\tilde{c}^\ominus} \right)^{\alpha_c}\left(\frac{\tilde{c}_{VO_2^+}}{\tilde{c}^\ominus} \right)^{\alpha_a}\left(\frac{\tilde{c}_{H^+}}{\tilde{c}^\ominus} \right)^{2\alpha_a}\left[e^{\alpha_a\tilde{\eta}} - e^{-\alpha_c\tilde{\eta}} \right] \tag{6.46}$$

$$\frac{\partial^2 \tilde{\phi}_s}{\partial \tilde{x}^2} = Da_s\left(\frac{\tilde{c}_{VO^{2+}}}{\tilde{c}^\ominus} \right)^{\alpha_c}\left(\frac{\tilde{c}_{VO_2^+}}{\tilde{c}^\ominus} \right)^{\alpha_a}\left(\frac{\tilde{c}_{H^+}}{\tilde{c}^\ominus} \right)^{2\alpha_a}\left[e^{\alpha_a\tilde{\eta}} - e^{-\alpha_c\tilde{\eta}} \right] \tag{6.47}$$

These characteristic parameters are defined in Equations 6.48 and 6.49, with respect to the characteristic variables of concentration, length and thermal potential, along with transport properties for the ionic species and electronic current. On the other hand, a steady-state analysis approach was considered to compare every transport time scale for the species (*i.e.*, τ_C for convection, τ_D for diffusion and τ_M for migration) to the charge-transfer reaction time scale (τ_{CT}). This was done by considering a Damköhler number for every transport mechanism defined as a function of the time scales, namely time scale of every transport mechanism over the time scale of the charge-transfer reaction, which allowed to obtain the characteristic penetration lengths (δ) as shown in Equation 6.48. Additionally, the required time for an applied current density was defined as, $\tau_R = l_{ca}Fc_k(x=0)/j_{appl}$. Table 6.3 summarises the characteristic parameters for the transport of species and electrons for the galvanostatic discharge at a SOC of 25% and 75% in the electrolyte tank (Figure 6.6).

$$\tau_C = \frac{l_{ca}}{v}, \quad \tau_D = \frac{l_{ca}^2}{D_{VO^{2+}}^{eff}}, \quad \tau_M = \frac{\tau_D}{z_k}, \quad \tau_{CT} = \frac{Fc_k(x=0)}{j_0(x=0)}, \quad j_0 = aFkc_{VO^{2+}}^{\alpha_c}c_{VO_2^+}^{\alpha_a}c_{H^+}^{2\alpha_a}$$

$$\delta_C = \frac{vFc_k(x=0)}{j_0(x=0)}, \quad \delta_D = \sqrt{\frac{D_k^{eff}Fc_k(x=0)}{j_0(x=0)}}, \quad \delta_M = \sqrt{z_k} \times \delta_D \tag{6.48}$$

$$Da_s = \frac{l_{ca}^2 F j_0(x=0)}{\sigma_s^{eff}RT} \tag{6.49}$$

In general, smaller time scales and larger penetration lengths indicate a fast transport

Table 6.5: Time scales and penetration lengths of transport mechanisms of ionic and electronic species during galvanostatic discharge at a SOC of 25% and 75% in the electrolyte tank. Convection (C), Diffusion (D), Migration (M), Charge-transfer (CT) and Required (R).

			SOC$_T$ (%)	
	Transport mechanisms		25	75
VO$_2^+$	Time scale / s	τ_C		840
		τ_D		158
		τ_M		158
		τ_{CT}	10.40	30.44
	Penetration length / μm	δ_C	2.6	7.6
		δ_D	53.9	92.2
		δ_M	53.9	92.2
	Electrons	Da_s	7.1×10^{-3}	7.3×10^{-3}
	Required time / s	τ_R	8.10	24.31

mechanism when compared to the charge-transfer reaction rate. Convective transport of species was the slowest process, however, since the velocities across the electrode were very small ($\sim 10^{-7}$) it is expected that neglecting the convective transport would not produce major changes on the displayed concentration profiles. The next slower process was the diffusion transport of species, having the same time scale than the migration transport for VO$_2^+$ ($z_{VO_2^+} = +1$) and twice the time scale of migration transport for VO^{2+} ($z_{VO^{2+}} = +2$). It was clear by comparing the time scales of diffusion for VO$_2^+$, charge-transfer reaction, and required time, $\tau_R < \tau_{CT} < \tau_D$, that the diffusive transport of species in the electrolyte was the limiting process. This also confirmed that the charge-transfer reaction could be the limiting process since its time scale was slightly lower in magnitude than the required time. The transport of electrons in the electrode was even faster, being about 1000 times faster than the charge-transfer reaction time scales. A rough estimation of the used electrode thickness at the SOC of 25% and 75% in the electrolyte tank can be obtained by the diffusion penetration length as shown in Table 6.3. This was confirmed by comparing the penetration lengths of diffusion with the used electrode thickness displayed in Figure 6.6a.

Pseudo-steady-state models have been used for the modelling of VRFBs (Chen et al., 2014; Ma et al., 2011; You et al., 2009b; Zheng et al., 2014c). The validity of such approximation was investigated for the Poisson-Nernst-Planck model by comparing the pseudo-Steady-State (SS) and Time-Dependent (TD) potential results for galvanostatic charge and discharge, as shown in Figure 6.7. In the steady-state approach, the evolution in time was represented by the evolution of SOC in the electrolyte tank, which was changed manually

at the flow channel/electrode interface ($x = 0$, Equation 6.32), and at every SOC the cell was assumed to reach a steady-state condition. In the time-dependent implementation of the model the value of the concentration of species at $x = 0$ over time was calculated by solving the ODEs in the electrolyte tank, Equations 6.34 and 6.35. In a continuous operation, the SOC changes from ~0% to ~100% during charge, and from ~100% to ~0% during discharge. The pseudo-SS simulations were a good approximation of the potential behaviour along variations of SOC in the electrolyte tank. During charge, the pseudo-SS results underestimated the overpotential of the cell, displaying lower values of electronic potential at the current collector/electrode interface. The electronic potential mismatch was higher at the beginning of charge (*e.g.*, $SOC_T < 10\%$), where the mass-transport limitation effects were observed. The maximum difference observed was of ~44 mV at the beginning of charge for an applied current density of 1000 A m^{-2}.
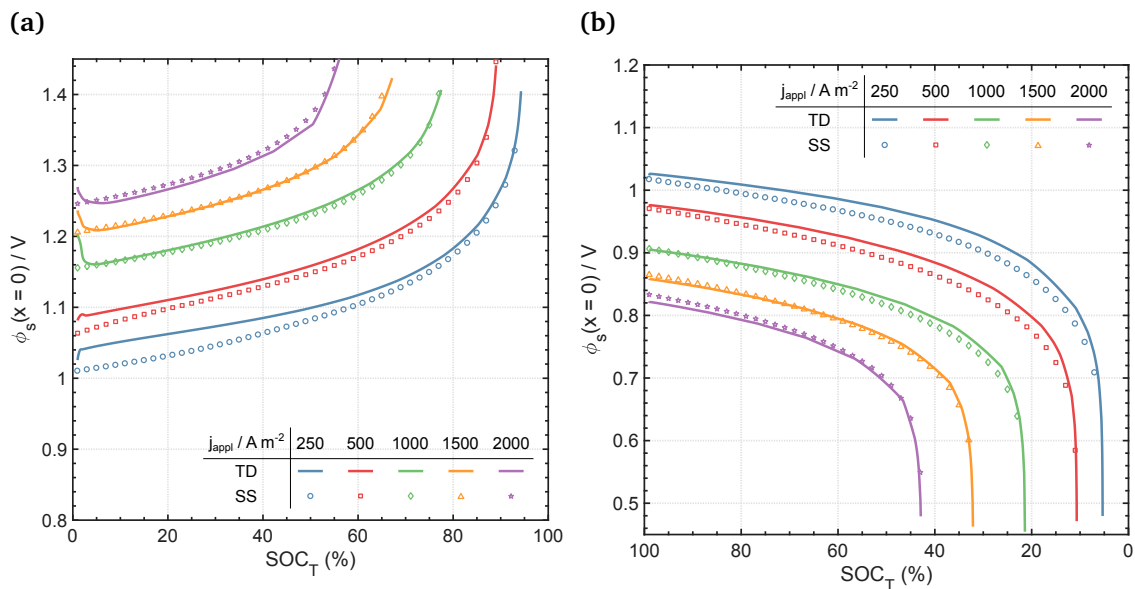

Figure 6.7: Comparison of Time-Dependent (TD) and Steady-State (SS) potential simulations for galvanostatic operation along variation of SOC in the electrolyte tank: (a) charge; and (b) discharge.

6.4 Spatial distribution of ionic potentials and concentrations of species

The ionic potential distribution across the electrode during galvanostatic charge and discharge at three values of applied current density and two SOCs in the electrolyte tank are presented in Figure 6.8. In these figures, the black segmented line indicates the electrode/membrane interface position in the x-coordinate, where the jump in the ionic potential occurs. The ionic potential presents a non-linear behaviour, primarily close to the flow channel in the electrode and close to the electrode/membrane interface in the membrane.

In these regions, most of the charge-transfer reaction and dissociation of HSO_4^- took place, and therefore the ionic potential changed as a result of changes in the concentration of ionic species. In the first section of the membrane, dissociation took place as a result of the change in the concentration of sulphuric acid species in a narrow region. This concentration change promoted the dissociation reaction to occur in the backward direction of Equation 6.16, reducing the concentration of H^+ and SO_4^{2-} and increasing the concentration of HSO_4^-. In the membrane, after the non-linear region, the profile of ionic potential was virtually linear, displaying a higher slope as the applied current density increased and indicating an ohmic behaviour. In agreement with what was observed for the electronic potential and cathodic overpotential, the ionic potential increased, *i.e.*, it has a less negative value, during charge as the applied current density increases, in order to produce higher positive values of overpotential (Equation 6.18). During discharge, the opposite occurred, while for both modes of operation the model predicted negative values of ionic potential. Figure 6.8c presents the ionic potential distribution across the electrode / membrane interfacial region during galvanostatic discharge at a SOC of 25%. An electrode / membrane interfacial region of 10 nm is presented with a scaled x-coordinate by substituting the electrode thickness, *i.e.*, $\Delta x = x - l_{ca}$. In this interfacial region the ionic potential changes continuously due to the Donnan exclusion phenomenon (Kodým et al., 2016). For the electrolyte composition and SOC presented in Figure 6.8c, the change of ionic potential across a narrow region of approximately 5 nm, which is represented by dotted vertical lines in Figure 6.8c, was less than 2 mV. As expected for a cation-exchange membrane as Nafion 115, the ionic potential difference across the interfacial region is negative ($\Delta\phi_D = \phi^m - \phi^{ca}$), displaying a higher value of ionic potential in the outer solution in the electrode and a lower value of ionic potential in the membrane.

Lei et al. (2015) reported a VRFB crossover model, considering a PNP model to describe electrolyte/membrane interfacial regions, where the membrane bulk region considered an electro-neutrality condition and the electrodes were modelled considering an electro-neutral lumped description. They reported that the ionic potential jumps observed were of about 2 mV across a region of approximately 4 nm, recognising that realistic continuous ionic potential profiles across the interfacial region could be simulated when using a PNP description, as well as suggesting the importance of the Donnan effect on the crossover flux of species across the membrane. The VRFB crossover study presented by Knehr et al. (2012a) employed an electro-neutrality condition and treated the electrode/membrane interface with complicated boundary conditions, allowing continuous concentration profiles for all ionic species except for SO_4^{2-}, which presented a discontinuous profile, in order to fulfil the electro-neutrality assumption. This work reported positive ionic potential differences for the cation-exchange membrane (Nafion) at the electrode/membrane interface, contrary to the theoretically expected values (Knehr et al.,
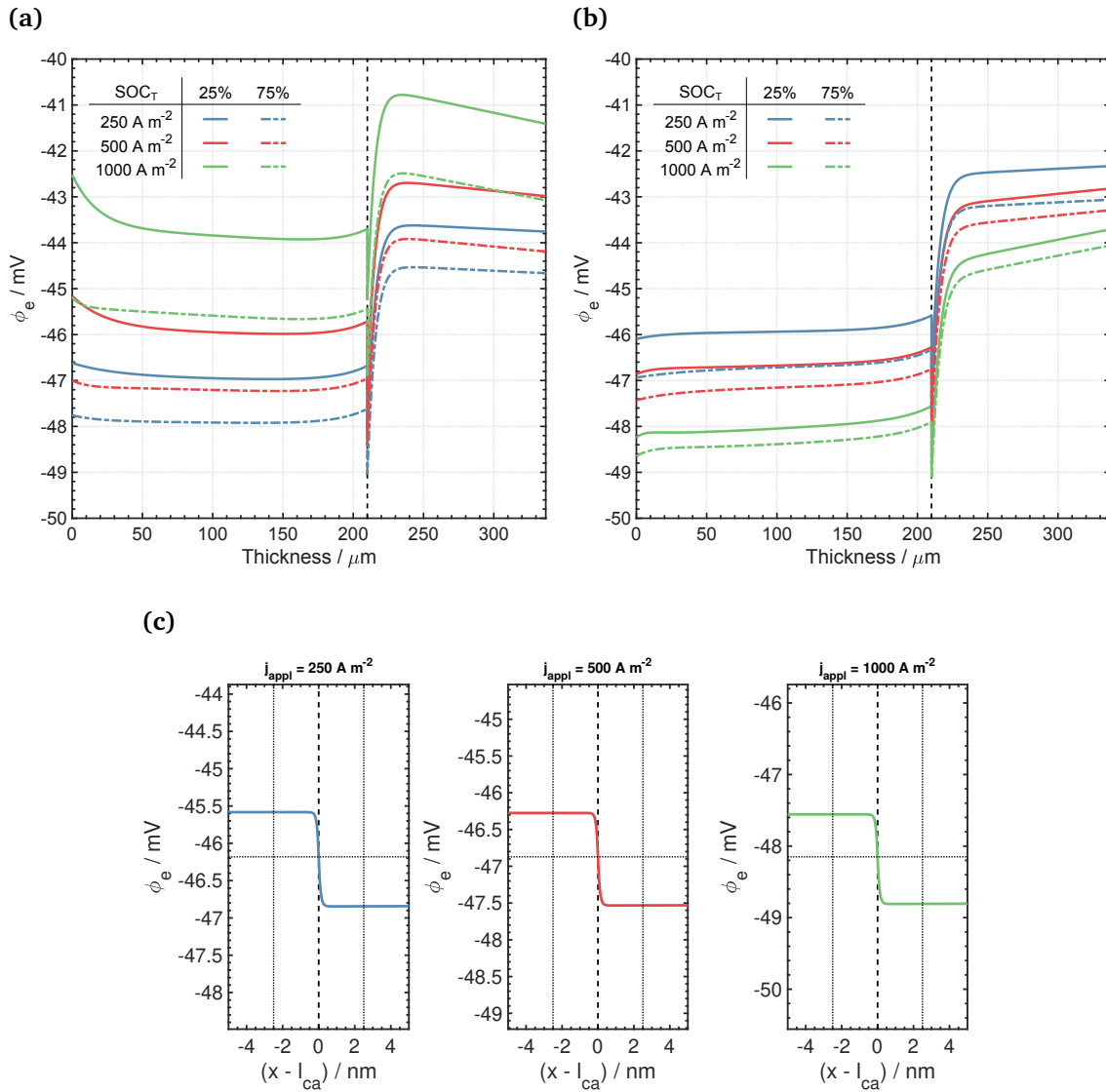
(a)

(b)

(c)

Figure 6.8: Ionic potential distribution in the electrode and membrane for galvanostatic operation at a current density of 250, 500 and 1000 $A\,m^{-2}$ during: (a) Charge and (b) Discharge at a SOC of 25% and 75% in the electrolyte tank; and (c) Discharge at the electrode / membrane interfacial region at a SOC of 25% in the electrolyte tank.

2012a). The VRFB crossover model presented by Yang et al. (2015b), which treated the electrodes and membrane as a continuous domain and used the electro-neutrality condition, displayed numerical artefacts in the profiles across the electrode/membrane interfacial regions.

Figure 6.9 presents the space-charge density distribution across the electrode / membrane interfacial region (Equation 6.28). The y-axis values have been divided by Faraday's constant and the space-charge density is given in units of concentration ($mol\,m^{-3}$). The space-charge density has the same sign as the fixed-charge groups inside the membrane and the opposite sign in the external solution (Kontturi et al., 2008). It is clear that charge separation was localised in a narrow thickness of electrode and membrane from the electrode/membrane interface ($x = l_{ca}$), and that farther away from this interface the electro-neutral condition was reached by the ionic species in the electrode and membrane.
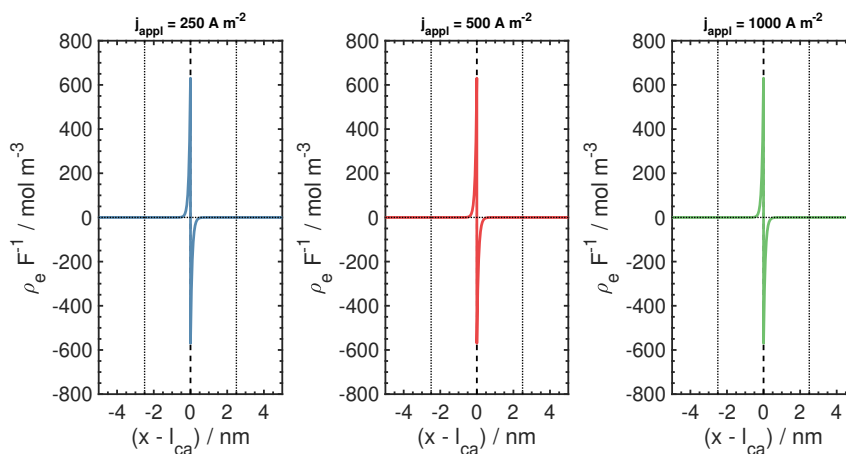
Figure 6.9: Space-charge density across the electrode / membrane interfacial region for galvanostatic discharge at an applied current density of 250, 500 and 1000 $A\,m^{-2}$ and a SOC of 25% in the electrolyte tank.

The concentration profile of VO^{2+}, VO_2^+, H^+ and HSO_4^- across the electrode and membrane during galvanostatic charge and discharge at three current densities and two values of SOC in the electrolyte tank are presented in Figures 6.10, 6.11, 6.12 and 6.13, respectively. Non-linear profiles were observed for all ionic species across the electrode and at the initial region of the membrane, while farther inside the membrane linear profiles dominated, which agreed with the ionic potential behaviour (Figures 6.8a and 6.8b). The concentration of VO^{2+} across the electrode and membrane decreased from low to high SOC, *i.e.*, as the time passes during charge, while the concentration of VO_2^+, H^+ and HSO_4^- increased. At high current densities, the gradient of concentrations of species are more pronounced, and at high SOC for charge (Figure 6.10a) and low SOC for discharge (Figure 6.11b), the reactants were consumed in a short thickness from the current collector, leading to the mass-transport limitations observed at the end of charge or discharge operation (Figure 6.3).

In Figures, 6.10 to 6.13, the concentration of species at the membrane/catalyst layer interface was not fixed during the simulations, instead an open boundary condition (Equation 6.33) was applied for all species. This allowed for the concentration of species to vary depending on the operating conditions used. During charge, H^+ are consumed in the catalyst layer due to the anodic charge-transfer reaction involving H_2 and H^+, therefore, the concentration of protons decreased in the membrane and towards the catalyst layer boundary ($x = l_{ca} + l_m$). As the applied current density increased the concentration of H^+ decreased at the catalyst layer (Figure 6.12a). The opposite was observed during discharge operation in Figure 6.12b.

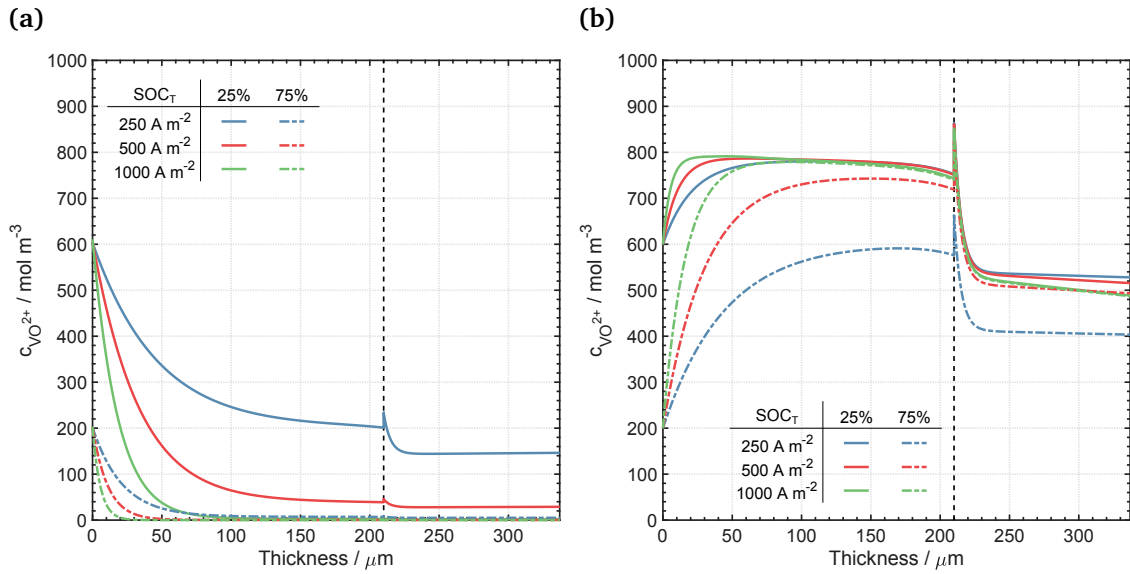All ionic species displayed a jump in concentration at the electrode/membrane in-

(a)

(b)

Figure 6.10: Concentration profile of VO^{2+} in the electrode and membrane for galvanostatic operation at a current density of 250, 500 and 1000 $A\,m^{-2}$ and at a SOC of 25% and 75% in the electrolyte tank during: (a) charge and (b) discharge.

(a)

(b)

Figure 6.11: Concentration profile of VO_2^+ in the electrode and membrane for galvanostatic operation at a current density of 250, 500 and 1000 $A\,m^{-2}$ and at a SOC of 25% and 75% in the electrolyte tank during: (a) charge and (b) discharge.
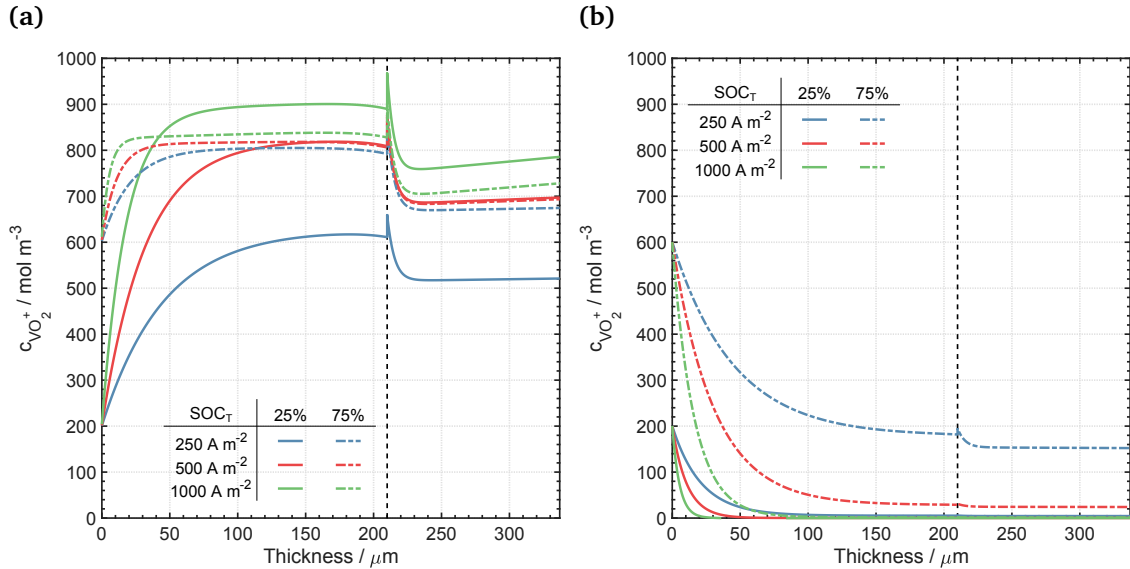
terface, which is presented in Figure 6.14 for H^+ and HSO_4^- for galvanostatic discharge at a SOC of 25% in the electrolyte tank. It is difficult to determine the borders of the interfacial region. Therefore, in order to estimate the jump of ionic potential and concentrations, equal and constant interfacial region thicknesses (δ_D) at each side of the electrode/membrane interface were assumed. For a 25% SOC, the change of concentration of H^+ and HSO_4^- across the narrow interfacial region was less than 400 and 250 $mol\,m^{-3}$, respectively. A positively charged ion like H^+ displayed an increase in concentration from the external solution in the electrode to the membrane, while a negatively charged ion like HSO_4^- displayed an increase in concentration. Therefore, the cation-exchange membrane
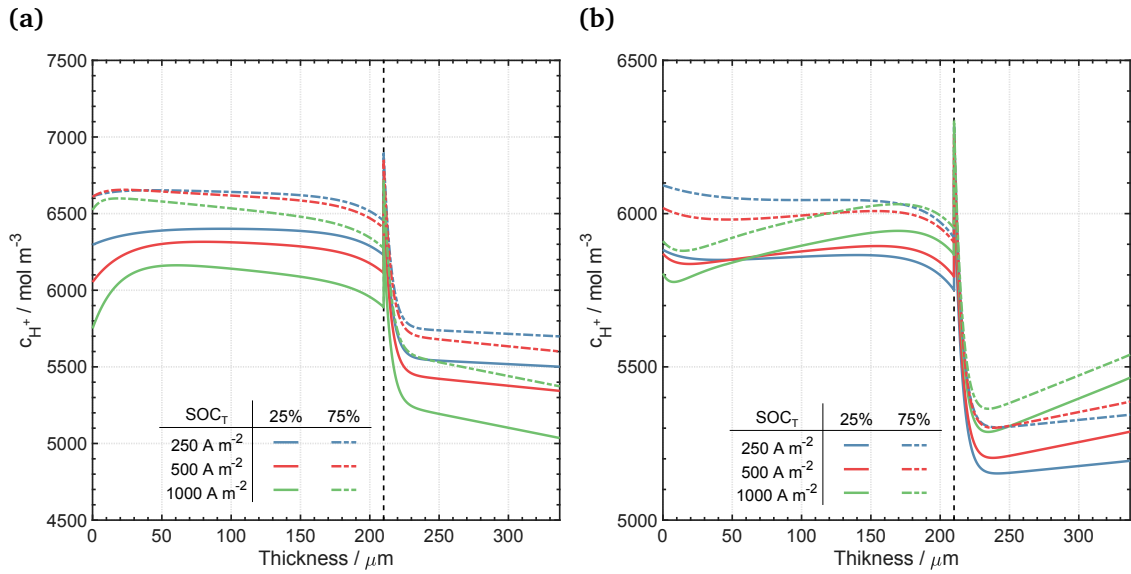
(a)

(b)

Figure 6.12: Concentration profile of H^+ in the electrode and membrane for galvanostatic operation at a current density of 250, 500 and 1500 $A\,m^{-2}$ and at a SOC of 25% and 75% in the electrolyte tank during: (a) charge and (b) discharge.

(a)

(b)

Figure 6.13: Concentration profile of HSO_4^- in the electrode and membrane for galvanostatic operation at a current density of 250, 500 and 1500 $A\,m^{-2}$ and at a SOC of 25% and 75% in the electrolyte tank during: (a) charge and (b) discharge.
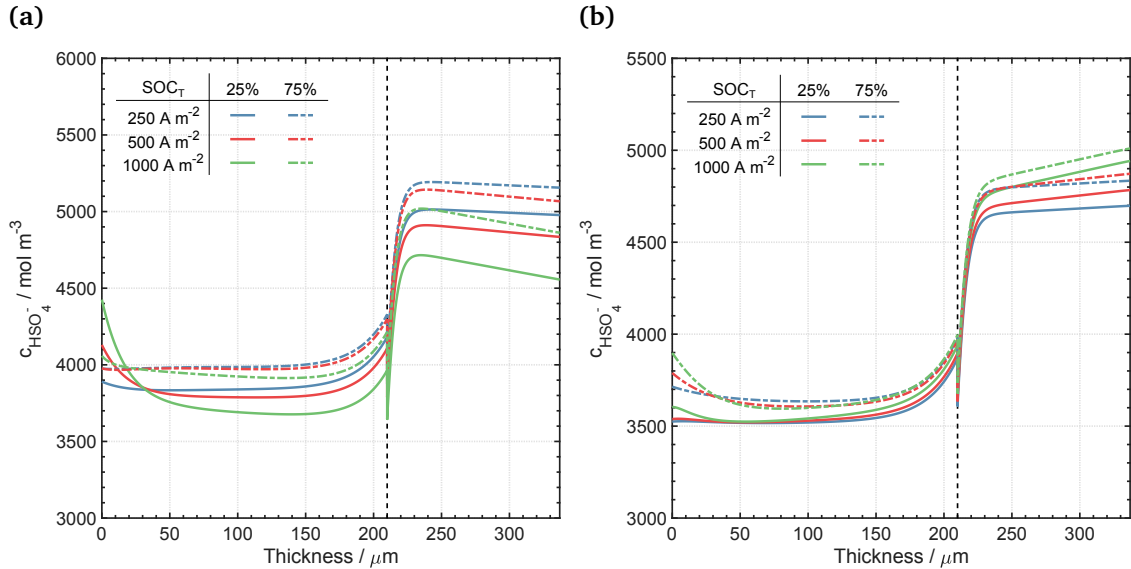
tends to uptake positively charged ions while excluding negatively charged ions. Similar behaviour was observed for the other ionic species (VO^{2+}, VO_2^+ and SO_4^{2-}).

Figure 6.15 presents a comparison of the ionic potential differences across the electrode/membrane interfacial region to test the validity of the Donnan approximation (Equation 6.29) for the potential jump under galvanostatic operation. According to the theory, the ionic potential difference ($\Delta\phi_D = \phi_e^m - \phi_e^{ca}$) should equal the difference in ionic potential calculated from the concentration difference across the interfacial region ($\Delta\phi_D^{c_k}$) as given in Equation 6.29 under equilibrium conditions. This ionic potential difference
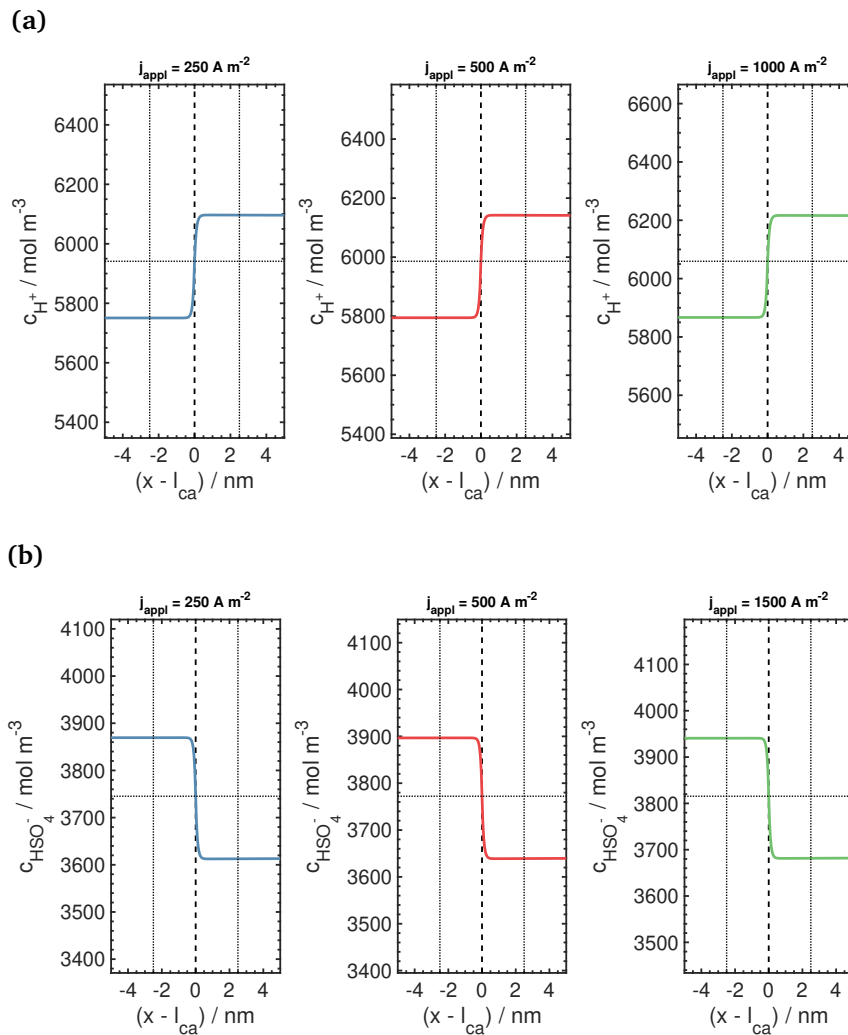
(a)

(b)

Figure 6.14: Concentration profile across the electrode / membrane interface for galvano-static discharge at an applied current density of 250, 500 and 1000 $\mathrm{A\,m^{-2}}$ and a SOC of 25% in the electrolyte tank: (a) $\mathrm{H^+}$; and (b) $\mathrm{HSO_4^-}$.

(Donnan approximation) was in general higher, *i.e.*, about -0.35 and -0.8 mV higher in the case of protons and vanadium species, respectively, than the one predicted by Poisson's equation. This discrepancy could also be influenced by the fact that the charge-transfer reaction and dissociation reaction were allowed to occur in the interfacial region. It is necessary to validate if the Donnan approximation matches the results from Poisson's equation under zero current conditions as well as without chemical or electrochemical reactions, which is considered as part of the future work. At the beginning of charge or discharge, the jump in ionic potential across the interfacial region varied strongly with respect to SOC until it levelled off to a virtually constant value. Recently, VRFB models have used a Donnan-Nernst-Planck (DNP) model by means of a Donnan approximation at the electrode/membrane interface and the electro-neutrality condition across the electrode and membrane to estimate the crossover transport of ionic species. Considering the results presented here, the crossover flux estimation by means of a DNP model may produce inaccurate results, under or overestimating the capacity loss of the cell. Therefore, assessing
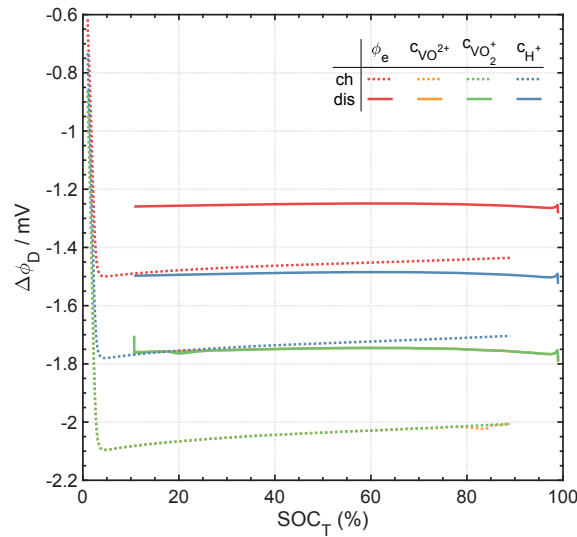
Figure 6.15: Ionic potential difference ($\Delta\phi_D$) and ionic potential difference calculated from concentration profiles at the interfacial region ($\Delta\phi_D^{c_k}$) in dependence on the SOC in the electrolyte tank at galvanostatic charge and discharge at an applied current density of $500\ \mathrm{A\,m^{-2}}$

its deviation with respect to the results of a PNP model could be of interest to correctly describe the cell degradation related to capacity loss due to the crossover of ionic species through the membrane.

6.5   Ionic transport across the cation-exchange-membrane

Figure 6.16 presents the crossover flux of vanadium and sulphuric acid species as a function of the applied current density for galvanostatic discharge at a SOC of 25% and 75% in the electrolyte tank. These crossover fluxes were evaluated at the membrane / catalyst layer interface ($x = l_{ca} + l_m$). The y-axis values have been multiplied by the Faraday's constant and the crossover fluxes are given in units of current density ($\mathrm{A\,m^{-2}}$). Positive fluxes are in the direction of the catalyst layer, while negative fluxes are in the direction of the cathodic flow channel. The main charge carriers in the membrane were protons, and therefore, the crossover flux of protons practically matched the applied current densities for both SOCs (Figure 6.16b). During discharge, protons are produced at the catalyst layer, displaying negative fluxes that increased in magnitude with the applied current density. The increase in the concentration of protons at the catalyst layer due to the anodic charge-transfer reaction produced a decrease in the concentration of SO_4^{2-} and an increase in the concentration of HSO_4^-, as the dissociation of HSO_4^- took place. This was confirmed by the negative and positive flux of HSO_4^- and SO_4^{2-} at the catalyst layer, respectively. During charge similar trends were observed, where the flux of protons practically matched the applied current density (positive values), and a positive and negative flux of HSO_4^- and SO_4^{2-} were observed, respectively. The vanadium species, namely VO^{2+} and VO_2^+, pre-

sented positive fluxes at the catalyst layer independently of the sign of the applied current density. Figure 6.16a shows that at high SOC and low applied current density during discharge the flux of VO_2^+ was positive, and as this reactant was depleted, either by increasing the applied current density or by reducing the SOC in the electrolyte tank (Figure 6.11b), the flux of VO_2^+ was reduced significantly. The flux of VO^{2+} at the catalyst layer was also positive and increased slightly with the applied current density. At a low SOC, a higher concentration of VO^{2+} is expected (Figure 6.10b) and higher crossover fluxes were observed. During charge, similar trends for the flux of vanadium species were observed, where the behaviour displayed by VO^{2+} and VO_2^+ was inverted.
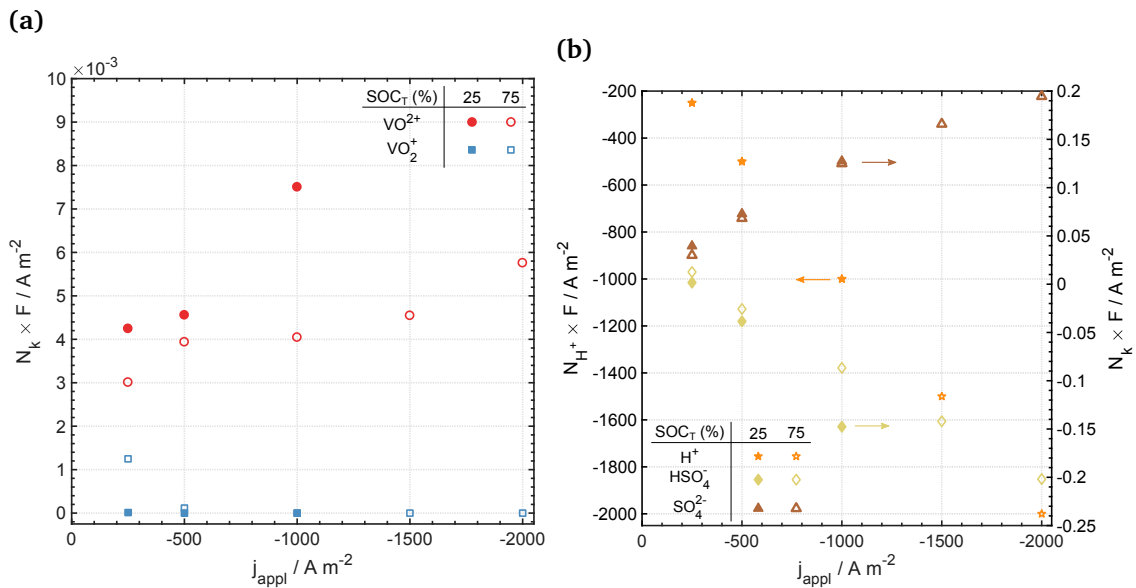
(a)

(b)

Figure 6.16: Crossover flux of ionic species in dependence on the applied current density for galvanostatic discharge at a SOC of 25% adn 75% in the electrolyte tank: (a) VO^{2+} and VO_2^+; and (b) H^+, HSO_4^- and SO_4^{2-}.

Figures 6.17 and 6.18 compare the crossover fluxes of VO^{2+} and H^+ due to the transport mechanisms at the galvanostatic charge and discharge for an applied current density of 500 $A\,m^{-2}$ and two SOCs in the electrolyte tank, respectively. In these figures, the fluxes have been multiplied by the Faraday's constant. Independently of the mode of operation, the convective flux was positive, *i.e.*, towards the catalyst layer. This is imposed by the negative pressure drop ($\Delta p = p_{CL} - p_{ch}$) considered across the modelling domain, which produced positive velocities (Figure 6.19). This velocity was constant across the modelling domain to fulfil Equation 6.5. A negative pressure drop was selected since the electrolyte was circulated at the cathode, while H_2 was passed through the cell, and the anodic gas outlet was opened in the current laboratory test cells. For the pressure drop used in the series of simulations a value of 1 atm was selected, producing convective fluxes significantly lower than the diffusion and migration fluxes, as well as virtually constant convective fluxes of species across the membrane during charge and discharge operation. At the first position in the membrane ($x_m^{(1)} = l_{ca} + 10\mu m$), the diffusive and migration

fluxes for VO^{2+} and H^+ displayed a positive and negative direction, respectively, and independently of the current direction. This behaviour correlated with the dissociation of HSO_4^-, which occurred mainly at the first section of the membrane in the presence of an increased concentration of H^+ and reduced concentration of HSO_4^- due to the membrane selectivity (Figures 6.12 and 6.13). Such an effect was also reflected in the concentration profile of other ionic species (Figures 6.10 and 6.11) and the ionic potential profile (Figure 6.8), producing negative migration fluxes of positively charged ions and positive migration fluxes of negatively charged ions.

Away from the initial section of the membrane, the diffusive and migration fluxes of VO^{2+} balanced each other to contribute slightly to the total flux of VO^{2+}, counteracting the convective flux during charge while promoting it during discharge.

The positive total flux observed for VO^{2+} and VO_2^+ at the catalyst layer in Figure 6.16a corresponded mainly to the convective positive flux of species. It was observed that during charge and at the higher SOC of 75% displayed in Figure 6.17a, the convective, diffusive and migration fluxes of VO^{2+} were reduced significantly in response to the low available concentration of VO^{2+} in the domains as the time passed or the SOC increased. For both modes of operation, it was seen that the total flux of protons across the membrane followed the expected current direction, *i.e.*, positive during charge and negative during discharge, virtually matching the applied current density as it was observed in Figure 6.16b. Away from the initial section of the membrane, the diffusive and migration flux of protons are both positive and negative for charge and discharge, respectively. This agreed with the production and consumption of protons at the membrane/catalyst layer interface during charge and discharge, respectively.

The simulated evolution of the concentration of VO^{2+} and electrolyte volume in the electrolyte tank during galvanostatic charge and discharge are presented in Figure 6.20. The electrolyte volume in the tank decreased slowly over time, independently of the sign of the current density, due to the positive velocities across the cathode and membrane (Figure 6.19a). The concentration of VO^{2+} in the electrolyte tank decreased virtually linearly with respect to time at the different values of applied current density. During charge, starting from an initial SOC in the electrolyte tank of 1.0%, the total conversion of VO^{2+} to VO_2^+ decreased with increasing the applied current density, *i.e.*, a lower SOC was reached at the end of charge operation or when a high cut-off potential was reached. During discharge, starting from an initial SOC of 99% in the electrolyte tank, a higher SOC was reached considering a low cut-off potential. Similar time-dependent behaviour was observed for the other ionic species.
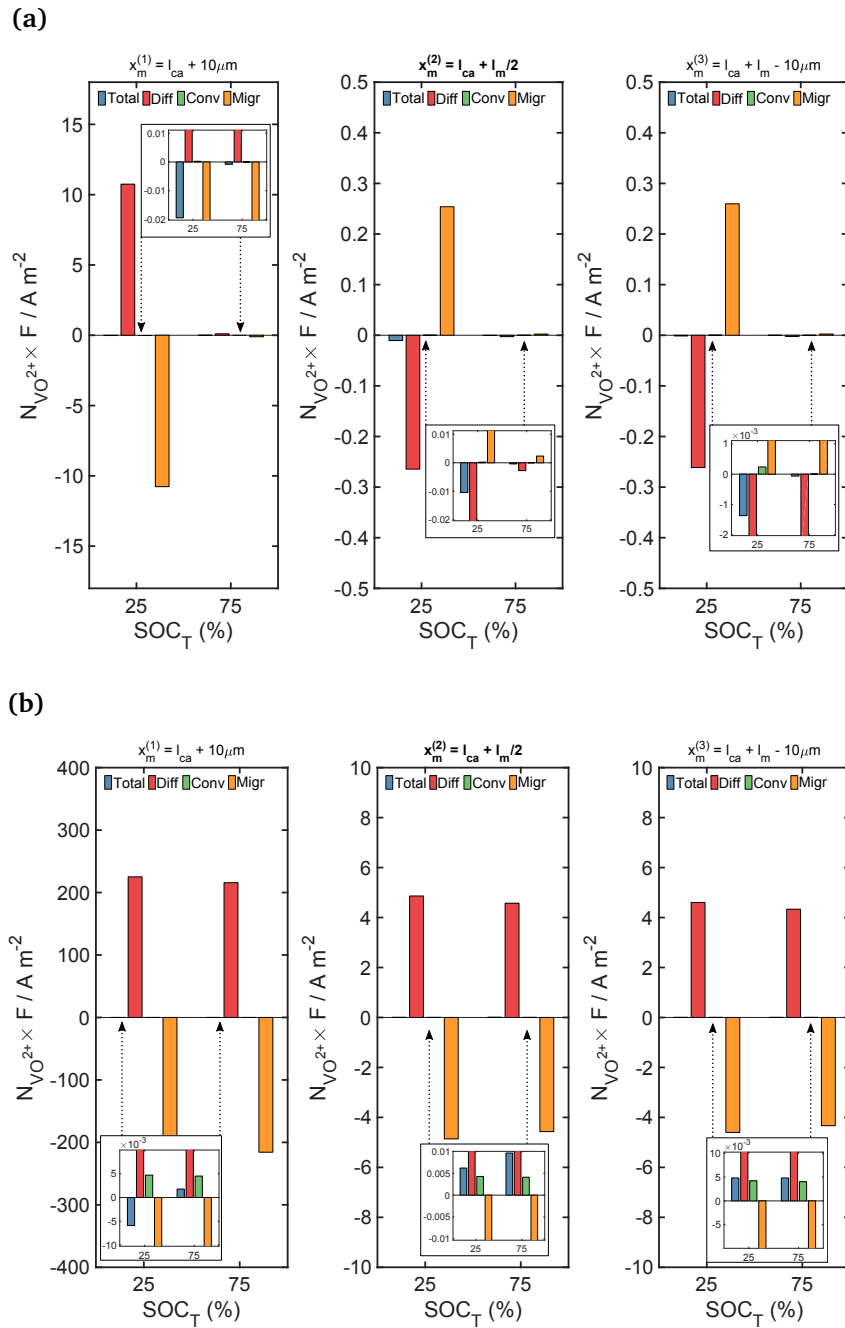
(a)

(b)

Figure 6.17: Comparison of crossover flux for VO^{2+} due to diffusion (Diff), convection (Conv) and migration (Migr) transport mechanisms at three points inside the membrane ($x_m^{(1)} = l_{ca} + 10\mu m$, $x_m^{(2)} = l_{ca} + l_m/2$, and $x_m^{(3)} = l_{ca} + l_m - 10\mu m$) during galvanostatic operation at an applied current density of $500\ A\,m^{-2}$ and a SOC in the electrolyte tank of 25% and 75%: (a) Charge; and (b) Discharge.

6.6 Conclusions

The work presented in this chapter is a preliminary study of crossover transport of species in an RHVFC and includes the implementation of a Poisson-Nernst-Planck model. A continuum mathematical description considering a one-dimensional PNP model was successfully implemented to simulate the transport of species across the cathode and membrane of the RHVFC. This model allowed for the description of the galvanostatic charge and dis-
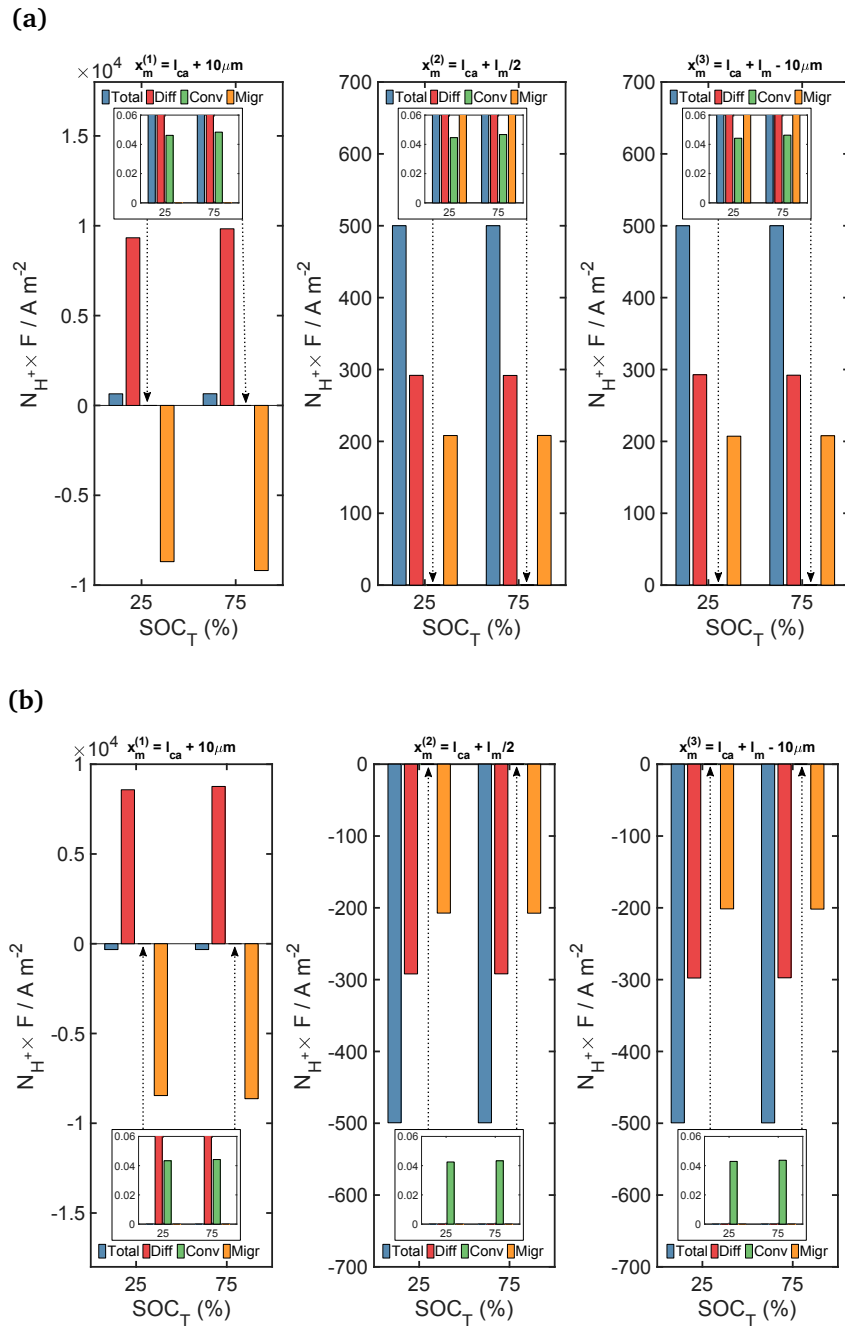
Figure 6.18: Comparison of crossover flux for H^+ due to diffusion (Diff), convection (Conv) and migration (Migr) transport mechanisms at three points inside the membrane ($x_m^{(1)} = l_{ca} + 10\mu m$, $x_m^{(2)} = l_{ca} + l_m/2$, and $x_m^{(3)} = l_{ca} + l_m - 10\mu m$) during galvanostatic operation at an applied current density of $500\,\mathrm{A\,m^{-2}}$ and a SOC in the electrolyte tank of 25% and 75%: (a) Charge; and (b) Discharge.

charge of the cell under pseudo-steady-state and time-dependent conditions, accounting for the charge-transfer reactions at the cathode and catalyst layer, and the dissociation of bi-sulphate ions across the modelling domain. The double-layer capacitance that appears when an ion-exchange membrane is in contact with an external solution was characterised, resulting in the continuous variation of ionic potential and concentration of species in a narrow electrode/membrane interfacial region due to the Donnan exclusion phenomenon. The ionic potential and concentration profiles across these regions were as
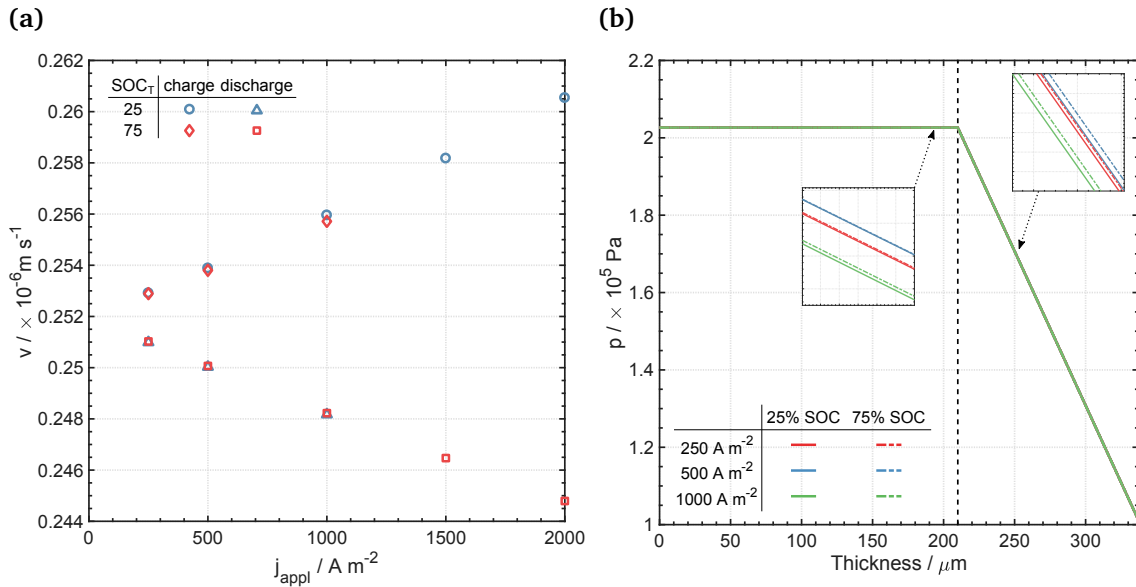
(a)

(b)

Figure 6.19: (a) Velocity across the modelling domain as a function of absolute current density; and (b) Distribution of pressure in the electrode and membrane for galvanostatic discharge at a current density of 250, 500 and 1000 $A\,m^{-2}$ and at a SOC of 25% and 75% in the electrolyte tank during.

(a)

(b)
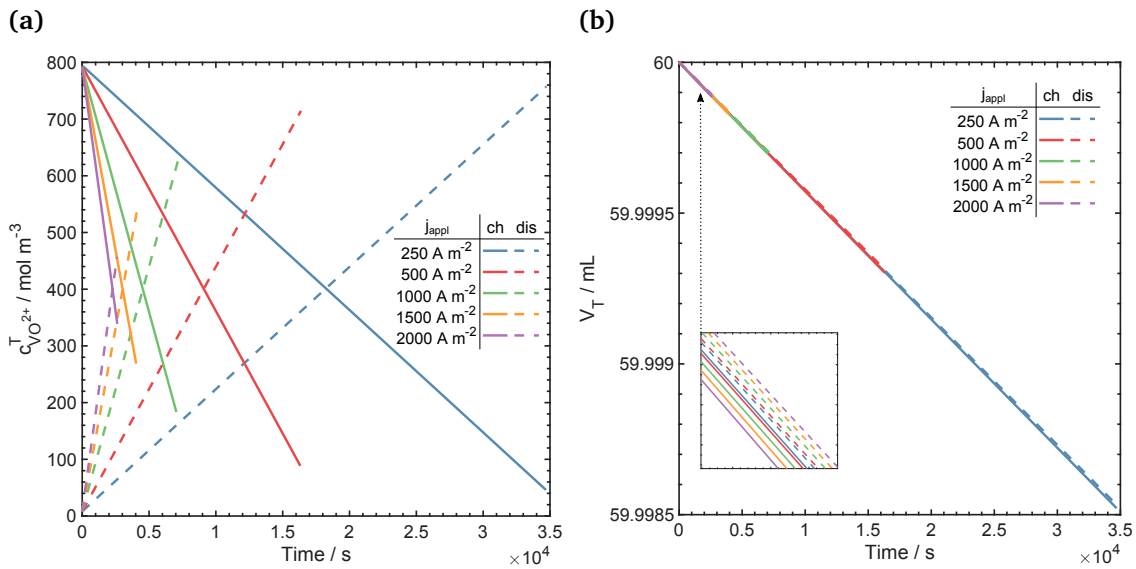
Figure 6.20: Catholyte tank during galvanostatic charge and discharge: (a) Concentration of VO^{2+}; and (b) Electrolyte volume.

expected for a cation-exchange membrane, which decreased the concentration of negatively charged ions like HSO_4^- from the external solution to the membrane, and increased the concentration of protons. The total ionic flux across the membrane was primarily given by the flux of protons, which were the main charge carriers matching the value of the applied current density. The flux of vanadium species at the membrane/catalyst layer interface was positive during charge and discharge operation. These vanadium crossover fluxes were dominated by the convective flux of species.

The simulated cell potential during galvanostatic charge and discharge displayed the

expected behaviour. At the beginning of charge and high applied current densities, a mass-transport limitation effect was observed which produced an initial increase in the cell overpotential. It was observed that the selected value for the diffusion coefficient of vanadium active species had an important effect on the presence of this initial behaviour and the cathodic overpotential. The distribution of electronic and ionic potential across the electrode varied to increase the cathodic overpotential during charge and decrease it during discharge. This agreed with the formulation of the kinetic equation by means of a conventional Butler-Volmer approach for the charge-transfer reaction at the cathode.

The Donnan approximation was used and its deviation was tested under galvanostatic discharge conditions. It was observed that the ionic potential difference calculated from the profile of the concentration of ionic species across the electrode/membrane interfacial region did not accurately predict the ionic potential difference obtained from Poisson's equation for the electrolyte composition used in this work. It is of interest to test a Donnan-Nernst-Planck (DNP) model to asses the deviation of the predicted crossover fluxes from the ones predicted by the PNP model. The DNP model does not require the explicit solution of ionic potential profile and concentration of species at the interfacial regions, instead, the continuity of the fluxes of ionic species across the electrode/membrane interface must be ensured. This model could lead to faster simulation times when studying continuous cycling performance of the cell.

Further work involves using the PNP model to predict the cell operation over cycling and to asses the capacity loss as a result of the simulated ionic crossover fluxes. The measurement of internal state variables inside an assembled cell is very challenging, and therefore, the total cell potential over cycling time is expected to be used as a global indicator of the accuracy of the model. Additionally, a Donnan-Nernst-Planck model is expected to be implemented to asses the discrepancies and test its agreement with the PNP model in order to use a simplified model when extending the RHVFC model to a two or three-dimensional approach. To test both crossover modelling approaches in order to predict the capacity loss of the RHVFC is considered as further work. Finally, it is important to quantify the impact of the dilute solution theory assumption, in order to incorporate possible corrections to the model if required.

Chapter references

Chen, C. L., Yeoh, H. K., and Chakrabarti, M. H. An enhancement to Vynnycky's model for the all-vanadium redox flow battery. *Electrochimica Acta*, 120:167–179, feb 2014.

Dickinson, E. J. F., Limon-Petersen, J. G., and Compton, R. G. The electroneutrality approximation in electrochemistry. *Journal of Solid State Electrochemistry*, 15(7-8):1335–

1345, 2011.

Gandomi, Y. A., Aaron, D. S., Zawodzinski, T. A., and Mench, M. M. In Situ Potential Distribution Measurement and Validated Model for All-Vanadium Redox Flow Battery. *Journal of The Electrochemical Society*, 163(1):A5188–A5201, 2016.

Hamann, C. H., Hamnett, A., and Vielstich, W. *Electrochemistry*. WILEY-VCH Verlag GmbH & Co. KGaA, Weinheim, second edition, 2007. ISBN 3-540-08986-1. doi: 10.1007/BFb0047025. URL http://www.springerlink.com/index/10.1007/BFb0047025.

Kee, R. J., Zhu, H., Hildenbrand, B. W., Vøllestad, E., Sanders, M. D., and O'Hayre, R. P. Modeling the Steady-State and Transient Response of Polarized and Non-Polarized Proton-Conducting Doped-Perovskite Membranes. *Journal of The Electrochemical Society*, 160(3):F290–F300, 2013.

Knehr, K. W., Agar, E., Dennison, C. R., Kalidindi, A. R., and Kumbur, E. C. A Transient Vanadium Flow Battery Model Incorporating Vanadium Crossover and Water Transport through the Membrane. *Journal of The Electrochemical Society*, 159(9):1446–1459, 2012a.

Knehr, K., Agar, E., Dennison, C. R., Kalidindi, A. R., and Kumbur, E. C. A Transient Vanadium Flow Battery Model Incorporating Vanadium Crossover and Water Transport through the Membrane. *Journal of the Electrochemical Society*, 159(9):A1446–A1459, aug 2012b.

Kodým, R., Fíla, V., Šnita, D., and Bouzek, K. PoissonNernstPlanck model of multiple ion transport across an ion-selective membrane under conditions close to chlor-alkali electrolysis. *Journal of Applied Electrochemistry*, 46(6):679–694, 2016.

Kontturi, K., Murtomäki, L., and Manzanares, J. A. *Ionic Transport Processes: In Electrochemistry and Membrane Science*. Oxford University Press Inc., New York, first edition, 2008. URL http://www.amazon.com/Ionic-Transport-Processes-Electrochemistry-Membrane/dp/0199553814.

Lei, Y., Zhang, B. W., Bai, B. F., and Zhao, T. S. A transient electrochemical model incorporating the Donnan effect for all-vanadium redox flow batteries. *Journal of Power Sources*, 299:202–211, dec 2015.

Ma, X., Zhang, H., and Xing, F. A three-dimensional model for negative half cell of the vanadium redox flow battery. *Electrochimica Acta*, 58:238–246, dec 2011.

Newman, J. S. and Thomas-Alyea, K. E. *Electrochemical Systems*. John Wiley & Sons, Inc., New York, 3rd edition, 2004. ISBN 0-471-47756-7.

Vøllestad, E., Zhu, H., and Kee, R. J. Interpretation of Defect and Gas-Phase Fluxes

through Mixed-Conducting Ceramics Using NernstPlanckPoisson and Integral Formulations. *Journal of The Electrochemical Society*, 161(1):F114–F124, 2013.

Yang, X.-G., Ye, Q., Cheng, P., and Zhao, T. S. Effects of the electric field on ion crossover in vanadium redox flow batteries. *Applied Energy*, 145:306–319, 2015.

You, D., Zhang, H., and Chen, J. A simple model for the vanadium redox battery. *Electrochimica Acta*, 54(27):6827–6836, nov 2009.

Zheng, Q., Zhang, H., Xing, F., Ma, X., Li, X., and Ning, G. A three-dimensional model for thermal analysis in a vanadium flow battery. *Applied Energy*, 113:1675–1685, jan 2014.

Chapter 7

Conclusions and further work

The overall aim of this project was to study the regenerative hydrogen vanadium fuel cell, by means of mathematical models that can represent the actual cell operation, as well as to study relevant transport phenomena involved in the electrodes and membrane. This document presented the development of a unit cell model, which was used along with experimental data to assess the performance of an RHVFC. Additionally, a study of the transport of ionic species across the membrane was developed by means of a Poisson-Nernst-Planck model following a one-dimensional approach.

The specific objectives considered in this work were the following:

1. To implement a unit cell model for VRFB that can simulate the potential dynamics and compared it to experimental data.

2. To propose a unit cell model for an RHVFC that can simulate the potential dynamics.

3. To validate the unit cell model for an RHVFC by comparing simulations with experimental results from different hydrogen-vanadium cells.

4. Based on the unit cell model results and the RHVFC experimental data to study the cell performance in term of the main figures of merit.

5. To propose a continuum model to simulate the species transport in the electrodes and the membrane.

6. To study and quantify the membrane crossover of ionic species in an RHVFC.

The fulfilment of each of these objectives was described separately in Chapters 3 (items 1), 4 (items 2 and 3), 5 (items 2, 3 and 4) and 6 (items 5 and 6). The key outcomes from each chapter are summarised below.

7.1 Conclusions

7.1.1 Chapter 3: A simplified base model for a redox flow battery: all-vanadium system

Unit cell or lumped models have represented reasonably well the all-vanadium cell potential behaviour and they have been consistently used for simulating performance. The main potential differences were observed at the end of charge and discharge when the simplified version of kinetic equations (*e.g.*, Butler-Volmer equation) is used. This equation did not reproduce well enough the observed mass-transport limitation effects. This equation neglects the effect of mass-transport limitations and the cathodic concentration of protons, while accounted only for the effect of vanadium species. Another source of discrepancies was found to be the incorrect representation of the equilibrium cell potential, where differences of $\sim 140\,\text{mV}$ have been observed between OCP experimental data and the simplified version of the Nernst equation. A complete Nernst equation which intends to include the effect of concentration of protons and Donnan potential at the electrode/membrane interfaces has been used to estimate the equilibrium potential. Even when an improvement in describing the equilibrium potential was observed, an additional potential correction was still found to be required. This correction may well be related to the assumption of unity activity coefficients and the use of dilute solution theory. Recently, a different expression for describing the equilibrium potential in a VRFB cell has been introduced. This new complete Nernst equation was derived from thermodynamics, however, it has not been adopted in the modelling community. When considering unit cell models to simulate, and hopefully to predict to a certain level of confidence, the performance of an electrochemical cell, it is critical to correctly estimate the equilibrium potential since the departure from such potential is what is simulated. Moreover, attention should be paid to capturing all-important effects on the kinetic behaviour that controls the departure from equilibrium. The analysis of the conventional VRFB and study of common modelling approaches used to set the guidelines for the development of an RHVFC model reported in this work.

7.1.2 Chapter 4: Development of a unit cell model for the regenerative hydrogen-vanadium fuel cell

Using a unit cell modelling approach a time-dependent model for an RHVFC was proposed. A complete Nernst equation was derived for the hydrogen-vanadium cell including the effect of concentration of protons and Donnan potential. Care must be taken when adding additional phenomena to conventional equations, like the Nernst equation since non-physical results can be obtained if this is not correctly done. It was seen that the proposed complete Nernst equation underestimated the open circuit potential data, and

these discrepancies were explained by the strong assumptions used in the model, such as the use of dilute solution theory and unity activity coefficients. The potential mismatch was taken into account when modelling the performance of the battery, by means of an empirical model of a correction factor, in order to ensure the correct estimation of cell overpotentials. On the other hand, the use of Butler-Volmer kinetics including the effect of the concentration of protons was proposed to describe the overpotential-current density relation in the cathode. This more general equation can account for the effect of acid concentration, as well as mass-transport limitations. An initial validation at moderated applied current densities showed that the model successfully simulated the cell potential in an intermediate SOC region, while discrepancies appeared at low and high SOC. Considering the simplifications and assumptions taken in the development of the unit cell model, the model discrepancies could be explained by several reasons, such as the spatial distribution of variables, the crossover of species across the membrane, and concentrated solution effects in the transport of species. However, the low-complexity modelling approach allowed for better understanding of the system performance by coupling physical and electrochemical processes occurring in the RHVFC, enabling identification of the key phenomena, highlighting areas requiring future in-depth study, and allowing for fast simulation of cell performance.

7.1.3 Chapter 5: Performance characterisation of the regenerative hydrogen-vanadium fuel cell

A $5\,\mathrm{cm}^2$ area RHVFC was characterised using extensive experimental measurements taken at different operating conditions. The polarisation performance of the cell had a maximum peak power density of $2840\,\mathrm{W\,m^{-2}}$ and a limiting current density over $4200\,\mathrm{A\,m^{-2}}$, while the cycling performance of the cell displayed a capacity loss of $5.6\,\mathrm{A\,s}$ per cycle. The cell performance degradation over continuous operation is expected to be produced to some degree by the crossover of ionic species in the cation-exchange membrane. In order to asses, this effect, a simplified crossover modelling approach used in VRFB models was implemented. A better agreement was found between model simulations and experimental data of single-cycle charge-discharge potential when the model considering crossover effects was used. Also, the model successfully predicted the polarisation response and power density of the cell. However, when cumulative effects over longer periods of operation were considered during cycling tests, the model showed higher discrepancies with respect to the potential data. This was attributed to more complex phenomena describing the capacity loss of the cell when different transport mechanisms are considered in the transport of species across the membrane. A sensitivity study of the model showed that the cell performance was more sensitive to the transfer coefficient of the cathodic reaction, the cathode porosity and the membrane thickness, which are directly related to the

cathodic overpotential from the Butler-Volmer equation, the cathodic ohmic overpotential, and the crossover effects, respectively. This highlighted the need for a kinetic study of the cathodic reaction at practical concentration levels of vanadium and sulphuric acid species, as well as careful estimation of microstructural parameters such as porosity and specific surface areas of electrodes. Additionally, the need for a more strict description of crossover transport across the cation-exchange membrane was recognised. This model could better describe the capacity loss of the cell under cycling, giving insight into any additional phenomena that impact this effect.

7.1.4 Chapter 6: Poisson-Nernst-Planck model of ionic crossover in the regenerative hydrogen-vanadium fuel cell

Using a continuum one-dimensional PNP model the transport of species across the cathode electrode and membrane of the RHVFC was simulated. The double-layer capacitance that appears when an ion-exchange membrane is in contact with an external solution was characterised, allowing for the jump in ionic potential and concentrations at the interface. At the electrode/membrane interface a Donnan approximation to describe the jump in the value of potential and ionic species was tested, showing an important discrepancy between the values assuming equilibrium and the results under galvanostatic operation. It is of interest to test this possible assumption in order to use simplified models to describe the interfacial behaviour, such a Donnan-Nernst-Planck (DNP) model.

The continuum model allowed the quantification of mass-transport limits effect at the beginning of charge operation, which was also observed in experimental measurements. It was recognised that the diffusion coefficient of vanadium species limited the performance of the cell. The dependence of the crossover fluxes of ionic species with respect to the applied current density was simulated, observing that at high currents the main charge carriers are protons.

7.2 Further work

1. To test the complete Nernst equation and complete Butler-Volmer equations in a unit cell model of a VRFB to assess their impact in the predicted cell performance.

2. To experimentally study the effect of the concentration levels of vanadium and sulphuric acid in the electrolytes on the kinetic behaviour of the cathodic reaction.

3. To consider other mechanisms of performance degradation such as side reactions that the vanadium species could undergo in the anodic catalyst layer in the unit cell model.

4. To use the time-dependent PNP model to predict the cell potential over cycling and to assess the capacity loss, considering an experimental validation. This could allow additional phenomena controlling cell degradation to be identified.

5. To implement a Donnan-Nernst-Planck model for the hybrid RFB and asses the discrepancies in estimating capacity loss with respect to the PNP model. The DNP model could then be used in a more complex cell model, considering correction of the discrepancies in estimating the crossover fluxes.

6. To extend the continuum model to a two- or three-dimensional representation in order to assess segregation effects in other coordinates as well as incorporating the effect of the flow-by configuration of the cell.

7. To assess the impact of the deviation from the dilute solution theory of the system, in order to include possible corrections to the model if required.

7.3 Dissemination

7.3.1 Papers

C. A. Pino-Muñoz, H. Hewa Dewage, V. Yufit and N. P. Brandon, "A unit cell model of a regenerative hydrogen-vanadium fuel cell", *Journal of The Electrochemical Society*, 164 (14) F1717-F1732 (2017). (Appendix C.1)

C. A. Pino-Muñoz, B. K. Chakrabarti, V. Yufit and N. P. Brandon,"Characterisation of a regenerative hydrogen-vanadium fuel cell using an experimentally validated unit cell model", *Journal of The Electrochemical Society*, 166 (15) A3511-A3524 (2019). (Appendix C.2)

C. A. Pino-Muñoz and N. P. Brandon,"Poisson-Nernst-Planck model of ionic transport across the cationic-exchange membrane of a regenerative hydrogen-vanadium fuel cell" (In preparation).

7.3.2 Oral presentations

C. A. Pino-Muñoz, H. Hewa Dewage, V. Yufit and N. P. Brandon, "*A unit cell model for the regenerative hydrogen-vanadium fuel cell (RHVFC)*", SCI Electrochemistry Postgraduate Conference 2017 (May, Southampton)

C. A. Pino-Muñoz, H. Hewa Dewage, V. Yufit and N. P. Brandon, "*A unit cell model for the Regenerative Hydrogen-Vanadium Fuel Cell*", ESE PhD Conference 2017 (July, London).

C. A. Pino-Muñoz, H. Hewa Dewage, V. Yufit and N. P. Brandon, "*A unit cell model of a Regenerative Hydrogen-Vanadium Fuel Cell*", 232nd ECS Meeting 2017 (October, National

Harbor MD).

C. A. Pino-Muñoz, V. Yufit and N. P. Brandon,*"Modelling of a Regenerative Hydrogen-Vanadium Fuel Cell"*, 1st New England-International Flow Battery Conference 2018 (June, Boston)

C. A. Pino-Muñoz, B. K. Chakrabarti, V. Yufit and N. P. Brandon, *"Characterisation of an RHVFC using an experimentally validated unit cell model"*, 16th Symposium on Modeling and Experimental Validation of Electrochemical Energy Technologies - Modval 2019 (March, Braunschweig).

C. A. Pino-Muñoz and N. P. Brandon, *"Modelling of membrane transport in a regenerative hydrogen-vanadium fuel cell"*, XII International Conference on Computational Heat, Mass and Momentum Transfer 2019 (September, Rome).

7.3.3 Poster presentations

C. A. Pino-Muñoz, V. Yufit, M. Lomberg, H. Hewa Dewage and N. P. Brandon, *"Unit cell model of a regenerative Hydrogen-Vanadium fuel cell"*, The International Flow Battery Forum 2016 (June, Karlsruhe)

C. A. Pino-Muñoz, V. Yufit and N. P. Brandon, *"Unit cell model of a Regenerative Hydrogen-Vanadium Fuel Fell"*, UK Energy Storage Conference 2016 (November, Birmingham)

C. A. Pino-Muñoz, H. Hewa Dewage, V. Yufit and N. P. Brandon, *"Unit cell model of a Regenerative Hydrogen-Vanadium Fuel Fell"*, UK Redox Flow Battery Network 2017 (June, Manchester).

C. A. Pino-Muñoz, H. Hewa Dewage, V. Yufit and N. P. Brandon, *"Unit cell model of a Regenerative Hydrogen-Vanadium Fuel Fell"*, Energy Storage for Low Carbon Grids and IMAGES Dissemination 2018 (January, London).

A complete set of references

Aaron, D. S., Liu, Q., Tang, Z., Grim, G. M., Papandrew, A. B., Turhan, A., Zawodzinski, T. A., and Mench, M. M. Dramatic performance gains in vanadium redox flow batteries through modified cell architecture. *Journal of Power Sources*, 206:450–453, 2012.

Agar, E., Knehr, K. W., Chen, D., Hickner, M. A., and Kumbur, E. C. Species transport mechanisms governing capacity loss in vanadium flow batteries: Comparing Nafion® and sulfonated Radel membranes. *Electrochimica Acta*, 98:66–74, may 2013.

Al-Fetlawi, H., Shah, A., and Walsh, F. Non-isothermal modelling of the all-vanadium redox flow battery. *Electrochimica Acta*, 55(1):78–89, dec 2009.

Al-Fetlawi, H., Shah, A., and Walsh, F. Modelling the effects of oxygen evolution in the all-vanadium redox flow battery. *Electrochimica Acta*, 55(9):3192–3205, mar 2010.

Alotto, P., Guarnieri, M., and Moro, F. Redox flow batteries for the storage of renewable energy: A review. *Renewable and Sustainable Energy Reviews*, 29:325–335, 2014.

Amphlett, J., Mann, R., Peppley, B., Roberge, P., and Rodrigues, A. A model predicting transient responses of proton exchange membrane fuel cells. *Journal of Power Sources*, 61(1-2):183–188, jul 1996.

Araya, M. M., Arrieta, J. J., Pérez-Correa, J. R., Biegler, L. T., and Jorquera, H. Fast and reliable calibration of solid substrate fermentation kinetic models using advanced non-linear programming techniques. *Electronic Journal of Biotechnology*, 10(1), 2007.

Arenas, L. F., León, C. P. D., and Walsh, F. C. Engineering aspects of the design , construction and performance of modular redox flow batteries for energy storage Electrochemical Engineering Laboratory , Energy Technology Research Group , Faculty of. *Journal of Energy Storage*, 11:1–72, 2017.

Badrinarayanan, R., Zhao, J., Tseng, K. J., and Skyllas-Kazacos, M. Extended dynamic model for ion diffusion in all-vanadium redox flow battery including the effects of temperature and bulk electrolyte transfer. *Journal of Power Sources*, 270:576–586, dec 2014.

Bard, A. J. and Faulkner, L. R. *ELECTROCHEMICAL METHODS: Fundamentals and applications*. 2001. ISBN 0471043729. doi: 10.1146/annurev.matsci.30.1.117. URL `http://tocs.ulb.tu-darmstadt.de/95069577.pdf`.

Bavarian, M., Soroush, M., Kevrekidis, I. G., and Benziger, J. B. Mathematical Modeling, Steady-State and Dynamic Behavior, and Control of Fuel Cells: A Review. *Industrial & Engineering Chemistry Research*, 49(17):7922–7950, 2010.

Bayanov, I. M. and Vanhaelst, R. The numerical simulation of vanadium RedOx flow batteries. *Journal of Mathematical Chemistry*, 49(9):2013–2031, 2011.

Bazant, M. Z. Phase-Field Theory of Ion Intercalation Kinetics. *Condensed Matter*, 4, 2012.

Bazant, M. Z. Theory of chemical kinetics and charge transfer based on nonequilibrium thermodynamics. *Accounts of Chemical Research*, 46(5):1144–1160, 2013.

Bazant, M. Z., Kilic, M. S., Storey, B. D., and Ajdari, A. Towards an understanding of induced-charge electrokinetics at large applied voltages in concentrated solutions. *Advances in Colloid and Interface Science*, 152(1-2):48–88, 2009.

Benziger, J., Chia, E., Karnas, E., Moxley, J., Teuscher, C., and Kevrekidis, I. G. The stirred tank reactor polymer electrolyte membrane fuel cell. *AIChE Journal*, 50(8):1889–1900, 2004.

Bernardi, D. M. and Verbrugge, M. W. Mathematical model of a gas diffusion electrode bonded to a polymer electrolyte. *AIChE Journal*, 37(8):1151–1163, 1991.

Bernardi, D. M. and Verbrugge, M. W. A Mathematical Model of the Solid-Polymer-Electrolyte Fuel Cell. *Journal of The Electrochemical Society*, 139(9):2477, 1992.

Bertei, A. and Nicolella, C. Common inconsistencies in modeling gas transport in porous electrodes: The dusty-gas model and the Fick law. *Journal of Power Sources*, 279:133–137, 2015.

Bertei, A., Mertens, J., and Nicolella, C. Electrochemical simulation of planar solid oxide fuel cells with detailed microstructural modeling. *Electrochimica Acta*, 146:151–163, 2014.

Bessler, W. G. A new computational approach for SOFC impedance from detailed electrochemical reaction-diffusion models. *Solid State Ionics*, 176(11-12):997–1011, 2005.

Bird, R. B., Stewart, W. E., and Lightfoot, E. N. *Fenómenos de transporte*. Reverté, Barcelona, 1st edition, 1964.

Blanc, C. and Rufer, A. Multiphysics and energetic modeling of a vanadium redox flow battery. *2008 IEEE International Conference on Sustainable Energy Technologies, ICSET 2008*, pages 696–701, 2008.

Bourke, A., Miller, M. A., Lynch, R. P., Gao, X., Landon, J., Wainright, J. S., Savinell, R. F., and Buckley, D. N. Electrode Kinetics of Vanadium Flow Batteries: Contrasting Responses of V ^{II} -V ^{III} and V ^{IV} -V ^{V} to Electrochemical Pretreatment of Carbon. *Journal of The Electrochemical Society*, 163(1):A5097–A5105, 2016.

Bromberger, K., Kaunert, J., and Smolinka, T. A Model for All-Vanadium Redox Flow Batteries: Introducing Electrode-Compression Effects on Voltage Losses and Hydraulics. *Energy Technology*, 2(1):64–76, jan 2014.

Carta, R., Palmas, S., Polcaro, A. M., and Tola, G. Behaviour of a carbon felt flow by electrodes Part I: Mass transfer characteristics. *Journal of Applied Electrochemistry*, 21 (9):793–798, 1991.

Chen, C. L., Yeoh, H. K., and Chakrabarti, M. H. An enhancement to Vynnycky's model for the all-vanadium redox flow battery. *Electrochimica Acta*, 120:167–179, feb 2014.

Chen, H., Cong, T. N., Yang, W., Tan, C., Li, Y., and Ding, Y. Progress in electrical energy storage system: A critical review. *Progress in Natural Science*, 19(3):291–312, 2009.

Chen, S. and Kucernak, A. Electrocatalysis under Conditions of High Mass Transport Rate: Investigation of hydrogen Oxidation on Single Submicron Pt Particles Supported on Carbon. *The Journal of Physical Chemistry B*, 108(10):3262–3276, 2004.

Cho, J., Jeong, S., and Kim, Y. Commercial and research battery technologies for electrical energy storage applications. *Prog. Energy Combust. Sci.*, 48(0):84, 2015.

Cho, K. T., Tucker, M. C., and Weber, A. Z. A Review of Hydrogen/Halogen Flow Cells. *Energy Technology*, 4(6):655–678, 2016.

Colmenar-Santos, A., Reino-Rio, C., Borge-Diez, D., and Collado-Fernández, E. Distributed generation: A review of factors that can contribute most to achieve a scenario of DG units embedded in the new distribution networks. *Renewable and Sustainable Energy Reviews*, 59:1130–1148, 2016.

Cooper, S. J., Bertei, A., Shearing, P. R., Kilner, J. A., and Brandon, N. P. TauFactor: An open-source application for calculating tortuosity factors from tomographic data. *SoftwareX*, 5:203–210, 2016.

Darling, R. M., Weber, A. Z., Tucker, M. C., and Perry, M. L. The Influence of Electric Field on Crossover in Redox-Flow Batteries. *Journal of the Electrochemical Society*, 163(1): A5014–A5022, 2015.

Dewage, H. H., Yufit, V., and Brandon, N. P. Study of Loss Mechanisms Using Half-Cell Measurements in a Regenerative Hydrogen Vanadium Fuel Cell. *Journal of The Electrochemical Society*, 163(1):A5236–A5243, 2016.

Dickinson, E. J. F., Limon-Petersen, J. G., and Compton, R. G. The electroneutrality approximation in electrochemistry. *Journal of Solid State Electrochemistry*, 15(7-8):1335–1345, 2011.

Dowd, R. P., Lakhanpal, V. S., and Van Nguyen, T. Performance Evaluation of a Hydrogen-

Vanadium Reversible Fuel Cell. *Journal of The Electrochemical Society*, 164(6):F564–F567, 2017a.

Dowd, R. P., Verma, A., Li, Y., Powers, D., Wycisk, R., Pintauro, P. N., and Van Nguyen, T. A Hydrogen-Vanadium Reversible Fuel Cell Crossover Study. *Journal of The Electrochemical Society*, 164(14):F1608–F1614, 2017b.

Ferguson, T. R. and Bazant, M. Z. Nonequilibrium Thermodynamics of Porous Electrodes. *Journal of the Electrochemical Society*, 159(12):A1967–A1985, 2012.

Ferreira, H. L., Garde, R., Fulli, G., Kling, W., and Lopes, J. P. Characterisation of electrical energy storage technologies. *Energy*, 53:288–298, 2013.

Fuel Cell Store. 0.3 mg/cm2 40% Platinum on Vulcan Carbon Paper Electrode, a. URL `http://www.fuelcellstore.com/fuel-cell-components/gas-diffusion-electrode/platinum-electrodes/03-ptc-paper-electrode`.

Fuel Cell Store. FREUDENBERG Gas Diffusion Layers for PEMFC and DMFC, b. URL `http://www.fuelcellstore.com/freudenberg-h2315`.

Fuel Cell Store. Properties of Nafion ® PFSA Membrane: 115, 117 and 1110, c. URL `http://www.fuelcellstore.com/nafion-117`.

Fuller, T. F. Water and Thermal Management in Solid-Polymer-Electrolyte Fuel Cells. *Journal of The Electrochemical Society*, 140(5):1218, 1993.

Gallo, A., Simões-Moreira, J., Costa, H., Santos, M., and Moutinho dos Santos, E. Energy storage in the energy transition context: A technology review. *Renewable and Sustainable Energy Reviews*, 65:800–822, 2016.

Gandomi, Y. A., Aaron, D. S., Houser, J. R., Daugherty, M. C., Clement, J. T., Pezeshki, A. M., Ertugrul, T. Y., Moseley, D. P., and Mench, M. M. Critical ReviewExperimental Diagnostics and Material Characterization Techniques Used on Redox Flow Batteries. *Journal of The Electrochemical Society*, 165(5):A970–A1010, 2018.

Gandomi, Y. A., Aaron, D. S., Zawodzinski, T. A., and Mench, M. M. In Situ Potential Distribution Measurement and Validated Model for All-Vanadium Redox Flow Battery. *Journal of The Electrochemical Society*, 163(1):A5188–A5201, 2016.

Gasteiger, H. A., Panels, J. E., and Yan, S. G. Dependence of PEM fuel cell performance on catalyst loading. *Journal of Power Sources*, 127(1-2):162–171, 2004.

Ge, S., Li, X., Yi, B., and Hsing, I.-M. Absorption, Desorption, and Transport of Water in Polymer Electrolyte Membranes for Fuel Cells. *Journal of The Electrochemical Society*, 152(6):A1149, 2005.

Gileadi, E. *Electrode Kinetics for Chemists, Chemical Engineers and Materials Scientists*. John Wiley & Sons, Inc, New York, 1993. ISBN 978-0-471-18858-2. URL `http://www.wiley.com/WileyCDA/WileyTitle/productCd-0471188581.html`.

Golbert, J. and Lewin, D. R. Model-based control of fuel cells: (1) Regulatory control. *Journal of Power Sources*, 135(1-2):135–151, 2004.

Gür, T. M. Review of electrical energy storage technologies, materials and systems: Challenges and prospects for large-scale grid storage. *Energy and Environmental Science*, 11 (10):2696–2767, 2018.

Hamann, C. H., Hamnett, A., and Vielstich, W. *Electrochemistry*. WILEY-VCH Verlag GmbH & Co. KGaA, Weinheim, second edition, 2007. ISBN 3-540-08986-1. doi: 10.1007/ BFb0047025. URL `http://www.springerlink.com/index/10.1007/BFb0047025`.

He, W., Yi, J. S., and Nguyen, T. V. Two-phase flow model of the cathode of PEM fuel cells using interdigitated flow fields. *AIChE Journal*, 46(10):2053, 2000.

Hewa Dewage, H. *Investigation of Hydrogen based Redox Flow Batteries*. PhD thesis, Imperial College London, 2016.

Hewa Dewage, H., Wu, B., Tsoi, A., Yufit, V., Offer, G., and Brandon, N. P. A novel regenerative hydrogen cerium fuel cell for energy storage applications. *J. Mater. Chem. A*, 3(18):9446–9450, 2015.

Huerta-Pérez, F. and Pérez-Correa, J. R. Optimizing ethanol recovery in a spinning cone column. *Journal of the Taiwan Institute of Chemical Engineers*, 83:1–9, 2018.

International Energy Agency. *Energy Technology Perspectives: Scenarios & Strategies To 2050*. 2010. ISBN 9789264085978. doi: 10.1049/et:20060114. URL `http://www.oecd-ilibrary.org.ezproxy.library.uq.edu.au/energy/energy-technology-perspectives-2010{_}energy{_}tech-2010-en`.

Jiao, K. and Li, X. Water transport in polymer electrolyte membrane fuel cells. *Progress in Energy and Combustion Science*, 37(3):221–291, 2011.

K, S. *Electrochemical Reaction Engineering K, Scott Academic Press Limited*. Academic Press Limited, 1991.

Kear, G., Shah, A., and Walsh, F. Development of the allvanadium redox flow battery for energy storage: a review of technological, financial and policy aspects. *International journal of energy research*, 36:1105–1120, 2012.

Kee, R. J., Zhu, H., Hildenbrand, B. W., Vøllestad, E., Sanders, M. D., and O'Hayre, R. P. Modeling the Steady-State and Transient Response of Polarized and Non-Polarized

Proton-Conducting Doped-Perovskite Membranes. *Journal of The Electrochemical Society*, 160(3):F290–F300, 2013.

Kim, K. J., Park, M. S., Kim, Y. J., Kim, J. H., Dou, S. X., and Skyllas-Kazacos, M. A technology review of electrodes and reaction mechanisms in vanadium redox flow batteries. *Journal of Materials Chemistry A*, 3(33):16913–16933, 2015.

Kim, S., Yan, J., Schwenzer, B., Zhang, J., Li, L., Liu, J., Yang, Z. G., and Hickner, M. A. Cycling performance and efficiency of sulfonated poly(sulfone) membranes in vanadium redox flow batteries. *Electrochemistry Communications*, 12(11):1650–1653, nov 2010.

Knehr, K. W., Agar, E., Dennison, C. R., Kalidindi, A. R., and Kumbur, E. C. A Transient Vanadium Flow Battery Model Incorporating Vanadium Crossover and Water Transport through the Membrane. *Journal of The Electrochemical Society*, 159(9):1446–1459, 2012a.

Knehr, K. and Kumbur, E. Open circuit voltage of vanadium redox flow batteries: Discrepancy between models and experiments. *Electrochemistry Communications*, 13(4): 342–345, apr 2011.

Knehr, K., Agar, E., Dennison, C. R., Kalidindi, A. R., and Kumbur, E. C. A Transient Vanadium Flow Battery Model Incorporating Vanadium Crossover and Water Transport through the Membrane. *Journal of the Electrochemical Society*, 159(9):A1446–A1459, aug 2012b.

Knopf, D. A., Luo, B. P., Krieger, U. K., and Koop, T. Thermodynamic dissociation constant of the bisulfate ion from Raman and ion interaction modeling studies of aqueous sulfuric acid at low temperatures. *Journal of Physical Chemistry A*, 107(21):4322–4332, 2003.

Kodým, R., Fíla, V., Šnita, D., and Bouzek, K. PoissonNernstPlanck model of multiple ion transport across an ion-selective membrane under conditions close to chlor-alkali electrolysis. *Journal of Applied Electrochemistry*, 46(6):679–694, 2016.

Kontturi, K., Murtomäki, L., and Manzanares, J. A. *Ionic Transport Processes: In Electrochemistry and Membrane Science*. Oxford University Press Inc., New York, first edition, 2008. URL `http://www.amazon.com/Ionic-Transport-Processes-Electrochemistry-Membrane/dp/0199533814`.

Kucernak, A. R. and Zalitis, C. General Models for the Electrochemical Hydrogen Oxidation and Hydrogen Evolution Reactions: Theoretical Derivation and Experimental Results under Near Mass-Transport Free Conditions. *Journal of Physical Chemistry C*, 120(20):10721–10745, 2016a.

Kucernak, A. R. J. and Zalitis, C. M. General Models for the Electrochemical Hydrogen Oxidation and Hydrogen Evolution Reactions Theoretical Derivation and Experimental

Results Under Near Mass-Transport Free Conditions. *The Journal of Physical Chemistry C*, page acs.jpcc.6b00011, 2016b.

Lei, Y., Zhang, B. W., Bai, B. F., and Zhao, T. S. A transient electrochemical model incorporating the Donnan effect for all-vanadium redox flow batteries. *Journal of Power Sources*, 299:202–211, dec 2015.

Leung, P., Li, X., Ponce de León, C., Berlouis, L., Low, C. T. J., and Walsh, F. C. Progress in redox flow batteries, remaining challenges and their applications in energy storage. *RSC Advances*, 2(27):10125, 2012.

Li, L., Kim, S., Wang, W., Vijayakumar, M., Nie, Z., Chen, B., Zhang, J., Xia, G., Hu, J., Graff, G., Liu, J., and Yang, Z. A stable vanadium redox-flow battery with high energy density for large-scale energy storage. *Advanced Energy Materials*, 1(3):394–400, 2011a.

Li, M. and Hikihara, T. A Coupled Dynamical Model of Redox Flow Battery Based on Chemical Reaction, Fluid Flow and Electrical Circuit. *Institute of Electronics, Information an Communication Engineers*, E91(7):1741–1747, 2008.

Li, S. E., Wang, B., Peng, H., and Hu, X. An electrochemistry-based impedance model for lithium-ion batteries. *Journal of Power Sources*, 258:9–18, 2014.

Li, X., Zhang, H., Mai, Z., Zhang, H., and Vankelecom, I. Ion exchange membranes for vanadium redox flow battery (VRB) applications. *Energy & Environmental Science*, 4(4): 1147, 2011b.

Ma, X., Zhang, H., and Xing, F. A three-dimensional model for negative half cell of the vanadium redox flow battery. *Electrochimica Acta*, 58:238–246, dec 2011.

Maa, X., Zhangb, H., Xua, X., Jianga, S., Wua, J., Chigana, T., Wang, H., Zhaoa, H., and Chena, N. RKP Vanadium Flow Battery and its Application. *235th ECS Meeting*, (MA2019-01):Abstract 444, 2019.

Manditereza, P. T. and Bansal, R. Renewable distributed generation: The hidden challenges A review from the protection perspective. *Renewable and Sustainable Energy Reviews*, 58:1457–1465, 2016.

Mason, E. and Malinauskas, A. *Gas transport in porous media: The Dusty-Gas Model*. Elsevier, Amsterdam - Oxford - New York, 1983.

McKay, D. a., Ott, W. T., and Stefanopoulou, a. G. Modeling, Parameter Identification, and Validation of Reactant and Water Dynamics for a Fuel Cell Stack. *International Mechanical Engineering Congress & Exposition*, 2005(April):1177–1186, 2005.

McKay, D. A., Siegel, J. B., Ott, W., and Stefanopoulou, A. G. Parameterization and pre-

diction of temporal fuel cell voltage behavior during flooding and drying conditions. *Journal of Power Sources*, 178(1):207–222, 2008.

Merei, G., Adler, S., Magnor, D., and Sauer, D. U. Multi-physics Model for the Aging Prediction of a Vanadium Redox Flow Battery System. *Electrochimica Acta*, 174:945–954, aug 2015.

Nam, J. H. and Kaviany, M. Effective diffusivity and water-saturation distribution in single- and two-layer PEMFC diffusion medium. *International Journal of Heat and Mass Transfer*, 46(24):4595–4611, nov 2003.

Newman, J. Thermoelectric Effects in Electrochemical Systems. *Industrial & Engineering Chemistry Research*, 34:3208–3216, 1995.

Newman, J. S. and Thomas-Alyea, K. E. *Electrochemical Systems*. John Wiley & Sons, Inc., New York, 3rd edition, 2004. ISBN 0-471-47756-7.

Ontiveros, L. J. and Mercado, P. E. Modeling of a Vanadium Redox Flow Battery for power system dynamic studies. *International Journal of Hydrogen Energy*, 39(16):8720–8727, 2014.

Pavelka, M., Wandschneider, F., and Mazur, P. Thermodynamic derivation of open circuit voltage in vanadium redox flow batteries. *Journal of Power Sources*, 293:400–408, 2015.

Perry, M. L. and Weber, A. Z. Advanced Redox-Flow Batteries: A Perspective. *Journal of The Electrochemical Society*, 163(1):A5064–A5067, 2015.

Pino-Muñoz, C. A., Hewa Dewage, H., Yufit, V., and Brandon, N. P. A Unit Cell Model of a Regenerative Hydrogen-Vanadium Fuel Cell. *Journal of The Electrochemical Society*, 164 (14):F1717–F1732, 2017.

Pino-Muñoz, C. A., Chakrabarti, B. K., Yufit, V., and Brandon, N. P. Characterisation of a Regenerative Hydrogen-Vanadium Fuel Cell Using an Experimentally Validated Unit Cell Model. *Journal of the Electrochemical Society*, 166(14):A1–A14, 2019.

Pletcher, D. *A first course in Electrode Processes*. The Royal Society of Chemistry, second edi edition, 2009.

Ponce de León, C., Frías-Ferrer, A., González-García, J., Szánto, D., and Walsh, F. Redox flow cells for energy conversion. *Journal of Power Sources*, 160(1):716–732, 2006.

Pugach, M., Kondratenko, M., Briola, S., and Bischi, A. Zero dimensional dynamic model of vanadium redox flow battery cell incorporating all modes of vanadium ions crossover. *Applied Energy*, 226(June):560–569, 2018.

Pukrushpan, J. T., Stefanopoulou, a. G., and Peng, H. P. H. Modeling and control for PEM

fuel cell stack system. *Proceedings of the 2002 American Control Conference IEEE Cat NoCH37301*, 4(12):3117–3122, 2002.

Qiu, G., Joshi, A. S., Dennison, C., Knehr, K., Kumbur, E., and Sun, Y. 3-D pore-scale resolved model for coupled species/charge/fluid transport in a vanadium redox flow battery. *Electrochimica Acta*, 64:46–64, mar 2012.

Reid, R. C., Prausnitz, J. M., and Sherwood, T. K. *The Properties of Gases and Liquids*. McGraw-Hill, New York, 1977.

Rubio-Garcia, J., Kucernak, A., Zhao, D., Li, D. I., Fahy, K. F., Yufit, V., Brandon, N. P., and Gomez-Gonzalez, M. Hydrogen / manganese hybrid redox flow battery (in press). *J. Phys. Energy*, 2018.

Sacher, J., Saa, P., Cárcamo, M., López, J., Gelmi, C. A., and Pérez-Correa, R. Improved calibration of a solid substrate fermentation model. *Electronic Journal of Biotechnology*, 14(5), 2011.

Sandia National Laboratories. United States Department of Energy's Global Energy Storage Database (GESDB), 2016. URL `http://www.energystorageexchange.org/projects`.

Scribner Associates. 5 cm 2 Graphite Flow Field with REF Channel.

Seborg, D. E., Edgar, T. F., Mellichamp, D. A., and Doyle, F. J. *Process Dynamics and Control*. John Wiley & Sons, Inc., third edition, 2011. ISBN 2013436106. doi: 10. 1360/zd-2013-43-6-1064.

Shah, A. A., Luo, K. H., Ralph, T. R., and Walsh, F. C. Recent trends and developments in polymer electrolyte membrane fuel cell modelling. *Electrochimica Acta*, 56(11):3731–3757, 2011a.

Shah, A., Watt-Smith, M., and Walsh, F. A dynamic performance model for redox-flow batteries involving soluble species. *Electrochimica Acta*, 53(27):8087–8100, nov 2008.

Shah, A., Al-Fetlawi, H., and Walsh, F. Dynamic modelling of hydrogen evolution effects in the all-vanadium redox flow battery. *Electrochimica Acta*, 55(3):1125–1139, jan 2010a.

Shah, A., Al-Fetlawi, H., and Walsh, F. Dynamic modelling of hydrogen evolution effects in the all-vanadium redox flow battery. *Electrochimica Acta*, 55(3):1125–1139, 2010b.

Shah, A., Li, X., Wills, R. G. A., and Walsh, F. C. A Mathematical Model for the Soluble Lead-Acid Flow Battery. *Journal of The Electrochemical Society*, 157(5):A589, 2010c.

Shah, A., Tangirala, R., Singh, R., Wills, R., and Walsh, F. A Dynamic Unit Cell Model for the All-Vanadium Flow Battery. *Journal of The Electrochemical Society*, 158(6):A671, 2011b.

Shampine, L. and Reichelt, M. Ode_Suite. *Journal of Scientific Computing*, 18:1–22, 1997.

Sharma, A., Vynnycky, M., Ling, C., Birgersson, E., and Han, M. The quasi-steady state of all-vanadium redox flow batteries: A scale analysis. *Electrochimica Acta*, 147:657–662, nov 2014.

Sharma, A., Ling, C., Birgersson, E., Vynnycky, M., and Han, M. Verified reduction of dimensionality for an all-vanadium redox flow battery model. *Journal of Power Sources*, 279:345–350, apr 2015.

Siegel, C. Review of computational heat and mass transfer modeling in polymer-electrolyte-membrane (PEM) fuel cells. *Energy*, 33(9):1331–1352, sep 2008.

Skyllas-Kazacos, M., Chakrabarti, M. H., Hajimolana, S. A., Mjalli, F. S., and Saleem, M. Progress in Flow Battery Research and Development. *Journal of The Electrochemical Society*, 158(8):R55, 2011.

Skyllas-Kazacos, M. and Goh, L. Modeling of vanadium ion diffusion across the ion exchange membrane in the vanadium redox battery. *Journal of Membrane Science*, 399-400:43–48, may 2012.

Smith, R. B. and Bazant, M. Z. Multiphase Porous Electrode Theory. 164(11), 2017.

Soloveichik, G. L. Regenerative fuel cells for energy storage. *Proceedings of the IEEE*, 102 (6):964–975, 2014.

Sousa, R. and Gonzalez, E. R. Mathematical modeling of polymer electrolyte fuel cells. *Journal of Power Sources*, 147:32–45, 2005.

Springer, T. E., Wilson, M. S., and Gottesfeld, S. Polymer Electrolyte Fuel Cells. 140(12), 1993.

Springer, T., Zawodzinski, T., and Gottesfeld, S. Polymer electrolyte fuel cell model. *Journal of the Electrochemical Society*, 138(8):2334–2342, 1991.

Staples, B. R. Activity and osmotic coefficients of aqueous sulfuric acid at 298.15 K. *Journal of Physical and Chemical Reference Data*, 10(3):779–798, 1981.

Sun, C.-N., More, K. L., Veith, G. M., and Zawodzinski, T. a. Composition Dependence of the Pore Structure and Water Transport of Composite Catalyst Layers for Polymer Electrolyte Fuel Cells. *Journal of the Electrochemical Society*, 160(9):F1000–F1005, 2013.

Sun, C., Chen, J., Zhang, H., Han, X., and Luo, Q. Investigations on transfer of water and vanadium ions across Nafion membrane in an operating vanadium redox flow battery. *Journal of Power Sources*, 195(3):890–897, feb 2010.

Tang, A., Bao, J., and Skyllas-Kazacos, M. Dynamic modelling of the effects of ion diffusion

and side reactions on the capacity loss for vanadium redox flow battery. *Journal of Power Sources*, 196(24):10737–10747, dec 2011.

Tang, A., Bao, J., and Skyllas-Kazacos, M. Thermal modelling of battery configuration and self-discharge reactions in vanadium redox flow battery. *Journal of Power Sources*, 216: 489–501, oct 2012a.

Tang, A., Ting, S., Bao, J., and Skyllas-Kazacos, M. Thermal modelling and simulation of the all-vanadium redox flow battery. *Journal of Power Sources*, 203:165–176, 2012b.

Tang, A., McCann, J., Bao, J., and Skyllas-Kazacos, M. Investigation of the effect of shunt current on battery efficiency and stack temperature in vanadium redox flow battery. *Journal of Power Sources*, 242:349–356, nov 2013a.

Tang, A., Bao, J., and Skyllas-Kazacos, M. Studies on pressure losses and flow rate optimization in vanadium redox flow battery. *Journal of Power Sources*, 248:154–162, feb 2014.

Tang, A., Bao, J., and Skyllas-Kazacos, M. Thermal modelling of battery configuration and self-discharge reactions in vanadium redox flow battery. *Journal of Power Sources*, 216: 489–501, 2012c.

Tang, Z., Svoboda, R., Lawton, J. S., Aaron, D. S., Papandrew, A. B., and Zawodzinski, T. A. Composition and Conductivity of Membranes Equilibrated with Solutions of Sulfuric Acid and Vanadyl Sulfate. *Journal of The Electrochemical Society*, 160(9):F1040–F1047, 2013b.

Tucker, M. C., Cho, K. T., Spingler, F. B., Weber, A. Z., and Lin, G. Impact of membrane characteristics on the performance and cycling of the Br2-H2 redox flow cell. *Journal of Power Sources*, 284:212–221, 2015.

Viswanathan, V., Crawford, A., Stephenson, D., Kim, S., Wang, W., Li, B., Coffey, G., Thomsen, E., Graff, G., Balducci, P., Kintner-Meyer, M., and Sprenkle, V. Cost and performance model for redox flow batteries. *Journal of Power Sources*, 247:1040–1051, feb 2014.

Vogler, M., Bieberle-hütter, A., Gauckler, L., Warnatz, J., and Bessler, W. G. Ni/YSZ Patterned Anode Modelling Study of Surface Reactions, Diffusion, and Spillover at a Modelling Study of Surface Reactions, Diffusion, and Spillover at a Ni/YSZ Patterned Anode. *J. Electrochem. Soc*, 156(5):663–672, 2009.

Vøllestad, E., Zhu, H., and Kee, R. J. Interpretation of Defect and Gas-Phase Fluxes through Mixed-Conducting Ceramics Using NernstPlanckPoisson and Integral Formulations. *Journal of The Electrochemical Society*, 161(1):F114–F124, 2013.

Vynnycky, M. Analysis of a model for the operation of a vanadium redox battery. *Energy*, 36(4):2242–2256, apr 2011.

Walsh, F. C. *A First Course in Electrochemical Engineering*. The Electrochemical Consultancy, 1993.

Wandschneider, F., Finke, D., Grosjean, S., Fischer, P., Pinkwart, K., Tübke, J., and Nirschl, H. Model of a vanadium redox flow battery with an anion exchange membrane and a Larminie-correction. *Journal of Power Sources*, 272:436–447, dec 2014.

Wang, J. X., Springer, T. E., and Adzic, R. R. Dual-Pathway Kinetic Equation for the Hydrogen Oxidation Reaction on Pt Electrodes. *Journal of The Electrochemical Society*, 153(9):A1732, 2006.

Wang, W., Luo, Q., Li, B., Wei, X., Li, L., and Yang, Z. Recent Progress in Redox Flow Battery Research and Development. *Advanced Functional Materials*, 23(8):970–986, 2013.

Weber, A. Z. and Newman, J. Modeling transport in polymer-electrolyte fuel cells. *Chemical Reviews*, 104(10):4679–4726, 2004.

Weber, A. Z., Mench, M. M., Meyers, J. P., Ross, P. N., Gostick, J., and Liu, Q. Redox flow batteries: a review. *Journal of Applied Electrochemistry*, 41(10):1137–1164, 2011.

Wei, Z., Zhao, J., Skyllas-Kazacos, M., and Xiong, B. Dynamic thermal-hydraulic modeling and stack flow pattern analysis for all-vanadium redox flow battery. *Journal of Power Sources*, 260:89–99, aug 2014.

White, F. *Fluid Mechanics*. McGraw-Hill, New York, 7th edition, 2011.

Wilkes, J. O. *Fluid mechanics for chemical engineers*. Prentice Hall PTR, 1st edition, 1999.

Won, S., Oh, K., and Ju, H. Numerical analysis of vanadium crossover effects in all-vanadium redox flow batteries. *Electrochimica Acta*, 177:310–320, sep 2015.

Wu, H., Li, X., and Berg, P. Numerical analysis of dynamic processes in fully humidified PEM fuel cells. *International Journal of Hydrogen Energy*, 32(12):2022–2031, aug 2007.

Wu, H., Li, X., and Berg, P. On the modeling of water transport in polymer electrolyte membrane fuel cells. *Electrochimica Acta*, 54(27):6913–6927, 2009.

Wu, H., Berg, P., and Li, X. Modeling of PEMFC Transients with Finite-Rate Phase-Transfer Processes. *Journal of The Electrochemical Society*, 157(1):B1, 2010.

Wu, H.-W. A review of recent development: Transport and performance modeling of PEM fuel cells. *Applied Energy*, 165:81–106, mar 2016.

Xing, F., Zhang, H., and Ma, X. Shunt current loss of the vanadium redox flow battery. *Journal of Power Sources*, 196(24):10753–10757, dec 2011.

Xiong, B., Zhao, J., Tseng, K., Skyllas-Kazacos, M., Lim, T. M., and Zhang, Y. Thermal hydraulic behavior and efficiency analysis of an all-vanadium redox flow battery. *Journal of Power Sources*, 242:314–324, nov 2013.

Xiong, B., Zhao, J., Wei, Z., and Skyllas-Kazacos, M. Extended Kalman filter method for state of charge estimation ofvanadium redox flow battery using thermal-dependent electrical model. *Journal of Power Sources*, 262:50–61, sep 2014.

Xu, Q. and Zhao, T. Fundamental models for flow batteries. *Progress in Energy and Combustion Science*, 49:40–58, 2015.

Xu, W., Zhang, H., Xing, F., Zhang, H., Li, Y., Cao, J., and Li, X. The numerical simulation of dynamic performance in the vanadium flow battery. *Electrochimica Acta*, 118:51–57, feb 2014.

Yang, W., He, Y., and Li, Y. Performance Modeling of a Vanadium Redox Flow Battery during Discharging. *Electrochimica Acta*, 155:279–287, feb 2015a.

Yang, X.-G., Ye, Q., Cheng, P., and Zhao, T. S. Effects of the electric field on ion crossover in vanadium redox flow batteries. *Applied Energy*, 145:306–319, 2015b.

Yang, Z., Zhang, J., Kintner-Meyer, M. C., Lu, X., Choi, D., Lemmon, J. P., and Liu, J. Electrochemical energy storage for green grid. *Chemical Reviews*, 111(5):3577–3613, 2011.

Ye, R., Henkensmeier, D., Yoon, S. J., Huang, Z., Kim, D. K., Chang, Z., Kim, S., and Chen, R. Redox Flow Batteries for Energy Storage: A Technology Review. *Journal of Electrochemical Energy Conversion and Storage*, 15(1):010801, 2017.

Yerramalla, S., Davari, A., Feliachi, A., and Biswas, T. Modeling and simulation of the dynamic behavior of a polymer electrolyte membrane fuel cell. *Journal of Power Sources*, 124(1):104–113, oct 2003.

Yi, J. S. and Nguyen, T. V. An Along-the-Channel Model for Proton Exchange Membrane Fuel Cells. *Journal of The Electrochemical Society*, 145(4):1149, 1998.

Yin, C., Gao, Y., Guo, S., and Tang, H. A coupled three dimensional model of vanadium redox flow battery for flow field designs. *Energy*, 74:886–895, 2014a.

Yin, C., Gao, Y., Guo, S., and Tang, H. A coupled three dimensional model of vanadium redox flow battery for flow field designs. *Energy*, 74:886–895, sep 2014b.

You, D., Zhang, H., and Chen, J. Theoretical analysis of the effects of operational and

designed parameters on the performance of a flow-through porous electrode. *Journal of Electroanalytical Chemistry*, 625(2):165–171, jan 2009a.

You, D., Zhang, H., and Chen, J. A simple model for the vanadium redox battery. *Electrochimica Acta*, 54(27):6827–6836, nov 2009b.

You, D., Zhang, H., Sun, C., and Ma, X. Simulation of the self-discharge process in vanadium redox flow battery. *Journal of Power Sources*, 196(3):1578–1585, feb 2011.

Yu, V. and Chen, D. Dynamic Model of a Vanadium Redox Flow Battery for System Performance Control. *Journal of Solar Energy Engineering*, 136(2):021005–1 – 0210057, 2014a.

Yu, V. and Chen, D. Peak power prediction of a vanadium redox flow battery. *Journal of Power Sources*, 268:261–268, dec 2014b.

Yufit, V., Hale, B., Matian, M., Mazur, P., and Brandon, N. P. Development of a Regenerative Hydrogen-Vanadium Fuel Cell for Energy Storage Applications. *Journal of The Electrochemical Society*, 160(6):A856–A861, 2013.

Zhao, P., Zhang, H., Zhou, H., Chen, J., Gao, S., and Yi, B. Characteristics and performance of 10kW class all-vanadium redox-flow battery stack. *Journal of Power Sources*, 162(2): 1416–1420, nov 2006.

Zheng, Q., Li, X., Cheng, Y., Ning, G., Xing, F., and Zhang, H. Development and perspective in vanadium flow battery modeling. *Applied Energy*, 132:254–266, nov 2014a.

Zheng, Q., Xing, F., Li, X., Liu, T., Lai, Q., Ning, G., and Zhang, H. Investigation on the performance evaluation method of flow batteries. *Journal of Power Sources*, 266: 145–149, 2014b.

Zheng, Q., Zhang, H., Xing, F., Ma, X., Li, X., and Ning, G. A three-dimensional model for thermal analysis in a vanadium flow battery. *Applied Energy*, 113:1675–1685, jan 2014c.

Zheng, Q., Xing, F., Li, X., Ning, G., and Zhang, H. Flow field design and optimization based on the mass transport polarization regulation in a flow-through type vanadium flow battery. *Journal of Power Sources*, 324:402–411, 2016.

Appendix A

Evolution of species concentration of V(II) and V(III) for experimental data and simulation reported by Shah et al. (2011b)

In Chapter 3 was explained that when the comparison with the experimental data and simulations results reported by Shah et al. (2011b) was developed using the applied current destiny reported of $1000\,\mathrm{A\,m^{-2}}$ a mismatch in the total time of charge or discharge was found. The time simulated by the unit cell model described in Chapter 3 was much higher when the same applied current density was used. In Chapter 3 is also explained that it was decided to run the simulation at an applied current density of $1250\,\mathrm{A\,m^{-2}}$ instead, allowing for a faster depletion or accumulation of species concentration. This decision was based on the comparison of the expected values of concentration reported by Shah et al. (2011b) and the calculated values of species concentration obtained by means of the analytical expressions also reported by Shah et al. (2011b). These analytical expressions are presented in Equations A.1 and A.2 for the electrolyte tanks and electrodes, respectively. These expressions were validated by re-deriving them from the ordinary differential equations of species concentration in the electrolyte tanks and electrodes. The value of parameters used to evaluate these expressions can be found in Chapter 3 and they correspond to the values reported by Shah et al. (2011b).

$$
\begin{aligned}
c_{\mathrm{i,T}} &= (\varepsilon\delta + 1)c_{\mathrm{i}}^{0} - \frac{\delta S}{F}j_{\mathrm{appl}}t - \varepsilon\delta c_{\mathrm{i}}, \quad \mathrm{i} = \mathrm{V(III)}, \mathrm{V(IV)} \\
c_{\mathrm{i,T}} &= (\varepsilon\delta + 1)c_{\mathrm{i}}^{0} + \frac{\delta S}{F}j_{\mathrm{appl}}t - \varepsilon\delta c_{\mathrm{i}}, \quad \mathrm{i} = \mathrm{V(II)}, \mathrm{V(V)}
\end{aligned}
\tag{A.1}
$$

$$c_i = c_i^0 + \frac{S j_{appl}}{\varepsilon \tilde{\varepsilon} F} \left(\frac{\varepsilon \delta + \exp(-\tilde{\varepsilon} t)}{1 + \varepsilon \delta} - 1 - \frac{\varepsilon \delta}{\tau} t \right), \quad i = \text{V(III)}, \text{V(IV)}$$

$$c_i = c_i^0 - \frac{S j_{appl}}{\varepsilon \tilde{\varepsilon} F} \left(\frac{\varepsilon \delta + \exp(-\tilde{\varepsilon} t)}{1 + \varepsilon \delta} - 1 - \frac{\varepsilon \delta}{\tau} t \right), \quad i = \text{V(II)}, \text{V(V)}$$

(A.2)

where,

$$\delta = \frac{V_e}{V_T}, \quad \tau = \frac{he}{u}, \quad \tilde{\varepsilon} = \frac{1}{\tau}(\varepsilon \delta + 1), \quad u = \frac{Q_V}{\varepsilon A_{in}}, \quad A_{in} = \frac{V_e}{h_e}$$

(A.3)

Table A.1 presents three current densities used to evaluate the analytical expressions of species concentrations, reporting the current density per cross-sectional area of the electrode and the calculated current density per area of pore walls. This last current density was calculated by considering the area, volume and specific surface area of the electrode reported by Shah et al. (2011b). Figure A.1 and A.2 shows the calculated concentration of V(III) and V(II) as a function of time for the anode and anolyte tank, respectively. Similar figures can be obtained for V(IV) and VO_2^+, which are not included here. It can be observed that when an applied current density (j_{appl}) of $1000 \, \text{A m}^{-2}$ is used along with initial concentrations of V(III) and V(II) of 1140 and $60 \, \text{mol m}^{-3}$, a time of over $40 \, \text{min}$ is required for almost fully depletion of V(III) or accumulation of V(II). However, Shah et al. (2011b) reported a time of about $32 \, \text{min}$ for the same operating conditions and using Equations A.1 and A.2. To obtain the same rate of depletion of V(III) as reported by Shah et al. (2011b), a higher current of $1250 \, \text{A m}^{-2}$ had to be used as presented in Figure A.1 and A.2. This higher current density represents a transfer current density, *i.e.* current per are of pore walls, of $700 \, \text{A m}^{-2}$ and allows to match the operating time for the evolution of species concentrations and cell potential. Therefore, this current density was used to test the unit cell model and the simulation results are presented in Chapter 3.

Table A.1: Tested current densities to estimate evolution of species concentration with analytical expressions reported by Shah et al. (2011b)

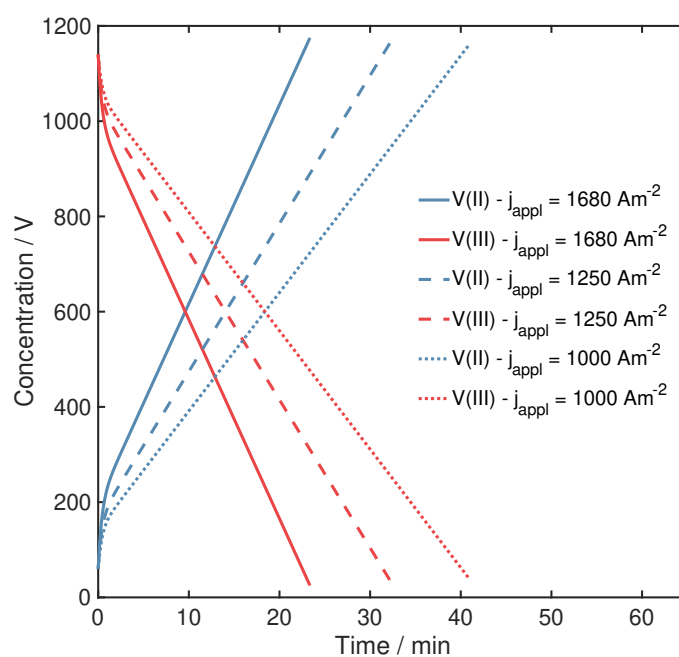| Current type	Unit	1	2	3
Current per cross-sectional area of electrode (j_{appl})	A m^{-2}	1860	1250	1000
Current per area of pore walls (or active area)	A m^{-2}	1000		

Figure A.1: Calculated concentration of V(III) and V(II) in the anode obtained by using the analytical expression reported by Shah et al. (2011b)
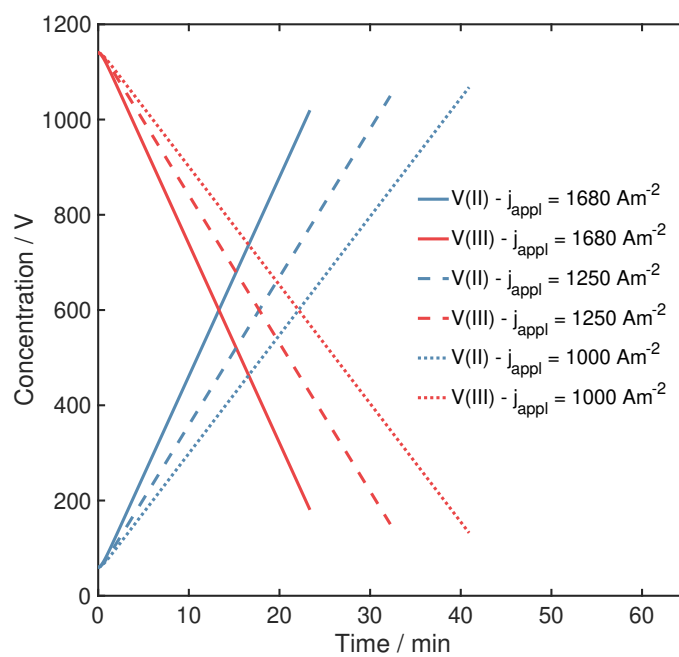

Figure A.2: Calculated concentration of V(III) and V(II) in the anolyte tank obtained by using the analytical expression reported by Shah et al. (2011b)

Appendix B

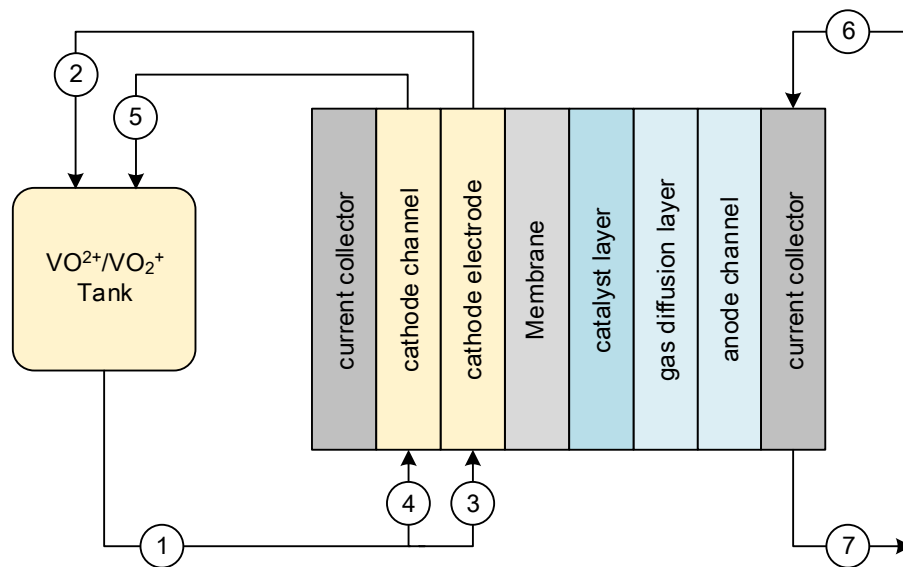# Degrees Of Freedom (DOF) analysis of the regenerative hydrogen-vanadium fuel cell

Figure B.1: Schematic of RHVFC domains for DOF analysis

Table B.1: Degree of freedom analysis based on Figure B.1

Item	Component	Variables/equations	#
Parameters	cell	V_T ρ_{el} μ_{el} T_{amb} α_a ε_{ca} t_{ca} h_{ca} w_{ca} K_{KC} h_{cc} w_{cc} K_f σ_{ca} ε_m V_w t_m β ε_{CL} k_{cond} k_{evap} ρ_m EW t_{an} ϵ_{H_2} ϵ_v σ_{H_2} σ_v ε_{GDL} t_{cc} R_C M_v M_{H_2} p_{atm} σ_{CL} σ_{GDL} σ_{cc} S_{ca} R_{an} d_p $k_{des}^{\varnothing}$ $D_{VO^{2+}}$ $D_{VO_2^+}$ D_{H^+} r_p d_f F c_f z_f E_a h_m w_m h_{an} w_{an}	54
Variables	cell	η_{ohm} E_{OCP} E_{cell} R_C η_{ohm}^C I_{appl}	6
	tank	$c_{VO^{2+},T}$ $c_{VO_2^+,T}$ $c_{H^+,T}$ $c_{HSO_4^-,T}$ $c_{SO_4^{2-},T}$ T_T ρ_T μ_T	8
	current collectors	η_{ohm}^{CC}	1
	ca. channel	Q_{ch} f_{ch}	2
	cathode	$c_{VO^{2+}}$ $c_{VO_2^+}$ c_{H^+} $c_{HSO_4^-}$ $c_{SO_4^{2-}}$ T_{ca} ρ_{ca} μ_{ca} S_d^{eq} j^{BV} κ Q_{ca} L_{ca} η_{ohm}^{ca} η_{ca} Q_M $c_{VO^{2+}}^s$ $c_{VO_2^+}^s$ $c_{H^+}^s$ σ_{ca}^{eff} σ_{ca-el}^{eff} $k_{ca,ref}$ δ_0	23
	membrane	T_m $\dot{n}_{H^+,m}$ $\dot{n}_{diff}$ $\dot{n}_{EO}$ $D_{dw,m}$ $c_{dw,c-m}$ η_{ohm}^m σ_m ξ_{drag}	9
	CL	T_{CL} ρ_{CL} μ_{CL} ε_m^{CL} γ_{des} R_w^{CL} $\dot{n}_{des}$ j^{TV} s_{CL} $c_{dw,CL}$ $c_{H^+,CL}$ $c_{H_2,CL}$ $c_{v,CL}$ λ_{CL} λ_{CL}^{eq} $a_{v,CL}$ p_{CL} η_{ohm}^{CL} η_{an} $\theta_{H_{ad}}^{TV}$ σ_{CL}^{eff} σ_{CL-m}^{eff}	22
	GDL	T_{GDL} $\dot{n}_{H_2,GDL}$ $\dot{n}_{v,GDL}$ $D_{H_2,v}^{eff}$ D_{Kn,H_2}^{eff} $D_{Kn,v}^{eff}$ K T^* Ω_D τ $\sigma_{H_2,v}$ $\epsilon_{H_2,v}$ η_{ohm}^{GDL}	13
	an. channel	T_{ch} ρ_{ch} μ_{ch} p_{ch} R_w^{ch} s_{ch} $c_{H_2,ch}$ $c_{v,ch}$	8
	flow 1	$c_{VO^{2+},1}$ $c_{VO_2^+,1}$ $c_{H^+,1}$ $c_{HSO_4^-,1}$ $c_{SO_4^{2-},1}$ T_1 ρ_1 μ_1 Q_V	9
	flow 2	$c_{VO^{2+},2}$ $c_{VO_2^+,2}$ $c_{H^+,2}$ $c_{HSO_4^-,2}$ $c_{SO_4^{2-},2}$ T_2 ρ_2 μ_2	8
	flow 3	$c_{VO^{2+},3}$ $c_{VO_2^+,3}$ $c_{H^+,3}$ $c_{HSO_4^-,3}$ $c_{SO_4^{2-},3}$ T_3 ρ_3 μ_3	8
	flow 4	$c_{VO^{2+},4}$ $c_{VO_2^+,4}$ $c_{H^+,4}$ $c_{HSO_4^-,4}$ $c_{SO_4^{2-},4}$ T_4 ρ_4 μ_4	8
	flow 5	$c_{VO^{2+},5}$ $c_{VO_2^+,5}$ $c_{H^+,5}$ $c_{HSO_4^-,5}$ $c_{SO_4^{2-},5}$ T_5 ρ_5 μ_5	8
	flow 6	T_{IN} ρ_{IN} p_{IN} $\dot{n}_{H_2,IN}$ Q_{H_2}	5
	flow 7	T_{OUT} ρ_{OUT} p_{OUT} G_{OUT} $\dot{n}_{H_2,OUT}$ $\dot{n}_{v,OUT}$	6
	Total		144
Constant relations		$T_T = T_1 = T_2 = T_3 = T_4 = T_5 = T_{ca} = T_m = T_{amb}$ $T_{CL} = T_{GDL} = T_{ch} = T_{IN} = T_{OUT} = T_{amb}$ $\rho_T = \rho_1 = \rho_2 = \rho_3 = \rho_4 = \rho_5 = \rho_{ca} = \rho_{el}$, $\quad \rho_{CL} = \rho_{ch} = \rho_w$ $\mu_T = \mu_1 = \mu_2 = \mu_3 = \mu_4 = \mu_5 = \mu_{ca} = \mu_{el}$, $\quad \mu_{CL} = \mu_{ch} = \mu_w$ $c_{i,1} = c_{i,T}$, $\quad c_{i,4} = c_{i,1}$, $\quad c_{i,3} = c_{i,1}$, $\quad c_{i,5} = c_{i,4}$, $\quad c_{i,2} = c_i$	56
Unknows			88

Table B.2: Continuation of Table B.1

Item	Component	Variables/equations	#
Equations	cell	Equations 4.43 and 4.53; $\eta_{\text{ohm}} = \sum \eta_{\text{ohm}}^{\text{k}} + \eta_{\text{ohm}}^{\text{C}}$; Equation 4.72	4
	tank	Equation 4.11	5
	current collectors	Equation 4.72	1
	ca. channel	Equation 4.17, 4.19 and 4.20	3
	cathode	Equations 4.6, 4.7, 4.8, 4.9 and 4.10; Equation 4.62; Equations 4.14 and 4.16; Equation 4.73; $I_{\text{appl}} = S_{\text{ca}} V_{\text{ca}} j^{\text{BV}}$; Equation 4.18; $L_{\text{ca}} = h_{\text{ca}}$; Equations 4.63, 4.64 and 4.65 Equations 4.76 (twice)	17
	membrane	$\dot{n}_{\text{H}^+,\text{m}} = A_{\text{m}} j / F$; $\dot{n}_{\text{diff}} = -A_{\text{m}} D_{\text{dw,m}}(c_{\text{dw,CL}} - c_{\text{dw,c-m}}) / l_{\text{m}}$; Equation 4.29; $c_{\text{dw,c-m}} = 22\rho_{\text{dm}}/EW$; Equation 4.72 and 4.74; Equations 4.76; $\xi_{\text{drag}} = 2.5\lambda/22$; $\dot{n}_{\text{EO}} = \xi_{\text{drag}} A_{\text{m}} j / F$	9
	CL	Equation 4.33 and 4.34; $\dot{n}_{\text{des}} = -V_{\text{CL}} \varepsilon_{\text{m}} \gamma_{\text{des}}(c_{\text{dw,CL}} - c_{\text{dw}}^{\text{eq}})$; $\varepsilon_{\text{m}}^{\text{CL}} = \varepsilon_{\text{m}}$; $I_{\text{appl}} = R_{\text{an}} A_{\text{CL}} j^{\text{TV}}$; Equations 4.24, 4.23, 4.21, 4.22 and 4.25; Equation 4.30, 4.31 and 4.32; $p_{\text{CL}} V_{\text{CL}}^{\text{g}} = n_{\text{g}} RT$; Equation 4.73; Equations 4.68 and 4.71; Equation 4.69; Equations 4.76	19
	GDL	$\dot{n}_{\text{H}_2,\text{GDL}}$ and $\dot{n}_{\text{v,GDL}}$ by Equation 4.35; Equation 4.36; $D_{\text{Kn,v}}^{\text{eff}}$ and $D_{\text{Kn,H}_2}^{\text{eff}}$ by Equation 4.37; Equations 4.38, 4.41, 4.40 and 4.42 (twice); $\tau = \varepsilon^{-1/2}$; Equation 4.73	12
	an. channel	Equation 4.34; Equations 4.27, 4.26 and 4.28	4
	flow 6	Equation 4.39; $\rho_{\text{IN}} = M_{\text{IN}} p_{\text{IN}}/(RT)$	2
	flow 7	$p_{\text{OUT}} = p_{\text{atm}}$; Equation 4.39; $\dot{n}_{\text{H}_2,\text{OUT}} = y_{\text{H}_2,\text{ch}} G_{\text{OUT}}$; $\dot{n}_{\text{v,OUT}} = y_{\text{v,ch}} G_{\text{OUT}}$; $\rho_{\text{OUT}} = M_{\text{OUT}} p_{\text{OUT}}/(RT)$	5
	Total		81
DOF			7
Manipulated variables		$I_{\text{appl}} \quad Q_{\text{V}} \quad Q_{\text{H}_2} \quad p_{\text{IN}}$	4
Fitted parameters		$R_{\text{C}} \quad k_{\text{ca,ref}} \quad \delta_0$	3

Appendix C

Publications

C.1 Publication 1

"A Unit Cell Model of a Regenerative Hydrogen-Vanadium Fuel Cell"

`http://jes.ecsdl.org/lookup/doi/10.1149/2.1431714jes`

A Unit Cell Model of a Regenerative Hydrogen-Vanadium Fuel Cell

C. A. Pino Muñoz,[*,z] H. Hewa Dewage, [a] V. Yufit,[**] and N. P. Brandon

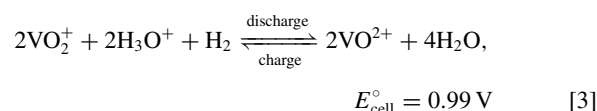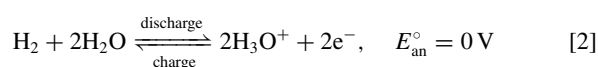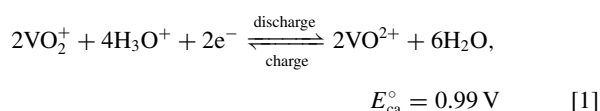*Department of Earth Science and Engineering, Imperial College London, London SW7 2AZ, United Kingdom*

In this study, a time dependent model for a regenerative hydrogen-vanadium fuel cell is introduced. This lumped isothermal model is based on mass conservation and electrochemical kinetics, and it simulates the cell working potential considering the major ohmic resistances, a complete Butler–Volmer kinetics for the cathode overpotential and a Tafel–Volmer kinetics near mass-transport free conditions for the anode overpotential. Comparison of model simulations against experimental data was performed by using a 25 cm² lab scale prototype operated in galvanostatic mode at different current density values $(50 - 600\,\text{A m}^{-2})$. A complete Nernst equation derived from thermodynamic principles was fitted to open circuit potential data, enabling a global activity coefficient to be estimated. The model prediction of the cell potential of one single charge-discharge cycle at a current density of $400\,\text{A m}^{-2}$ was used to calibrate the model and a model validation was carried out against six additional data sets, which showed a reasonably good agreement between the model simulation of the cell potential and the experimental data with a Root Mean Square Error (RMSE) in the range of 0.3–6.1% and 1.3–8.8% for charge and discharge, respectively. The results for the evolution of species concentrations in the cathode and anode are presented for one data set. The proposed model permits study of the key factors that limit the performance of the system and is capable of converging to a meaningful solution relatively fast (s–min).

Redox flow batteries are considered to be an exceptional candidate for grid-scale energy storage. One attractive feature is their capability to decouple power and energy.[1–4] All-Vanadium Redox Flow Batteries (VRFBs) have been considered a promising system due to the limited impact of cross-contamination. However, they have faced challenges related to cost, scale-up and optimization. Current research is also focused on improvement of electrolyte stability for use over a wider temperature window and concentrations, development of electrode materials resistant to overcharge, and mitigation of membrane degradation.[1,2] Cost dependency with regarding to vanadium can be mitigated through utilization of new systems that employ only half of the vanadium.[1] Recently, a Regenerative Hydrogen-Vanadium Fuel Cell (RHVFC) based on an aqueous vanadium electrolyte V(V) and V(IV) and hydrogen has been introduced[5] and is illustrated schematically in Figure 1. This system contains a porous carbon layer for the positive electrode reaction, membrane and catalyzed porous carbon layer for the negative electrode reaction. Hydrogen evolution, which is an adverse reaction in VRFBs, is here the main anodic process. During discharge, V(V) is reduced to V(IV) and H_2 is oxidized, while the reverse process occurs during charge and H_2 is stored. The vanadium reaction takes place in the positive electrode (cathode), while the hydrogen reaction occurs in the catalyst layer (CL) of the negative electrode (anode). The redox reactions that occur at the electrodes are presented in Equations 2 and 1, and the overall cell reaction in Equation 3, where the charged species VO^{2+} and VO_2^+ represent the V(IV) and V(V) oxidation states, respectively; and E° is standard potential with the subscripts ca and an referring to positive and negative side respectively.

$$2VO_2^+ + 4H_3O^+ + 2e^- \xrightleftharpoons[\text{charge}]{\text{discharge}} 2VO^{2+} + 6H_2O,$$

$$E^{\circ}_{\text{ca}} = 0.99\,\text{V} \qquad [1]$$

$$H_2 + 2H_2O \xrightleftharpoons[\text{charge}]{\text{discharge}} 2H_3O^+ + 2e^-, \quad E^{\circ}_{\text{an}} = 0\,\text{V} \qquad [2]$$

$$2VO_2^+ + 2H_3O^+ + H_2 \xrightleftharpoons[\text{charge}]{\text{discharge}} 2VO^{2+} + 4H_2O,$$

$$E^{\circ}_{\text{cell}} = 0.99\,\text{V} \qquad [3]$$

The RHVFC could offer a better energy storage solution because of its fast hydrogen kinetics and absence of cross-mixing: even when the crossover of catholyte is possible, this could be collected at the anode side and pumped back to the catholyte tank.[5–7] An in depth analysis of the system by means of experimental studies has been reported previously by our group.[5,7] Yufit et al.[5] studied the performance of a RHVFC and observed that higher current densities or lower catholyte flow rates produce lower coulombic efficiencies, which can be explained by the mass transport limitations. Hewa Dewage et al.[7] studied the loss mechanisms of a RHVFC, observing crossover of vanadium, which could be adsorbed onto the anode Pt catalyst, and a negligible influence of the hydrogen flow rate. A better performance could be obtained if improved component materials and operating conditions were used. Modelling and simulation is an indispensable tool, saving time and reducing cost. To the best of the authors' knowledge, only one RHVFC model has been developed, as part of a PhD project,[8] which presented a one-dimensional steady-state approach. Common VRFB assumptions were considered for the cathode,[8–10] while the Membrane Electrolyte Assembly (MEA) was modeled using the assumptions developed by Bernardi and Verbrugge.[11,12] Only protons were allowed to cross the membrane, which was assumed
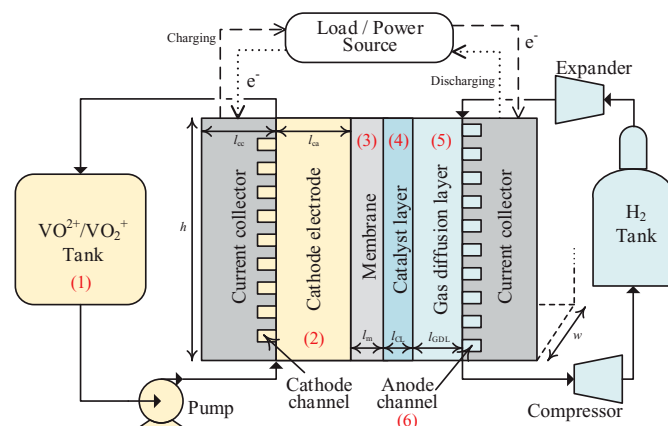
*Electrochemical Society Student Member.
**Electrochemical Society Member.
[a]Present address: M-KOPA SOLAR Kenya Ltd.
[z]E-mail: c.pino15@imperial.ac.uk

Figure 1. Schematic of the RHVFC and model domains.

C.2 Publication 2

"Characterisation of a Regenerative Hydrogen-Vanadium Fuel Cell Using an Experimentally Validated Unit Cell Model"

Characterization of a Regenerative Hydrogen-Vanadium Fuel Cell Using an Experimentally Validated Unit Cell Model

C. A. Pino-Muñoz, [z] B. K. Chakrabarti, V. Yufit, and N. P. Brandon

Department of Earth Science and Engineering, Imperial College London, London SW7 2AZ, United Kingdom

A hydrogen-vanadium electrochemical system was characterized using extensive experimental tests at different current densities and flow rates of vanadium electrolyte. The maximum peak power density achieved was 2840 W m^{-2} along with a limiting current density of over 4200 A m^{-2}. The cycling performance presented a stable coulombic efficiency over 51 cycles with a mean value of 99.8%, while the voltage efficiency decreased slowly over time from a value of 90.3% to 87.0%. The capacity loss was of 5.6 A s per cycle, which could be related to crossover of ionic species and liquid water. A unit cell model, previously proposed by the authors, was modified to include the effect of species crossover and used to predict the cell potential. Reasonable agreement between the model simulations and the experimental charge-discharge data was observed, with Normalized Root-Mean-Square Errors (NRMSEs) within the range of 0.8–5.3% and 2.9–19.0% for charge and discharge, respectively. Also, a good degree of accuracy was observed in the simulated trend of the polarization and power density, with NRMSEs of 3.1% and 1.0%, and 1.1% and 1.9%, for the operation at a flow rate of vanadium electrolyte of 100 and 50 mL min^{-1}, respectively, while the voltage efficiency during the cycling test were estimated within a Root-Mean-Square Error (RMSE) of 1.9%. A study of the effect of the component properties on the cell potential was carried out by means of a model sensitivity analysis. The cell potential was sensitive to the cathodic transfer coefficient and the cathode porosity, which are directly related to the cathodic overpotential through the Butler-Volmer equation and the cathodic ohmic overpotential. It was recognized that a kinetic study for the cathodic reaction is needed to obtain more reliable kinetic parameters at practical vanadium concentrations, as well as reliable microstructural parameters of carbon electrodes.

The rapid growth in the deployment of renewable energy sources such as wind, solar and others, has increased interest in electrochemical energy storage.[1,2] All-Vanadium Redox Flow Batteries (VRFBs), having the ability to decouple power and energy, with limited impact of cross-mixing, have drawn increasing attention from researchers.[3–6] Amongst VRFB limitations are the relatively low solubility and stability of vanadium ions in sulphuric acid solutions, and the high cost of vanadium-based electrolytes and membranes.[2–4,7] Electrolyte imbalance due to species crossover across the membrane can also be a challenge. To reduce cost dependency with regards to vanadium, new systems that employ only half of the vanadium required in a VRFB have been proposed and demonstrated.[3] Alternatively, hybrid-type Redox Flow Batteries (RFBs) such as hydrogen-halogen, have gained interest due to their fast reversible kinetics and the facile separation of crossover species if present.[8,9] However, significant safety concerns related to high vapor pressures, including leakage or release of toxic fumes exist for cells utilizing chlorine or bromine.[3,10] A Regenerative Hydrogen-Vanadium Fuel Cell (RHVFC) benefits from the advantages of the mixed liquid-gas RFBs, and reduces the overall system cost by utilizing only half of the vanadium electrolyte required for a VRFB. Still, a precious metal catalyst is required at the anode for the Hydrogen Oxidation/Evolution Reaction (HOR/HER). Capacity loss in the RHVFC due to crossover of catholyte solution to the anodic half-cell can be regained by collecting any crossover of vanadium electrolyte and returning it to the vanadium tank,[11] while capacity loss due to self-discharge or side reactions[12] could be regained by similar methods to those used in conventional VRFBs. The RHVFC was first proposed and demonstrated by Yufit et al.,[11] with a peak performance of 114 mW cm^{-2} at 100% SOC. The RHVFC utilizes V(V) and V(IV) as the cathodic redox couple, and hydrogen and protons as the anodic redox couple. The cell structure generally contains a porous carbon layer for the cathode, a cation exchange membrane and a catalyzed porous carbon layer for the anode, along with serpentine or interdigitated flow fields.[9,11,13] Figure 1 shows the typical single-cell assembly for the hydrogen-vanadium system. During discharge, V(V) is reduced to V(IV) and H$_2$ is oxidized to H$^+$, while the reverse process occurs during charge and H$_2$ is produced. A study of the loss mechanisms of the RHVFC was introduced,[9] observing that

the cathodic diffusion and ohmic losses are the largest contribution to the total polarization, and the possible adsorption of vanadium ions onto the platinum catalyst. The cathodic losses could be explained by the partial wettability of the cathode due to its hydrophobic nature and the need for heat-treatment.[14–16] More recently, a first modelling approximation of the various physico-chemical phenomena involved in a RHVFC was proposed and validated.[17] Mathematical modelling and simulation of electrochemical cells are used to relate operational conditions to performance, predict and rationalize experimental findings and to study performance optimization.[2,18] The model combines a series of differential and algebraic equations assuming a uniform spatial distribution of species concentrations.[17] The model formulation, i.e., a zero-dimensional approach, maintains simplicity in comparison to spatially distributed approaches in order to allow its practical use in system monitoring and design where the fast computational speed is essential. Despite the implemented simplifications, the unit cell model was able to describe the potential dynamics of a hydrogen-vanadium cell of 25 cm^2 electrode cross-sectional area. This cell presented, however, some limitations including high ohmic losses that made it difficult to extract the electrode overpotentials in the cell. As part of this unit cell model, a complete Nernst equation was proposed to estimate the cell Open Circuit Potential (OCP), along with a complete Butler-Volmer (BV) approach to describe the relationship between current density and overpotential at the cathode. Unlike previous VRFB models, this complete BV approach includes all active ionic species involved in the redox reaction at the cathode. Also recently, Dowd et al.[13] demonstrated an improved performance for the RHVFC, reaching a power density of 540 mW cm^{-2} when using a carbon nanotube cathode, thinner membranes, and interdigitated flow fields. They also presented a crossover study,[12] showing that Electrospun Blended Nanofiber (EBN) based membranes (Nafion/PVDF, 30–40 μm) were capable of reducing the crossover rates while maintaining similar performance in comparison to those shown by conventional Nafion membranes.

In this study, a characterization of the performance of the RHVFC is presented. This performance study is based on experimental data obtained using a cell of 5 cm^2 electrode cross-sectional area and simulations from a validated unit cell model. In the following section, we calibrate and validate the unit cell model, using experimental measurements of electrochemical impedance spectroscopy (EIS), OCP, single-cycle charge-discharge potential at galvanostatic operational mode, polarization curves and cycling. Then, a sensitivity analysis of

[z]E-mail: c.pino15@imperial.ac.uk